Modelling droplet impact in fluid-structure interaction problems

Michael Negus

Keble College

University of Oxford

A thesis submitted for the degree of

Doctor of Philosophy

October 2022

Acknowledgements

Completing this thesis over the past four years has been one of the most fulfilling and challenging tasks I have ever undertaken, and it would not have been possible without the support and guidance of the people who stuck around me throughout the process.

First of all, I would like to thank my supervisors, Professor James Oliver, Dr Matthew Moore and Dr Radu Cimpeanu. Their continued expertise and guidance has helped me mature into a more confident researcher and all-round human. I want to particularly thank them for supporting me continuously throughout these turbulent few years, whether in-person or remotely.

I have been incredibly fortunate to have been surrounding by an amazing group of friends and colleagues in the Mathematical Institute, including (but not limited to) Edwina Yeo, Helen Saville, Amy Kent, Matthew Shirley, Philip Winchester, Arkady Wey and George Atkinson. Thank you for the coffee breaks, afternoon walks, virtual lunches, cross-continental trips and, most of all, for putting up with my regular rants.

My transition into the bizarre world of Oxford was made incredibly enjoyable by all those I met at Keble in my first year, and have stuck around right until the end. In particular, I want to thank Caiban Butcher, Heike Kuhn, James Paterson and Joanna Perks for making my time in Oxford so enjoyable. And of course, I want to thank Shannon Brunette for being by my side from day one, I could not have done this without your care and support, and I am forever grateful for that.

In addition, I want to thank Laurence Cullen and Ellie Winter for graciously showing me their immense hospitality and support over the last two months in the challenging final stages of writing this thesis.

Lastly, I want to thank my entire family for always believing in me, and showing me the love and support that brought me here. I would have never thought this boy from Camborne could have reached this point, and I owe it to you all that I am here.

Abstract

The impact of a liquid droplet onto a deformable substrate is a physical phenomenon that appears ubiquitously in both natural and industrial contexts. The fluid-structure interaction between the droplet and the substrate results in a complex and highly nonlinear system, and is a significant modelling challenge. In this thesis, analytical and numerical modelling techniques for these systems are presented with the aim of providing physical insight and quantitative predictions on the dynamics of the droplet as the properties of the substrate are changed.

In Chapter 1, we motivate the thesis by outlining relevant real-world scenarios involving droplet impact onto deformable substrates, and present a review of the existing literature. In Chapter 2, we setup the canonical droplet impact system that will be used throughout the thesis, including the statement of governing equations, non-dimensionalisation and any assumptions that apply throughout. We present an analytical model for this system in Chapter 3, where we exploit the small timescale of impact phenomena to derive a matched asymptotic solution based on Wagner's theory of impact. To validate the analytical model and investigate regimes which Wagner theory cannot reach, a numerical modelling technique is then considered in Chapter 4, where we use the volume-of-fluid method to conduct direct numerical simulations of the system. We present a novel approach to model the fluid-structure interaction within a two-phase scenario by employing a moving frame coordinate transformation. In Chapters 5 and 6, we apply the previously developed models to study droplet impact onto a spring-supported plate and an elastic membrane, respectively. We find how the deformation of the substrate affects the dynamics of the droplet via slowing down the spreading, decreasing the pressure and reducing the amount of fluid ejected across the substrate. By making use of both modelling techniques, we explore a wide range of substrates by varying the elasticity, tension, mass and dampening properties of the substrate. We then quantify how changing these physical properties of the substrate affects the dynamics of the droplet and in turn the displacement of the substrate during the impact process. Finally, in Chapter 7, we summarise the main results and discuss directions for further work.

Contents

Chapter 1

Introduction

1.1 Motivation and background

The impact of a liquid droplet onto a deformable substrate is a physical phenomenon that appears ubiquitously in both natural and industrial contexts. The fluid-structure interaction between the droplet and the substrate results in a complex and highly nonlinear system, and poses a significant modelling challenge. In this thesis, analytical and numerical modelling techniques for these systems are presented with the aim of providing physical insight and quantitative predictions on the dynamics of the droplet as the properties of the substrate are changed.

Scientific interest in these droplet impact systems originates at least as far back as Worthington (1877) [99], who used early photographic techniques to categorise the shapes of droplets impacting onto a plate. Much progress has been made since then, and modern research in the area involves a collaboration of experimental, mathematical and computational approaches. The dynamics of droplet impact depends on the complex interplay between a number of physical properties of the system, such as the inertia of the droplet, the viscosity and surface tension of the liquid and surrounding gas, the gravitational forces and the material properties of the substrate. Depending on the physical context, the importance of each of these factors will differ, however for this thesis we will focus on inertia-dominated regimes, such as the scenario of falling raindrops, which are typically on the millimetric scale with a terminal velocity of approximately 9 m/s. However, there are a wealth of other regimes which are of interest for their applications in both nature and industry (which we will detail in the following), and we direct the reader to Josserand and Thoroddsen (2016) [48] for a more extensive review on droplet impact.

The focus of investigation into droplet impact can depend on a number of important phenomena relevant to industry and nature. Example quantities of interest

include the maximum width of spreading across the substrate or the entrapment of gas between the impacting droplet and the substrate. However one phenomenon which has received particular attention in recent years is splashing. The definition of splashing differs between authors, but for this thesis we use the definition outlined in Yarin (2006) [102], which is when at any point during the impact, the interface of the droplet breaks apart and numerous small secondary droplets are ejected. Understanding splashing is important for a wide range of contexts. In some instances, splashing can be non-ideal such as for inkjet printing (Derby (2010) [21]) or medical contexts where splashing of infectious fluids needs to be prevented (Harrel and Molinari (2004) [36]). Equally, sometimes splashing is desirable, such as on the surface of a car windscreen where rain droplets need to be broken up and dispersed (Gaylard et al. (2017) [28]), and for the distribution of pesticides on the leaves of crops (Knoche (1994) [50]). It is thought that splashing is driven by instabilities in the liquid-gas interface as the droplet spreads across the surface, and that these instabilities are more likely to occur when the liquid is travelling faster. Thus a quantity of interest for many experimental practitioners is the so-called *splashing threshold*, which is defined to be the velocity threshold in which droplets either splash or do not splash if their velocity is above or below the threshold upon impact. The value of the splashing threshold is a contentious point in the literature, and different authors' derivations of its value have varying levels of agreement with experimental results (see Palacios et al. (2013) [68] for a thorough experimental study). Whilst historically most formulae of the splashing threshold have only taken into account the Reynolds and Weber numbers of the droplet (such as Mundo et al. (1995) [64]), numerous experimental studies have shown that a wealth of other properties of the system can alter the splashing threshold. For example, Xu et al. (2005) [101] showed that decreasing the pressure in the surrounding air can suppress splashing, and Xu (2007) [100] found that the roughness of the substrate can promote splashing behaviour.

There have also been recent research efforts to investigate how deformation of the substrate can affect the splashing threshold. In the experimental study of Pepper et al. (2008) [72], identical millimetric ethanol droplets were impacted onto an elastic sheet in which the tension could be adjusted. They found that by reducing the tension in the membrane, the splashing could be suppressed, therefore raising the splashing threshold. Through laser interferometry techniques, they measured that the deformation in the membrane was greater during the impact when the tension was decreased, thus meaning that the compliance of the substrate was linked to the reduction in splashing. Instabilities in the lamellae, the thin sheets of liquid that

is ejected across the substrate that can eventually break up into the splash, were observed within the first few hundred microseconds of the impact, and the resulting splash was seen after approximately one millisecond. Thus the early times of the impact process were identified as being important in understanding the dynamics of the splash. Using high-speed video imaging, they found that the velocity and deceleration of the lamella was lower during the first hundred microseconds for the cases with lower membrane tension, indicating that the membrane acted to slow down the spreading of the droplet across the membrane at early times, far before the splash actually occurred. The fact the lamella velocity was lower in these low tension cases provided a possible explanation as to why the splashing was suppressed, as lower lamella velocities meant they were less prone to Rayleigh-Taylor-type instabilities from the air.

A similar experimental investigation was carried out by Howland et al. (2016) [46], where high-speed millimetric ethanol droplets were impacted onto silicone gels of different stiffnesses. They found that the splashing threshold was increased when the stiffness of the substrate (measured by its Young's modulus) was decreased. The reduction in splashing in these cases was also determined to be due to deformations in the substrate, as they also tested the impact of a droplet onto a glass slide coated with a 3 μm thick coating of gel, in which they found the impact on this surface to be much more violent than impacts onto deep substrates made of the same gel. Using high-speed photography, they showed that the ejection of the lamella was significantly slowed down during the impacts onto softer gels, which is similar to the findings of Pepper et al. (2008) [72] when impacting onto membranes with lower tension. By conducting direct numerical simulations, Howland et al. (2016) [46] found that the pressure in the droplet was reduced when the substrate deformation was higher. When the pressure in the droplet is lower, the lamella will be ejected at a lower speed, thus making the droplet less likely to splash.

Both Pepper et al. (2008) [72] and Howland et al. (2016) [46] identified that the early stages of the impact process when the lamella is first ejected onto the substrate as being important for determining whether or not the droplet splashes at later times. However, there is currently not a full understanding into the physical mechanisms at play during these early times due to the difficulty of experimentally measuring the small length-scales and short time-scales of the process. These studies emphasise the importance of the early times of the impact with regard to splashing, however we are yet to define what categorises the different timescales of the droplet impact process as a whole. Although these definitions are not strict, in the following we will detail

four different stages of impact that will be relevant to the discussions in this thesis, and the experimental and modelling challenges that they present.

1.1.1 Pre-impact

Prior to impact, the droplet will be travelling downwards towards the substrate through the surrounding gas. When the droplet is far away from the substrate, so long as the droplet velocity is much less than the speed of sound of the gas (which is approximately 343 m/s in air), the surrounding gas will readily move away from the droplet and will have little influence on the droplet. However, as the droplet approaches the substrate, a region of high pressure in the gas will form below the droplet, as it cannot escape as easily as before. This region of high-pressure gas can cause the bottom of the droplet to dimple prior to impact, an effect referred to as *air-cushioning*. The dimple at the bottom of the droplet will cause it to make contact with the substrate off-centre, and, after touchdown, this dimple can contract to form a bubble, which was observed using high-speed photography techniques by Thoroddsen et al. (2003) [90]. With the advancement of recent imaging capabilities, there has been a wealth of experimental investigations studying the dynamics of these entrapped bubbles, and we direct the reader to Josserand and Thoroddsen (2016) [48] for an extensive review.

Early models of the effects of air-cushioning in two-dimensions were derived by Wilson (1991) [98], Smith et al. (2003) [83] and Korobkin et al. (2008) [53], where usually the entrapped air was modelled as a thin, viscous layer and the bulk fluid was treated as inviscid. The dimensional arguments of these articles are summarised well in Mandre et al. (2009) [58]. Hicks and Purvis (2010) [39] extended the theory to axisymmetric impacts, allowing for the air-cushioning of droplet impact to be modelled under the condition that the surface tension and viscosity of the liquid can be neglected. As well as impact on solid surfaces, air-cushioning has also been studied for impact on a porous-medium (Hicks and Purvis (2017) [41]) and droplet impact onto liquid layers and other droplets of the same fluid (Hicks and Purvis (2011) [40]). If the substrate in question is deformable, the high-pressure air layer can also act to deform the substrate prior to impact as well as the droplet. The recent studies of Pegg (2019) [69] and Henman et al. (2021) [38] applied air-cushioning models to droplets impacting onto deformable substrates, while Pegg (2019) [69] considered the axisymmetric impact of a droplet onto an elastic plate and Henman et al. (2021) [38] consider the two-dimensional impact onto a more generalised substrate. Typically, the deformation of the substrate in these cases acted to delay the touchdown time of

the droplet more than would be the case were the substrate stationary. However, for many physically relevant cases, the force required to deform a solid substrate will be much greater than that of the liquid droplet, so typically the air-cushioning mainly affects the droplet; nevertheless there may be regimes in which this deformation has an important role to play in the impact dynamics, such as impact onto leaves.

1.1.2 Early impact

Shortly after touchdown, the bulk of the droplet will still be unaffected by the impact. It is only in a small region near the substrate that the droplet starts to change its shape as it begins to spread across the surface. Mathematical progress can be made at this early impact stage by finding approximate solutions to the flow under the assumption that the droplet has been slightly perturbed from its initial profile. As observed experimentally by Thoroddsen (2002) [89], the lamella is ejected at very early times, where the bulk of the droplet is still relatively unperturbed. Since the lamella is ejected so early, Howland et al. (2016) [46] proposed that the deformation of the soft surface during this stage has a major impact on whether the droplet splashes at later times, which motivates the need for analytical models to understand the dynamics of this stage.

To review early time droplet impact problems, we first focus on the closely-related field of the water-entry of solid bodies into a body of liquid, usually under the assumption that the body is travelling fast enough that the viscosity, surface tension and surrounding gas can be safely neglected. The earliest studies of this problem were by von Kármán (1929) [93] and Wagner (1932) [94], who investigated the force felt on the floats of a seaplane as it landed on water. Wagner modelled the float as a long wedge falling downwards and impacting into a stationary pool of liquid. A key part of Wagner's theory was that, for a sufficiently shallow body profile, the problem is analogous to the impact on a free surface of a flat plate whose width is changing in time (see Korobkin and Pukhnachov (1988) [56] for an extensive review). This significantly simplifies the problem, and allows a leading-order solution to be found using complex variable techniques. This "flat plate analogy" is why these methods fall under so-called *Wagner theory*.

In the following years, Wagner theory was extended from its original formulation. Upon impact, high velocity jets of fluid travel up the sides of the wedge, as seen experimentally by Greenhow (1987) [32]. Wagner was aware of these jets, however did not solve the flow problem for these, as he was primarily concerned with calculating

the hydrodynamic force felt by the wedge, and, to leading-order, the jets do not contribute to this force. However, as shown by Cointe et al. (2004) [19], half of the kinetic energy given to the fluid from the impactor goes into the jets, meaning they cannot be neglected if energy is to be conserved. Wagner theory has also been extended to consider non-wedge shaped bodies, such as blunt bodies (Korobkin and Pukhnachov (1981) [55]), cylinders (Cointe and Armand (1987) [18]) and parabolas (Howison et al. (1991) [45]), and Wagner theory was formalised using matched asymptotic expansions by Wilson (1989) [97] and Howison et al. (1991) [45]. This analytical framework has also been extended to three-dimensional bodies, with approximate solutions via numerical algorithms given by Korobkin (1982) [51] and Howison et al. (1991) [45].

As first considered by Howison et al. (2005) [44], the Wagner theory formulation can be applied to the early times of droplet impact. A key assumption in Wagner theory is that the impacting body has a small deadrise angle, meaning that close to the point of contact, the body is almost flat. If we zoom in to the point of contact of a fluid impacting onto a substrate at early times, then the radius of curvature of the undisturbed free surface is much larger than the size of the contact region between the liquid and substrate. Therefore, the impacting fluid will look almost flat from this point of view. It is for this reason that the results of Wagner theory for water-entry problems can be almost immediately transferred to droplet impact problems. Subsequently, the force felt on an axisymmetric paraboloid impacting into a deep pool (see Oliver (2002) [66]) will be the same as the force the substrate feels after an impact of an axisymmetric droplet (see Philippi (2016) [74]). This mathematical equivalence allows the application of years of research into water-entry problems to be constructively adapted to problems in fluid impact.

Wagner theory can be utilised for fluid impacts on various types of substrates. Due to its simplifying assumptions of neglecting viscosity, the chemical properties of the substrate do not play a role in the theory. Subsequently, the results derived when considering liquid impact on a solid substrate can be readily transformed to liquid-liquid impacts, such as droplet impact on a liquid layer in Howison et al. (2005) [44] and droplet-droplet impacts in Cimpeanu and Moore (2018) [15]. The studies of Oliver (2002) [66] and Moore (2014) [62] considered both two-dimensional and three-dimensional impactors with time dependent vertical velocities. These results can be transformed to consider fluid impact onto substrates which can move in the vertical direction. To create a simple model of a movable substrate, a physical law coupling the displacement of the substrate to the hydrodynamic force from the fluid can be used (such as was considered by Negus et al. (2021) [65]). Wagner theory has

also been used to model wave impact onto an Euler beam (Korobkin (1998) [52]) and droplet impact onto an elastic plate (Pegg et al. (2018) [70]). However, more complex deformable substrates, such as elastic half-spaces and oil-coated substrates, have not yet been considered.

The analytical solution for the velocity field found from Wagner theory can be used to find the distribution of the kinetic energy of the impacting liquid, as derived by Cointe et al. (2004) [19] for water-entry problems. This type of energy analysis was conducted by Korobkin and Khabakhpasheva (2006) [54] for wave impact onto an elastic plate and Scolan (2004) [81] for the water-entry of an elastic conical shell. In the context of droplets impacting onto soft substrates, such as in Howland et al. (2016) [46], this analysis could give insight into the mechanism by which splashing is suppressed by finding the amount of energy that is lost deforming the substrate.

One of the shortcomings of using Wagner theory to model the early stages of impact is that it relies on neglecting the influence of viscosity, surface tension and the surrounding gas. As discussed in the previous subsection, we know that in some instances surrounding gas can cause a bubble to be entrapped inside the droplet upon impact, resulting in the droplet initially contacting the substrate off-centre. By neglecting the surrounding gas, traditionally the Wagner model does not take this entrapped bubble into account in the early time dynamics, assuming that the droplet initially touches the substrate at its centre. However, pre-impact air cushioning effects have recently been incorporated into post-impact Wagner theory by Moore (2021) [63]. It is difficult to assess the effects of neglecting these physical effects, including viscosity and surface tension, via direct comparisons with experiments due to the short time-scales and small length-scales. Thus, numerical methods provide a viable alternative for cross-validation, which we will detail in the following subsection.

1.1.3 Intermediate impact

The Wagner model relies on the assumption that the droplet has only been perturbed from its initial shape in a small region close to the initial point of contact. Thus, as discussed in greater depth in Chapters 5 and 6, the Wagner model begins to break down once the droplet has spread across the substrate enough such that the contact region is of the same order of size as the diameter of the droplet. Typically, during this intermediate time, the upper part of the droplet still remains relatively unaffected by the impact (for example see Figure 2 in Howland et al. (2016) [46]), but the rest of the droplet has been significantly deformed from its initial shape. At this timescale,

one must usually resort to numerical methods in order to model the dynamics. Computational modelling of such systems poses a considerable challenge, since we need to model a two-phase flow problem with high contrast in density and viscosity between the phases, as well as taking surface tension into account. Efficient computation of such systems has only been realistically possible within the last 10-15 years with the development of advanced computational fluid dynamics algorithms. We will briefly review recent advances in the efforts to model these systems numerically here, and provide a more extensive review of such computational methods in Chapter 4.

Although there are numerous numerical methods available for modelling two-phase flow, the volume-of-fluid (VOF) method has become one of the most popular choices over the last decade. Direct numerical simulation (DNS) methods using the VOF method use a continuous scalar field to distinguish between the liquid and gas phases, and solve the full Navier-Stokes equations and advects this scalar field with the fluid flow. The scalar function is then used to reconstruct the interface location between the two fluid phases. VOF methods are attractive as they are inherently mass conserving, unlike similar methods such as the level set method (see Mirjalili et al. (2017) [59] for a more comprehensive discussion). However, one of the challenges of the VOF method is the accurate determination of surface tension, as often the interface location is only given piecewise, which makes accurate determination of the interface curvature difficult. Some of the most popular implementations of the VOF method are the open-source codes *Gerris* (https://gfs.sourceforge.net/), and its successor *Basilisk* (http://basilisk.fr/). *Gerris* was first introduced by Popinet (2003) [75] as an incompressible flow solver for the Euler equations. One of the strengths of *Gerris* was its use of adaptive grid refinement. Many two-phase flow problems are multi-scale, with localised areas of interest. This is often the case in droplet impact, where typically the dynamics of the problem are localised close to the droplet interface, with the bulk of the droplet remaining predominately undisturbed at early-to-intermediate times. With adaptive grid refinement, areas of interest in the problem can be resolved to high accuracy, whilst keeping the computational grid coarse in other regions. Thus Popinet (2003) [75] developed an efficient implementation of the VOF scheme that allowed for accurate computation at a fraction of the cost of schemes that use a uniform grid. Subsequently, in Popinet (2009) [76], *Gerris* was extended to solve the full Navier-Stokes equations, including a second-order accurate scheme for determining the effect of surface tension in two-phase flow problems. In the last decade, this has opened the way for researchers to study a variety of droplet impact systems using

DNS. Some notable examples include Thoraval et al. (2012) [88], where *Gerris*' adaptive grid capabilities allowed them to observe a von Kármán vortex street within an impacting droplet onto a liquid pool; Philippi et al. (2016) [74] studied the impact of a droplet onto a solid surface and provided extensive cross-comparisons between the DNS predictions and axisymmetric Wagner theory; and Cimpeanu and Papageorgiou (2018) [16] developed DNS for studying three-dimensional droplet impact onto solid substrates at arbitrary angles.

The open-source code *Basilisk*, the successor of *Gerris*, was first presented by Popinet (2015) [77]. *Basilisk* implements the same VOF scheme as *Gerris*, but within the framework of the *C* programming language [79], which more readily allows users to develop additional features to the code. This makes *Basilisk* a popular option amongst the research community over closed-source fluid dynamics packages such as Ansys Fluent [3] and COMSOL Multiphysics [20]. As a result, *Basilisk* has been at the centre of many of the most recent developments in DNS methods.

As the efficient simulation of two-phase flows has only recently become possible, the progress in including fluid-structure interaction into these simulations is still in its infancy. A particular challenge in this regard is resolving the triple-contact points where liquid, gas and solid meet as the droplet spreads across the substrate. In this endeavour, recent developments in the *Basilisk* community have included initial implementations of three-phase flow simulations (for example, see http://basilisk.fr/sandbox/vatsal/ThreePhase/), which can handle these triple contact points. However, two-phase flow simulations which include a moving embedded boundary are not currently supported by *Basilisk*, and this has been identified as a high-priority avenue for future development.

1.1.4 Late impact

The late time of impact is characterised as when the entire droplet interface has been significantly deformed by the impact, and the droplet begins to flatten and spread across the substrate. Many factors such as the impact speed, viscosity and surface tension determine the dynamics at this time, a complex behaviour which is extensively reviewed by Yarin (2006) [102] and Bonn et al. (2009) [10]. The properties of the substrate have a particularly important role to play at this late time, as the kinetic energy of the droplet is progressively balanced and eventually dominated by capillary effects. Typically, droplets at these late times either break up into a crown splash, or otherwise the droplet reaches a maximum spreading radius once the kinetic energy of the droplet has been completely converted into surface energy. If the substrate

is hydrophobic, the surface energy can then cause the droplet to retract back and eventually rebound off the substrate, otherwise if the surface is wettable, the droplet can remain in place after spreading (see Yarin (2006) [102] for a full discussion). Many experimental investigations focus on these late time dynamics, as they typically occur over a longer time and length scale than the early-to-intermediate stages, making them more readily observed using video acquisition techniques. Particular experimental focus on the influence of the interaction between the droplet and a movable substrate has gained ground in recent years. Inspired by the natural phenomenon of rain droplet impact onto leaves, Gart et al. (2015) [27] investigated the impact of droplets onto the end of cantilever beams. They found that oscillations induced in the beam by the droplet affected the late-time spreading of the droplet, and the vibrations had the capacity to propel the droplet off the beam vertically. Similarly, Weisensee et al. (2017) [95] studied the impact of droplets onto elastic superhydrophobic substrates, and found that the oscillations induced by the impact could reduce the amount of time the droplet made contact with the substrate before it is repelled off at the rebound stage. For this thesis, we will not investigate the late impact stage in detail, however a wealth of analytical and computational investigations of this stage exist, such as the studies by Eggers et al. (2010) [24] and Wildeman et al. (2016) [96].

1.2 Aim and structure of thesis

The aim of this thesis is to investigate the fluid-structure interaction of a high-speed droplet impacting onto a movable substrate at the early-to-intermediate time stages. As discussed in the previous section, these timescales are difficult to measure experimentally due to their multi-scale features and rapidly changing topologies. In addition, the studies of Pepper et al. (2008) [72] and Howland et al. (2016) [46] identified the early time of impact to be critical in determining whether or not a droplet splashes when impacting onto a deformable substrate, and the exact mechanism for which the fluid-structure interaction can suppress splashing is still unknown. In this endeavour, we will employ two different modelling strategies, using an analytical model based on inviscid Wagner theory and direct numerical simulations using the volume-of-fluid solver Basilisk. The analytical modelling will allow us to gain deeper insight into the early time dynamics of the impact at little to no computational cost, with the DNS being used to cross-validate the results of the analytical model and assess the effects of the features of the system neglected by the analytical model. The DNS will also be used to explore the intermediate timescale of the problem which is out of reach of the

analytical model, however coming at a much greater computational cost. By utilising the analytical model, we will be able to explore a wide range of substrate parameter spaces at low computational cost, which can then inform us of regimes of interest to explore more extensively via DNS. By developing these two models in tandem, we will be able to use the results of each model to inform the direction we take the other, in order to develop a modelling framework that can be used to extensively investigate these fluid-structure interaction systems.

We begin the thesis in Chapter 2, where we define the governing equations and modelling assumptions that we will use throughout the thesis for both the analytical model and the DNS. The analytical model is derived in Chapter 3 for both two-dimensional and axisymmetric impact onto a movable substrate, and in Chapter 4 we present the framework developed and used to conduct the DNS. In Chapter 5, we apply the analytical model and DNS to study the axisymmetric impact of a droplet onto a spring-supported plate, and in Chapter 6 we do the same for the two-dimensional impact of a droplet onto an elastic membrane. Finally, in Chapter 7, we conclude the thesis and discuss avenues for future work.

1.3 Statement of originality

The analytical model derived in Chapter 3 is predominantly based on previous inviscid Wagner theory studies, however originality arises from deploying these models in the context of droplet impact onto movable substrates. We are not aware of any previous study which determined the jet dynamics across a substrate moving in space and time in two dimensions as in §3.2.5. We also believe the consideration of the outer-outer region in an axisymmetric coordinate system in §3.3.5 is original. The derivation of the composite force in §3.2.8 and §3.3.7 is also novel, as its determination was motivated by comparisons to results from the DNS. Previous studies modelling droplet impact using *Basilisk* do exist, and the linearised boundary setup from §4.4.2 was originally considered by Howland et al. (2016) [46]. To the best of our knowledge however, the moving frame setup for impact onto a rigid moving substrate in §4.4.1 is a new contribution to the field. The novel work of modelling impact onto a spring-supported plate in Chapter 5 is published in Negus et al. (2021) [65], although in this thesis we explore the parameter space in greater detail. For Chapter 6, the normal modes method for the analytical model was previously utilised by Korobkin (1998) [52] for wave impact onto an Euler beam and Pegg et al. (2018) [71] for droplet impact

onto elastic plates, but the solution via the finite difference method in §6.1.2 and the cross-comparisons between the analytical model and DNS in this chapter are original.

Chapter 2

System definitions

2.1 Setup and modelling assumptions

We consider the impact of a liquid droplet onto an initially flat impermeable substrate, where the droplet is initially spherical with radius R_d^* at a height $H^* > 0$ above the substrate. Here and hereafter, all dimensional quantities are denoted with a superscript $*$. The droplet is travelling downwards towards the substrate at speed V^*, and is surrounded by an incompressible gas. A Cartesian coordinate system (x^*, y^*, z^*) is defined such that the top surface of the substrate initially lies in the $z^* = 0$ plane, the droplet falls along the $z^* > 0$ axis, and the bottom of the droplet is at $x^* = 0$, $y^* = 0$, $z^* = H^*$ at the onset. The substrate is taken to be symmetric about the z^* axis, with its centre at $x^* = z^* = 0$. The system is initialised at a time $t^* = t_0^* = -H^*/V^*$, such that if the gas were absent and the substrate were stationary, then the bottom of the droplet would impact at $t^* = 0$. A schematic of the general setup at $t^* = t_0^*$ is shown in Figure 2.1.

We assume that the fluids comprising the droplet and the surrounding gas have densities ρ_l^*, ρ_g^* and viscosities μ_l^*, μ_g^* respectively. We take the interface between the liquid and gas as infinitesimally thin, with a constant surface tension coefficient denoted by σ^*. The acceleration due to gravity is $-\mathbf{g}^* = -g^*\hat{\mathbf{n}}_z$, where $\hat{\mathbf{n}}_z$ is the unit vector in the z^*-direction. Throughout this thesis, we study the early time scenarios where we assume the inertial effects of the impact are more significant than the effects of viscosity, surface tension and gravity. Hence we assume that the droplet Reynolds number Re, Weber number We and Froude number Fr^2 are large throughout the early stages of impact; these are defined by:

$$\mathrm{Re} = \frac{\rho_l^* R_d^* V^*}{\mu_l^*}, \quad \mathrm{We} = \frac{\rho_l^* R_d^* V^{*2}}{\sigma^*}, \quad \mathrm{Fr}^2 = \frac{V^{*2}}{g^* R_d^*}. \tag{2.1}$$

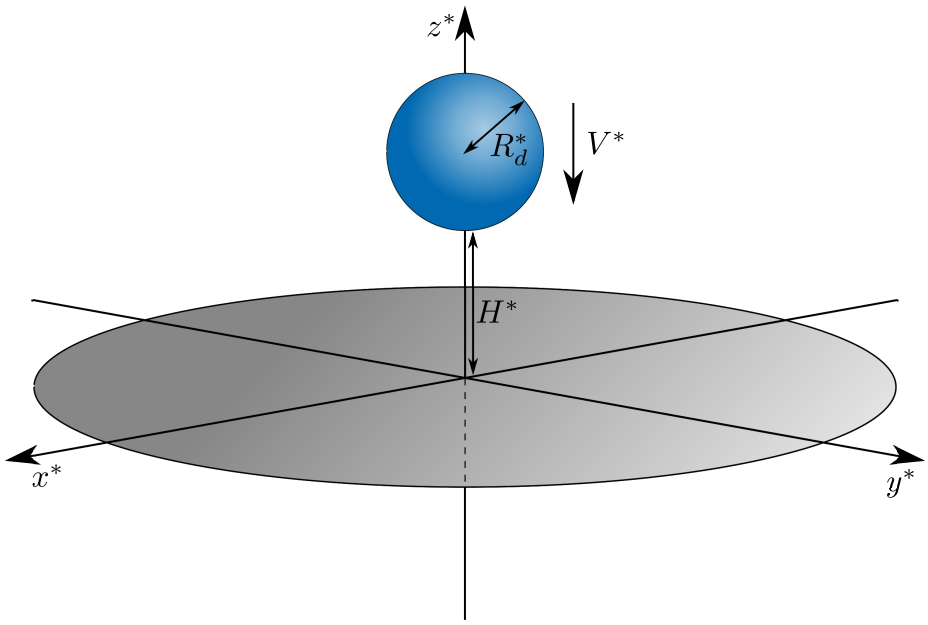

Figure 2.1: Schematic diagram for the general impact setup for an initially spherical droplet of radius R_d^* falling towards an initially flat substrate at speed V^*.

We also assume that the inertial and viscous effects in the surrounding gas are much smaller than those in the liquid. By defining the density and viscosity ratios as

$$\rho_R = \frac{\rho_g^*}{\rho_l^*}, \quad \mu_R = \frac{\mu_g^*}{\mu_l^*}, \tag{2.2}$$

then this corresponds to assuming that $\rho_R \ll 1$ and $\mu_R \ll 1$, such that the Reynolds and Weber numbers in the gas are much smaller than in the liquid. As an illustrative example, consider the impact of a droplet of water with density $\rho_l^* = 998$ kg/m^3, radius $R_d^* = 1$ mm and velocity $V^* = 5$ m/s, surrounded by air under atmospheric conditions, such is typical for raindrops. In this scenario, the Reynolds, Weber and Froude numbers in the liquid are

$$\mathrm{Re} \approx 4990, \quad \mathrm{We} \approx 342, \quad \mathrm{Fr}^2 \approx 2550, \tag{2.3}$$

and with corresponding density and viscosity ratios

$$\rho_R \approx 1.20 \times 10^{-3}, \quad \mu_R \approx 1.83 \times 10^{-2}, \tag{2.4}$$

such that our assumptions on these dimensionless quantities are clearly sensible for this case.

Within the bulk of the droplet and gas, we assume that the fluid velocities are much less than their respective sound speeds, meaning the flow can be assumed to be

incompressible. However, the presence of the gas means there will be a pressure build up prior to the impact with the substrate, causing the bottom of the droplet to dimple and eventually entrap a thin layer of air, as seen experimentally by, for example, Thoroddsen et al. (2003) [90]. This phenomenon is known as air cushioning, and as discussed by Mandre et al. (2009) [58], compressibility effects in this small region can become significant due to the high pressure build up. For simplicity, in this study, we assume the gas remains incompressible throughout, and note how incompressible models for this entrapped gas layer such as the one derived by Hicks & Purvis (2010) [39] still find good agreement with experimental results.

When the liquid and gas have a finite viscosity, the no-slip boundary condition applies at the surface of the substrate. However, for the analytical model in Chapter 3, we neglect the influence of the viscosity and therefore cannot apply a slip condition on the substrate. The points at which the liquid, gas and substrate meet are known as triple-contact points, and the angle between the tangent of the liquid-gas interface and the tangent to the substrate at these points is referred to as the contact angle. For sessile droplets in equilibrium, this contact angle is determined via the Young equation (see Good (1992) [30]), which balances the surface tension forces between the liquid, gas and substrate. Typically, if the substrate has a contact angle between 0° and 90°, then it is described as *wettable*, whilst substrates with a contact angle between 90° and 180° are described as *hydrophobic*. However, it is observed experimentally that the contact angles whilst the droplet is spreading, and also receding, across substrates differ from the equilibrium contact angle, an effect known as contact angle hysteresis (see Yarin (2006) [102] for a comprehensive review). The dynamics of the contact points have a strong influence on the late time splashing behaviour of the droplet. However for the purposes of this thesis, we focus on inertia-dominated regimes at the early times of impact, where only the spreading contact angle is considered. For the analytical model, we find in §3.2.5 that the inviscid theory cannot make any predictions about where the contact points are, as the leading-order solutions give that the jets have an infinite extent. For the direct numerical simulations in Chapter 4, we assume that the contact angle is 90° for all times, which models the substrate as somewhere in the middle of the range between wettable and hydrophobic. If the models presented in this thesis were to be extended to model the later time splashing behaviour, then a dynamic contact angle model would need to be incorporated into the simulations, such as was considered by Yokoi et al. (2009) [103] using the coupled level set and volume of fluid (CLSVOF) method.

We assume that the substrate deforms in response to the stresses from the liquid and gas. We will consider two different types of physical substrate with their respective governing equations determining the nature of this fluid-structure interaction. In both cases, we will assume that the deformation of this substrate is small in comparison to the length scale of the droplet. This is seen experimentally both in the droplet impact onto elastic membrane experiments conducted by Pepper et al. (2008) [72] and the impact onto soft silicone gels conducted by Howland et al. (2016) [46], where the substrate deformations at early times were found to be orders of magnitude smaller than the droplet radii. Due to this small deformation, we assume that the gas below the substrate remains relatively undisturbed during impact, such that we assume it remains at a constant atmospheric pressure and exerts a negligible amount of stress on the substrate. Finally, we assume that the fluid and the substrate remain symmetric about the z^* axis for all time.

2.2 Dimensional governing equations

Denoting the variables in the liquid and gas with a subscript l and g respectively, the incompressible Navier-Stokes equations are assumed to hold in each fluid,

$$\rho_i^* \left(\frac{\partial \mathbf{u}_i^*}{\partial t^*} + (\mathbf{u}_i^* \cdot \boldsymbol{\nabla}^*)\mathbf{u}_i^* \right) = -\boldsymbol{\nabla}^* p_i^* + \mu_i^* \boldsymbol{\nabla}^{*2} \mathbf{u}_i^* - \rho_i^* \mathbf{g}^*, \tag{2.5}$$

$$\boldsymbol{\nabla}^* \cdot \mathbf{u}_i^* = 0, \tag{2.6}$$

where $i = l, g$, $\mathbf{u}_i^*$ is the velocity vector and p_i^* is the pressure in each fluid. The kinematic condition at the interface between the droplet and the gas, located at $z^* = h^*(x^*, y^*, t^*)$, is given by

$$\mathbf{u}_i^* \cdot \hat{\mathbf{n}}_z = \frac{\partial h^*}{\partial t^*} + \mathbf{u}_i^* \cdot \boldsymbol{\nabla}^* h^* \text{ on } z^* = h^*(x^*, y^*, t^*), \tag{2.7}$$

where h^* needs to be determined as part of the problem. We also have continuity of velocity and normal stress across the interface, given by

$$\mathbf{u}_g^* = \mathbf{u}_l^*, \quad \hat{\mathbf{n}} \cdot [\boldsymbol{\mathcal{T}}_g^* - \boldsymbol{\mathcal{T}}_l^*] = -\sigma^* \kappa^* \hat{\mathbf{n}} \text{ on } z^* = h^*(x^*, y^*, t^*), \tag{2.8}$$

where $\hat{\mathbf{n}}$ is the unit normal vector to the interface pointing into the gas, $\boldsymbol{\mathcal{T}}_i^*$ is the Cauchy stress tensor in each fluid, defined by

$$\boldsymbol{\mathcal{T}}_i^* = -p_i^* \boldsymbol{I} + \mu_i^* \left(\boldsymbol{\nabla}^* \mathbf{u}_i^* + (\boldsymbol{\nabla}^* \mathbf{u}_i^*)^T \right), \tag{2.9}$$

and $\kappa^* = -\boldsymbol{\nabla}^* \cdot \hat{\mathbf{n}}$ is the curvature of the interface, equal to $-2/R_d^*$ at $t^* = t_0^*$. The vertical position of the top surface of the substrate is defined to be at $z^* = -w^*(x^*, y^*, t^*)$. As the substrate is impermeable, we apply the kinematic boundary condition given by

$$\mathbf{u}_i^* \cdot \hat{\mathbf{n}}_z = -\frac{\partial w^*}{\partial t^*} - \mathbf{u}_i^* \cdot \boldsymbol{\nabla}^* w^* \text{ on } z^* = -w^*(x^*, y^*, t^*). \tag{2.10}$$

Far from the droplet, we assume that the surrounding gas remains stationary and undisturbed at all times, so that

$$\mathbf{u}_g^* \to \mathbf{0},\ p_g^* \sim p_{\text{atm}}^* - \rho_g^* g^* z^* \text{ as } x^{*2} + y^{*2} + z^{*2} \to \infty, \tag{2.11}$$

where p_{atm}^* denotes atmospheric pressure. Initially, at $t^* = t_0^*$, the liquid has a uniform downwards velocity V^*,

$$\mathbf{u}_l^* \equiv -V^* \hat{\mathbf{n}}_z \text{ at } t^* = t_0^*, \tag{2.12}$$

while the centre of the droplet is at $z^* = H^* + R_d^*$, meaning the interface position $h^*(x^*, y^*, t_0^*)$ satisfies

$$x^{*2} + y^{*2} + (h^*(x^*, y^*, t_0^*) - H^* - R_d^*)^2 = R_d^{*2}. \tag{2.13}$$

The velocity of the gas and the pressure in both phases are initialised such that they satisfy the far-field conditions (2.11) and the boundary conditions at the interface of the droplet (2.7)-(2.8) at $t^* = t_0^*$.

In this thesis, we consider two specific physical models for the substrate. The first we refer to as a *spring-supported plate*, which consists of a rigid, planar, circular plate supported by a Hookean spring and a linear dashpot. As the plate is rigid, we have $w^*(x^*, y^*, t^*) = w^*(t^*)$ in this case. The spring has a spring constant k^*, the dashpot has a damping factor c^*, and the plate has a total mass M^*, a radius L^* and is assumed to be infinitesimally thin. A schematic of the spring-supported plate setup is shown in Figure 2.2. At $t^* = t_0^*$, the plate is assumed to be in equilibrium, hence by Newton's third law, the force due to the compression of the spring balances the weight of the plate. Denoting the net hydrodynamic force applied to the plate in the downwards direction $-\hat{\mathbf{n}}_z$ as $F^*(t^*)$, the displacement of the plate from this equilibrium is governed by

$$M^* \ddot{w}^*(t^*) = F^*(t^*) - c^* \dot{w}^*(t^*) - k^* w^*(t^*), \quad w^*(t_0^*) = \dot{w}^*(t_0^*) = 0, \tag{2.14}$$

where the overdot denotes differentiation with respect to time. The net hydrodynamic force $F^*(t^*)$ is equal to the sum of the contributions from the hydrodynamic pressure

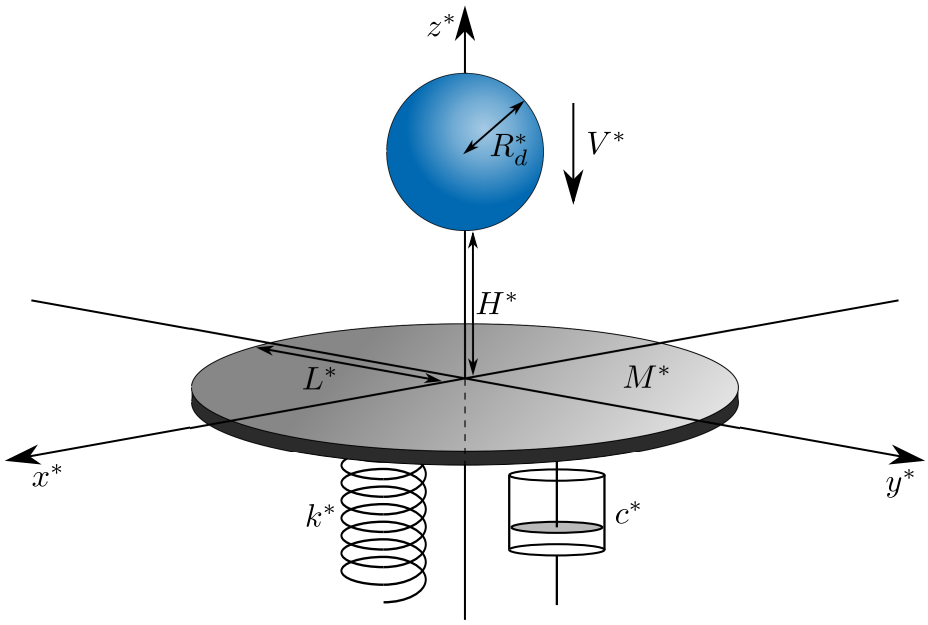

Figure 2.2: Schematic diagram for the spring-supported plate setup considered in Chapter 5.

and viscous stress above and below the plate. Assuming that the gas below the plate is at a constant atmospheric pressure p^*_{atm} and exerts a negligible amount of force due to viscous stress, then

$$F^*(t^*) = \iint\limits_{\substack{\sqrt{x^{*2}+y^{*2}} \le L^* \\ z^* = -w^*(t^*)}} (p^* - p^*_{\text{atm}}) - 2\mu^* \frac{\partial v^*}{\partial z^*} \, \mathrm{d}x^* \, \mathrm{d}y^* \,, \tag{2.15}$$

where v^* is the velocity in the z^* direction, and we take $p^* = p^*_l$, $\mu^* = \mu^*_l$, $v^* = v^*_l$ where the plate is wetted and $p^* = p^*_g$, $\mu^* = \mu^*_g$, $v^* = v^*_g$ where the plate is unwetted. We will consider the spring-supported plate setup in detail in Chapter 5.

The second substrate model is that of an *elastic membrane*. For this model, we only consider the two-dimensional case, where all y^* dependence is dropped, so that the membrane location is $z^* = -w^*(x^*, t^*)$. The membrane has a width $2L^*$ in the x^* direction with the centre at $x^* = 0$, a thickness δ^*, a density ρ^*_m, is held under a constant uniform tension per unit length T^*, has a Young's modulus value of E^* and a moment of inertia $I^* = {\delta^*}^3/3$. The elastic membrane setup at $t = t^*_0$ is depicted in Figure 2.3. We assume that the width $2L^*$ is of the same order of magnitude as the droplet radius R^*_d, and that the membrane's thickness δ^* is much smaller than L^*. Under these assumptions, we model the displacement of the membrane using the

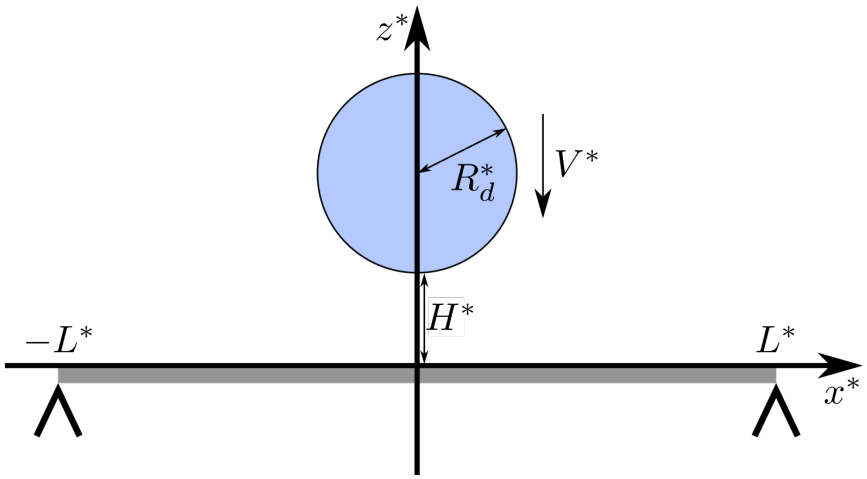

Figure 2.3: Schematic diagram for the elastic membrane setup considered in Chapter 6.

linear beam equation, which is given in Howell et al. (2008) [43] by

$$\delta^* \rho_m^* \frac{\partial^2 w^*}{\partial t^{*2}} - T^* \frac{\partial^2 w^*}{\partial x^{*2}} + E^* I^* \frac{\partial^4 w^*}{\partial x^{*4}} = p^*(x^*, -w^*(x^*, t^*), t^*) - p_{\text{atm}}^* - 2\mu_i^* \frac{\partial v_i^*}{\partial z^*}, \quad (2.16)$$

where the right-hand side of (2.16) represents the sum of the net forcing due to the difference between the pressure above and below the membrane and the viscous stress. The membrane is taken to be simply supported at the end points, giving the boundary conditions

$$w^* = \frac{\partial^2 w^*}{\partial x^{*2}} = 0 \text{ at } x^* = \pm L^*. \quad (2.17)$$

We assume that the droplet is initialised at a height H^* large enough that the viscous stress is zero and the pressure is atmospheric on the substrate at $t^* = t_0^*$, so we have the initial condition for $w^*(x^*, t^*)$ given by

$$w^* = \frac{\partial w^*}{\partial t^*} = 0 \text{ at } t^* = t_0^*. \quad (2.18)$$

We will consider the elastic membrane setup in detail in Chapter 6.

Finally, it will be informative for our analysis to determine the energy distribution within the system. This energy distribution was relevant to the experiments of Howland et al. (2016) [46], where it was found that droplet splashing can be inhibited by impacting onto soft substrates of varying stiffnesses. They found that droplets impacting onto the soft substrates needed up to 75% more kinetic energy to splash in comparison to impact onto a solid substrate. However, it was also found that the energy absorbed by the softer substrate was only a few percent more than the rigid substrates, meaning energy loss to the substrate could not alone account for the high

energy requirement to splash on a soft substrate. By observing that the bulk of the droplets were relatively unaffected by the difference in the substrate stiffnesses, they concluded that this so-called splash-suppression mechanism must remove energy from the ejection sheet, which thus makes it slower and less likely to break up into a splash. The ejection of this sheet happens at times currently too early to experimentally observe, however it is vital to understand how the substrate deformation affects the emergence of the ejection sheet in order to understand these observations.

In the absence of thermal fluctuations, the droplet will have three components of energy: kinetic, gravitational potential and surface energy. In general, this energy will not be conserved due to energy loss from viscous dissipation in both the liquid and gas, as well as through the fluid-structure interaction with the substrate. As the droplet is initially travelling downwards at constant speed in the lab frame, it will initially have a high kinetic energy in the lab frame, and at early times this will change by a small amount once it impacts the substrate. Therefore it is instead more informative for our analysis to consider the energy in a frame moving downwards at the initial droplet velocity, such that at $t^* = t_0^*$, the droplet will only have potential and surface energy. Therefore, by defining the variables in the moving frame with a prime $'$, we have

$$x^* = x^{*\prime}, \quad y^* = y^{*\prime}, \quad z^* = z^{*\prime} - t^*, \quad \mathbf{u}^* = \mathbf{u}^{*\prime} - V^* \hat{\mathbf{n}}_z. \tag{2.19}$$

If we define the droplet domain by $\Omega^*(t^*)$, then the kinetic, gravitational potential and surface energy of the droplet are given by

$$E_K^*(t^*) = \frac{1}{2}\rho_l^* \iiint_{\Omega^*(t^*)} |\mathbf{u}^{*\prime}|^2 \,\mathrm{d}x^{*\prime}\,\mathrm{d}y^{*\prime}\,\mathrm{d}z^{*\prime} \tag{2.20}$$

$$E_P^*(t^*) = \rho_l^* g^* \iiint_{\Omega^*(t^*)} z^{*\prime} \,\mathrm{d}x^{*\prime}\,\mathrm{d}y^{*\prime}\,\mathrm{d}z^{*\prime} \tag{2.21}$$

$$E_S^*(t^*) = \sigma^* \iint_{\partial\Omega^*(t)} \mathrm{d}S^*\,, \tag{2.22}$$

where $\partial\Omega^*(t^*)$ is the boundary of the droplet and $\mathrm{d}S^*$ is the surface element of the droplet.

2.3 Non-dimensionalisation

We take the initial droplet radius, R_d^*, and speed, V^*, as the characteristic length and velocity scales, respectively, so we non-dimensionalise by setting

$$(x^*,\, y^*,\, z^*,\, h^*) = R_d^*(x,\, y,\, z,\, h), \quad \mathbf{u}_i^* = V^* \mathbf{u}_i, \tag{2.23}$$

Then, by choosing the inertial pressure scaling, the pressure and force on the substrate are non-dimensionalised by

$$p_i^* = p_{\text{atm}}^* + \rho_l^* V^{*2} p_i, \quad F^*(t^*) = \rho_l^* V^{*2} R_d^{*2} F(t). \tag{2.24}$$

For the time and the substrate position variables, we introduce an arbitrary parameter $\epsilon > 0$, where

$$t^* = \epsilon^2 \frac{R_d^*}{V^*} t, \quad w^* = \epsilon^2 R_d^* w, \tag{2.25}$$

such that the choice of ϵ allows the study of either early ($\epsilon \ll 1$) or intermediate ($\epsilon = 1$) stages of impact. If the substrate and gas were not present, then the bottom of the droplet at time t would be at $z = -\epsilon^2 t$, so we have chosen the scaling for the substrate position $z = -\epsilon^2 w(x, y, t)$ to have the same order.

Under the scalings (2.23)-(2.25), the momentum and continuity equations in each phase (2.5)-(2.6) become

$$\rho_i \left(\frac{1}{\epsilon^2} \frac{\partial \mathbf{u_i}}{\partial t} + (\mathbf{u}_i \cdot \boldsymbol{\nabla}) \mathbf{u}_i \right) = -\boldsymbol{\nabla} p_i + \frac{\mu_i}{\text{Re}} \boldsymbol{\nabla}^2 \mathbf{u}_i - \frac{\rho_i}{\text{Fr}^2} \hat{\mathbf{n}}_z, \tag{2.26}$$

$$\boldsymbol{\nabla} \cdot \mathbf{u}_i = 0, \tag{2.27}$$

where $\rho_l = 1$, $\mu_l = 1$ and $\rho_g = \rho_R$, $\mu_g = \mu_R$. The impermeability condition on the substrate (2.10) becomes

$$\mathbf{u}_i \cdot \hat{\mathbf{n}}_z = -\frac{\partial w}{\partial t} - \epsilon^2 \mathbf{u}_i \cdot \boldsymbol{\nabla} w \text{ on } z = -w(x, y, t), \tag{2.28}$$

while the interface conditions (2.7)-(2.8) become

$$\mathbf{u}_i \cdot \hat{\mathbf{n}}_z = \frac{\partial h}{\partial t} + \mathbf{u}_i \cdot \boldsymbol{\nabla} h, \quad \mathbf{u}_g = \mathbf{u}_l, \quad \hat{\mathbf{n}} \cdot [\boldsymbol{\mathcal{T}}_g - \boldsymbol{\mathcal{T}}_l] = -\frac{\kappa}{\text{We}} \hat{\mathbf{n}} \text{ on } z = h(x, y, t), \tag{2.29}$$

where

$$\boldsymbol{\mathcal{T}}_i = \frac{1}{\rho_l^* V^{*2}} \boldsymbol{\mathcal{T}}_i^* = -\left(\frac{p_{\text{atm}}^*}{\rho_l^* V^{*2}} + p \right) \boldsymbol{I} + \frac{\mu_i}{\text{Re}} \left(\boldsymbol{\nabla} \mathbf{u}_i + (\boldsymbol{\nabla} \mathbf{u}_i)^T \right), \tag{2.30}$$

and $\kappa = -\boldsymbol{\nabla} \cdot \hat{\mathbf{n}}$ is the non-dimensional curvature of the interface. The far-field conditions in the gas (2.11) become

$$\mathbf{u}_g \to \mathbf{0}, \quad p_g \sim -\frac{\rho_g}{\text{Fr}^2} z \text{ as } x^2 + y^2 + z^2 \to \infty, \tag{2.31}$$

and at $t = t_0 = V^* t_0^* / R_d^*$, the initial conditions for the fluid variables are

$$\mathbf{u}_l \equiv -\hat{\mathbf{n}}_z, \quad x^2 + y^2 + (h(x, y, t_0) - H - 1)^2 = 1, \tag{2.32}$$

where $H = H^*/R_d^*$ and the initial conditions for $\mathbf{u}_g$ and p are chosen to satisfy the boundary conditions (2.29) and far-field conditions (2.31).

For the spring-supported plate, we define the dimensionless plate radius by $L = L^*/R_d^*$, so that the governing equation for $w^*(t^*)$ (2.14) becomes

$$\frac{\alpha}{\epsilon^2}\ddot{w}(t) + \beta\dot{w}(t) + \epsilon^2\gamma w(t) = F(t), \quad w(t_0) = \dot{w}(t_0) = 0, \tag{2.33}$$

where

$$\alpha = \frac{M^*}{\rho_l^* R_d^{*3}}, \quad \beta = \frac{c^*}{\rho_l^* V^* R_d^{*2}}, \quad \gamma = \frac{k^*}{\rho_l^* V^{*2} R_d^*}, \tag{2.34}$$

and the non-dimensional hydrodynamic force is given by

$$F(t) = \iint\limits_{\substack{\sqrt{x^2+y^2}\leq L \\ z=-\epsilon^2 w(t)}} p - \frac{2\mu}{\mathrm{Re}}\frac{\partial v}{\partial z}\,\mathrm{d}x\,\mathrm{d}y\,, \tag{2.35}$$

where we take $p = p_l$, $\mu = \mu_l$, $v = v_l$ where the plate is wetted and $p = p_g$, $\mu = \mu_g$, $v = v_g$ where the plate is unwetted. We refer to α as the mass ratio, as it is proportional to the ratio of the mass of the plate to the mass of the droplet. The damping factor, β, measures the strength of the resistance to motion due to the damping from the dashpot, and the stiffness factor, γ, measures the strength of the restoring force due to elastic compression of the spring.

For the elastic membrane case, we define the dimensionless membrane width by $2L$, where $L = L^*/R_d^*$, and the governing equation for $w^*(x^*, t^*)$ (2.16) becomes

$$\frac{\alpha}{\epsilon^2}\frac{\partial^2 w}{\partial t^2} - \epsilon^2\beta\frac{\partial^2 w}{\partial x^2} + \epsilon^2\gamma\frac{\partial^4 w}{\partial x^4} = p_i(x, -\epsilon^2 w(x,t), t) - \frac{2\mu_i}{\mathrm{Re}}\frac{\partial v}{\partial z}, \tag{2.36}$$

where

$$\alpha = \frac{\rho_m^*}{\rho_l^*}\delta, \quad \beta = \frac{T^*}{\rho_l^* R_d^* V^{*2}}, \quad \gamma = \frac{E^*}{3\rho_l^* V^{*2}}\delta^3, \quad \delta = \frac{\delta^*}{R_d^*}. \tag{2.37}$$

Here, we refer to δ as the thickness factor, as it represents the ratio between the thickness of the membrane δ^* and the radius of the droplet R_d^*. For any given δ, α is referred to as the density factor, as it is proportional to the ratio between the density of the membrane ρ_m^* and the liquid ρ_m^*. The tension factor, β, measures the strength of the tension in the membrane and the stiffness factor, γ, measures the strength of the substrate stiffness, given by the Young's modulus E^*. The boundary and initial conditions for the elastic membrane are

$$w = \frac{\partial^2 w}{\partial x^2} = 0 \text{ at } x = \pm L, \quad w = \frac{\partial w}{\partial t} = 0 \text{ at } t = t_0. \tag{2.38}$$

We discuss the additional assumptions made of the physical parameters for the substrate models in Chapters 5 and 6 respectively.

In this inertial regime, we non-dimensionalise the energy by

$$E^*(t^*) = \rho_l^* V^{*2} R^{*3} E(t),$$

such that the kinetic, potential and surface energies (2.20)-(2.22) in the moving frame are given by

$$E_K(t) = \frac{1}{2} \iiint_{\Omega(t)} |\mathbf{u}'|^2 \, \mathrm{d}x' \, \mathrm{d}y' \, \mathrm{d}z' \tag{2.39}$$

$$E_P(t) = \frac{1}{\mathrm{Fr}^2} \iiint_{\Omega(t)} z' \, \mathrm{d}x' \, \mathrm{d}y' \, \mathrm{d}z' \tag{2.40}$$

$$E_S(t) = \frac{1}{\mathrm{We}} \iint_{\partial\Omega(t)} \mathrm{d}S \, . \tag{2.41}$$

The governing equations presented in this section will be solved both using an analytical modelling technique that we describe in Chapter 3, and using direct numerical simulations which we detail in Chapter 4.

Chapter 3

Analytical model

In the this chapter, we present an analytical model for the droplet impact system presented in Chapter 2. The modelling technique we utilise is known as *Wagner theory*, an inviscid model that dates back to Wagner (1932) [94], where the theory was developed to model the impact of seaplanes on water. The method was much later formalised using the approach of matched asymptotic expansions by Cointe and Armand (1987) [18], Cointe (1989) [17], Wilson (1989) [97] and Howison et al. (1991) [45]. Since then, Wagner theory has become one of the most popular methods for modelling the impact of solid bodies into liquid pools.

The mathematical formulation of Wagner theory is such that it is also well characterised for studying systems where the liquid instead impacts onto a solid body or another liquid. In particular, Wagner theory can be applied to model droplet impact problems at early times, such as by Howison et al. (2005) [44], Philippi et al. (2016) [74] and Cimpeanu and Moore (2018) [15]. For this thesis, we aim to model droplet impact problems where the substrate is deformable, such that, in general, the substrate has both non-zero velocity and curvature upon impact. Notable examples relating to this problem include Korobkin (1998) [52], where Wagner theory was used to model the impact of a two-dimensional wave onto an elastic beam, and Pegg et al. (2018) [71], who modelled the impact of a three-dimensional droplet onto an elastic plate.

In this chapter, we apply Wagner theory to model the early-time dynamics of a droplet impacting onto a generalised deformable substrate, in both two-dimensional and three-dimensional geometries. In Chapters 5 and 6, we will apply the solutions found in this chapter to two specific deformable substrate setups, namely a spring-supported plate and an elastic membrane. We do not consider the elastic membrane in three dimensions, hence in this chapter we only derive the three-dimensional solutions for a rigid substrate setup. However the work of Pegg et al. (2018) [71] does utilise

axisymmetric Wagner theory to model the impact of a three-dimensional droplet onto a non-rigid elastic plate.

3.1 Assumptions

Based on the assumptions made in §2.1, for the analytical model we consider the regime in which the Reynolds, Weber and Froude numbers, given by (2.1), are large; and where the density and viscosity ratios, given by (2.2), are small. This means (at leading order) we may neglect the influence of the liquid viscosity, surface tension, gravity and the surrounding gas. With these assumptions, the droplet-gas interface is subject to negligible tangential stress. Although the term *free surface* is generically used for a surface that is a priori unknown, and has to be determined as part of the solution, it is also used more specifically for an unknown surface that is, additionally, subject to zero tangential stress, and we adopt this latter terminology within the analytical model. As the gas phase is ignored, all expressed quantities are in the liquid, and the subscript l is dropped for brevity. In this context, the droplet impacts the substrate at $t = 0$, where the displacement and velocity of the substrate are both zero at $t = 0$.

Under these assumptions, the flow is irrotational for $t < 0$ and hence by Kelvin's circulation theorem will remain irrotational for $t > 0$. Therefore a velocity potential, ϕ, can be introduced, such that $\mathbf{u} = \boldsymbol{\nabla}\phi$. The continuity equation (2.27) transforms to Laplace's equation for ϕ, i.e.

$$\boldsymbol{\nabla}^2\phi = 0, \tag{3.1}$$

and by integrating the momentum equation (2.26) we obtain Bernoulli's equation,

$$p + \frac{1}{\epsilon^2}\frac{\partial\phi}{\partial t} + \frac{1}{2}|\boldsymbol{\nabla}\phi|^2 = a(t), \tag{3.2}$$

for an arbitrary time-dependent function $a(t)$. The boundary conditions on the substrate and free surface (2.28)-(2.29) become

$$\frac{\partial\phi}{\partial z} = -\frac{\partial w}{\partial t} - \epsilon^2\boldsymbol{\nabla}\phi\cdot\boldsymbol{\nabla}w, \quad \text{on } z = -w(x,y,t), \tag{3.3}$$

$$\frac{\partial\phi}{\partial z} = \frac{1}{\epsilon^2}\frac{\partial h}{\partial t} + \boldsymbol{\nabla}\phi\cdot\boldsymbol{\nabla}h, \quad \text{on } z = h(x,y,t), \tag{3.4}$$

$$p = 0, \quad \text{on } z = h(x,y,t). \tag{3.5}$$

As we have neglected the gas phase, the problem is initialised at $t = 0$, with the bottom of the droplet just making contact with the substrate. Without loss of

generality, we take $a(t) = 1/2$, as we have the freedom to add spatially independent terms to ϕ without affecting the solution, and this choice allows us to set the initial conditions from (2.32) to be

$$\phi = -z, \quad x^2 + y^2 + (h(x, y, 0) - 1)^2 = 1. \tag{3.6}$$

Although in this chapter, the position of the substrate $z = -\epsilon^2 w(x, y, t)$ is left in a general form, we will need to make assumptions on the solution for w later in order for the leading-order asymptotic solutions to remain valid. We will make clear when these additional assumptions are required and return to them in Chapters 5 and 6 when we investigate the fluid-structure interaction in greater detail.

We study the early times of these impact phenomena using the method of matched asymptotic expansions assuming that the parameter ϵ from (2.25) is small. The spatial problem breaks down into distinct asymptotic regions, in which we find the leading-order asymptotic expansions for the velocity potential, free surface location and pressure, and we use the method of matched asymptotic expansions to ensure these quantities match across the liquid domain.

3.2 Two-dimensional impact

In this section, we consider the impact of a two-dimensional droplet, meaning we drop any dependence on y in the governing equations and focus on the (x, z) coordinate system. The droplet is then considered to be initially circular in the (x, z) plane. Although this limits the physical applicability of the model, studying the problem in two-dimensions allows us to make more mathematical progress by building on previous studies involving Wagner theory for the impact of curved bodies onto liquid pools [44, 45, 52, 66, 94] and gains us physical insight into the dynamics. In two-dimensions, the governing equations (3.1)-(3.6) hence become

$$\frac{\partial^2 \phi}{\partial x^2} + \frac{\partial^2 \phi}{\partial z^2} = 0, \quad \text{in the liquid,} \tag{3.7}$$

$$p + \frac{1}{\epsilon^2}\frac{\partial \phi}{\partial t} + \frac{1}{2}\left[\left(\frac{\partial \phi}{\partial x}\right)^2 + \left(\frac{\partial \phi}{\partial z}\right)^2\right] = \frac{1}{2}, \quad \text{in the liquid,} \tag{3.8}$$

$$\frac{\partial \phi}{\partial z} + \frac{\partial w}{\partial t} + \epsilon^2 \frac{\partial \phi}{\partial x}\frac{\partial w}{\partial x} = 0, \quad \text{on } z = -\epsilon^2 w(x, t), \tag{3.9}$$

$$\frac{\partial \phi}{\partial z} - \frac{1}{\epsilon^2}\frac{\partial h}{\partial t} - \frac{\partial \phi}{\partial x}\frac{\partial h}{\partial x} = 0, \quad \text{on } z = h(x, t), \tag{3.10}$$

$$p = 0, \quad \text{on } z = h(x, t), \tag{3.11}$$

with initial conditions given by

$$\phi(x, z, 0) = -z, \quad \text{for } x^2 + (z-1)^2 \leq 1, \tag{3.12}$$

$$x^2 + (h(x, 0) - 1)^2 = 1, \quad \text{for } x^2 \leq 1, \tag{3.13}$$

The system (3.7)-(3.13) is a set of non-linear, second-order partial differential equations for the velocity potential ϕ, free surface location h and pressure p. It will at times be convenient to work directly with the velocity, given by

$$\mathbf{u} = (u(x, z, t),\, v(x, z, t)) = \left(\frac{\partial \phi}{\partial x},\, \frac{\partial \phi}{\partial z}\right). \tag{3.14}$$

3.2.1 Asymptotic structure

Were the substrate not present, the droplet would continue to fall undisturbed for $t > 0$, creating a region of fluid below the x axis referred to as the *penetration region*. At early times, this region would have an $O(\epsilon\sqrt{t})$ horizontal extent. However, as illustrated in Figure 3.1, with the substrate present, the free surface is violently displaced close to the point of contact, and the fluid is ejected across the substrate into two thin jets. The points at which the free surface becomes vertical at the root of these jets are referred to as the *turnover points*, and at early times we assume their horizontal extent is on the same order as the horizontal extent of the penetration region. We hence define the x-coordinates of these turnover points to be

$$x = \pm \epsilon d(t), \tag{3.15}$$

as depicted in Figure 3.1, where $d(t)$ is an unknown such that $d(t) = O(1)$ as $\epsilon \to 0$, and must be determined as part of the solution.

As $\epsilon \to 0$, the problem breaks down into four distinct spatial regions, as depicted in Figure 3.1. The $O(\epsilon) \times O(\epsilon)$ region close to the centre of the substrate is referred to as the outer region, where to leading order the substrate appears flat and the governing equations transform into a mixed-boundary value problem in the upper half plane. The outer solution breaks down close to the turnover points, where the velocity and pressure become singular, which is corrected by introducing inner regions of size $O(\epsilon^3) \times O(\epsilon^3)$ in which the free surfaces turns over, ejecting fluid into the jets. The thin, fast-moving jets are of size $O(\epsilon) \times O(\epsilon^3)$, emanating across the surface of the substrate from the inner regions, where we assume the jets do not detach from the substrate. Finally, in the outer-outer region, for which $(x, z) = O(1) \times O(1)$, the bulk of the droplet is largely unaffected by the impact, and experiences small perturbations driven by the dynamics in the outer region close to the point of contact.

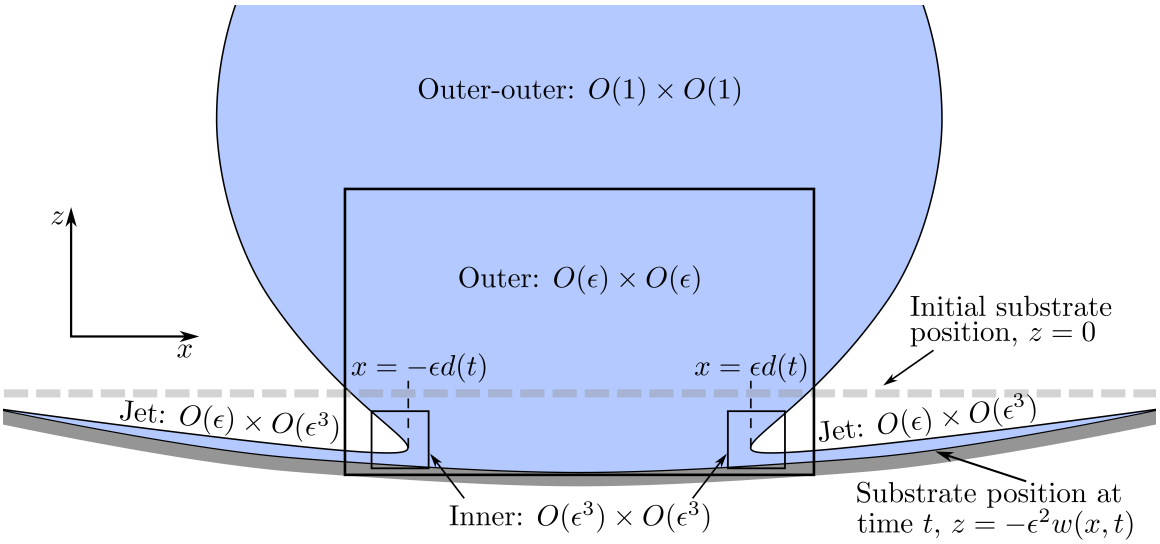

Figure 3.1: Schematic of the asymptotic structure of the two-dimensional system. The horizontal extent of the inner regions and the displacement of the substrate $z = -\epsilon^2 w(x,t)$ are exaggerated for visual clarity.

In the following, we will consider all of these regions in detail. As our eventual aim is to model the fluid structure interaction between the droplet and the substrate, we draw particular focus on how the substrate motion affects the solutions for the velocity, free surface location and pressure of the droplet. To determine the position of the substrate in Chapters 5 and 6, we also need to determine the solution for the pressure along the surface of the substrate and the resulting hydrodynamic force exerted by the droplet onto the substrate.

3.2.2 Imposed substrate

The asymptotic analysis conducted in this chapter will keep the substrate position $z = -\epsilon^2 w(x,t)$ general, as we will find solutions for $w(x,t)$ in Chapters 5 and 6 by solving (2.33) and (2.36) respectively. However, as we will see later, many of the leading-order solutions presented in this chapter cannot be found exactly for all forms of $w(x,t)$, such as the pressure in the liquid domain of the outer region, meaning we have to resort to numerical methods. To better understand the effect the substrate motion has on the fluid, we will consider three different examples throughout this chapter where the substrate motion is imposed (i.e. the motion is independent of the fluid problem). The forms of these imposed substrate cases will be such that they share important features of the spring-supported plate and elastic membrane systems considered in Chapters 5 and 6, but in addition are of a form that we can find exact

solutions without having to rely on numerical methods. In particular, in Appendix A, we find that the leading-order solutions presented in this chapter can be solved exactly if the substrate at time t is given by an even quadratic function in x. Given this, we choose three different imposed substrate solutions for $w(x,t)$. For all of these examples, we take $\epsilon = 0.1$, and consider times from $t = 0$ up to $t = 1$.

The first case is simply where the substrate is stationary, such that $w(x,t) \equiv 0$. This will be an important control case in which we can compare to the moving substrate cases to see the effects the substrate motion has on the fluid.

As we will see later in Chapter 5, the solutions for the spring-supported plate position from (2.33) exhibit an initial acceleration stage, followed by oscillatory behaviour due to the elasticity of the spring. Therefore, for the second imposed substrate case, we consider a rigid body motion $w(x,t) = w(t)$, where $w(t)$ is given by

$$w(t) = q(t^2 + 1 - \cos(\omega t)), \tag{3.16}$$

where we take $q = 0.1$ and $\omega = 3$, and we have that $w(0) = \dot{w}(0) = 0$. The parameters q and ω are chosen to ensure that $w(t) = O(1)$ when $t = O(1)$, and that the oscillation is not initially too strong. We plot $w(t)$ and its time derivatives $\dot{w}(t)$ and $\ddot{w}(t)$ in Figure 3.2. As we can see from Figure 3.2, the solution for $w(t)$ from (3.16) starts with an initial acceleration stage due to the t^2 term, and after $t \approx 0.5$, the velocity changes direction once the cosine term becomes large enough.

In Chapter 6, we will solve the membrane equation (2.16) for $w(x,t)$ using a normal modes expansion, a spectral method where we express $w(x,t)$ as a sum of cosines. As for the analytical model, the substrate is initially flat and is contacted by the droplet at its centre. We will see in Chapter 6 that at early times the substrate displaces close to the origin, and the horizontal extent of the displacement grows with time as the droplet spreads. Some of the asymptotic solutions, such as the pressure in the liquid away from the substrate, cannot be solved exactly when the spatial displacement of the substrate is given by these trigonometric terms. However, as we detail in Appendix A, we can find exact solutions when the displacement is given by an quadratic in x. Exploiting this, the third imposed substrate case is given by a time-dependent quadratic function

$$w(x,t) = w(t)\left(1 - \frac{x^2}{\left(\epsilon a\sqrt{t}\right)^2}\right), \tag{3.17}$$

where $w(t)$ is given by (3.16) and $w(x,t)$ has roots at $x = \pm\epsilon a\sqrt{t}$, where we choose $a = 1.25$ for this chapter. The solution for $w(x,t)$ in this case is shown in Figure

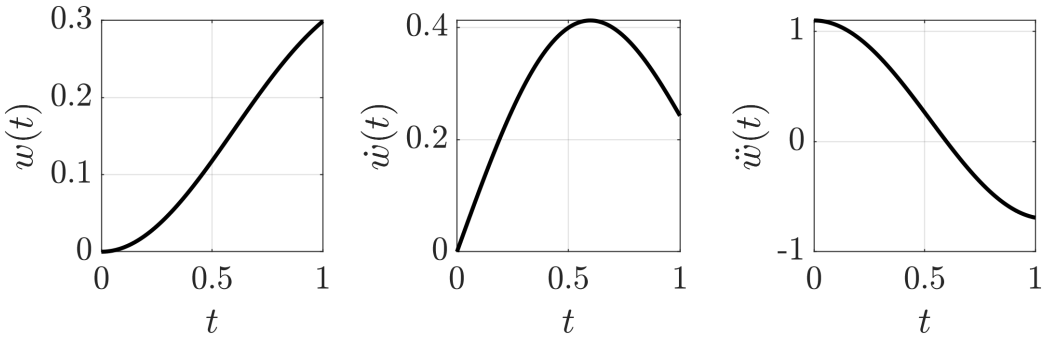

Figure 3.2: Flat imposed substrate solution from (3.16), and its time derivatives, where $q = 0.1$ and $\omega = 3$.

3.3 for $0 \leq t \leq 1$. It is worth noting that for $t > 0$, the solution $w(x,t) \to -\infty$ as $x \to \infty$, however, as can been seen in Figure 3.3, we maintain $w(x,t) = O(1)$ along the wetted region of the substrate for the timescales chosen. In addition, at $t = 0$, the substrate velocity given by $-w(x,t) = qx^2\left(\omega^2+2\right)/(2a^2\epsilon^2)$, which is non-zero everywhere apart from $x = 0$. However, for the analytical model, the droplet only touches the substrate at $x = 0$ at $t = 0$, so the initial condition for w away from $x = 0$ does not affect the analytical solutions.

In Appendix A, we find the leading-order solutions to the problem in the case of a general quadratic substrate given by $w(x,t) = a(t) + b(t)x^2/\epsilon^2$, where $a(t)$ and $b(t)$ are $O(1)$. The three imposed substrate cases detailed above can all be expressed in this form with appropriate choices of $a(t)$ and $b(t)$, and we will use these solutions throughout this chapter to provide examples of how the substrate motion can affect the fluid problem. However note that these imposed substrate cases are only considered as illustrative examples, and are not representative of all types of substrate motion or necessarily physically realistic.

3.2.3 Outer region

The outer region follows the structure of previous works on two-dimensional Wagner theory [44, 45]. It is defined to be the region above the substrate, close to the turnover points, where we expect the velocity to be $O(1)$ as it enters from above. Given that the turnover points are at $x = \pm\epsilon d(t)$, the relevant outer scalings are given by

$$x = \epsilon\hat{x}, \quad z = \epsilon\hat{z}, \quad \phi = \epsilon\hat{\phi}, \quad h = \epsilon^2\hat{h}, \quad p = \hat{p}/\epsilon, \quad w(x,t) = \hat{w}(\hat{x},t). \tag{3.18}$$

Upon substituting (3.18) into (3.7)-(3.11) and asymptotically expanding the outer variables $(\hat{\phi},\, \hat{h},\, \hat{p},\, \hat{w},\, d) = (\hat{\phi}_0,\, \hat{h}_0,\, \hat{p}_0,\, \hat{w}_0,\, d_0) + o(1)$ as $\epsilon \to 0$, the mixed boundary

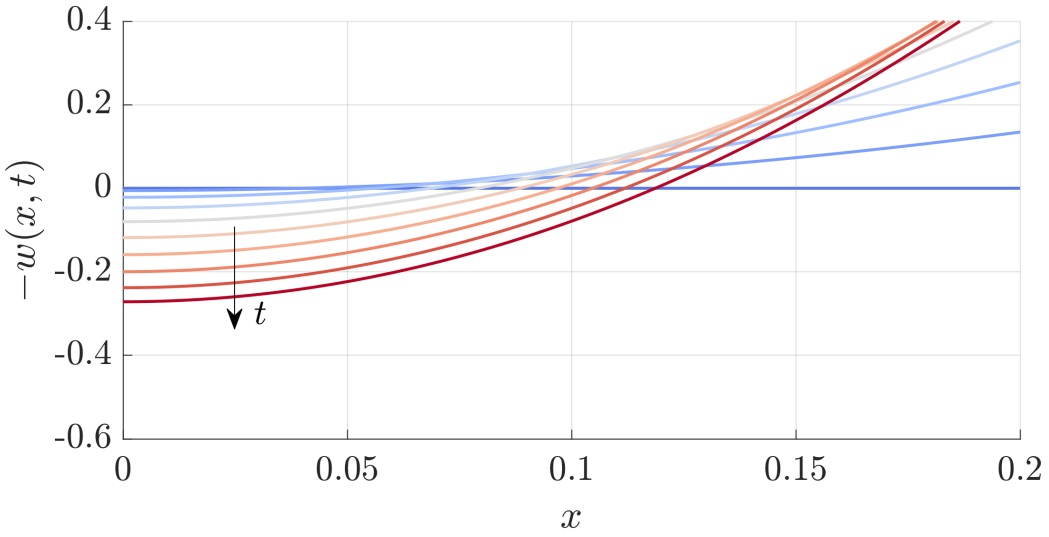

Figure 3.3: Curved imposed substrate solution from (3.17), where $\epsilon = 0.1$ and $a = 1.25$. The lines are plotted in equal temporal spacing from $t = 0$ (blue) to $t = 1$ (red).

value problem in the upper half plane is given by

$$\frac{\partial^2 \hat{\phi}_0}{\partial \hat{x}^2} + \frac{\partial^2 \hat{\phi}_0}{\partial \hat{z}^2} = 0, \qquad \text{for } \hat{z} \geq 0, \tag{3.19}$$

$$\hat{p}_0 = -\frac{\partial \hat{\phi}_0}{\partial t}, \qquad \text{for } \hat{z} \geq 0, \tag{3.20}$$

$$\frac{\partial \hat{\phi}_0}{\partial \hat{z}} = -\frac{\partial \hat{w}_0}{\partial t}, \qquad \text{on } |\hat{x}| < d_0(t),\ \hat{z} = 0, \tag{3.21}$$

$$\frac{\partial \hat{\phi}_0}{\partial \hat{z}} = \frac{\partial \hat{h}_0}{\partial t}, \qquad \text{on } |\hat{x}| > d_0(t),\ \hat{z} = 0, \tag{3.22}$$

$$\hat{\phi}_0 = 0, \qquad \text{on } |\hat{x}| > d_0(t),\ \hat{z} = 0. \tag{3.23}$$

The boundary condition (3.23) is derived by combining the dynamic boundary condition on the free surface (3.11) with the leading-order Bernoulli equation (3.20), and then integrating with respect to time and applying the initial condition (3.6).

The far-field conditions as we tend towards the outer-outer region state that, to leading-order, the flow is travelling downwards with unit speed and the free surface is parabolic in $\hat{x}$, such that

$$\hat{\phi}_0(\hat{x}, \hat{z}, t) \sim -\hat{z} \text{ as } \hat{x}^2 + \hat{z}^2 \to \infty, \quad \hat{h}_0(\hat{x}, t) \sim \frac{1}{2}\hat{x}^2 - t \text{ as } \hat{x}^2 \to \infty. \tag{3.24}$$

In order to match with the inner regions, we require that the potential $\hat{\phi}_0$ has a square-root singularity at the turnover points [45], i.e.

$$\hat{\phi}_0 = O\left((d_0(t)^2 - (\hat{x} + i\hat{z})^2)^{1/2}\right) \text{ as } \hat{x} + i\hat{z} \to \pm d_0(t), \tag{3.25}$$

as well as the so-called Wagner condition [94]

$$\hat{h}_0(\pm d_0(t), t) = -\hat{w}_0(\pm d_0(t), t), \tag{3.26}$$

which states that the leading-order free surface meets the substrate at the turnover points. We note that in this symmetric two-dimensional setup, the Wagner condition can be derived on the basis of global conservation of mass at leading order, as in Wilson (1989) [97], but is formally a matching condition with the inner regions.

To close the leading-order problem, the initial conditions of the system are

$$\hat{\phi}_0(\hat{x}, \hat{z}, 0) = -\hat{z}, \quad \hat{h}_0(\hat{x}, 0) = \frac{1}{2}\hat{x}^2, \quad \hat{w}_0(\hat{x}, 0) = 0, \quad d_0(0) = 0. \tag{3.27}$$

3.2.3.1 Solution for the velocity potential

The mixed boundary value problem (3.19)-(3.23) can be solved using the Riemann-Hilbert method, considered in detail by Gakhov (1966) [26], though we follow more closely the work of Gillow (1998) [29]. We start by defining the complex velocity potential

$$W(\zeta, t) = \hat{\phi}_0 + i\hat{\psi}_0,$$

where $\hat{\psi}_0$ is the leading-order streamfunction and $\zeta = \hat{x} + i\hat{z}$. Without loss of generality, we specify that $\hat{\psi}_0(0, 0, t) = 0$. It follows that $W \to i\zeta$ as $\zeta \to \infty$, so we define the function

$$F(\zeta, t) = i(W(\zeta, t) - i\zeta) = iW(\zeta, t) + \zeta,$$

such that $F(\zeta, t)$ is bounded as $\zeta \to \infty$. We can also analytically continue F onto the whole complex plane using the Schwarz reflection formula,

$$F(\zeta, t) = \overline{F(\bar{\zeta}, t)} \text{ for } \hat{z} < 0. \tag{3.28}$$

Note that for $|\hat{x}| > d_0(t)$, $\hat{z} = 0^+$, we have

$$\mathrm{Im}(F(\hat{x} + 0i, t)) = -\mathrm{Re}(W(\hat{x} + 0i, t)) = -\hat{\phi}_0 = 0,$$

where Re and Im denote the real and imaginary part of a complex number, respectively. So by the Schwarz reflection formula (3.28), we have $\mathrm{Im}(F(\hat{x} - 0i, t)) = 0$ and we can conclude that $F(\zeta, t)$ is continuous across the $\hat{x}$ axis when $|\hat{x}| > d_0(t)$. For $|\hat{x}| < d_0(t)$, $\hat{z} = 0^+$, we make use of the Cauchy-Riemann equations for $\hat{\phi}_0$ and $\hat{\psi}_0$ to conclude,

$$\frac{\partial \hat{\psi}_0}{\partial \hat{x}} = -\frac{\partial \hat{\phi}_0}{\partial \hat{z}} = \frac{\partial \hat{w}_0}{\partial t},$$

and by integrating with respect to $\hat{x}$ we have

$$\hat{\psi}_0(\hat{x},0,t) = \int_0^{\hat{x}} \hat{w}_{0t}(s,t)\,\mathrm{d}s = m_t(\hat{x},t),$$

where the subscript t denotes partial differentiation with respect to t and $m(\hat{x},t)$ is defined by

$$m(\hat{x},t) = \int_0^{\hat{x}} \hat{w}_0(s,t)\,\mathrm{d}s\,. \tag{3.29}$$

This means that

$$\mathrm{Re}(F(\hat{x}+0i,t)) = -\mathrm{Im}(W(\hat{x}+0i,t)) + \hat{x} = \hat{x} - m_t(\hat{x},t).$$

for $|\hat{x}| < d_0(t)$. Therefore, using the Schwarz reflection formula (3.28), we find we have a discontinuity across the $\hat{x}$ axis given by

$$F(\hat{x}+0i,t) = -F(\hat{x}-0i,t) + 2(\hat{x} - m_t(\hat{x},t)) \text{ for } |\hat{x}| < d_0(t).$$

As F is bounded at $\hat{x} = \pm d_0(t)$ and at infinity, the solution for F is found via the Riemann-Hilbert method [29] to be given by

$$F(\zeta,t) = \frac{(\zeta^2 - d_0(t)^2)^{1/2}}{2\pi i} \int_{-d_0(t)}^{d_0(t)} \frac{2(s - m_t(s,t))}{(s^2 - d_0(t)^2)^{1/2}(s-\zeta)}\,\mathrm{d}s\,,$$

where the branch cut for the square root is taken to be along $|\hat{x}| \le d_0(t)$, $\hat{z} = 0$, with $(\zeta^2 - d_0(t)^2)^{1/2} \sim \zeta$ as $\zeta \to \infty$. The solution for the complex velocity is therefore given by

$$\begin{aligned} W(\zeta,t) = i\zeta - \frac{(\zeta^2 - d_0(t)^2)^{1/2}}{\pi} \underbrace{\int_{-d_0(t)}^{d_0(t)} \frac{s}{(s^2 - d_0(t)^2)^{1/2}(s-\zeta)}\,\mathrm{d}s}_{I_1} \\ + \frac{(\zeta^2 - d_0(t)^2)^{1/2}}{\pi} \int_{-d_0(t)}^{d_0(t)} \frac{m_t(s,t)}{(s^2 - d_0(t)^2)^{1/2}(s-\zeta)}\,\mathrm{d}s\,. \end{aligned} \tag{3.30}$$

As $m_t(s,t)$ is unknown, we can only evaluate the first integral in (3.30) explicitly, labelled I_1. The evaluation of I_1 via contour integration is given in Appendix B by (B.2), resulting in the solution for the leading-order complex velocity potential being given by

$$\begin{aligned} W(\zeta,t) &= \hat{\phi}_0 + i\hat{\psi}_0 \\ &= i(\zeta^2 - d_0(t)^2)^{1/2} \left[1 - \frac{1}{\pi} \int_{-d_0(t)}^{d_0(t)} \frac{m_t(s,t)}{\sqrt{d_0(t)^2 - s^2}(s-\zeta)}\,\mathrm{d}s\right]. \end{aligned} \tag{3.31}$$

We can also differentiate (3.31) with respect to ζ to find the leading-order velocities $\hat{u}_0$ and $\hat{v}_0$ in the outer region to be given by

$$\begin{aligned}\hat{u}_0 - i\hat{v}_0 =& \frac{i\zeta}{(\zeta^2 - d_0(t)^2)^{1/2}}\left[1 - \frac{1}{\pi}\int_{-d_0(t)}^{d_0(t)} \frac{m_t(s,t)}{\sqrt{d_0(t)^2 - s^2}(s-\zeta)}\,\mathrm{d}s\right] \\ &- \frac{i(\zeta^2 - d_0(t)^2)^{1/2}}{\pi}\int_{-d_0(t)}^{d_0(t)} \frac{m_t(s,t)}{\sqrt{d_0(t)^2 - s^2}(s-\zeta)^2}\,\mathrm{d}s\,,\end{aligned} \tag{3.32}$$

which we note are singular as $\zeta \to \pm d_0(t)$, motivating the need to study the inner regions in §3.2.4.

3.2.3.2 Solution for the free surface location

In order to find the location of the free surface $\hat{h}_0(\hat{x}, t)$, we must integrate the leading-order kinematic boundary condition on the free surface (3.22) with respect to time. To this end, we define the leading-order displacement potential Υ_0, first considered by Korobkin (1982) [51], by

$$\Upsilon_0(\hat{x}, \hat{z}, t) = \int_0^t \hat{\phi}_0(\hat{x}, \hat{z}, \tau)\,\mathrm{d}\tau\,. \tag{3.33}$$

For determining the displacement potential, we assume that the leading-order solution for the turnover point $d_0(t)$ has an inverse $\omega_0(\hat{x})$, such that

$$\hat{x} = d_0(t) \iff t = \omega_0(\hat{x}). \tag{3.34}$$

It follows that $\omega_0(\hat{x})$ only exists if $\dot{d}_0(t) > 0$ for all t. If at any point $\dot{d}_0(t) \leq 0$, then the outer problem would be equivalent to the water exit problem discussed in Howison et al. (1991) [45] and Gillow (1998) [29]. In these studies, it was shown that the water exit problem is unstable to perturbations in the y direction, and hence for the purposes of this study, we will assume that $\dot{d}_0(t) > 0$ for all t.

Given the definition of $\omega_0(\hat{x})$ (3.34), for $|\hat{x}| < d_0(t)$, $\hat{z} = 0$, we have

$$\begin{aligned}\frac{\partial \Upsilon_0}{\partial \hat{z}} &= \int_0^t \frac{\partial \hat{\phi}_0}{\partial \hat{z}}\,\mathrm{d}\tau = \int_0^{\omega_0(\hat{x})} \frac{\partial \hat{h}_0}{\partial t}\,\mathrm{d}\tau - \int_{\omega_0(\hat{x})}^t \frac{\partial \hat{w}}{\partial t}\,\mathrm{d}\tau \\ &= \hat{h}_0(\hat{x}, \omega_0(\hat{x})) - \hat{h}_0(\hat{x}, 0) - \hat{w}_0(\hat{x}, t) + \hat{w}_0(\hat{x}, \omega(\hat{x})) = -\frac{1}{2}\hat{x}^2 - \hat{w}_0(\hat{x}, t),\end{aligned} \tag{3.35}$$

where we made use of the leading-order kinematic boundary conditions on the substrate (3.21) and the free surface (3.22), as well as the Wagner condition (3.26). As,

by (3.23), $\hat{\phi}_0 = 0$ for $|\hat{x}| > d_0(t)$, $\hat{z} = 0$, we also have that $\Upsilon_0 = 0$ there. Therefore the governing equations for the leading-order displacement potential are

$$\frac{\partial^2 \Upsilon_0}{\partial \hat{x}^2} + \frac{\partial^2 \Upsilon_0}{\partial \hat{z}^2} = 0 \qquad \text{for } \hat{z} > 0, \tag{3.36}$$

$$\frac{\partial \Upsilon_0}{\partial \hat{z}} = -\frac{1}{2}\hat{x}^2 - \hat{w}_0(\hat{x}, t) \qquad \text{on } |\hat{x}| < d_0(t),\ \hat{z} = 0, \tag{3.37}$$

$$\frac{\partial \Upsilon_0}{\partial \hat{z}} = \hat{h}_0(\hat{x}, t) - \frac{1}{2}\hat{x}^2, \qquad \text{on } |\hat{x}| > d_0(t),\ \hat{z} = 0, \tag{3.38}$$

$$\Upsilon_0 = 0, \qquad \text{on } |\hat{x}| > d_0(t),\ \hat{z} = 0, \tag{3.39}$$

with far-field and initial conditions given by

$$\Upsilon_0(\hat{x}, \hat{z}, t) \sim -t\hat{z} \text{ as } \hat{x}^2 + \hat{z}^2 \to \infty, \quad \Upsilon_0(\hat{x}, \hat{z}, 0) = 0, \tag{3.40}$$

and in addition we know from (3.25) that Υ_0 is bounded as $\hat{x} + i\hat{z} \to \pm d_0(t)$.

Similar to the solution presented in §3.2.3.1, we solve this mixed boundary value problem for Υ_0 using the Riemann-Hilbert method. We first define the complex displacement potential by

$$G(\zeta, t) = i(\Upsilon_0 + i\Psi_0 - it\zeta), \tag{3.41}$$

where Ψ_0 is defined in terms of the streamfunction $\hat{\psi}_0$ by

$$\Psi_0 = \int_0^t \psi_0(\hat{x}, \hat{z}, \tau)\, \mathrm{d}\tau\,,$$

and we know that G is bounded as $\zeta \to \infty$. By the Cauchy-Riemann equations, we have $\partial \Upsilon_0 / \partial \hat{z} = -\partial \Psi_0 / \partial \hat{x}$, so by integrating the kinematic condition on the substrate (3.37) with respect to $\hat{x}$, we have

$$\Psi_0(\hat{x}, 0, t) = \frac{1}{6}\hat{x}^3 + m(\hat{x}, t) \text{ for } |\hat{x}| < d_0(t), \tag{3.42}$$

where recall $m(\hat{x}, t)$ is defined in (3.29) as the integral of $\hat{w}_0$ in $\hat{x}$. As before, we now analytically continue G onto the whole complex plane using the Scharz reflection formula

$$G(\zeta, t) = \overline{G(\bar{\zeta}, t)} \text{ for } \hat{z} < 0. \tag{3.43}$$

As with $F(\zeta, t)$, we have that $\mathrm{Im}(G(\hat{x} + 0i)) = 0$ for $|\hat{x}| > d_0(t)$, $\hat{z} = 0^+$, and hence by the Schwarz reflection formula, $G(\zeta, t)$ is continuous across the $\hat{x}$ axis for $|\hat{x}| > d_0(t)$. For $|\hat{x}| < d_0(t)$, we have the jump condition

$$G(\hat{x} + 0i, t) = -G(\hat{x} - 0i) + 2\left(t\hat{x} - \frac{1}{6}\hat{x}^3 - m(\hat{x}, t)\right). \tag{3.44}$$

Since G is bounded at $\hat{x} = \pm d_0(t)$ and at infinity, we apply the Riemann-Hilbert method [29] to find

$$\begin{aligned} G(\zeta,t) = \frac{(\zeta^2 - d_0(t)^2)^{1/2}}{\pi i} \underbrace{\int_{-d_0(t)}^{d_0(t)} \frac{ts - s^3/6}{(s^2 - d_0(t)^2)^{1/2}(s-\zeta)}\,\mathrm{d}s}_{I_2} \\ - \frac{(\zeta^2 - d_0(t)^2)^{1/2}}{\pi i} \int_{-d_0(t)}^{d_0(t)} \frac{m(s,t)}{(s^2 - d_0(t)^2)^{1/2}(s-\zeta)}\,\mathrm{d}s\,. \end{aligned} \tag{3.45}$$

As before, the evaluation the first integral in (3.45), labelled I_2, is given in Appendix B by (B.4). The solution for the complex displacement potential is therefore

$$\begin{aligned} \Upsilon_0 + i\Psi_0 = \frac{i}{6}\left[\zeta^3 - (\zeta^2 - d_0(t)^2)^{3/2}\right] + i\left(t - \frac{d_0(t)^2}{4}\right)(\zeta^2 - d_0(t)^2)^{1/2} \\ - \frac{i(\zeta^2 - d_0(t)^2)^{1/2}}{\pi} \int_{-d_0(t)}^{d_0(t)} \frac{m(s,t)}{\sqrt{d_0(t)^2 - s^2}(s-\zeta)}\,\mathrm{d}s\,. \end{aligned} \tag{3.46}$$

We determine the leading-order free surface location $\hat{h}_0$ by solving the kinematic boundary condition (3.38), so we must find the solution for $\partial\Upsilon_0/\partial\hat{z}$ on $|\hat{x}| > d_0(t)$, $\hat{z} = 0$. To this end, we differentiate (3.46) with respect to ζ to find

$$\begin{aligned} \frac{\mathrm{d}}{\mathrm{d}\zeta}(\Upsilon_0 + i\Psi_0) &= \frac{\partial\Upsilon_0}{\partial\hat{x}} - i\frac{\partial\Upsilon_0}{\partial\hat{z}} \\ &= \frac{i}{2}\left[\zeta^2 - \zeta(\zeta^2 - d_0(t)^2)^{1/2}\right] \\ &+ \frac{i\zeta}{(\zeta^2 - d_0(t)^2)^{1/2}}\left[t - \frac{d_0(t)^2}{4} - \frac{1}{\pi}\int_{-d_0(t)}^{d_0(t)} \frac{m(s,t)}{\sqrt{d_0(t)^2 - s^2}(s-\zeta)}\,\mathrm{d}s\right] \\ &- \frac{i\,(\zeta^2 - d_0(t)^2)^{1/2}}{\pi} \int_{-d_0(t)}^{d_0(t)} \frac{m(s,t)}{\sqrt{d_0(t)^2 - s^2}(s-\zeta)^2}\,\mathrm{d}s\,. \end{aligned} \tag{3.47}$$

Then, without loss of generality, we let $\zeta = \hat{x}$ for $\hat{x} > d_0(t)$, noting that for $\hat{x} < -d_0(t)$, we have $\hat{h}_0(\hat{x},t) = \hat{h}_0(-\hat{x},t)$ by symmetry. Hence by taking the imaginary part of (3.47) and substituting into (3.38), we find the solution for $\hat{h}_0(\hat{x},t)$ to be

$$\begin{aligned} \hat{h}_0(\hat{x},t) = \frac{1}{2}\hat{x}\sqrt{\hat{x}^2 - d_0(t)^2} \\ + \frac{\sqrt{\hat{x}^2 - d_0(t)^2}}{\pi} \int_{d_0(t)}^{d_0(t)} \frac{m(s,t)}{\sqrt{d_0(t)^2 - s^2}(s-\hat{x})^2}\,\mathrm{d}s \\ - \frac{\hat{x}}{\sqrt{\hat{x}^2 - d_0(t)^2}}\left[t - \frac{d_0(t)^2}{4} - \frac{1}{\pi}\int_{-d_0(t)}^{d_0(t)} \frac{m(s,t)}{\sqrt{d_0(t)^2 - s^2}(s-\hat{x})}\,\mathrm{d}s\right], \end{aligned} \tag{3.48}$$

for $\hat{x} > d_0(t)$. Note that later we will see that the term inside the final bracket is $O(\sqrt{\hat{x}^2 - d_0(t)^2})$ as $\hat{x} \to d_0(t)$, so that $\hat{h}_0(\hat{x},t)$ is still bounded at the turnover points.

3.2.3.3 Solution for the turnover point

Besides the substrate position $\hat{w}_0(\hat{x},t)$, the solutions for the velocity potential (3.31) and the free surface (3.48) also depend on the unknown position of the turnover point, $d_0(t)$. Given that we know $\hat{\phi}_0 = O((d_0(t)^2-\zeta^2)^{1/2})$ as $\zeta \to \pm d_0(t)$, we can find an equation for $d_0(t)$ by enforcing that

$$\Upsilon_0 + i\Psi_0 = C_\pm + O((d_0(t)^2-\zeta^2)^{3/2}) \text{ as } \zeta \to \pm d_0(t), \tag{3.49}$$

where $C_\pm$ are complex constants. Specifically, in the following we find an asymptotic expansion of the solution for the complex displacement potential in (3.46) as $\zeta \to d_0(t)$, and ensure that any $O((d_0(t)^2-\zeta^2)^{1/2})$ terms cancel out.

Without loss of generality, we let $\zeta = d_0(t)(1+\nu)$, where $0 < \nu \ll 1$, and find the leading-order expansion of (3.46) as $\nu \to 0$. We define the $m(s,t)$ dependent integral in (3.46) to be I_3, and in Appendix B, the expansion of I_3 as $\nu \to 0$ is given by (B.7), such that

$$\begin{aligned} I_3 &= \int_{-d_0(t)}^{d_0(t)} \frac{m(s,t)}{\sqrt{d_0(t)^2-s^2}(s-\zeta)}\,\mathrm{d}s \\ &= -\frac{\pi m(d_0(t),t)}{\sqrt{2\nu}d_0(t)} + 2\int_0^{d_0(t)} \frac{\hat{w}_0(s,t)}{\sqrt{d_0(t)^2-s^2}}\,\mathrm{d}s + O(\sqrt{\nu}). \end{aligned} \tag{3.50}$$

By substituting the expansion for I_3 given by (3.50) into (3.46) and enforcing that the $O(\sqrt{\nu})$ terms cancel out, we conclude that

$$t - \frac{d_0(t)^2}{4} = \frac{2}{\pi}\int_0^{d_0(t)} \frac{\hat{w}_0(s,t)}{\sqrt{d_0(t)^2-s^2}}\,\mathrm{d}s\,, \tag{3.51}$$

which is an implicit equation for $d_0(t)$ that is coupled to the problem for $\hat{w}_0$. By substituting $s = d_0(t)\sin(\theta)$, we can write (3.51) as

$$t - \frac{d_0(t)^2}{4} = \frac{2}{\pi}\int_0^{\pi/2} \hat{w}_0(d_0(t)\sin(\theta),t)\,\mathrm{d}\theta\,, \tag{3.52}$$

which agrees with equation (11) in Korobkin (1998) [52].

The speed of the turnover point, $\dot{d}_0(t)/\epsilon$, is also of interest, so by differentiating (3.52) with respect to t, we find

$$\begin{aligned} 1 - \frac{\dot{d}_0(t)d_0(t)}{2} &= \frac{1}{\pi}\frac{\mathrm{d}}{\mathrm{d}t}\int_{-\pi/2}^{\pi/2} \hat{w}_0(d_0(t)\sin(\theta),t)\,\mathrm{d}\theta \\ &= \frac{1}{\pi}\int_{-\pi/2}^{\pi/2} \dot{d}_0(t)\sin(\theta)\hat{w}_{0\hat{x}}(d_0(t)\sin(\theta),t) + \hat{w}_{0t}(d_0(t)\sin(\theta),t)\,\mathrm{d}\theta \\ &= \frac{\dot{d}_0(t)}{\pi d_0(t)}\int_{-d_0(t)}^{d_0(t)} \frac{s\hat{w}_{0\hat{x}}(s,t)}{\sqrt{d_0(t)^2-s^2}}\,\mathrm{d}s + \frac{1}{\pi}\int_{-d_0(t)}^{d_0(t)} \frac{\hat{w}_{0t}(s,t)}{\sqrt{d_0(t)^2-s^2}}\,\mathrm{d}s\,, \end{aligned}$$

and hence re-arranging for $\dot{d}_0(t)$ yields the solution

$$\dot{d}_0(t) = \left(1 - \frac{1}{\pi}\int_{-d_0(t)}^{d_0(t)} \frac{\hat{w}_{0t}(s,t)}{\sqrt{d_0(t)^2 - s^2}}\,\mathrm{d}s\right) \Bigg/ \left(\frac{d_0(t)}{2} + \frac{1}{\pi d_0(t)}\int_{-d_0(t)}^{d_0(t)} \frac{s\hat{w}_{0\hat{x}}(s,t)}{\sqrt{d_0(t)^2 - s^2}}\,\mathrm{d}s\right). \tag{3.53}$$

This is an explicit equation for $\dot{d}_0(t)$, which may be found once $d_0(t)$, $\hat{w}_{0t}(\hat{x},t)$ and $\hat{w}_{0\hat{x}}(\hat{x},t)$ are known. We can see that in order for $\dot{d}_0(t)$ to be positive, as was required in our derivation of the displacement potential, the numerator and denominator of (3.53) must have the same sign.

For the case of a flat, stationary substrate, where $w(x,t) \equiv 0$, the turnover point and its derivative are given by

$$d_0(t) = 2\sqrt{t}, \quad \dot{d}_0(t) = \frac{1}{\sqrt{t}}. \tag{3.54}$$

In Figure 3.4, we plot the turnover point evolution for the stationary substrate case, given by (3.54), as well as the rigid and curved substrate examples, with solution given by (A.2). It can be seen that the rigid, moving substrate motion acts to decrease the spreading of the droplet in comparison to the stationary case. However the speed of the turnover point is increased in the curved substrate case.

The reasoning for the differences in the turnover point evolution between the cases is more clear when observing the shape of the free surfaces given in Figure 3.5. In Figure 3.5, the solid lines denote the free surface location at $\hat{z} = \epsilon\hat{h}_0$, the dashed lines show the free surface location at $\hat{z} = -\epsilon\hat{w}(\hat{x},t)$, black lines denote the stationary substrate case, and the red and blue lines denoting the rigid and curved moving substrate cases, respectively. For the rigid moving substrate case, we can see how the free surface falls below the $\hat{x}$ axis as expected due to the plate motion, and similarly for the curved substrate case, the free surface moves upwards along the substrate as it spreads. For all of these cases, the far-field condition for $\hat{h}_0$ (3.24) is independent of the substrate motion. This means that, in order to conserve mass, the horizontal spreading of the rigid moving substrate case must be slower than the stationary substrate case as the fluid falls below the $\hat{x}$ axis. Similarly, the horizontal spreading must be faster in the curved substrate case as the fluid moves up the substrate above the $\hat{x}$ axis. This explains the relationship between the turnover points in Figure 3.4.

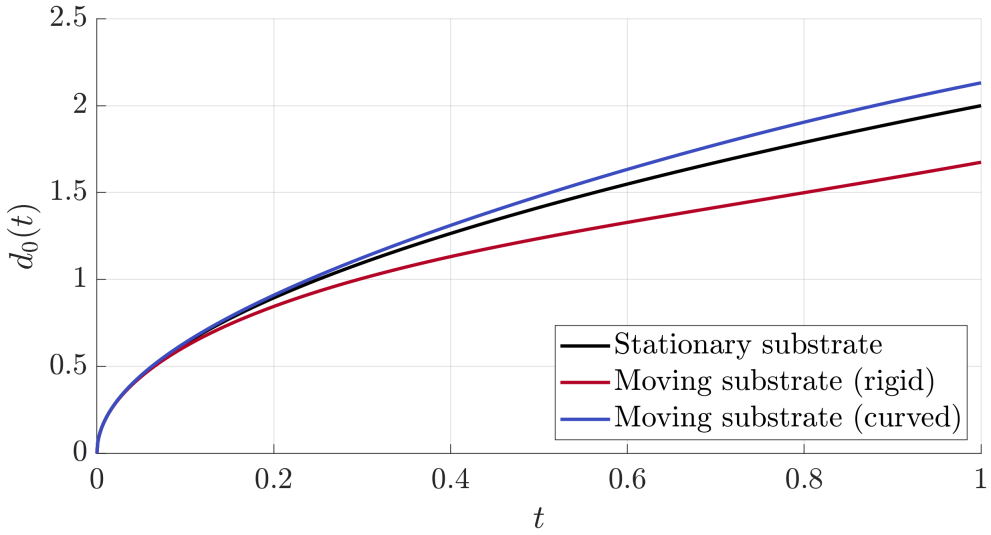

Figure 3.4: Leading-order solutions for the turnover point location $\hat{x} = d_0(t)$, given by (3.51).

3.2.3.4 Solution for the pressure

It is important to understand the pressure distribution within the droplet, as it is the pressure on the substrate drives the substrate motion governed by (2.33) and (2.36). The leading-order pressure is given by Bernoulli's equation (3.20), giving $\hat{p}_0 = -\partial\hat{\phi}_0/\partial t$. Substituting this into the governing equations for the velocity potential (3.19), (3.20), (3.21) and (3.23) yields

$$\frac{\partial^2\hat{p}_0}{\partial\hat{x}^2} + \frac{\partial^2\hat{p}_0}{\partial\hat{z}^2} = 0 \qquad \text{for } \hat{z} \geq 0, \tag{3.55}$$

$$\frac{\partial\hat{p}_0}{\partial\hat{z}} = \frac{\partial^2\hat{w}_0}{\partial t^2}, \qquad \text{on } |\hat{x}| < d_0(t), \hat{z} = 0^+, \tag{3.56}$$

$$\hat{p}_0 = 0, \qquad \text{on } |\hat{x}| > d_0(t), \hat{z} = 0^+, \tag{3.57}$$

with the far-field condition given by

$$\hat{p}_0 \to 0 \text{ as } \hat{x}^2 + \hat{z}^2 \to \infty, \tag{3.58}$$

and in addition we know from (3.25) that

$$\hat{p}_0 = O((d_0(t)^2 - (\hat{x} + i\hat{z})^2)^{-1/2}) \text{ as } \hat{x} + i\hat{z} \to \pm d_0(t). \tag{3.59}$$

We now define a new complex potential given by

$$H(\zeta, t) = -i(\hat{p}_0 + i\hat{q}_0) = \hat{q}_0 - i\hat{p}_0, \tag{3.60}$$

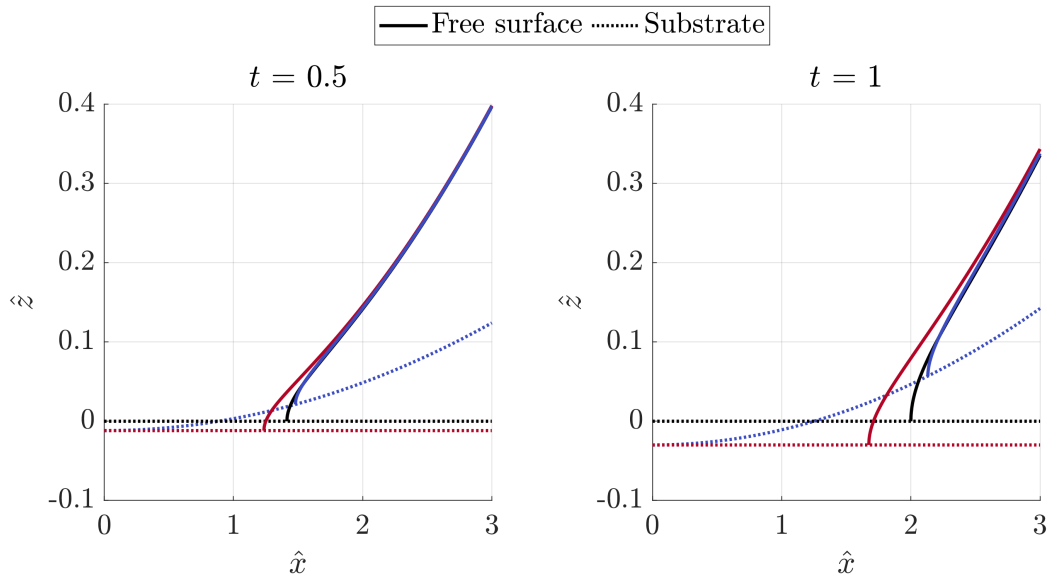

Figure 3.5: Leading-order solutions for the free surface location in the outer region $\hat{z} = \epsilon\hat{h}_0(\hat{x}, t)$ given by (3.48) (solid lines), alongside the substrate location $\hat{z} = -\epsilon\hat{w}_0(\hat{x}, t)$ (dotted lines). The black lines denote the stationary substrate case, the red lines denote the rigid moving substrate case (with $\hat{w}_0$ given by (3.16)) and the blue lines denote the curved moving substrate case (with $\hat{w}_0$ given by (3.17)).

where $-\hat{q}_0$ is the time-derivative of the streamfunction $\hat{\psi}_0$, and we have that H is bounded as $\zeta \to \infty$. By the Cauchy-Riemann equations, we know $\partial\hat{p}_0/\partial\hat{z} = -\partial\hat{q}_0/\partial\hat{x}$, so for $|\hat{x}| < d_0(t)$, $\hat{z} = 0^+$,

$$\frac{\partial\hat{q}_0}{\partial\hat{x}} = -\frac{\partial\hat{p}_0}{\partial\hat{z}} = -\frac{\partial^2\hat{w}_0}{\partial t^2} \implies \hat{q}_0 = -K(t) - \int_0^{\hat{x}} \hat{w}_{0tt}(\xi, t)\,\mathrm{d}\xi = -K(t) - m_{tt}(\hat{x}, t),$$

where $K(t)$ is an unknown function of t. As before, we analytically continue H onto the whole complex plane by defining

$$H(\zeta, t) = \overline{H(\bar{\zeta}, t)} \text{ for } \hat{z} < 0. \tag{3.61}$$

As $\hat{p}_0 = 0$ for $|\hat{x}| > d_0(t)$, $\hat{z} = 0^+$, we know $H(\zeta, t)$ is continuous across the $\hat{x}$ axis for $|\hat{x}| > d_0(t)$, and for $|\hat{x}| < d_0(t)$ we have the jump condition

$$H(\hat{x} + 0i, t) = -H(\hat{x} - 0i, t) - 2(K(t) + m_{tt}(\hat{x}, t)) \text{ for } |\hat{x}| < d_0(t).$$

As H is unbounded at $\zeta = \pm d_0(t)$ and bounded as $\zeta \to \infty$, the solution to the

Riemann-Hilbert problem [29] is given by

$$H(\zeta,t) = \frac{1}{(\zeta^2 - d_0(t)^2)^{1/2}} \left[A(t) - \frac{K(t)}{\pi i} \underbrace{\int_{-d_0(t)}^{d_0(t)} \frac{(s^2 - d_0(t)^2)^{1/2}}{s-\zeta}\,\mathrm{d}s}_{I_4} \right] - \frac{1}{\pi i(\zeta^2 - d_0(t)^2)^{1/2}} \int_{-d_0(t)}^{d_0(t)} \frac{(s^2 - d_0(t)^2)^{1/2} m_{tt}(s,t)}{s-\zeta}\,\mathrm{d}s\,, \tag{3.62}$$

where $A(t)$ is an unknown function of t to be determined. The solution for the labelled integral, I_4, is derived in Appendix B and given by (B.9). Note that $H(\zeta,t) = iW_t(\zeta,t)$, where W_t is the time derivative of the complex potential $W = \hat{\phi}_0 + i\psi_0$, so the solution for W_t is

$$W_t(\zeta,t) = \frac{i(K(t)\zeta - A(t))}{(\zeta^2 - d_0(t)^2)^{1/2}} - iK(t) + \frac{i}{\pi(\zeta^2 - d_0(t)^2)^{1/2}} \int_{-d_0(t)}^{d_0(t)} \frac{\sqrt{d_0(t)^2 - s^2}\, m_{tt}(s,t)}{s-\zeta}\,\mathrm{d}s\,. \tag{3.63}$$

In order to determine the unknowns $A(t)$ and $K(t)$, we find the asymptotic behaviour of the solutions for $W(\zeta,t)$ from (3.31) and $W_t(\zeta,t)$ from (3.63) as $\zeta \to \infty$ and compare the coefficients of the powers of ζ. First, expanding (3.63) for $\zeta \to \infty$, we have

$$\begin{aligned} W_t(\zeta,t) &= -\frac{iA(t)}{\zeta} + \frac{i}{\zeta^2}\left[\frac{K(t)d_0(t)^2}{2} - \frac{1}{\pi}\int_{-d_0(t)}^{d_0(t)} \sqrt{d_0(t)^2 - s^2}\, m_{tt}(s,t)\,\mathrm{d}s \right] + O\left(\frac{1}{\zeta^3}\right) \\ &= -\frac{iA(t)}{\zeta} + \frac{iK(t)d_0(t)^2}{2\zeta^2} + O\left(\frac{1}{\zeta^3}\right), \end{aligned} \tag{3.64}$$

where we used the fact that $m_{tt}(s,t)$ is odd in s to evaluate the integral. Next, we expand the solution for $W(\zeta,t)$ from (3.31) as $\zeta \to \infty$, giving

$$\begin{aligned} W(\zeta,t) &= i\zeta\left(1 - \frac{d_0(t)^2}{2\zeta^2}\right)\left[1 + \frac{1}{\pi\zeta}\int_{-d_0(t)}^{d_0(t)} \frac{m_t(s,t)}{\sqrt{d_0(t)^2 - s^2}}\left(\frac{s}{\zeta}\right)\mathrm{d}s\right] + O\left(\frac{1}{\zeta^3}\right) \\ &= i\zeta + \frac{i}{\zeta}\left[-\frac{d_0(t)^2}{2} + \frac{1}{\pi}\int_{-d_0(t)}^{d_0(t)} \frac{s m_t(s,t)}{\sqrt{d_0(t)^2 - s^2}}\,\mathrm{d}s \right] + O\left(\frac{1}{\zeta^3}\right), \end{aligned} \tag{3.65}$$

where we again used the fact that $m_t(s,t)$ is odd in s to evaluate the integrals with odd integrands. Here, we note that there are no $O(1/\zeta^2)$ terms in the expansion for

$W(\zeta,t)$ as $\zeta\to\infty$, which means there should be none in $W_t(\zeta,t)$ either. Therefore by comparing to the expansion (3.64), we conclude that $K(t)=0$.

To determine $A(t)$, we focus on the $O(1/\zeta)$ terms. First, we simplify the final integral that appears in (3.65),

$$\int_{-d_0(t)}^{d_0(t)}\frac{sm_t(s,t)}{\sqrt{d_0(t)^2-s^2}}\,\mathrm{d}s=\int_{-d_0(t)}^{d_0(t)}\sqrt{d_0(t)^2-s^2}\hat{w}_{0t}(s,t)\,\mathrm{d}s\,, \tag{3.66}$$

and then comparing the $O(1/\zeta)$ term of (3.64) with the time derivative of the $O(1/\zeta)$ term of (3.65) yields the solution for $A(t)$ given by

$$\begin{aligned}A(t)&=\frac{\mathrm{d}}{\mathrm{d}t}\left[\frac{d_0(t)^2}{2}-\frac{1}{\pi}\int_{-d_0(t)}^{d_0(t)}\sqrt{d_0(t)^2-s^2}\hat{w}_{0t}(s,t)\,\mathrm{d}s\right]\\&=d_0(t)\dot{d}_0(t)\left[1-\frac{1}{\pi}\int_{-d_0(t)}^{d_0(t)}\frac{\hat{w}_{0t}(s,t)}{\sqrt{d_0(t)^2-s^2}}\,\mathrm{d}s\right]\\&\quad-\frac{1}{\pi}\int_{-d_0(t)}^{d_0(t)}\sqrt{d_0(t)^2-s^2}\hat{w}_{0tt}(s,t)\,\mathrm{d}s\,.\end{aligned} \tag{3.67}$$

Therefore the solution for W_t is

$$W_t(\zeta,t)=-\frac{i}{(\zeta^2-d_0(t)^2)^{1/2}}\left[A(t)-\frac{1}{\pi}\int_{-d_0(t)}^{d_0(t)}\frac{\sqrt{d_0(t)^2-s^2}m_{tt}(s,t)}{s-\zeta}\,\mathrm{d}s\right], \tag{3.68}$$

where the leading-order pressure is given by

$$\hat{p}_0=\mathrm{Re}\left\{\frac{i}{(\zeta^2-d_0(t)^2)^{1/2}}\left[A(t)-\frac{1}{\pi}\int_{-d_0(t)}^{d_0(t)}\frac{\sqrt{d_0(t)^2-s^2}m_{tt}(s,t)}{s-\zeta}\,\mathrm{d}s\right]\right\}, \tag{3.69}$$

and $A(t)$ is given by (3.67).

In Figure 3.6, we plot the solution for the pressure (3.69) in the stationary substrate case (left) and the rigid moving substrate case (right), at $t=0.5$ for $\epsilon=0.1$. In both cases, we can see how the pressure diverges close to the turnover points, shown with black dots, as reflected by the square-root singularity in (3.69) as $\zeta\to\pm d_0(t)$. Referring to Figure 3.2, we can see that at this time, the moving substrate is accelerating downwards, subsequently giving a lower pressure than the stationary substrate case both due to the $A(t)$ term given by (3.67) and the contour integral in (3.69). We have also plotted a number of streamlines from (3.31). For the stationary substrate, we can see how the kinematic boundary condition on the substrate (3.21) enforces that the vertical velocity for $|\hat{x}|<d_0(t)$ is zero, meaning the streamlines hence all terminate for $|\hat{x}|>d_0(t)$, where the kinematic boundary condition on the free surface

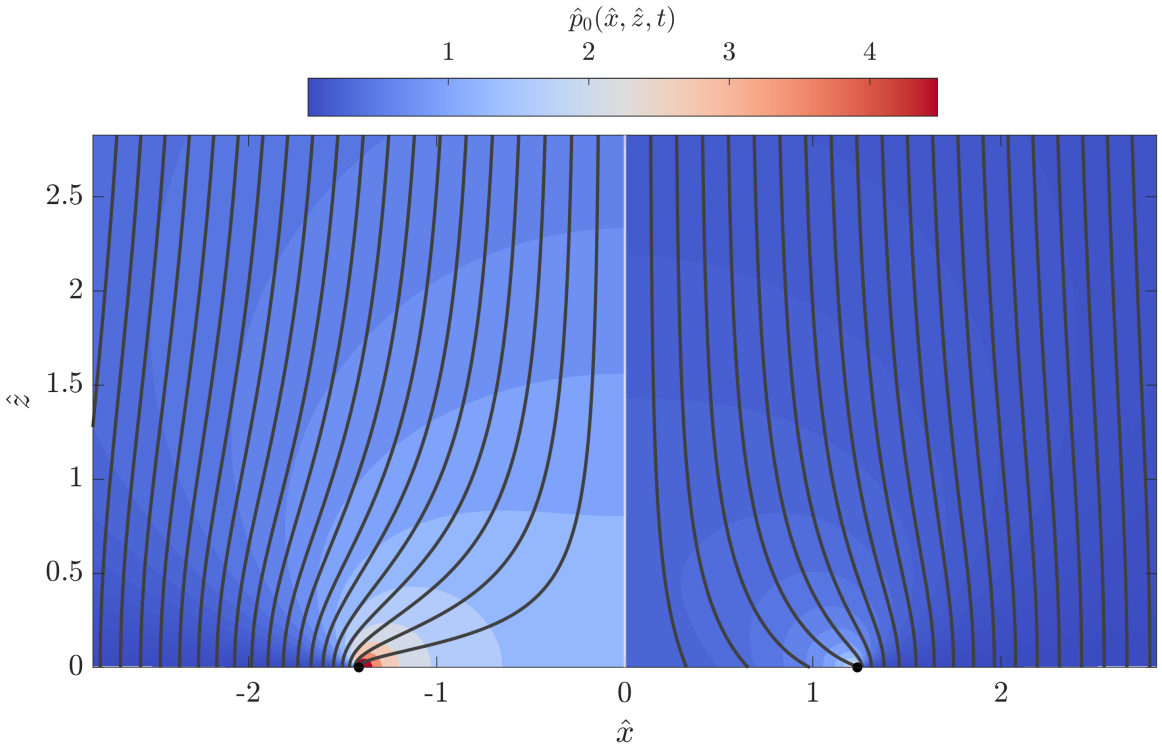

Figure 3.6: Leading-order solutions for the pressure in the outer region (3.69), where the stationary substrate case is plotted for $\hat{x} < 0$, and the rigid moving substrate case is plotted for $\hat{x} > 0$. The solid lines show the streamlines from (3.31).

(3.22) is applied to enforce the fluid velocity matches the free surface velocity. However for the moving substrate case, we have a non-zero velocity for $|\hat{x}| < d_0(t)$, which means some of the streamlines do terminate on the substrate, as seen in Figure 3.6. It is worth noting that the pressure in the moving substrate cases can also become greater than the stationary substrate case, such as situations where the substrate is accelerating upwards towards the droplet (i.e. see later times of Figure 3.2).

3.2.4 Inner region

In the previous subsection, we saw how the leading-order solutions for the velocity and pressure diverge close to the turnover points. As these should be finite physically, this motivates considering inner regions surrounding each turnover point to resolve the flow locally. Without loss of generality, given that the problem is symmetric in x, we focus on the inner region surrounding the right hand turnover point. In previous two-dimensional Wagner theory studies, such as Wilson (1989) [97] and Moore (2014) [62], it was found that the inner region has to be two orders of magnitude smaller than the outer region with an $O(1/\epsilon)$ velocity in order to match. Motivated by this,

we introduce the inner variables

$$\begin{gathered} x = \epsilon d(t) + \epsilon^3 \tilde{x}, \quad z = -\epsilon^2 w(\epsilon d(t), t) + \epsilon^3 \tilde{z}, \\ \phi = \epsilon^2 \left[\dot{d}(t)\tilde{x} - \epsilon w_t(\epsilon d(t), t)\tilde{z} + \tilde{\phi} \right], \quad h = -\epsilon^2 w(\epsilon d(t), t) + \epsilon^3 \tilde{h}, \quad p = \frac{1}{\epsilon^2}\tilde{p}, \end{gathered} \tag{3.70}$$

where we validate these scalings later by matching with the outer region solutions in §3.2.4.4. We then substitute (3.70) into (3.7)-(3.11) and expand $(\tilde{\phi},\, \tilde{h},\, \tilde{p}) = (\tilde{\phi}_0,\, \tilde{h}_0,\, \tilde{p}_0) + o(1)$ as $\epsilon \to 0$, such that to leading-order in ϵ, we have

$$\frac{\partial^2 \tilde{\phi}_0}{\partial \tilde{x}^2} + \frac{\partial^2 \tilde{\phi}_0}{\partial \tilde{z}^2} = 0 \qquad \text{in the fluid,} \tag{3.71}$$

$$\tilde{p}_0 + \frac{1}{2}\left[\left(\frac{\partial \tilde{\phi}_0}{\partial \tilde{x}} \right)^2 + \left(\frac{\partial \tilde{\phi}_0}{\partial \tilde{z}} \right)^2 \right] = \frac{1}{2}\dot{d}_0(t)^2 \qquad \text{in the fluid,} \tag{3.72}$$

$$\frac{\partial \tilde{\phi}_0}{\partial \tilde{z}} = 0 \qquad \text{on } \tilde{z} = 0, \tag{3.73}$$

$$\frac{\partial \tilde{\phi}_0}{\partial \tilde{x}} \frac{\partial \tilde{h}_0}{\partial \tilde{x}} = \frac{\partial \tilde{\phi}_0}{\partial \tilde{z}} \qquad \text{on } \tilde{z} = \tilde{h}_0(\tilde{x}, t), \tag{3.74}$$

$$\left(\frac{\partial \tilde{\phi}_0}{\partial \tilde{x}} \right)^2 + \left(\frac{\partial \tilde{\phi}_0}{\partial \tilde{z}} \right)^2 = \dot{d}_0(t)^2 \qquad \text{on } \tilde{z} = \tilde{h}_0(\tilde{x}, t), \tag{3.75}$$

subject to the far-field condition

$$\tilde{\phi}_0 \sim -\dot{d}_0(t)\tilde{x} + S(t)\,\mathrm{Re}\left(i\sqrt{\tilde{x} + i\tilde{z}} \right) \text{ as } \tilde{x} + i\tilde{z} \to \infty, \tag{3.76}$$

where $S(t)$ is determined via matching with the outer region in §3.2.4.4.

The resulting problem is a quasi-static Helmholtz flow, which is summarised in Figure 3.7. The fluid enters in from above, and either ends up in the jet, heading towards $\tilde{x} \to \infty$, or into the outer region for $\tilde{x} \to -\infty$. The dashed line in Figure 3.7 shows the streamline which divides these two portions of the flow, which ends at the relative stagnation point A. The far-field condition (3.76) implies that the flow enters from above with velocity $\tilde{u}_0 \sim -\dot{d}_0(t)$. Combining this with the kinematic condition on the free surface (3.75) and conservation of mass, we must have that

$$\tilde{\phi}_0 \sim \dot{d}_0(t)\tilde{x}, \quad \tilde{h}_0 \to J(t), \text{ as } \tilde{x} \to \infty \text{ in the jet,} \tag{3.77}$$

where $J(t)$ is the asymptotic jet thickness, and must be determined as part of the solution.

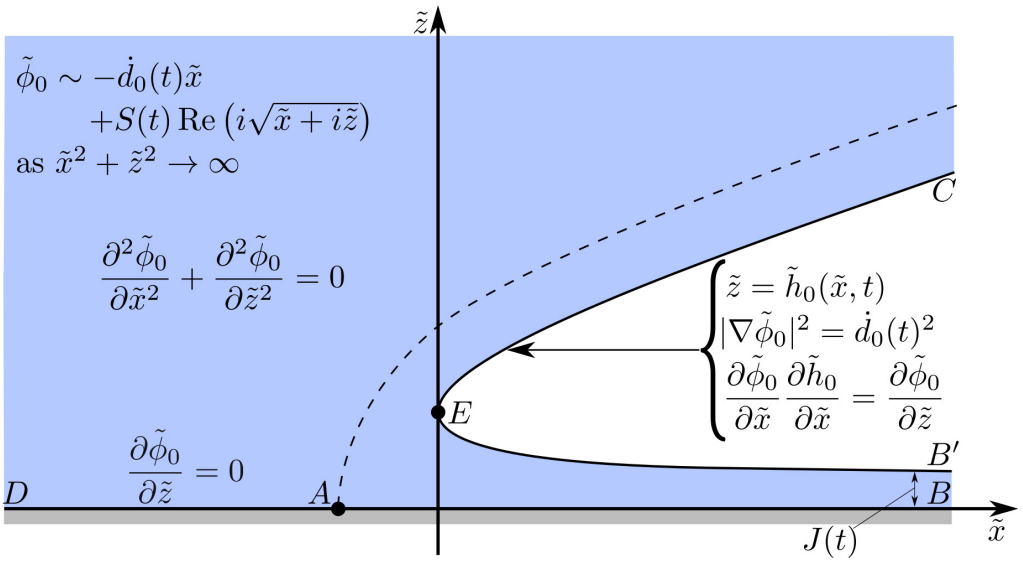

Figure 3.7: The leading-order problem for the right-hand inner region for $\tilde{\phi}_0$ and $\tilde{h}_0$. The dashed line is the dividing streamline that passes through the stagnation point A (relative to the frame moving with the inner region). The asymptotic jet thickness is denoted by $J(t)$.

3.2.4.1 Solution for the velocity potential

We now solve for the velocity potential. We start by constructing the complex potential

$$\widetilde{W}(\tilde{\zeta},t)=\frac{1}{\dot{d}_0(t)}\left(\tilde{\phi}_0+i\tilde{\psi}_0\right), \tag{3.78}$$

where $\tilde{\zeta}=\tilde{x}+i\tilde{z}$, $\tilde{\psi}_0$ is the leading-order inner streamfunction and the factor of $1/\dot{d}_0(t)$ is to simplify the resulting algebra. Without loss of generality, we set $\tilde{\psi}_0(0,0,t)=0$. We then define the complex velocity, $\widetilde{W}'$, by

$$\widetilde{W}'=\frac{\mathrm{d}\widetilde{W}}{\mathrm{d}\tilde{\zeta}}=\frac{1}{\dot{d}_0(t)}\left(\tilde{u}_0-i\tilde{v}_0\right), \tag{3.79}$$

where $\tilde{u}_0$ and $\tilde{v}_0$ are the leading-order velocities in the $\tilde{x}$ and $\tilde{z}$ directions respectively, given in terms of $\tilde{\phi}_0$ by

$$\tilde{u}_0=\frac{\partial\tilde{\phi}_0}{\partial\tilde{x}},\quad \tilde{v}_0=\frac{\partial\tilde{\phi}_0}{\partial\tilde{z}}. \tag{3.80}$$

In the following, we will determine the complex potential $\widetilde{W}$ using the hodograph technique, which involves finding a conformal map from the liquid domain in the $\widetilde{W}$ plane to that in the $\widetilde{W}'$ plane. Given the governing equations (3.71)-(3.77), the potential and hodograph planes are depicted in Figures 3.8a and 3.8b respectively,

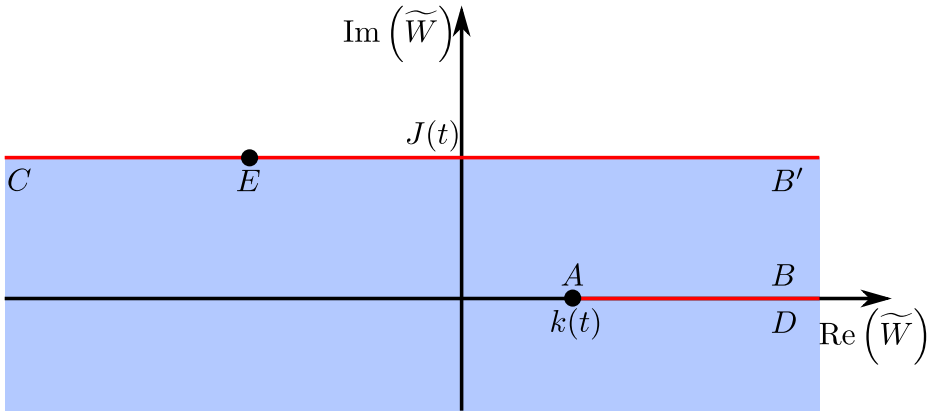

(a) Potential plane.

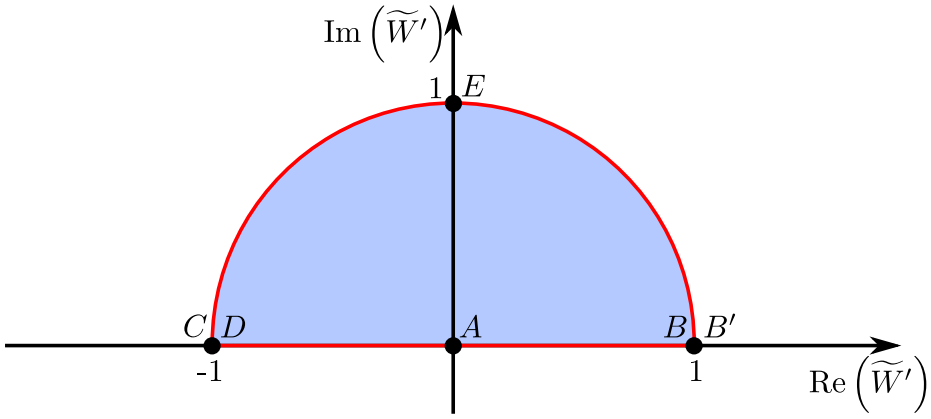

(b) Hodograph plane.

Figure 3.8: The potential and hodograph planes, where $\widetilde{W}$ and $\widetilde{W}'$ are defined in (3.78) and (3.79) respectively. The blue regions map to the liquid domain and the labelled points map to those in Figure 3.7.

where the blue regions denote the liquid domain and the labelled points correspond to those in Figure 3.7.

To find the conformal mapping from the $\widetilde{W}$-plane to the $\widetilde{W}'$-plane, we first introduce a new complex variable η and map the $\widetilde{W}$ plane to the upper half of the η-plane, depicted in Figure 3.9. Using the conformal map given by Figure 26 of Appendix 2 in Brown and Churchill (2009) [12], we have

$$\widetilde{W} = k(t) - \frac{J(t)}{\pi}\left[\eta + \log(\eta) - i\pi + 1\right], \tag{3.81}$$

where the branch cut for $\log(\eta)$ is taken to be the negative real axis, such that $\log(\eta)$ is real on the positive real axis. Here $k(t)$ is an integration variable that, as discussed by Oliver (2002) [66], cannot be determined from the leading-order problem. As seen in Figure 3.9, (3.81) maps all of the labelled points onto the real axis.

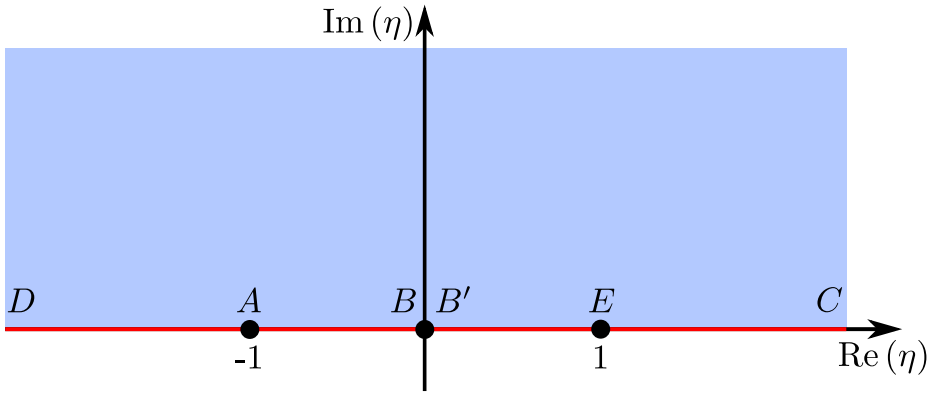

Figure 3.9: The η plane, defined in terms of the complex velocity potential $\widetilde{W}$ in (3.81). The labelled points map to those in Figure 3.7, and the red line maps to the streamlines along the substrate and the free surface.

Next, we construct a map from the hodograph plane $\widetilde{W}'$ onto the η plane, which is found by first applying a Möbius transformation to map the semi-circle to a quarter plane, and then squaring to map that to the upper-half plane. The resulting mapping is hence

$$\eta = -\left(\frac{\widetilde{W}' - 1}{\widetilde{W}' + 1}\right)^2 .$$

Re-arranging this equation for $\widetilde{W}'$, taking the root which maps E from $\eta = 1$ to $\widetilde{W}' = i$, we have

$$\widetilde{W}' = \frac{1 + i\eta^{1/2}}{1 - i\eta^{1/2}}, \tag{3.82}$$

where the branch cut for $\eta^{1/2}$ is taken to be along the negative real axis, with $\eta^{1/2} > 0$ on the positive real axis.

We now have expressions for $\widetilde{W}$ and $\widetilde{W}'$ in terms of η in (3.81) and (3.82) respectively. To complete the solution, we need to find $\tilde{\zeta}$ as a function of η. We first make the following change of variables to (3.82),

$$\frac{1 + i\eta^{1/2}}{1 - i\eta^{1/2}} = \widetilde{W}' = \frac{\mathrm{d}\widetilde{W}}{\mathrm{d}\tilde{\zeta}} = \frac{\mathrm{d}\widetilde{W}}{\mathrm{d}\eta}\frac{\mathrm{d}\eta}{\mathrm{d}\tilde{\zeta}}, \tag{3.83}$$

where by (3.81),

$$\frac{\mathrm{d}\widetilde{W}}{\mathrm{d}\eta} = -\frac{J(t)}{\pi}\left(1 + \frac{1}{\eta}\right), \tag{3.84}$$

so by re-arranging (3.83), we have an ODE for $\tilde{\zeta}$ given by

$$\frac{\mathrm{d}\tilde{\zeta}}{\mathrm{d}\eta} = \frac{1 - i\eta^{1/2}}{1 + i\eta^{1/2}}\frac{\mathrm{d}\widetilde{W}}{\mathrm{d}\eta} = -\frac{J(t)}{\pi}\frac{(1 + \eta^{-1})(1 - i\eta^{1/2})}{1 + i\eta^{1/2}} = -\frac{J(t)}{\pi}\left[\eta^{-1} - 2i\eta^{-1/2} - 1\right].$$

Integrating with respect to η then yields the solution for $\tilde{\zeta}$ given by

$$\tilde{\zeta} = \tilde{\zeta}_0 + \frac{J(t)}{\pi}\left[\eta + 4i\eta^{1/2} - \log(\eta)\right], \tag{3.85}$$

where $\tilde{\zeta}_0$ is an integration constant. By comparing Figures 3.7 and 3.9, we know $\tilde{x} = 0$ when $\eta = 1$ and $\tilde{z} \to J(t)$ as $\eta \downarrow 0$, giving $\tilde{\zeta}_0 = J(t)(-1/\pi + i)$. Therefore, the solution for the complex potential and velocity are given parametrically in terms of η by the set of equations

$$\tilde{\phi}_0 + i\tilde{\psi}_0 = \dot{d}_0(t)k(t) - \frac{\dot{d}_0(t)J(t)}{\pi}\left[\eta + \log(\eta) - i\pi + 1\right], \tag{3.86}$$

$$\tilde{u}_0 - i\tilde{v}_0 = \dot{d}_0(t)\frac{1 + i\eta^{1/2}}{1 - i\eta^{1/2}}, \tag{3.87}$$

$$\tilde{\zeta} = \tilde{x} + i\tilde{z} = \frac{J(t)}{\pi}\left[\eta + 4i\eta^{1/2} - \log(\eta) + i\pi - 1\right], \tag{3.88}$$

where we can use Figure 3.9 defining the η-plane to aid in finding the solutions at the points labelled in the schematic diagram for the inner region, Figure 3.7. This solution is equivalent to the inner region solution considered by Oliver (2002) [66] for infinite depth water entry, except in our case the fluid enters from above and has a finite velocity as $\tilde{z} \to \infty$.

3.2.4.2 Solution for the free surface location

The free surface is located at $\tilde{z} = \tilde{h}_0(\tilde{x}, t)$, lying along the line $B'EC$ in Figure 3.7. From the depiction of the η plane in Figure 3.9, we can see that the free surface is parameterised by $\eta = \sigma$ for $0 < \sigma < \infty$. Substituting this value of η into (3.88) for $\tilde{z} = \tilde{h}_0$, we have the parametric solution

$$\left(\tilde{x},\, \tilde{h}_0(\tilde{x}, t)\right) = \frac{J(t)}{\pi}\left(\sigma - \log(\sigma) - 1,\, \pi + 4\sqrt{\sigma}\right), \tag{3.89}$$

which is multivalued in $\tilde{x}$. As $\sigma \to 0$, the solution tends towards the jet region, while as $\sigma \to \infty$, the solution tends towards the outer region, with the turnover point location at $\sigma = 1$.

Given the solution for the free surface location (3.89), we can find the specific value of the height of the free surface above the substrate at the turnover curve to be

$$H(t) = \tilde{h}_0(0, t) = \left(1 + \frac{4}{\pi}\right) J(t), \tag{3.90}$$

which we find by setting $\sigma = 1$ in (3.89).

3.2.4.3 Solution for the pressure

The leading-order pressure in the inner region is given by Bernoulli's equation (3.72), which we re-write in terms of the complex velocity $\widetilde{W}'$ as

$$\tilde{p}_0 = \frac{1}{2}\left[\dot{d}_0(t)^2 - \left(\frac{\partial\tilde{\phi}_0}{\partial\tilde{x}}\right)^2 - \left(\frac{\partial\tilde{\phi}_0}{\partial\tilde{z}}\right)^2\right] = \frac{\dot{d}_0(t)^2}{2}\left(1 - \left|\widetilde{W}'\right|^2\right). \tag{3.91}$$

Substituting in the solution for $\widetilde{W}'$ in terms of η from (3.82), we have the parametric solution for the pressure in the inner region

$$\tilde{p}_0 = \frac{\dot{d}_0(t)^2}{2}\left(1 - \left|\frac{1+i\eta^{1/2}}{1-i\eta^{1/2}}\right|^2\right), \tag{3.92}$$

where the solution for $\tilde{\zeta} = \tilde{x} + i\tilde{z}$ in terms of η is given by (3.88). Hence the pressure in the inner region is higher when $\dot{d}_0(t)$ is higher, such as was the case for the curved substrate solution shown in Figure 3.4.

As the inner region is quasi-steady, we can divide $\tilde{p}_0$ by $\dot{d}_0(t)^2$ to find a time-independent representation of the pressure, which we plot in Figure 3.10, along with a representative number of streamlines.

It is worth noting here that we have found that the leading-order solutions for the velocities and pressure in the inner region are finite, correcting for the singularities in their counterparts from the outer region local to the turnover points. In particular, we find that the maximum value for $\tilde{p}_0$ is given by

$$\max(\tilde{p}_0) = \frac{\dot{d}_0(t)^2}{2}, \tag{3.93}$$

and that this maximum occurs at the relative stagnation point where $\eta = -1$. Substituting this value of η into (3.88), we find this maximum occurs at $\tilde{x} = -6J(t)/\pi$, $\tilde{z} = 0$, which can be seen visually in Figure 3.10.

3.2.4.4 Matching with the outer region

The only unknown left to be determined in the inner region is the jet thickness, $J(t)$. We can determine this by matching the leading-order solutions for the velocity potential in the outer and inner regions via an intermediate variable technique. We first express the outer variables in terms of the inner variables such that

$$\hat{x} = d(t) + \epsilon^2\tilde{x},\ \hat{z} = -\epsilon w(\epsilon d(t), t) + \epsilon^2\tilde{z},\ \hat{\phi} = \epsilon\left[\dot{d}(t)\tilde{x} - \epsilon w_t(\epsilon d(t), t)\tilde{z} + \tilde{\phi}\right].$$

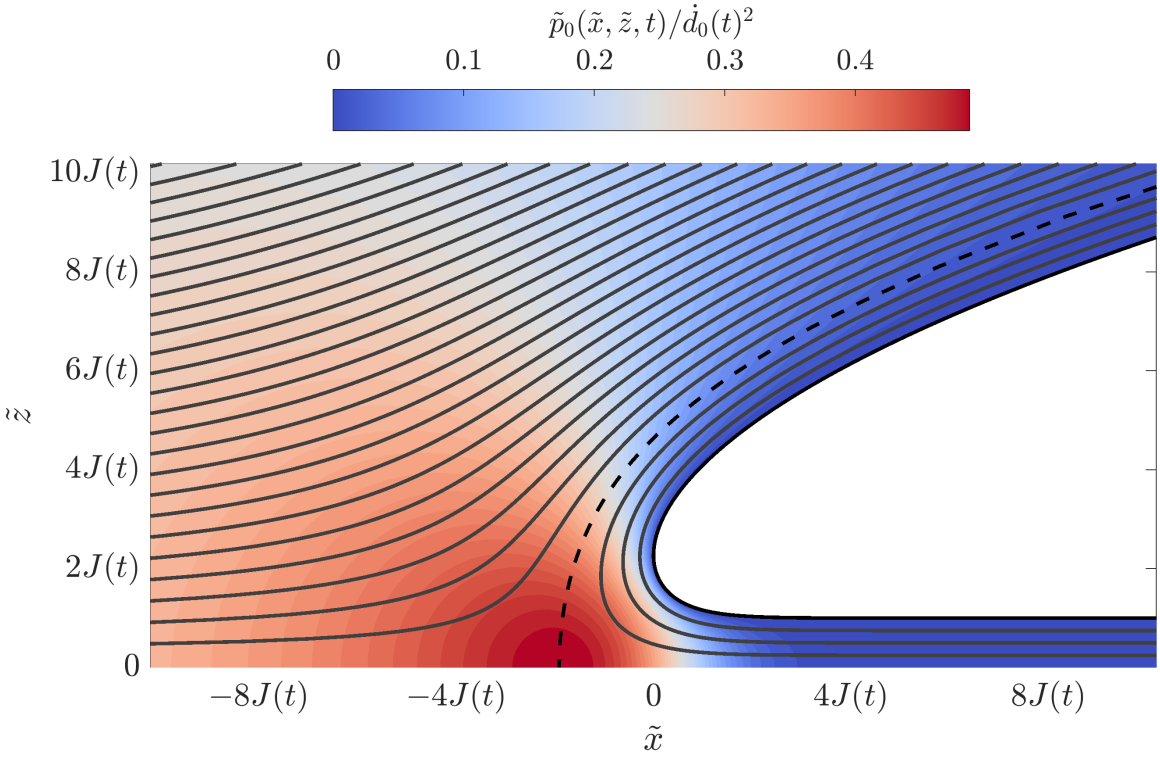

Figure 3.10: Leading-order solution in the right-hand inner region. The colour shows the leading-order solution for the pressure, given by (3.92), scaled by $\dot{d}_0(t)^2$. The solid lines show the streamlines, which are lines of constant $\tilde{\psi}_0$ given by (3.86), with the dashed line showing the dividing streamline ending at the relative stagnation point. The spatial coordinates $(\tilde{x},\tilde{z})$ are expressed in terms of the jet thickness, $J(t)$.

Next, we use capital letters to denote an intermediate variable, and define

$$\hat{x} = d(t) + \epsilon^\alpha X,\ \hat{z} = -\epsilon w(\epsilon d(t),t) + \epsilon^\alpha Z,\ \hat{\phi} = \epsilon^{\alpha-1}\left[\dot{d}(t)X - \epsilon w_t(\epsilon d(t),t)Z + \Phi\right],$$

where $0 < \alpha < 2$. We then need to write down the leading-order solutions for the velocity potential in the outer and inner regions in the intermediate variables and match their expansions as $\epsilon \to 0$.

First, recall that the leading-order solution for the velocity potential in the inner region is given by (3.86),

$$\tilde{\phi}_0 = \dot{d}_0(t)k(t) - \frac{\dot{d}_0(t)J(t)}{\pi}\mathrm{Re}\left(\eta + \log(\eta) + 1\right),$$
$$\tilde{x} + i\tilde{z} = \epsilon^{\alpha-2}(X + iZ) = \frac{J(t)}{\pi}\left[\eta + 4i\eta^{1/2} - \log(\eta) + i\pi - 1\right].$$

Given that the branch cut for $\eta^{1/2}$ is taken along the negative real axis, and $\eta^{1/2} > 0$ on the positive axis, the far-field expansion as $|\eta| \to \infty$ gives

$$\eta \sim \epsilon^{\alpha-2}\frac{\pi}{J(t)}(X + iZ) - 4i\epsilon^{\alpha/2-1}\sqrt{\frac{\pi}{J(t)}(X + iZ)},$$

and hence substituting this expansion into the leading-order velocity potential and expanding for $\epsilon \to 0$ results in

$$\Phi = \epsilon^{2-\alpha}\tilde{\phi} \sim -\dot{d}_0(t)X + 4\epsilon^{1-\alpha/2}\dot{d}_0(t)\sqrt{\frac{J(t)}{\pi}}\mathrm{Re}\left(i\sqrt{X+iZ}\right). \tag{3.94}$$

Next, recall that the leading-order solution for the velocity potential in the outer region is given by (3.31),

$$\hat{\phi}_0 = \mathrm{Re}\left(i(\zeta^2 - d_0(t)^2)^{1/2}\left[1 - \frac{1}{\pi}\int_{-d_0(t)}^{d_0(t)} \frac{m_t(s,t)}{\sqrt{d_0(t)^2 - s^2}(s-\zeta)}\,\mathrm{d}s\right]\right) \tag{3.95}$$

where

$$\zeta = \hat{x} + i\hat{z} = d(t) - i\epsilon w(\epsilon d(t), t) + \epsilon^{\alpha}(X + iZ).$$

We employ the same method that was used to determine the contour integral in §B.3 to find the expansion of the integral in (3.95) to be given by

$$\frac{1}{\pi}\int_{-d_0(t)}^{d_0(t)} \frac{m_t(s,t)}{\sqrt{d_0(t)^2 - s^2}(s-\zeta)}\,\mathrm{d}s = B(t) + O\left(\sqrt{1 - \frac{\zeta}{d_0(t)}}\right), \tag{3.96}$$

for $\zeta \to d_0(t)$, where

$$B(t) = \frac{1}{\pi}\int_{-d_0(t)}^{d_0(t)} \frac{\hat{w}_{0t}(s,t)}{\sqrt{d_0(t)^2 - s^2}}\,\mathrm{d}s\,.$$

For the square-root term in (3.95), given that $0 < \alpha < 2$, we have

$$(\zeta^2 - d_0(t))^{1/2} \sim \begin{cases} \epsilon^{\alpha/2}\sqrt{2d_0(t)}\,(X+iZ)^{1/2} & \text{if } \alpha < 1, \\ \epsilon^{1/2}\sqrt{2d_0(t)}\Big(X + iZ + d_1(t) - i\hat{w}_0(d_0(t),t)\Big)^{1/2} & \text{if } \alpha = 1, \\ \epsilon^{1/2}\sqrt{2d_0(t)}\,(d_1(t) - i\hat{w}_0(d_0(t),t))^{1/2} & \text{if } \alpha > 1. \end{cases}$$

as $\epsilon \to 0$. If $\alpha \geq 1$, then given the expansion for the integral (3.96) and the expansion for $(\zeta^2 - d_0(t)^2)^{1/2}$, we can only match with (3.94) if $\alpha = 1$. In this case, the asymptotic size of the intermediate region would be the same as the first-order correction to the turnover point, $\epsilon d_1(t)$, meaning we cannot have an overlap between the two leading-order solutions at this scale. Therefore we must have $0 < \alpha < 1$, in which case the outer expansion local to the inner region is

$$\Phi \sim -\dot{d}_0(t)X + \epsilon^{1-\alpha/2}\sqrt{2d_0(t)}(1 - B(t))\mathrm{Re}\left(i\sqrt{X+iZ}\right), \tag{3.97}$$

and matching (3.94) and (3.97) gives the asymptotic jet thickness as

$$J(t) = \frac{\pi(1-B(t))^2 d_0(t)}{8\dot{d}_0(t)^2}, \quad B(t) = \frac{1}{\pi}\int_{-d_0(t)}^{d_0(t)} \frac{\hat{w}_{0t}(s,t)}{\sqrt{d_0(t)^2 - s^2}}\,\mathrm{d}s\,. \tag{3.98}$$

The solutions for $J(t)$ for the stationary, the rigid moving and the curved moving substrates are shown in Figure 3.11. It is clear that the downwards motion of the substrate, which acts to increase $B(t)$ given by (3.98), results in the jet thickness of the moving substrate cases to be smaller than the stationary substrate. Interestingly, even though the turnover point evolution is faster in the curved substrate case (see Figure 3.4), the resulting jet thickness is smaller than the rigid substrate case.

3.2.5 Jet region

Upon impact, the fluid near the bottom of the droplet is violently disturbed and is ejected into two jets emanating from the turnover points. From the leading-order inner solutions derived in §3.2.4, we know these jets are ejected with a large $O(1/\epsilon)$ horizontal velocity with a small $O(\epsilon^3)$ thickness. Without loss of generality, in this section we consider the jet emanating from the right-hand inner region, where the left-hand jet is given by symmetry in x. We follow the methods previously employed for solving the jet regions, such as by Wilson (1989) [97], where in addition we take into account the time-dependency of the shape of the substrate.

We consider a curvilinear frame moving with the substrate, parameterised by (x', z'), where $x' = x$ and z' is distance along the from the point $(x', -\epsilon^2 w(x', t))$ in the upwards normal direction from the substrate. If $\mathbf{i}$ and $\mathbf{j}$ are the unit coordinate vectors in the (x, z) plane, then the substrate is parameterised by

$$\mathbf{R}'(x', t) = x'\mathbf{i} - \epsilon^2 w(x', t)\mathbf{j}, \tag{3.99}$$

and the unit tangent and normal vectors to the substrate at $x = x'$ are

$$\mathbf{e}(x', t) = \frac{1}{q(x', t)}\left(\mathbf{i} - \epsilon^2 w_x(x', t)\mathbf{j}\right), \quad \mathbf{n}(x', t) = \frac{1}{q(x', t)}\left(\epsilon^2 w_x(x', t)\mathbf{i} + \mathbf{j}\right), \tag{3.100}$$

where $q(x', t) = \sqrt{1 + \epsilon^4 w_x(x', t)^2}$. Given this, a point with coordinates (x', z') in the moving frame corresponds to a point in the lab frame with position vector

$$\begin{aligned} \mathbf{r}(x', z', t) &= \mathbf{R}'(x', t) + z'\mathbf{n}(x', t) \\ &= \frac{1}{q}\left(x' + \epsilon^4 w w_x\right)\mathbf{e}(x', t) + \left[\frac{\epsilon^2}{q}\left(x' w_x - w\right) + z'\right]\mathbf{n}(x', t). \end{aligned} \tag{3.101}$$

The scale factor for the x' derivative is given by

$$M(x', z', t) = \left|\frac{\partial \mathbf{r}}{\partial x'}\right| = \left(1 + z'\kappa(x', t)\right) q(x', t), \tag{3.102}$$

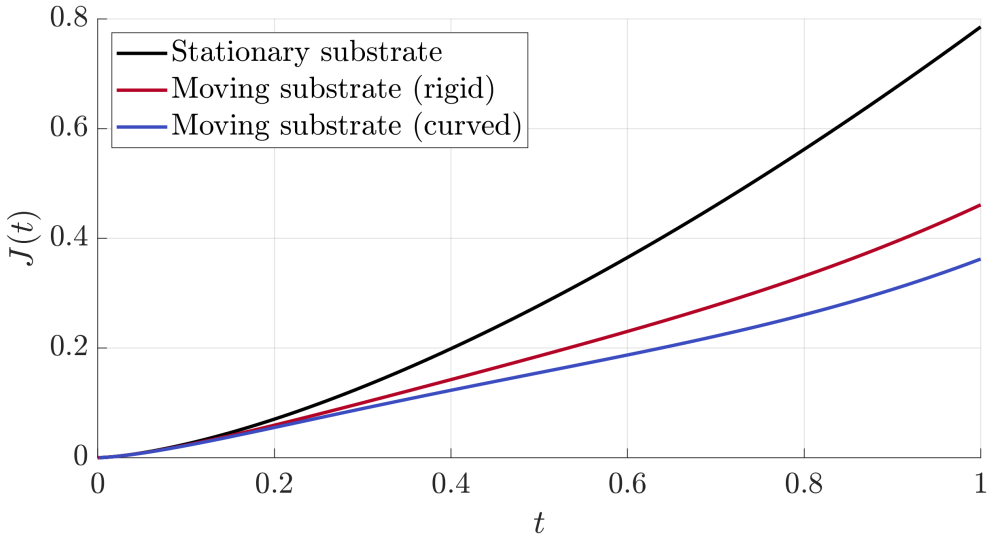

Figure 3.11: Solutions for the asymptotic jet thickness, $J(t)$, given by (3.98).

where $\kappa(x',t) = \epsilon^2 w_{xx}(x',t)/q(x',t)^3$ is the curvature of the substrate. The scale factor for the z' derivative is 1, therefore the gradient operator in the curvilinear frame is given by

$$\boldsymbol{\nabla}' = \frac{1}{M}\mathbf{e}\frac{\partial}{\partial x'} + \mathbf{n}\frac{\partial}{\partial z'}. \tag{3.103}$$

We can also define the operators for the divergence and curl in the moving frame acting on a vector $\mathbf{F} = F_e\mathbf{e} + F_n\mathbf{n}$ from Appendix 2 of Batchelor (1999) [7] to be

$$\boldsymbol{\nabla}' \cdot \mathbf{F} = \frac{1}{M}\left[\frac{\partial F_e}{\partial x'} + \frac{\partial}{\partial z'}\left(MF_n\right)\right], \tag{3.104}$$

$$\boldsymbol{\nabla}' \times \mathbf{F} = \frac{\mathbf{k}}{M}\left[\frac{\partial F_n}{\partial x'} - \frac{\partial}{\partial z'}\left(MF_e\right)\right]. \tag{3.105}$$

In the moving frame, the fluid velocity is given by $\mathbf{u}' = u'\mathbf{e} + v'\mathbf{n}$ and the substrate velocity is $\mathbf{U}' = \mathbf{R}_t'/\epsilon^2 = U'\mathbf{e} + V'\mathbf{n}$, where

$$U'(x',t) = w_t(x',t)\sin\big(\epsilon^2\theta(x',t)\big), \quad V'(x',t) = -w_t(x',t)\cos\big(\epsilon^2\theta(x',t)\big), \tag{3.106}$$

where we define $\epsilon^2\theta(x',t)$ to be the angle from the vertical of the substrate at x', such that

$$\tan\big(\epsilon^2\theta(x',t)\big) = \epsilon^2 w_x(x',t). \tag{3.107}$$

This means the moving frame is rotating with a spatially dependent angular velocity $-\theta_t$ local to any point $\mathbf{r}$, where differentiating (3.107) with respect to t gives

$$\epsilon^2\theta_t\left(1 + \tan^2(\epsilon^2\theta)\right) = \epsilon^2 w_{xt} \implies \theta_t = \frac{w_{xt}}{1+\epsilon^4 w_x^2} = \frac{w_{xt}}{q^2}. \tag{3.108}$$

The lab frame velocity is then given by $\mathbf{u} = \mathbf{u}' - \theta_t \mathbf{k} \times \mathbf{r}$, where $\mathbf{k}$ is the unit vector in the y direction, and

$$\mathbf{k} \times \mathbf{r} = -\left[\frac{\epsilon^2}{q}\left(x' w_x - w\right) + z'\right]\mathbf{e} + \frac{1}{q}\left(x' + \epsilon^4 w w_x\right)\mathbf{n}, \tag{3.109}$$

In order to transform the continuity equation (2.27) into the moving frame, we need to determine the divergence of $\theta_t \mathbf{k} \times \mathbf{r}$, which is given by

$$\begin{aligned}\boldsymbol{\nabla}' \cdot (\theta_t \mathbf{k} \times \mathbf{r}) &= \theta_t \left[\mathbf{r} \cdot (\boldsymbol{\nabla}' \times \mathbf{k}) - \mathbf{k} \cdot (\boldsymbol{\nabla}' \times \mathbf{r})\right] + (\boldsymbol{\nabla}' \theta_t) \cdot (\mathbf{k} \times \mathbf{r}) \\ &= -\frac{\theta_{x't}}{M}\left[\frac{\epsilon^2}{q}\left(x' w_x - w\right) + z'\right],\end{aligned} \tag{3.110}$$

where we determined that $\boldsymbol{\nabla}' \times \mathbf{r} = \mathbf{0}$ using (3.105). Therefore, the continuity equation (2.27) in the moving frame is given by

$$u'_{x'} + \frac{\partial}{\partial z'}\left(M v'\right) = \theta_{x't}\left[\frac{\epsilon^2}{q}\left(w - x' w_x\right) - z'\right]. \tag{3.111}$$

As we assume the flow is irrotational in the lab frame, such that $\boldsymbol{\nabla} \times \mathbf{u} = \mathbf{0}$, we must also determine

$$\begin{aligned}\boldsymbol{\nabla}' \times (\theta_t \mathbf{k} \times \mathbf{r}) &= \theta_t \boldsymbol{\nabla}' \times (\mathbf{k} \times \mathbf{r}) + (\boldsymbol{\nabla}' \theta_t) \times (\mathbf{k} \times \mathbf{r}) \\ &= \left[2\theta_t + \frac{\theta_{x't}}{qM}\left(x' + \epsilon^4 w w_x\right)\right]\mathbf{k},\end{aligned} \tag{3.112}$$

such that the irrotationality condition in the moving frame is

$$v'_{x'} - \frac{\partial}{\partial z'}\left(M u'\right) = 2M\theta_t + \frac{\theta_{x't}}{q}\left(x' + \epsilon^4 w w_x\right) \tag{3.113}$$

By transforming the time-derivative to the moving frame coordinates, we have that the convective derivative in the moving frame is given by

$$\frac{1}{\epsilon^2}\frac{\partial}{\partial t} + \left(\mathbf{u}' - \mathbf{U}' - \frac{1}{\epsilon^2} z' \mathbf{n}_t(x', t)\right) \cdot \boldsymbol{\nabla}',$$

where $\mathbf{n}_t(x', t)/\epsilon^2 = \theta_t(x', t)\mathbf{e}(x', t)$. By defining the pressure in the moving frame by $p = p'$, the tangential and normal components of the momentum equations (2.26) are given by

$$\frac{1}{\epsilon^2} u'_t + \theta_t v' + \frac{1}{M}\left(u' - U' - z'\theta_t\right)\left(u'_{x'} + \kappa q v'\right) + \left(v' - V'\right) u'_{z'} = -\frac{1}{M} p'_{x'}, \tag{3.114}$$

$$\frac{1}{\epsilon^2} v'_t - \theta_t u' + \frac{1}{M}\left(u' - U' - z'\theta_t\right)\left(v'_{x'} - \kappa q u'\right) + \left(v' - V'\right) v'_{z'} = -p'_{z'}. \tag{3.115}$$

If the free surface of the jet is at $z' = h'(x', t)$ in the moving frame, then the boundary conditions at the substrate (3.9) and free surface (3.10)-(3.11) are given by

$$v' - V' = 0 \qquad \text{on } z' = 0, \tag{3.116}$$

$$v' - V' = \frac{1}{\epsilon^2} h'_t + \frac{1}{M}\left(u' - U' - h'\theta_t\right) h'_{x'}, \quad p' = 0 \qquad \text{on } z' = h'(x', t). \tag{3.117}$$

From the leading-order solution in the inner region from §3.2.4, we know the fluid is ejected into the jet at a tangential velocity $O(1/\epsilon)$ with a thickness $O(\epsilon^3)$. In order to balance the continuity equation (3.111), the relevant jet scalings are

$$\begin{gathered} x' = \epsilon\bar{x}, \quad z' = \epsilon^3\bar{z}, \quad w(x', t) = \bar{w}(\bar{x}, t), \\ u' = \frac{1}{\epsilon}\bar{u}, \quad v' = -\frac{\bar{w}_t(x', t)}{q(x', t)} + \epsilon\bar{v}, \quad h' = \epsilon^3\bar{h}, \quad p' = \epsilon\bar{p}. \end{gathered} \tag{3.118}$$

Then, expanding $(\bar{u},\, \bar{v}, \bar{h},\, \bar{p},\, \bar{w}) = (\bar{u}_0,\, \bar{v}_0, \bar{h}_0,\, \bar{p}_0,\, \bar{w}_0) + o(1)$ as $\epsilon \to 0$, we have that

$$\begin{gathered} q = \sqrt{1 + \epsilon^2\bar{w}_{\bar{x}}^2} = 1 + O(\epsilon^2), \quad \kappa = \frac{\bar{w}_{\bar{x}\bar{x}}}{q^3} = \bar{w}_{0\bar{x}\bar{x}} + O(\epsilon) \\ U' = \frac{\epsilon\bar{w}_t\bar{w}_{\bar{x}}}{q} = \epsilon\bar{w}_{0t}\bar{w}_{0\bar{x}} + O(\epsilon^2), \quad V' = -\frac{\bar{w}_t}{q} = -\bar{w}_{0t} + O(\epsilon), \\ M = (1 + \epsilon^3\bar{z}\kappa)q = 1 + O(\epsilon^2), \quad \theta_t = \frac{\bar{w}_{\bar{x}t}}{\epsilon q^2} = \frac{1}{\epsilon}\bar{w}_{0\bar{x}t} + O(1). \end{gathered}$$

Note that this means, to leading-order, the irrotationality condition (3.113) reduces to $\bar{u}_{0\bar{z}} = 0$, which means $\bar{u}_0$ is independent of $\bar{z}$, and we subsequently write $\bar{u}_0(\bar{x}, \bar{z}, t) = \bar{u}_0(\bar{x}, t)$. The continuity equation (3.111) and kinematic boundary condition on the substrate (3.116) reduce to

$$\bar{u}_{0\bar{x}} + \bar{v}_{0\bar{z}} = 0 \text{ for } \bar{z} \geq 0, \quad \bar{v}_0 = 0 \text{ for } \bar{z} = 0, \tag{3.119}$$

which, given that $\bar{u}_0$ is independent of $\bar{z}$, means we can integrate the continuity equation with respect to $\bar{z}$ to find that $\bar{v}_0 = -\bar{z}\bar{u}_{0\bar{x}}$. The leading-order tangential momentum equation (3.114) then reduces to

$$\bar{u}_{0t} + \bar{u}_0\bar{u}_{0\bar{x}} = 0, \tag{3.120}$$

and substituting the solution for $\bar{v}_0$ into the leading-order kinematic boundary condition at the free surface (3.117) gives

$$\bar{h}_{0t} + \bar{u}_0\bar{h}_{0\bar{x}} + \bar{h}_0\bar{u}_{0\bar{x}} = 0. \tag{3.121}$$

Finally, by finding the leading-order normal momentum equation (3.115), integrating with respect to $\bar{z}$ and applying the dynamic boundary condition (3.117) on $\bar{z} = h_0$, we have that the pressure is given by

$$\bar{p}_0 = -\left(\bar{w}_{0tt} + 2\bar{w}_{0\bar{x}t}\bar{u}_0 + \bar{w}_{0\bar{x}\bar{x}}\bar{u}_0^2\right)(\bar{h}_0 - \bar{z}). \tag{3.122}$$

To match with the inner solution, we take the boundary conditions for $\bar{u}_0$ and $\bar{h}_0$ to be at $\bar{x} = d_0(t)$ and match them to the far-field conditions of the inner region travelling into the jet (3.77), such that

$$\bar{u}_0(d_0(t), t) = 2\dot{d}_0(t), \quad \bar{h}_0(d_0(t), t) = J(t). \tag{3.123}$$

The horizontal velocity $\bar{u}_0$ and free surface location $\bar{h}_0$ are found by solving (3.120)-(3.121), which are the zero-gravity shallow water equations. As (3.120) is independent of $\bar{h}_0$, we can solve (3.120) for $\bar{u}_0$ using the method of characteristics. We first parameterise the boundary conditions (3.123), which are time-dependent, with a parameter τ such that

$$t = \tau, \quad \bar{x} = d_0(\tau), \quad \bar{u}_0(d_0(\tau), \tau) = 2\dot{d}_0(\tau), \quad \bar{h}_0(d_0(\tau), \tau) = J(\tau). \tag{3.124}$$

The characteristic equations for (3.120), parameterised by $\xi > 0$, are

$$\frac{\partial t}{\partial \xi} = 1, \quad \frac{\partial \bar{x}}{\partial \xi} = \bar{u}_0, \quad \frac{\partial \bar{u}_0}{\partial \xi} = 0,$$

hence by integrating with respect to ξ and applying the boundary conditions (3.124) at $\xi = 0$, we have a parametric solution for $\bar{u}_0(\bar{x}, t)$ given by

$$t = \tau + \xi, \quad \bar{x} = 2\dot{d}_0(\tau)\xi + d_0(\tau), \quad \bar{u}_0 = 2\dot{d}_0(\tau). \tag{3.125}$$

In order to determine the solution for $\bar{h}_0$ from (3.121), we must find $\partial\bar{u}_0/\partial\bar{x}$ in terms of the characteristic parameters τ and ξ. The change of variables from (ξ, τ) to $(\bar{x}, t)$ is described by the matrix equation

$$\begin{bmatrix} \dfrac{\partial}{\partial \xi} \\ \dfrac{\partial}{\partial \tau} \end{bmatrix} = \underbrace{\begin{bmatrix} 2\dot{d}_0(\tau) & 1 \\ 2\ddot{d}_0(\tau)\xi + \dot{d}_0(\tau) & 1 \end{bmatrix}}_{\mathbf{J}} \begin{bmatrix} \dfrac{\partial}{\partial \bar{x}} \\ \dfrac{\partial}{\partial t} \end{bmatrix} \tag{3.126}$$

where $\mathbf{J}$ is the Jacobian matrix. The parameterisation is only valid if the Jacobian is invertible, which means we must have

$$\det(\mathbf{J}) = \dot{d}_0(\tau) - 2\ddot{d}_0(\tau)\xi \neq 0. \tag{3.127}$$

Assuming $\det(\mathbf{J}) \neq 0$, we can invert the matrix equation (3.126) to find

$$\frac{\partial \bar{u}_0}{\partial \bar{x}} = \frac{2\ddot{d}_0(\tau)}{2\ddot{d}_0(\tau)\xi - \dot{d}_0(\tau)}.$$

Thus, the characteristic equations for (3.121) are

$$\frac{\partial t}{\partial \xi} = 1, \quad \frac{\partial \bar{x}}{\partial \xi} = 2\dot{d}_0(\tau), \quad \frac{\partial \bar{h}_0}{\partial \xi} = -\frac{2\ddot{d}_0(\tau)}{2\ddot{d}_0(\tau)\xi - \dot{d}_0(\tau)}\bar{h}_0, \tag{3.128}$$

where again by integrating with respect to ξ and applying the boundary conditions (3.123), we have a parametric solution for $\bar{h}_0$ given by

$$t = \tau + \xi, \quad \bar{x} = 2\dot{d}_0(\tau)\xi + d_0(\tau), \quad \bar{h}_0 = \frac{\dot{d}_0(\tau)J(\tau)}{\dot{d}_0(\tau) - 2\ddot{d}_0(\tau)\xi}. \tag{3.129}$$

Finally, we can remove the ξ parameter by substituting in $\xi = t - \tau$, and hence the parameterised solutions for $\bar{u}_0$ and $\bar{h}_0$ is

$$\bar{u}_0 = 2\dot{d}_0(\tau), \quad \bar{h}_0 = \frac{\dot{d}_0(\tau)J(\tau)}{\dot{d}_0(\tau) - 2\ddot{d}_0(\tau)(t-\tau)}, \tag{3.130}$$

with

$$\bar{x} = 2\dot{d}_0(\tau)(t-\tau) + d_0(\tau), \tag{3.131}$$

where $0 < \tau \leq t$ and $t > 0$. From the solution for $\dot{d}_0(t)$ in (3.53), we have $\dot{d}_0(t) \sim 1/\sqrt{t}$ as $t \to 0$, so from (3.131) we can see that the jet has an infinite extent in the $\bar{x}$ direction. However, the free surface height $\bar{h}_0 \to 0$ as $\bar{x} \to \infty$, such that the area of the jet remains finite. In addition, as $\dot{d}_0(t)$ only has a square-root singularity at $t = 0$, from (3.131) we see that at $t = 0$, the parametric solution (3.131) gives $\bar{x} = 0$, reflecting that the jets do not emerge until $t > 0$.

The evolution of the free surface of the jet $\bar{h}_0$ for the three example cases is shown in Figure 3.12, for t ranging from 0 to 1, where the solid lines denote the free surface location and the dashed lines plot the evolution of the jet root $\bar{h}_0(d_0(t), t) = J(t)$ (which are plotted beyond $t = 1$ for visualisation purposes). The resulting free surface profiles are determined by the solutions for the turnover point $d_0(t)$ (see Figure 3.4) and the jet thickness $J(t)$ (see Figure 3.11), and it can clearly be seen how the evolution of these free surfaces is affected by these quantities at their point of origins. However we can also see differences in the resulting shapes of the free surface, in particular for the flat moving substrate case, which begins to have a pileup near the jet root at later times.

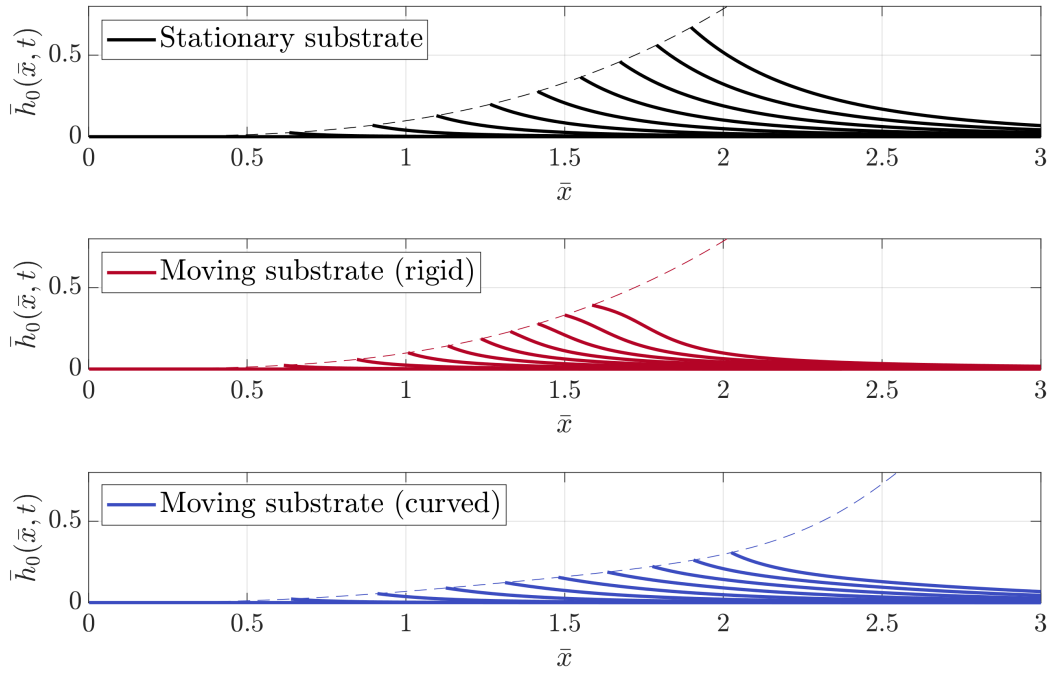

Figure 3.12: Leading-order solutions for the free surface location in the jet regions given by $\bar{z} = \bar{h}_0(\bar{x}, t)$ from (3.130) (solid lines). The lines are plotted in equal temporal steps from $t = 0$ to $t = 1$. The dashed lines plot the evolution of the point $\bar{h}_0(d_0(t), t) = J(t)$, and are plotted beyond $t = 1$ for illustrative.

Given the solutions for $\bar{u}_0$ and $\bar{h}_0$, the leading-order pressure (3.122) can then be found by parameterising the solution for $\bar{w}_0$ and its derivatives with $\bar{x}$ from (3.131). It is worth noting that if $\bar{w}_0 \equiv 0$, then $\bar{p}_0 = 0$, and the pressure in the jets is instead $O(\epsilon^2)$.

3.2.6 Outer-outer region

The final region to resolve is the outer-outer region, which contains the portion of the droplet above the outer region and away from the point of contact with the substrate. In this early time regime, we expect the bulk of the droplet to remain mostly unaffected by the substrate and continue to move downwards with unit speed, with small perturbations felt due to the regions of high pressure close to the substrate.

In order to find the scalings for the outer-outer region, we first study the far-field behaviour of the leading-order solutions for the velocity potential and free surface position in the outer region. Expanding the outer solution for the complex velocity potential $W(\zeta, t)$ (3.31) as $\zeta = \hat{x} + i\hat{z} \to \infty$ gives

$$W = \hat{\phi}_0 + i\psi_0 = i\zeta - \frac{iD(t)}{\zeta} + O\left(\frac{1}{\zeta^3}\right), \tag{3.132}$$

where

$$D(t) = \frac{d_0(t)^2}{2} - \frac{1}{\pi}\int_{d_0(t)}^{d_0(t)} \sqrt{d_0(t)^2 - s^2}\hat{w}_{0t}(s,t)\,\mathrm{d}s\,. \tag{3.133}$$

In addition, expanding the outer solution for the free surface location $\hat{h}_0$ (3.48) as $\hat{x} \to \infty$ gives

$$\hat{h}_0(\hat{x},t) = \frac{1}{2}\hat{x}^2 - t - \frac{E(t)}{\hat{x}^2} + O\left(\frac{1}{\hat{x}^4}\right), \tag{3.134}$$

where

$$E(t) = \left[\left(t - \frac{d_0(t)^2}{8}\right)\frac{d_0(t)^2}{2} - \frac{1}{\pi}\int_{-d_0(t)}^{d_0(t)} \sqrt{d_0(t)^2 - s^2}\hat{w}_0(s,t)\,\mathrm{d}s\right]. \tag{3.135}$$

Moreover, since $\partial\hat{h}_0/\partial t = \partial\hat{\phi}_0/\partial\hat{z}$ on the free surface, we have that $\dot{E}(t) = D(t)$.

As the outer variables are defined by $\hat{x} + i\hat{z} = (x+iz)/\epsilon$, $\hat{\phi} = \phi/\epsilon$ and $\hat{h} = h/\epsilon^2$, then the far-field limits (3.132) and (3.134) motivate defining the outer-outer variables by

$$\phi = -z + \epsilon^2\Phi, \quad h(x,t) = 1 \pm \sqrt{1-x^2} - \epsilon^2 t + \epsilon^4 H_\pm(x,t), \quad p = P, \tag{3.136}$$

where the $\pm$ in the definition of h takes into account the top and bottom half of the droplet. Given these scalings, the governing equations in the outer-outer region are,

$$\frac{\partial^2\Phi}{\partial x^2} + \frac{\partial^2\Phi}{\partial z^2} = 0 \qquad \text{in the fluid,} \tag{3.137}$$

$$P + \frac{\partial\Phi}{\partial t} + \frac{\epsilon^4}{2}|\boldsymbol{\nabla}\Phi|^2 - \epsilon^2\frac{\partial\Phi}{\partial z} = 0 \qquad \text{in the fluid,} \tag{3.138}$$

$$\frac{\partial H_\pm}{\partial t} \mp \frac{x}{\sqrt{1-x^2}}\frac{\partial\Phi}{\partial x} - \frac{\partial\Phi}{\partial z} + \epsilon^4\frac{\partial\Phi}{\partial x}\frac{\partial H_\pm}{\partial x} = 0 \qquad \text{on } z = h(x,t), \tag{3.139}$$

$$P = 0, \qquad \text{on } z = h(x,t), \tag{3.140}$$

with initial conditions

$$\Phi(x,z,0) = 0, \quad H_\pm(x,0) = 0. \tag{3.141}$$

We then expand $(\Phi,\, H_\pm,\, P) = (\Phi_0,\, H_{\pm 0},\, P_0) + o(1)$ as $\epsilon \to 0$, which results in the following boundary value problem in the circle $z = h(x,0)$,

$$\frac{\partial^2\Phi_0}{\partial x^2} + \frac{\partial^2\Phi_0}{\partial z^2} = 0 \qquad \text{for } x^2 + (z-1)^2 \le 1, \tag{3.142}$$

$$\frac{\partial\Phi_0}{\partial t} = -P_0 \qquad \text{for } x^2 + (z-1)^2 \le 1, \tag{3.143}$$

$$\Phi_0 = 0 \qquad \text{on } x^2 + (z-1)^2 = 1, \tag{3.144}$$

$$\frac{\partial H_{\pm 0}}{\partial t} \mp \frac{x}{\sqrt{1-x^2}}\frac{\partial\Phi_0}{\partial x} - \frac{\partial\Phi_0}{\partial z} = 0 \qquad \text{on } x^2 + (z-1)^2 = 1, \tag{3.145}$$

with the matching conditions

$$\Phi_0 \sim -\frac{D(t)z}{x^2+z^2} \text{ as } x^2+z^2 \to 0, \quad H_-(x,t) \sim -\frac{E(t)}{x^2} \text{ as } x \to 0. \tag{3.146}$$

The unique solution for Φ_0 which satisfies the boundary conditions on the interface and the matching condition at the origin is given by

$$\Phi_0(x,z,t) = \frac{D(t)(x^2+(z-1)^2-1)}{2(x^2+z^2)}, \tag{3.147}$$

which we can readily check satisfies Laplace's equation (3.142). We then determine the leading-order perturbations to the horizontal and vertical velocity components, given by $u \sim \epsilon^2 U_0$ and $v \sim -1+\epsilon^2 V_0$ as $\epsilon \to 0$, by

$$U_0 = \frac{\partial \Phi_0}{\partial x} = \frac{2D(t)xz}{(x^2+z^2)^2}, \quad V_0 = \frac{\partial \Phi_0}{\partial z} = \frac{D(t)(z^2-x^2)}{(x^2+z^2)^2}. \tag{3.148}$$

Applying (3.148) at $z = h(x,0) = 1 \pm \sqrt{1-x^2}$, the leading-order kinematic boundary condition on the free surface (3.145) gives,

$$\frac{\partial H_{\pm 0}}{\partial t} = \frac{D(t)}{2(1-x^2 \pm \sqrt{1-x^2})},$$

which we solve by integrating with respect to time, applying the initial condition $H_\pm(x,0) = 0$, and recalling that $\dot{E}(t) = D(t)$ to find

$$H_{\pm 0}(x,t) = \frac{E(t)}{2(1-x^2 \pm \sqrt{1-x^2})}, \tag{3.149}$$

which satisfies the far-field condition for H_{-0} (3.146) as $x \to 0$. Finally, the leading-order pressure in the outer-outer region $P_0(x,z,t)$ is given by the Bernoulli equation (3.143),

$$P_0(x,z,t) = -\frac{\partial \Phi_0}{\partial t} = \frac{A(t)(1-x^2-(z-1)^2)}{2(x^2+z^2)}, \tag{3.150}$$

where by the solution for $A(t)$, given by (3.67), we have $\dot{D}(t) = A(t)$.

The pressure P_0 from (3.150) is shown in Figure 3.13 at time $t = 0.5$, where the stationary substrate case is shown for $x < 0$ and the curved moving substrate case for $x > 0$. The decay of the pressure away from the origin is clear, with the inset showing the pressure singularity close to the point of contact. Similar to the outer pressure shown in Figure 3.6, the curved substrate solution has a lower pressure than the stationary substrate due to the downwards acceleration of the substrate at $t = 0.5$. Indeed, the pressure in the outer-outer region is driven by $A(t)$, which is the leading-order coefficient of the pressure from the outer region given in (3.69).

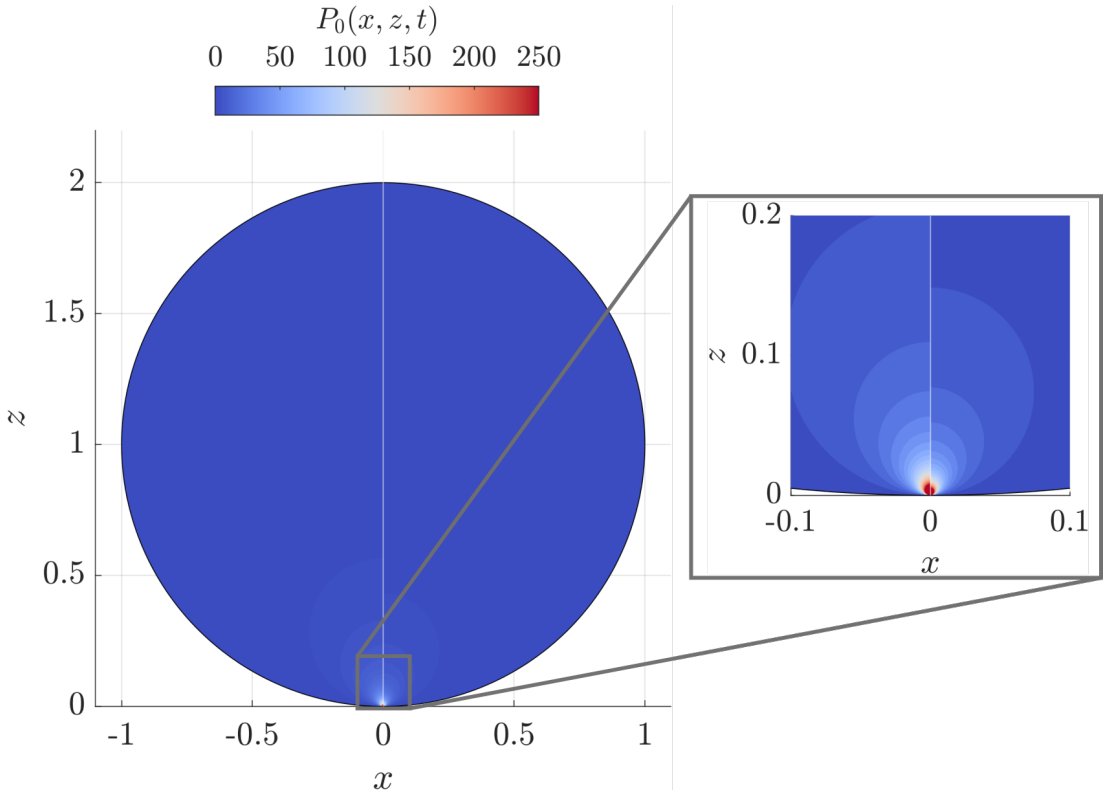

Figure 3.13: Leading-order solution for the pressure in the outer-outer region (3.150), where the stationary substrate case is plotted for $x < 0$ and the curved moving substrate case for $x > 0$. The inset shows the pressure singularity close to the origin.

3.2.7 Pressure on the substrate

The solution for the substrate in Chapters 5 and 6 is found by solving (2.33) or (2.36) respectively, both of which depend on the pressure along the substrate either explicitly or via the force (2.35). In the previous sections, we found the leading-order solutions for the pressure in the four asymptotic regions, and here we evaluate them along the substrate, as well as deriving an additive composite expansion.

The outer solution (3.69) evaluated at the substrate for $|\hat{x}| < d_0(t)$ is given by

$$\hat{p}_0(\hat{x},0,t) = \frac{1}{\sqrt{d_0(t)^2 - \hat{x}^2}} \left[A(t) - \frac{1}{\pi} \fint_{-d_0(t)}^{d_0(t)} \frac{\sqrt{d_0(t)^2 - s^2}\, m_{tt}(s,t)}{s - \hat{x}} \, \mathrm{d}s \right], \tag{3.151}$$

where the integral is interpreted in a principal value sense. To evaluate the inner solution for the pressure (3.92) at the substrate, we let $\eta = -e^{-2\sigma}$, where $-\infty < \sigma < \infty$, in the solution for $\tilde{x} + i\tilde{z}$ (3.88) to find a parametric solution for the pressure given by

$$\tilde{p}_0(\tilde{x},0,t) = \frac{2\dot{d}_0(t)^2 e^{-\sigma}}{(1+e^{-\sigma})^2}, \quad \tilde{x} = \frac{J(t)}{\pi}\left(2\sigma - e^{-2\sigma} - 4e^{-\sigma} - 1\right). \tag{3.152}$$

For the jet solution, we let $\bar{z} = 0$ in (3.122) to find

$$\bar{p}_0(\bar{x}, 0, t) = -\left(\bar{w}_{0tt} + 2\bar{w}_{0\bar{x}t}\bar{u}_0 + \bar{w}_{0\bar{x}\bar{x}}\bar{u}_0^2\right)\bar{h}_0, \tag{3.153}$$

where $\bar{u}_0$ and $\bar{h}_0$ are given by (3.130). Note we do not have a contribution from the outer-outer region as it does meet the substrate.

Recall that $p = O(1/\epsilon)$ in the outer region, $p = O(1/\epsilon^2)$ in the inner regions and $p = O(\epsilon)$ in the jet regions. Thus it is clear then that the pressure along the substrate is dominated by the outer and inner regions, and is negligible in the jets by comparison. This motivates us to form a composite expansion based on the outer and inner regions, as it is this pressure that will affect the substrate deformation at leading-order. To do this, we use an intermediate variable technique to find the overlap pressure between the outer and the inner. Following from the matching conducted in §3.2.4.4, here choosing $\alpha = 1/2$, we define an intermediate variable $\hat{x} = d(t) + \epsilon^{1/2}X$. Substituting this into the leading-order solution for the pressure in the outer region (3.151) and expanding for $\epsilon \to 0$ with $X = O(1)$ gives

$$\begin{aligned}
&\hat{p}_0(d(t) + \epsilon^{1/2}X, 0, t) \\
&\quad = \frac{1}{\epsilon^{1/4}\sqrt{2d_0(t)}\sqrt{-X}}\left(A(t) + \frac{1}{\pi}\underbrace{\int_{-d_0(t)}^{d_0(t)} \frac{m_{tt}(s,t)\sqrt{d_0(t)+s}}{\sqrt{d_0(t)-s}}\,\mathrm{d}s}_{I}\right) + O(\epsilon^{1/4}),
\end{aligned}$$

where $X < 0$. We can simplify the integral, which we denote by I, via integration by parts such that

$$\begin{aligned}
I &= \int_{-d_0(t)}^{d_0(t)} \frac{m_{tt}(s,t)\sqrt{d_0(t)+s}}{\sqrt{d_0(t)-s}}\,\mathrm{d}s \\
&= 2\int_{-d_0(t)}^{d_0(t)} \sqrt{d_0(t)^2 - s^2}\hat{w}_{0tt}(s,t)\,\mathrm{d}s + \int_{-d_0(t)}^{d_0(t)} \frac{m_{tt}(s,t)\sqrt{d_0(t)-s}}{\sqrt{d_0(t)+s}}\,\mathrm{d}s\,.
\end{aligned}$$

Given that $m_{tt}(s,t)$ is odd in s, we re-arrange to find that

$$I = \int_{-d_0(t)}^{d_0(t)} \sqrt{d_0(t)^2 - s^2}\hat{w}_{0tt}(s,t)\,\mathrm{d}s\,,$$

and therefore, by retaining only the leading-order term, we define the overlap pressure

$$p_{\text{overlap}}(x,t) = \frac{C(t)}{\sqrt{2\epsilon d_0(t)}\sqrt{\epsilon d_0(t) - x}}, \tag{3.154}$$

where

$$\begin{aligned} C(t) &= A(t) + \frac{1}{\pi}\int_{-d_0(t)}^{d_0(t)} \sqrt{d_0(t)^2 - s^2}\hat{w}_{0tt}(s,t)\,\mathrm{d}s \\ &= d_0(t)\dot{d}_0(t)\left(1 - B(t)\right), \end{aligned} \tag{3.155}$$

where $A(t)$ and $B(t)$ are given by (3.67) and (3.98), respectively.

Combining (3.151), (3.152) and (3.154), we create an additive composite expansion for the pressure along the substrate (for $x > 0$) given by

$$\begin{aligned} p_{\text{comp}}(x,t) = H(\epsilon d_0(t) - x)&\left[\frac{1}{\epsilon}\hat{p}_0(x/\epsilon, 0, t) - p_{\text{overlap}}(x,t)\right] \\ &+ \frac{1}{\epsilon^2}\tilde{p}_0(x/\epsilon^3 - d_0(t)/\epsilon^2, 0, t), \end{aligned} \tag{3.156}$$

where H is the Heaviside step function. For $x < 0$, by the symmetry of the problem we have that $p_{\text{comp}}(x,t) = p_{\text{comp}}(-x,t)$. The solution for the pressure along the stationary substrate for $\epsilon = 0.1$ at $t = 1$ for is shown in Figure 3.14, with the composite pressure $p_{\text{comp}}(x,t)$ shown as the solid black line, and the corresponding outer solution $\hat{p}_0/\epsilon$ and inner solution $\tilde{p}_0/\epsilon^2$, shown as the red dashed and blue dotted lines respectively. Note how we have an exponential decay in the composite pressure once x exceeds the turnover point as we tend towards the jet region.

In Figure 3.15, we show the evolution of the composite pressure $p_{\text{comp}}(x,t)$ with solid lines, plotted with equal temporal spacing from $t = 0.05$ to 1. The dashed lines show the evolution of the maximum pressure, given by (3.93) (which we again plot for t beyond 1 for visual clarity). For the stationary substrate case, we see that the maximum value of the pressure decreases uniformly in time, corresponding to the solution for the maximum pressure in the inner region (3.93). It is clear that the rigid moving substrate case has a much lower pressure along the substrate than the stationary substrate case, as well as a slower horizontal evolution due to the corresponding slower turnover point velocity depicted in Figure 3.4. At later times it can be seen how the oscillation of the substrate causes the maximum pressure curve to have a corresponding oscillatory evolution. For the curved substrate, the pressure is comparatively higher, which is due to the higher turnover point velocity increasing the pressure in the inner region given by (3.152).

3.2.8 Force on the substrate

In this subsection, we find the force that the droplet exerts downwards onto the substrate, which is needed to solve (2.33) to find the substrate position in the spring-supported plate case presented in Chapter 5.

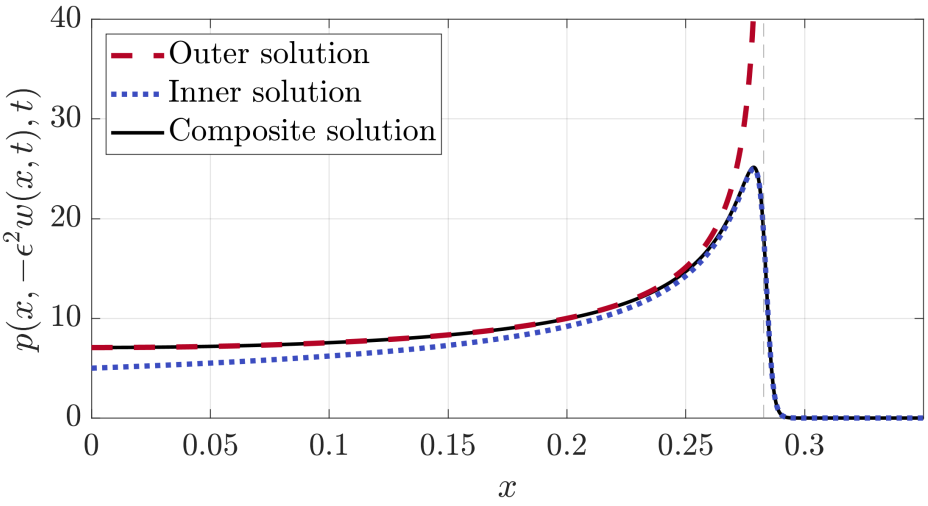

Figure 3.14: Solution for the pressure along the stationary substrate for $\epsilon = 0.1$ at $t = 1$. The leading-order outer solution $\hat{p}_0/\epsilon$ (3.151) is plotted with the red dashed line, the leading-order inner solution $\tilde{p}_0/\epsilon^2$ with the blue dotted line and the additive composite solution between the inner and outer $p_{\text{comp}}(x,t)$ (3.156) with the solid black line. The vertical dashed grey line denotes the leading-order turnover point location at $x = \epsilon d_0(t)$.

In this inviscid regime, the downwards pointing force on the substrate (2.35) is given by

$$F(t) = \int_{-L}^{L} p(x, -\epsilon^2 w(x,t), t)\,\mathrm{d}x\,, \tag{3.157}$$

where we assume that $L \gg \epsilon$ such that the outer and inner regions are contained within the bounds of the substrate. In the previous subsections, we found that the pressure in the outer region is $O(1/\epsilon)$, while in the inner regions the pressure is $O(1/\epsilon^2)$. However, the outer region has an $O(\epsilon)$ width, whilst the inner regions have a $O(\epsilon^3)$ width. This means the force has an $O(1)$ contribution from the outer regions, with only an $O(\epsilon)$ contribution from the inner regions. Given this, the leading-order solution for the force as $\epsilon \to 0$ is given by $F(t) \sim F_0(t)$ is given by integrating the pressure across the outer region, where

$$\begin{aligned} F_0(t) &= \int_{-d_0(t)}^{d_0(t)} \hat{p}_0(\hat{x}, 0, t)\,\mathrm{d}\hat{x} \\ &= \pi A(t) - \frac{1}{\pi}\int_{-d_0(t)}^{d_0(t)} \fint_{-d_0(t)}^{d_0(t)} \frac{\sqrt{d_0(t)^2 - s^2}\, m_{tt}(s,t)}{\sqrt{d_0(t)^2 - \hat{x}^2}(s - \hat{x})}\,\mathrm{d}s\,\mathrm{d}\hat{x}\,, \end{aligned} \tag{3.158}$$

where the solution for $\hat{p}_0$ along the substrate is given by (3.151). It is worth noting that by expanding (3.53) as $t \to 0$, we have that $\dot{d}_0(t) \sim 2/d_0(t)$ as $t \to 0$, which means that $F_0(0) = 2\pi$, despite the fact that $d_0(0) = 0$. This means that the substrate

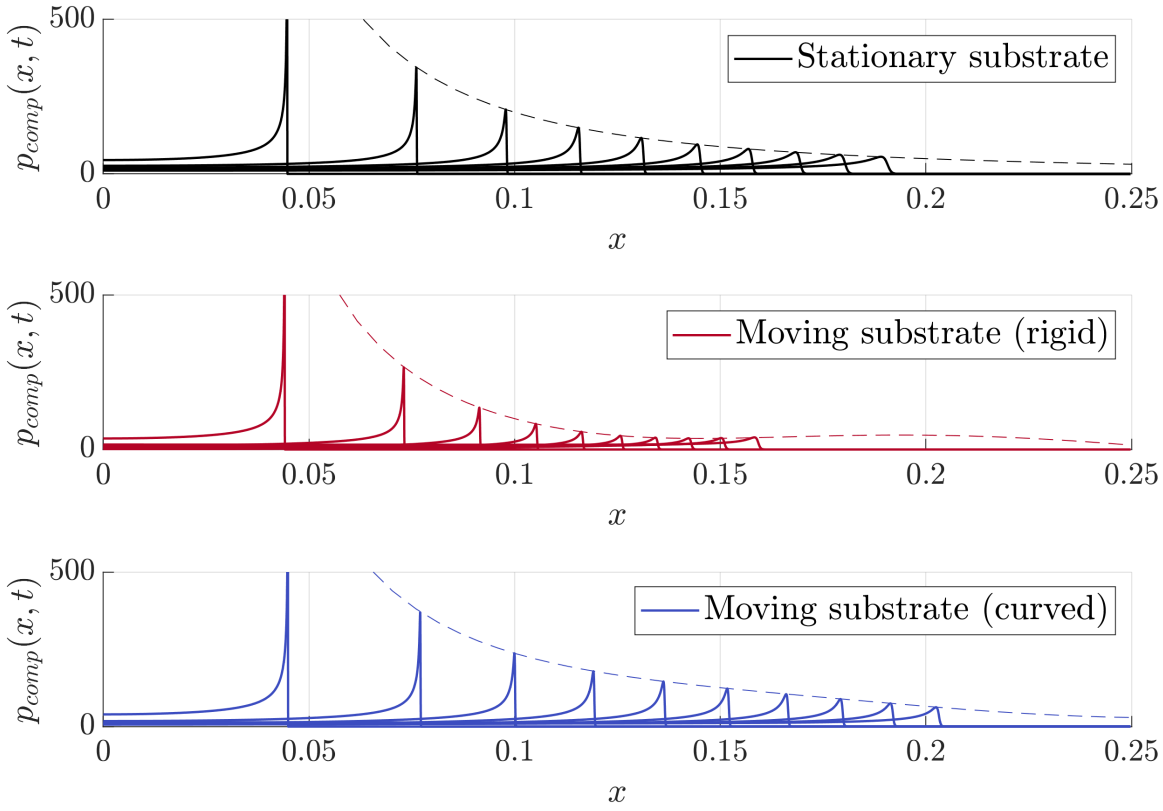

Figure 3.15: Temporal evolution of the composite pressure on the substrate $p_{\text{comp}}(x,t)$ (3.156), plotted with solid lines in equal intervals from $t = 0.05$ to 1. The dashed lines plot the evolution of the maximum pressure given by (3.93).

experiences a sudden instantaneous force once the droplet makes contact. As we will see in the next section, this is not the case in three-dimensions, where we find that the leading-order force is zero at $t = 0$.

Whilst this gives the leading-order force, in the previous subsection we derived an additive composite expansion for the pressure $p_{\text{comp}}(x,t)$ using the outer and inner expansions. In the following, we will directly integrate $p_{\text{comp}}(x,t)$ from $-L$ to L to find what we refer to as the composite force, $F_{\text{comp}}(t)$. As p_{comp} is an additive composite expansion, we can consider the contributions from each term in the expansion separately, and sum their contributions at the end. We already found the contribution from the outer term in (3.158), so we start with the contribution from the inner term.

As the inner solution (3.152) is given in terms of the parameter σ, we must change the integration variable from x to σ. In order to do this, we define a time-dependent function $c(t)$ such that $x = \epsilon d_0(t) + \epsilon^3 \tilde{x} = 0$ when $\sigma = -\log(c(t))$, where $c(t)$ is given

implicitly by

$$c(t)^2 + 4c(t) + 2\log(c(t)) + 1 = \frac{\pi d_0(t)}{\epsilon^2 J(t)}. \tag{3.159}$$

Given this, the contribution to $F_{\text{comp}}(t)$ from the inner pressure term is given by

$$\begin{aligned} F_{\text{inner}}(t) &= 2\epsilon \int_{-\log(c(t))}^{\infty} \frac{2\dot{d}_0(t)^2 e^{-\sigma}}{(1+e^{-\sigma})^2} \cdot \frac{J(t)}{\pi} \left(2 + 2e^{-2\sigma} + 4e^{-\sigma}\right) \mathrm{d}\sigma \\ &= \frac{8\epsilon \dot{d}_0(t)^2 J(t)}{\pi} \int_{-\log(c(t))}^{\infty} e^{-\sigma} \,\mathrm{d}\sigma = \frac{8\epsilon \dot{d}_0(t)^2 J(t) c(t)}{\pi}, \end{aligned} \tag{3.160}$$

where we replaced the upper limit of the integral by ∞ as this only introduces exponentially small errors due to the exponential decay of $\tilde{p}_0$ as $\tilde{x} \to \infty$. In practice, (3.159) has to be solved numerically to find $c(t)$ once $d_0(t)$ and $J(t)$ are known.

Finally, we determine the contribution from the overlap pressure term, given by (3.154), as

$$\begin{aligned} F_{\text{overlap}}(t) &= 2\int_0^{\epsilon d_0(t)} \frac{C(t)}{\sqrt{2\epsilon d_0(t)}\sqrt{\epsilon d_0(t) - x}} \,\mathrm{d}x = 2\sqrt{2} C(t) \\ &= 2\sqrt{2} d_0(t) \dot{d}_0(t) \left(1 - B(t)\right), \end{aligned} \tag{3.161}$$

where we substituted in the expression for $C(t)$ from (3.155). Therefore, the composite force $F_{\text{comp}}(t)$ is given by,

$$\begin{aligned} F_{\text{comp}}(t) = \pi A(t) &- \frac{1}{\pi} \int_{-d_0(t)}^{d_0(t)} \fint_{-d_0(t)}^{d_0(t)} \frac{\sqrt{d_0(t)^2 - s^2}\, m_{tt}(s,t)}{\sqrt{d_0(t)^2 - \hat{x}^2}(s - \hat{x})} \,\mathrm{d}s \,\mathrm{d}\hat{x} \\ &+ \frac{8\epsilon \dot{d}_0(t)^2 J(t) c(t)}{\pi} - 2\sqrt{2} d_0(t) \dot{d}_0(t) \left(1 - B(t)\right). \end{aligned} \tag{3.162}$$

Note that $F_{\text{comp}}(t)$ is not an asymptotic expansion for $F(t)$, rather it is simply a result of integrating the composite pressure (3.156) from $x = -L$ to L. This means that if we expand $F_{\text{comp}}(t)$ to leading-order as $\epsilon \to 0$, we should be left with $F_0(t)$. To confirm this, we expand $c(t) \sim c_0(t)$ as $\epsilon \to 0$, finding

$$c_0(t) = \frac{1}{\epsilon}\sqrt{\frac{\pi d_0(t)}{J(t)}}, \tag{3.163}$$

and substituting this expansion into (3.160) gives

$$F_{\text{inner}}(t) \sim \frac{8\dot{d}_0(t)^2 J(t)}{\pi}\sqrt{\frac{\pi d_0(t)}{J(t)}} = 8\dot{d}_0(t)^2\sqrt{\frac{d_0(t) J(t)}{\pi}} = 2\sqrt{2}(1 - B(t)) d_0(t) \dot{d}_0(t),$$

where we made use of the $J(t)$ given by(3.98). This means that $F_{\text{inner}}(t) \sim F_{\text{overlap}}(t)$ as $\epsilon \to 0$, and therefore, as anticipated, we have that $F_{\text{comp}}(t) \sim F_0(t)$ as $\epsilon \to 0$.

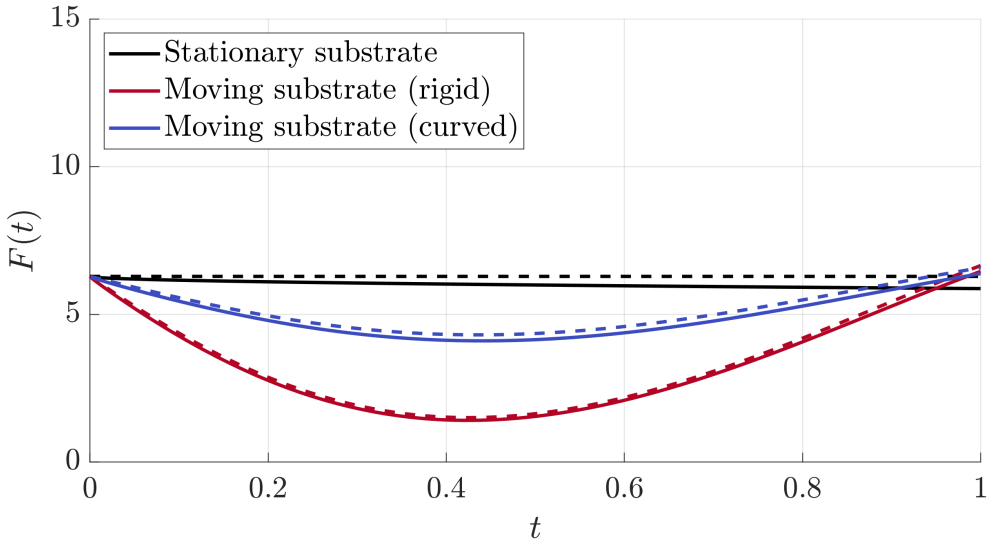

Figure 3.16: Solutions for the force on the substrate. The dashed lines show the leading-order force $F_0(t)$ (3.158), while the solid lines show the composite force $F_{\text{comp}}(t)$ (3.162).

In Figure 3.16, we show the force for the three imposed substrate cases, where the dashed lines denote the leading-order force $F_0(t)$ and the solid lines denote the composite force $F_{\text{comp}}(t)$. For the stationary substrate case, where $w(x,t) \equiv 0$, we find that $F_0(t) = \pi A(t) = 2\pi$ for all time. However it can be seen that the composite force does decrease in time, and although $F_{\text{comp}}(t) \sim F_0(t)$ as $\epsilon \to 0$, this does indicate how the inner regions have an increasing effect on the force as time is increased. As we will see in later chapters, we find that the composite force $F_{\text{comp}}(t)$ agrees more favourably with numerical simulations for intermediate times than the leading-order solution $F_0(t)$. For the moving substrate cases, we can see how the acceleration of the substrate, as shown in Figure 3.2, does have a significant effect on the force, and the acceleration terms in (3.158) mean the force experiences non-monotonic behaviour corresponding to the substrate motion.

3.2.9 Energy distribution

To conclude our analysis of the two-dimensional case, we will now discuss the distribution of energy in the system. This energy distribution was relevant to the experiments of Howland et al. (2016) [46], where it was found that droplet splashing can be inhibited by impacting onto soft substrates of varying stiffnesses. They found that droplets impacting onto the soft substrates needed up to 75% more kinetic energy to splash in comparison to the same droplet impacting onto a solid substrate. However,

it was found that the energy absorbed by the softer substrate was only a few percent more than the rigid substrates, meaning energy loss to the substrate could not alone account for the high energy requirement to splash on a soft substrate. By observing that the bulk of the droplets were relatively unaffected by the difference substrate stiffnesses, they concluded that this so-called splash-suppression mechanism must remove energy from the ejection sheet, which thus makes it slower and less likely to break up into a splash. The ejection of this sheet happens at times currently too early to experimentally observe, however it is vital to understand how the substrate deformation affects the emergence of the ejection sheet in order to understand these observations.

Motivated by these experiments, we will now use the leading-order solutions derived in the previous subsections to find the energy distribution within the droplet. In this regime, where the viscous, surface tension and gravitational forces are dominated by the inertia, the only source of energy in the liquid is kinetic. As we are in a two-dimensional geometry, we consider the kinetic energy *per unit length*, where the length here is considered to be in the y^* direction. Given this, the kinetic energy per unit length in the droplet is

$$E_K^*(t^*) = \frac{1}{2}\rho_l^* \iint_\Omega |\mathbf{u}^*|^2 \,\mathrm{d}x^* \,\mathrm{d}z^* \,, \tag{3.164}$$

where Ω is taken to be the fluid domain. We hence non-dimensionalise the kinetic energy by letting $E_K^* = \rho_l^* R_d^{*2} V^{*2} E_K$.

Given that the droplet is initially travelling downwards with unit speed, the bulk of the kinetic energy in the lab frame will be in the outer-outer region. Hence it is more informative to instead consider the energy in a frame of reference moving downwards at the initial droplet speed, with the substrate approaching from below at unit speed. Denoting these moving frame variables with a prime $'$, we have

$$x = x', \quad z = z' - \epsilon^2 t, \quad (u,\, v) = (u', v' - 1), \quad \phi = \phi' - z' + \epsilon^2 t. \tag{3.165}$$

We define the kinetic energy within a spatial region Γ in the moving frame by

$$E_{K,\Gamma}(t) = \frac{1}{2}\iint_\Gamma |\boldsymbol{\nabla}\phi'|^2 \,\mathrm{d}x' \,\mathrm{d}z' = \frac{1}{2}\oint_{\partial\Gamma} \phi' \boldsymbol{\nabla}\phi' \cdot \hat{\mathbf{n}} \,\mathrm{d}s \,, \tag{3.166}$$

where for the second equality we applied Green's first identity, with $\partial\Gamma$ being the boundary of Γ, $\hat{\mathbf{n}}$ the outward unit normal for $\partial\Gamma$. Given the formula for the kinetic energy (3.166), we will derive the leading-order energy contributions from each region, ensuring to take care of any resulting overlap between adjacent regions in the area integral.

For the outer region, we have

$$x' = \epsilon\hat{x},\ z' = \epsilon\hat{z} + \epsilon^2 t,\ \phi' = \epsilon\hat{\phi} - \epsilon\hat{z}.$$

We take the boundary for the outer region $\partial\Gamma$ to be a semi-circle of radius $R > d_0(t)$, centred on the origin and lying on the $\hat{x}$ axis on its straight edge. Along the semi-circle, for any fixed ϵ, we know from the far-field expansion (3.132) that $\phi' = O(1/R)$ and $\boldsymbol{\nabla}\phi' \cdot \hat{\mathbf{n}} = O(1/R^2)$ as $R \to \infty$, and that the line element $\mathrm{d}s = O(R)$. This means the energy contribution from this semi-circle is $O(1/R)$ as $R \to \infty$. Along the straight edge, where $\hat{z} = 0$, by (3.23) we have that $\hat{\phi}_0 = 0$ for $|\hat{x}| > d_0(t)$. For $|\hat{x}| < d_0(t)$, we have from (3.31) that

$$\phi' = \epsilon\hat{\phi}_0 + O(\epsilon^2) = -\epsilon\sqrt{d_0(t)^2 - \hat{x}^2}\left[1 - \frac{1}{\pi}\fint_{-d_0(t)}^{d_0(t)} \frac{m_t(s,t)}{\sqrt{d_0(t)^2 - s^2}(s - \hat{x})}\,\mathrm{d}s\right] + O(\epsilon^2),$$

and by the kinematic boundary condition (3.21) we have

$$\boldsymbol{\nabla}\phi' \cdot \hat{\mathbf{n}} = -\left(1 - \frac{\partial\hat{w}_0}{\partial t}\right) + O(\epsilon).$$

Therefore, as $R \to \infty$, the leading-order contribution to the kinetic energy will be from the line $-d_0(t) < \hat{x} < d_0(t)$ for $\hat{z} = 0$, giving

$$E_{K,\mathrm{outer}}(t) = \frac{\epsilon^2}{2}\int_{-d_0(t)}^{d_0(t)} g(\hat{x},t)\sqrt{d_0(t)^2 - \hat{x}^2}\,\mathrm{d}\hat{x} + O(\epsilon^3), \tag{3.167}$$

where

$$g(\hat{x},t) = \left(1 - \frac{\partial\hat{w}_0}{\partial t}\right)\left[1 - \frac{1}{\pi}\fint_{-d_0(t)}^{d_0(t)} \frac{m_t(s,t)}{\sqrt{d_0(t)^2 - s^2}(s - \hat{x})}\,\mathrm{d}s\right]. \tag{3.168}$$

For the inner regions, the contributions to the kinetic energy come from the lines along the substrate $\tilde{z} = 0$ and the free surface, along all of which the surface element $\mathrm{d}s = O(\epsilon^3)$. Given the scalings for the inner region (3.70) and the solution for the velocity potential (3.86), we have an $O(\epsilon^5)$ contribution from the substrate line and an $O(\epsilon^4)$ contribution from the free surface line, giving $E_{K,\mathrm{inner}}(t) = O(\epsilon^4)$, which is two orders of magnitude smaller than the kinetic energy in the outer region.

We find the kinetic energy in the jet regions by integrating the flux of energy that is entering them in time. For the right-hand jet, the fluid enters through the right-hand inner region, which is moving in the x' direction with speed $\sim \dot{d}_0(t)/\epsilon$.

Downstream, the fluid has a velocity $\sim 2\dot{d}_0(t)/\epsilon$ with a vertical height $\sim \epsilon^3 J(t)$. Given this, the energy flux entering the right-hand jet is

$$Q(t) = \frac{1}{2}\left(\frac{2\dot{d}_0(t)}{\epsilon}\right)^2 \left(\frac{2\dot{d}_0(t)}{\epsilon} - \frac{\dot{d}_0(t)}{\epsilon}\right)\epsilon^3 J(t) + O(\epsilon) = 2\dot{d}_0(t)^3 J(t) + O(\epsilon), \quad (3.169)$$

By integrating the flux (taking into account the ϵ^2 time scaling), and using the solution for $J(t)$ (3.98), it follows that the kinetic energy in the jets is

$$E_{K,\text{jets}} = \frac{\epsilon^2 \pi}{2}\int_0^t (1 - B(\tau))^2 d_0(\tau)\dot{d}_0(\tau)\,\mathrm{d}\tau + O(\epsilon^3). \quad (3.170)$$

For the outer-outer region, we have that the velocity $(u', v') = O(\epsilon^2)$, and the region is $O(1)$ in size, giving $E_{K,\text{outer-outer}}(t) = O(\epsilon^4)$, which is again two orders of magnitude smaller than the energy in the outer region and the jets.

Therefore, to leading order, the kinetic energy is transferred into the outer and jet regions, giving a total kinetic energy from (3.167) and (3.170) to be

$$\begin{aligned} E_{K,\text{droplet}}(t) = {} & \frac{\epsilon^2}{2}\int_{-d_0(t)}^{d_0(t)} g(\hat{x}, t)\sqrt{d_0(t)^2 - \hat{x}^2}\,\mathrm{d}\hat{x} \\ & + \frac{\pi\epsilon^2}{2}\int_0^t (1 - B(\tau))^2 d_0(\tau)\dot{d}_0(\tau)\,\mathrm{d}\tau + O(\epsilon^3). \end{aligned} \quad (3.171)$$

From the result of Scolan (2003) [82], for the stationary substrate case we expect that the leading-order kinetic energy in the outer region is equal to that of the jet regions. For $w(x,t) = 0$, we have from (3.54) that $d_0(t) = 2\sqrt{t}$, so hence

$$\begin{aligned} E_{K,\text{outer}}(t) &= \frac{\epsilon^2 \pi d_0(t)^2}{4} + O(\epsilon^3) = \epsilon^2 \pi t + O(\epsilon^3), \\ E_{K,\text{jets}}(t) &= \frac{\epsilon^2 \pi}{2}\int_0^t 2\,\mathrm{d}\tau + O(\epsilon^3) = \epsilon^2 \pi t + O(\epsilon^3), \end{aligned} \quad (3.172)$$

which agrees with this result. Of interest for our later analysis will be how the ratio of energy between these region changes depending on the substrate location $w(x,t)$.

Motivated by the earlier discussed experiments of Howland et al. (2016) [46], we are particularly interested into how the ratio between the energy in the outer and jet regions differ when the substrate is deformable. In Figure 3.17, we plot the kinetic energy in the outer region $E_{K,\text{outer}}(t)$ with solid lines and the kinetic energy in the jets $E_{K,\text{jets}}(t)$ with dashed lines for the three imposed substrate cases. As discussed above, we see how these energies are equal and follow a linear time trend for the stationary substrate case. However for the moving substrate cases, these trends exhibit more complex behaviour, and in particular we see how the distribution of energy across

the two regions can change significantly in time. Note however that, as we do not have any fluid-structure interaction in these imposed substrate cases, the solutions shown here are purely for illustrative purposes to demonstrate how the distribution of energy between the two regions may differ when the substrate is deformable. We will discuss more extensively in Chapters 5 and 6 how the fluid-structure interaction affects the energy distribution.

3.2.10 Summary

In this section, we have used Wagner theory to model the impact of a two-dimensional droplet onto a deformable substrate. Here we left the substrate motion general, allowing it to deform in time and space. Although this two-dimensional setup is not directly applicable to real-world droplets, the methods employed here and the insight gained will be useful in the next section when we move to an axisymmetric setup. Although we have specifically focused on droplets here, the nature of Wagner theory is that the problem can be readily transformed to other settings. One notable example is how, apart from the outer-outer region, the setup here is equivalent to the parabolic wave impact problem studied by Korobkin (1998) [52]. Similarly, we could also make a coordinate transformation to re-frame the setup as a water entry problem of a deformable solid boundary, which is more akin to classic Wagner theory applications [45, 66]. The analytical model we have derived here will be used in Chapter 6 to study the impact of a two-dimensional droplet onto a deformable elastic membrane.

3.3 Axisymmetric impact

We will now move on to considering the axisymmetric impact of a three-dimensional droplet using cylindrical polar coordinates (r, z). As we only consider the spring-supported plate case in this axisymmetric setting, we shall for simplicity take $w(r, t) = w(t)$; where the more general case is discussed in Pegg et al.(2018) [71]. This significantly simplifies the problem, and allows us to more directly build upon previous studies involving axisymmetric Wagner theory [57, 62, 66, 71].

As the substrate is rigid, we will only consider two imposed substrate examples for this chapter, namely the stationary substrate case (where $w(t) = 0$) and the moving substrate case (where $w(t)$ is given by (3.16)).

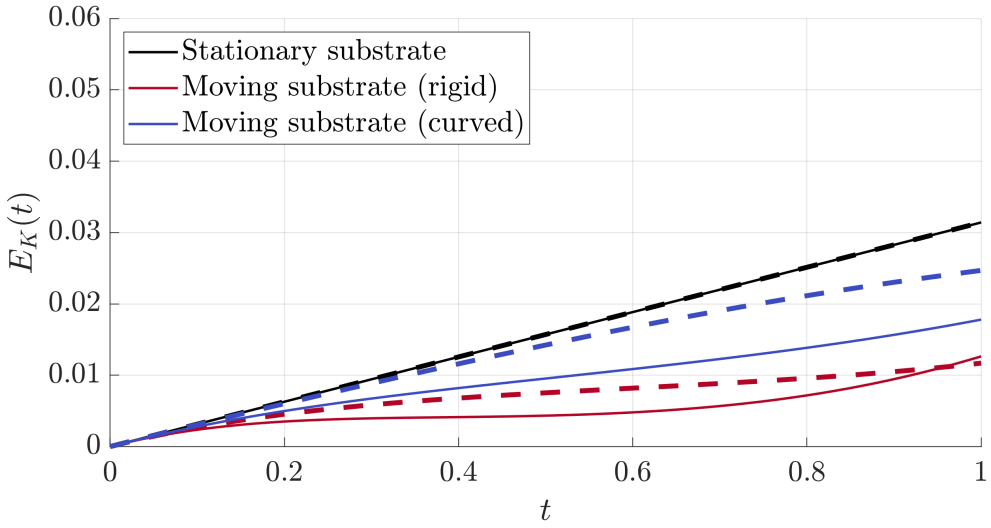

Figure 3.17: Evolution of the kinetic energy in the droplet against time, where the solid lines denote the kinetic energy in the outer region (3.167) and the dashed lines denote the energy in the jets (3.170).

The governing equations (3.1)-(3.6) for the velocity potential $\phi(r,z,t)$, pressure $p(r,z,t)$ and free surface position $h(r,z,t)$ become

$$\frac{\partial^2\phi}{\partial r^2}+\frac{1}{r}\frac{\partial\phi}{\partial r}+\frac{\partial^2\phi}{\partial z^2}=0, \quad \text{in the liquid,} \tag{3.173}$$

$$p+\frac{1}{\epsilon^2}\frac{\partial\phi}{\partial t}+\frac{1}{2}\left[\left(\frac{\partial\phi}{\partial r}\right)^2+\left(\frac{\partial\phi}{\partial z}\right)^2\right]=\frac{1}{2}, \quad \text{in the liquid,} \tag{3.174}$$

$$\frac{\partial\phi}{\partial z}+\frac{\partial w}{\partial t}=0, \quad \text{on } z=-\epsilon^2 w(t), \tag{3.175}$$

$$\frac{\partial\phi}{\partial z}-\frac{1}{\epsilon^2}\frac{\partial h}{\partial t}-\frac{\partial\phi}{\partial r}\frac{\partial h}{\partial r}=0, \quad \text{on } z=h(r,t), \tag{3.176}$$

$$p=0, \quad \text{on } z=h(r,t), \tag{3.177}$$

with initial conditions,

$$\phi(r,z,0)=-z, \quad \text{for } r^2+(z-1)^2\leq 1, \tag{3.178}$$

$$r^2+(h(r,0)-1)^2=1, \quad \text{for } r^2\leq 1, \tag{3.179}$$

As in the two-dimensional analysis, it will sometimes be convenient to work directly with the velocity, given by

$$\mathbf{u}=u(r,z,t)\hat{\mathbf{r}}+v(r,z,t)\mathbf{j}=\frac{\partial\phi}{\partial r}\hat{\mathbf{r}}+\frac{\partial\phi}{\partial z}\mathbf{j}, \tag{3.180}$$

where $\hat{\mathbf{r}}$ and $\mathbf{j}$ are the unit vectors in the radial and vertical directions, respectively.

3.3.1 Asymptotic structure

The asymptotic structure in the axisymmetric case breaks down in the same way as the two-dimensional case, as detailed in §3.2.1. In this three-dimensional setting, the free surface turns vertical along a set of points referred to as the *turnover curve*, where we define the radial coordinate of the turnover curve to be $r = \epsilon d(t)$, where $d(t) = O(1)$ as $\epsilon \to 0$.

As $\epsilon \to 0$, the problem breaks down into four distinct asymptotic regions, depicted in Figure 3.18, which have the same sizes as their two-dimensional counterparts in §3.2. In this case, we instead refer to the fluid being ejected from the inner region as the *splash sheet*. As before, we will derive the leading-order asymptotic solutions in all four of these regions, drawing focus on how the substrate motion affects these solutions.

3.3.2 Outer region

Similar to the two-dimensional case in §3.2.3, in the outer region we substitute the outer variables

$$r = \epsilon\hat{r}, \quad z = \epsilon\hat{z}, \quad \phi = \epsilon\hat{\phi}, \quad h = \epsilon^2\hat{h}, \quad p = \hat{p}/\epsilon, \tag{3.181}$$

into (3.173)-(3.179) and expand $(\hat{\phi},\, \hat{h},\, \hat{p},\, d,\, w) = (\hat{\phi}_0,\, \hat{h}_0,\, \hat{p}_0,\, d_0,\, w_0) + o(1)$ as $\epsilon \to 0$. The resulting leading-order mixed boundary value problem is similar to the two-dimensional case (3.19)-(3.23), with $\hat{x}$ replaced by $\hat{r}$ and Laplace's equation (3.19) being replaced by the axisymmetric form given by (3.173).

The far-field conditions as we tend towards the outer-outer region state that, to leading-order, the flow is travelling downwards with unit speed, and the free surface is parabolic in $\hat{r}$, such that

$$\hat{\phi}_0(\hat{r}, \hat{z}, t) \sim -\hat{z} \text{ as } \hat{r}^2 + \hat{z} \to \infty, \quad \hat{h}_0(\hat{r}, t) \sim \frac{1}{2}\hat{r}^2 - t \text{ as } \hat{r}^2 \to \infty, \tag{3.182}$$

while the initial conditions are given by

$$\hat{\phi}_0(\hat{r}, \hat{z}, 0) = -\hat{z}, \quad \hat{h}_0(\hat{r}, 0) = \frac{1}{2}\hat{r}^2, \quad d_0(0) = 0. \tag{3.183}$$

In order to match with the inner regions, we require that the potential $\hat{\phi}_0$ satisfies

$$\hat{\phi}_0 = O\left((d_0(t)^2 - \hat{r}^2 - \hat{z}^2)^{1/2}\right) \text{ as } (\hat{r},\, \hat{z}) \to (d_0(t),\, 0), \tag{3.184}$$

as well as the Wagner condition

$$\hat{h}_0(d_0(t), t) = -w_0(t), \tag{3.185}$$

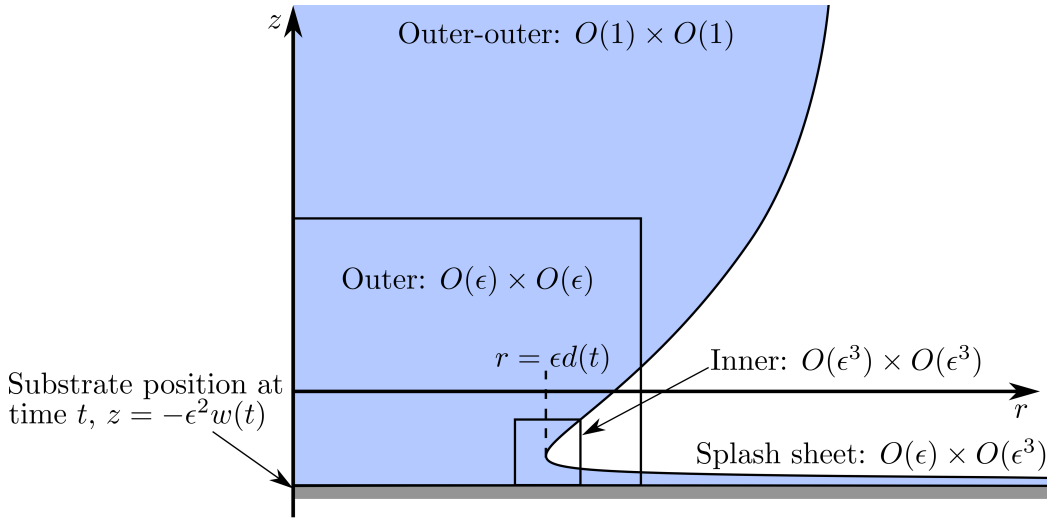

Figure 3.18: Schematic of the asymptotic structure of the axisymmetric system. The radial extent of the inner region and the displacement of the substrate $z = -\epsilon^2 w(t)$ are exaggerated for visual clarity.

which, as with its two-dimensional equivalent (3.26), states that the leading-order free surface meets the substrate at the turnover curve.

3.3.2.1 Solution for the displacement potential

It is once again convenient to re-formulate the boundary-value problem in terms of the displacement potential $\Upsilon_0(\hat{r}, \hat{z}, t)$, here defined by

$$\Upsilon_0 = t\hat{z} + \int_0^t \hat{\phi}_0(\hat{r}, \hat{z}, \tau)\, \mathrm{d}\tau\,, \tag{3.186}$$

noting the slight difference with the two-dimensional case in (3.33) as we have included the $t\hat{z}$ term for convenience. As in §3.2.3.2, we again assume that $\hat{r} = d_0(t)$ is invertible, with an inverse $\omega_0(\hat{r}) = t$, requiring that $\dot{d}_0(t) > 0$ for all time i.e. that the splash sheet advances throughout the impact. In a similar manner to the two-dimensional case, the appropriate mixed boundary value problem for Υ_0 is

$$\frac{\partial^2 \Upsilon_0}{\partial \hat{r}^2} + \frac{1}{\hat{r}}\frac{\partial \Upsilon_0}{\partial \hat{r}} + \frac{\partial^2 \Upsilon_0}{\partial \hat{z}^2} = 0, \qquad \text{for } \hat{z} > 0, \tag{3.187}$$

$$\frac{\partial \Upsilon_0}{\partial \hat{z}} = (t - w_0(t)) - \frac{1}{2}\hat{r}^2, \qquad \text{on } \hat{z} = 0, \hat{r} < d_0(t), \tag{3.188}$$

$$\frac{\partial \Upsilon_0}{\partial \hat{z}} = t + \hat{h}_0(\hat{r}, t) - \frac{1}{2}\hat{r}^2, \qquad \text{on } \hat{z} = 0, \hat{r} > d_0(t), \tag{3.189}$$

$$\Upsilon_0 = 0, \qquad \text{for } \hat{z} = 0, \hat{r} > d_0(t). \tag{3.190}$$

As $\hat{\phi}_0 \sim -\hat{z}$ as $\hat{r}^2 + \hat{z}^2 \to \infty$, the far-field and initial conditions are given by

$$\Upsilon_0(\hat{r}, \hat{z}, t) \to 0 \text{ as } \hat{r}^2 + \hat{z}^2 \to \infty, \quad \Upsilon_0(\hat{r}, \hat{z}, 0) = 0, \tag{3.191}$$

and from (3.184) it follows that

$$\Upsilon_0 = C + O\left((d_0(t)^2 - \hat{r}^2 - \hat{z}^2)^{3/2}\right) \text{ as } (\hat{r},\, \hat{z}) \to (d_0(t),\, 0), \tag{3.192}$$

where C is a constant. The general solution for Laplace's equation (3.187) is given by

$$\Upsilon_0(\hat{r}, \hat{z}, t) = \int_0^\infty \nu(\lambda, t) e^{-\lambda \hat{z}} J_0(\lambda \hat{r})\, \mathrm{d}\lambda\,, \tag{3.193}$$

where J_0 is a Bessel function of the first-kind of order 0, and $\nu(\lambda, t)$ is an unknown coefficient function.

We find the solution for $\nu(\lambda, t)$ by applying the boundary conditions (3.188) and (3.190) along $\hat{z} = 0$. To this end, following the method detailed in Sneddon (1966) [84], we first introduce a new function χ that satisfies

$$\nu(\lambda, t) = \int_0^{d_0(t)} \chi(\sigma, t) \sin(\lambda\sigma)\, \mathrm{d}\sigma\,, \quad \chi(0, t) = 0, \tag{3.194}$$

such that we can make use of the following trigonometric integral identities involving Bessel functions from §6.671 of Gradsheyn et al. (2014) [31],

$$\int_0^\infty \sin(\lambda\sigma) J_0(\lambda\hat{r})\, \mathrm{d}\lambda = \begin{cases} (\sigma^2 - \hat{r}^2)^{-1/2} & 0 \le \hat{r} < \sigma, \\ 0 & \sigma \le \hat{r}, \end{cases} \tag{3.195}$$

$$\int_0^\infty \cos(\lambda\sigma) J_0(\lambda\hat{r})\, \mathrm{d}\lambda = \begin{cases} 0 & 0 \le \hat{r} \le \sigma, \\ (\hat{r}^2 - \sigma^2)^{-1/2} & \sigma < \hat{r}. \end{cases} \tag{3.196}$$

By substituting the representation (3.194) into the general solution (3.193), and exchanging the order of integration, we find that Υ_0 along $\hat{z} = 0$ is given by

$$\Upsilon_0(\hat{r}, 0, t) = \begin{cases} \displaystyle\int_{\hat{r}}^{d_0(t)} \frac{\chi(\sigma, t)}{\sqrt{\sigma^2 - \hat{r}^2}}\, \mathrm{d}\sigma\,, & \text{for } \hat{r} < d_0(t), \\ 0, & \text{for } \hat{r} > d_0(t), \end{cases} \tag{3.197}$$

where we applied the identity (3.195) in both cases. This confirms that the representation (3.194) immediately enforces the dynamic boundary condition (3.190) for $\hat{r} < d_0(t)$.

To apply the kinematic boundary conditions (3.188)-(3.189), we must find the $\hat{z}$ derivative of Υ_0 on $\hat{z} = 0$. It follows from the general solution (3.193) and the representation (3.194) that

$$\begin{aligned}\frac{\partial \Upsilon_0}{\partial \hat{z}} &= -\int_0^\infty \left(\int_0^{d_0(t)} \chi(\sigma, t)\lambda \sin(\lambda\sigma)\, \mathrm{d}\sigma \right) J_0(\lambda\hat{r})\, \mathrm{d}\lambda \\ &= \chi(d_0(t), t) \int_0^\infty \cos(\lambda d_0(t)) J_0(\lambda\hat{r})\, \mathrm{d}\lambda - \int_0^{d_0(t)} \chi_\sigma(\sigma, t) \int_0^\infty \cos(\lambda\sigma) J_0(\lambda\hat{r})\, \mathrm{d}\lambda\, \mathrm{d}\sigma\,,\end{aligned}$$

where χ_σ denotes the partial derivative of χ with respect to σ. By applying the identity (3.196), we find that on $\hat{z} = 0$,

$$\frac{\partial \Upsilon_0}{\partial \hat{z}} = \begin{cases} -\displaystyle\int_0^{\hat{r}} \frac{\chi_\sigma(\sigma, t)}{\sqrt{\hat{r}^2 - \sigma^2}}\, \mathrm{d}\sigma\,, & \text{for } \hat{r} < d_0(t), \\ \displaystyle\frac{\chi(d_0(t), t)}{\sqrt{\hat{r}^2 - d_0(t)^2}} - \int_0^{d_0(t)} \frac{\chi_\sigma(\sigma, t)}{\sqrt{\hat{r}^2 - \sigma^2}}\, \mathrm{d}\sigma\,, & \text{for } \hat{r} > d_0(t). \end{cases} \tag{3.198}$$

Therefore, applying the kinematic boundary condition (3.188) on $\hat{r} < d_0(t)$, it follows from (3.198) that χ is given by the integral equation

$$\int_0^{\hat{r}} \frac{\chi_\sigma(\sigma, t)}{\sqrt{\hat{r}^2 - \sigma^2}}\, \mathrm{d}\sigma = \frac{1}{2}\hat{r}^2 - (t - w_0(t)). \tag{3.199}$$

This is an Abel type integral equation, and can be inverted via the method detailed in Sneddon (1966) [84] to find that $\chi_\sigma(\sigma, t)$ is given by

$$\chi_\sigma(\sigma, t) = \frac{2}{\pi} \frac{\mathrm{d}}{\mathrm{d}\sigma} \int_0^\sigma \frac{\xi\,(\xi^2/2 - (t - w_0(t)))}{\sqrt{\sigma^2 - \xi^2}}\, \mathrm{d}\xi\,, \tag{3.200}$$

and then by integrating with respect to σ and recalling that $\chi(0, t) = 0$, it follows that χ is given by

$$\chi(\sigma, t) = \frac{2}{\pi} \int_0^\sigma \frac{\xi(\xi^2/2 - (t - w_0(t)))}{\sqrt{\sigma^2 - \xi^2}}\, \mathrm{d}\xi = \frac{2}{\pi}\sigma \left[\frac{1}{3}\sigma^2 - (t - w_0(t)) \right]. \tag{3.201}$$

Finally, we then find ν by substituting (3.201) into the representation for ν (3.194), viz.

$$\nu(\lambda, t) = \frac{2}{\pi} \int_0^{d_0(t)} \sigma \left[\frac{1}{3}\sigma^2 - (t - w_0(t)) \right] \sin(\lambda\sigma)\, \mathrm{d}\sigma\,. \tag{3.202}$$

Although we can evaluate the integral (3.202) explicitly, we will save this computation until we have found the solution for $d_0(t)$. Therefore the solution for the displacement potential Υ_0 is given by (3.193) with the solution (3.202) for the coefficient function $\nu(\lambda, t)$. In general, for $\hat{z} > 0$, the integral in λ cannot be determined analytically, but numerical solutions can be readily found using numerical integration methods.

3.3.2.2 Solution for the free surface location

To determine the free surface location, we substitute the solution for $\partial\Upsilon_0/\partial\hat{z}$ for $\hat{r} > d_0(t)$ from (3.198) into the kinematic boundary condition at the free surface (3.189) to find

$$\frac{\chi(d_0(t),t)}{\sqrt{\hat{r}^2 - d_0(t)^2}} - \int_0^{d_0(t)} \frac{\chi_\sigma(\sigma,t)}{\sqrt{\hat{r}^2-\sigma^2}}\,\mathrm{d}\sigma = t + \hat{h}_0(\hat{r},t) - \frac{1}{2}\hat{r}^2. \tag{3.203}$$

Note here that the first term on the left-hand side is singular at $\hat{r} = d_0(t)$, which is incompatible with the Wagner condition (3.185), which states $\hat{h}_0(d_0(t),t) = -w_0(t)$. Therefore, we must enforce that $\chi(d_0(t),t) = 0$, so that by using (3.201), we have

$$d_0(t) = \sqrt{3(t - w_0(t))}, \tag{3.204}$$

and the time derivatives of $d_0(t)$ are hence

$$\dot{d}_0(t) = \frac{\sqrt{3}(1-\dot{w}_0(t))}{2\sqrt{t-w_0(t)}}, \quad \ddot{d}_0(t) = -\frac{\sqrt{3}\left(2(t-w_0(t))\ddot{w}_0(t) + (1-\dot{w}_0(t))^2\right)}{4(t-w_0(t))^{3/2}}. \tag{3.205}$$

Given that we required $d_0(t)$ to be invertible to define $\omega_0(\hat{r})$, we must have that $\dot{w}_0(t) < 1$. As $w_0(0) = 0$, this implies that $w_0(t) < t$, which ensures that $d_0(t)$ is real-valued and that the substrate is not moving faster than the incoming droplet.

In Figure 3.19, we show the solution for the turnover curve given by (3.204) for the stationary and moving substrate cases. By comparing to the two-dimensional case in Figure 3.4, we can see how the turnover curve in the stationary case evolves more slowly in the axisymmetric setting versus the two-dimensional setting, due to the $\sqrt{3}$ factor in (3.204) versus the factor of 2 in (3.54). We also see how the moving substrate case here still does exhibit a slower spreading in comparison to the stationary substrate case, which is directly accounted for in (3.204) when $w_0(t) > 0$. This behaviour can be understood by the same conservation of mass argument presented in §3.2.3.3 for the two-dimensional case.

Using the solutions for $d_0(t)$ (3.204) and $\chi(\sigma,t)$ (3.201), we re-arrange (3.203) to find the leading-order solution for the free surface location given by

$$\begin{aligned}\hat{h}_0(\hat{r},t) = \frac{1}{2}\hat{r}^2 - t + \frac{1}{\pi}d_0(t)\sqrt{\hat{r}^2 - d_0(t)^2} \\ + \frac{2}{\pi}\arcsin\left(\frac{d_0(t)}{\hat{r}}\right)\left((t-w_0(t)) - \frac{1}{2}\hat{r}^2\right).\end{aligned} \tag{3.206}$$

We plot the free-surfaces given by $\hat{z} = \epsilon\hat{h}_0$ in Figure 3.20 with solid lines, and the substrate position $\hat{z} = -\epsilon w_0(t)$ with dashed lines. Similar to the two-dimensional case, we can see here how fluid that falls below the $\hat{r}$ axis in the moving substrate case causes the slowing of the spreading due to mass conservation.

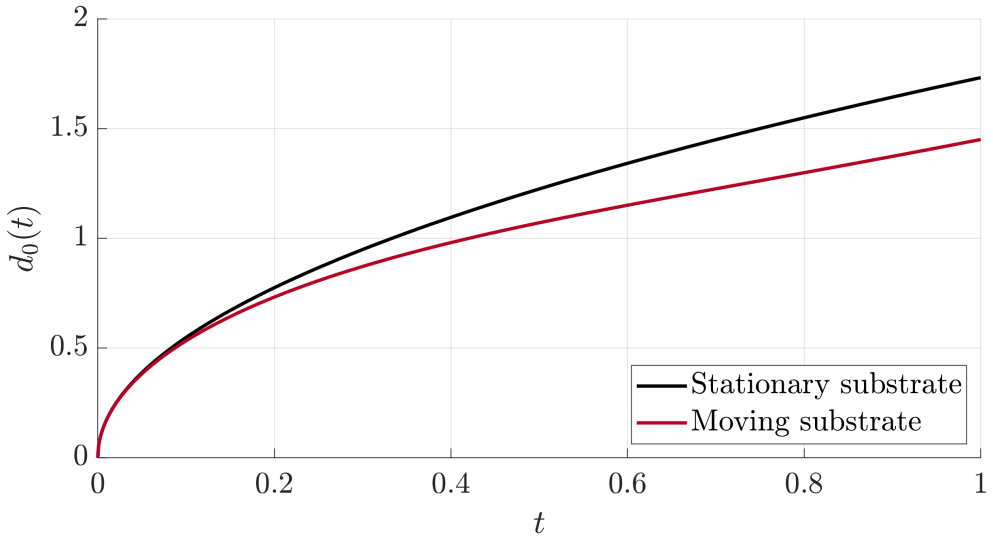

Figure 3.19: Leading-order solutions for the turnover curve location $\hat{r} = d_0(t)$, given by (3.204).

3.3.2.3 Solution for the velocity potential

By the definition of the displacement potential (3.186), the velocity potential $\hat{\phi}_0$ is

$$\hat{\phi}_0(\hat{r}, \hat{z}, t) = -\hat{z} + \int_0^\infty \nu_t(\lambda, t) e^{-\lambda \hat{z}} J_0(\lambda \hat{r}) \, \mathrm{d}\lambda \,, \tag{3.207}$$

Now that we have the solution for $d_0(t)$ (3.204), we can simplify the integral (3.202) to find that $\nu(\lambda, t)$ is given by

$$\nu(\lambda, t) = \frac{4}{3\pi\lambda^4} \left[\left(d_0(t)^2 \lambda^2 - 3 \right) \sin(d_0(t)\lambda) + 3 d_0(t) \lambda \cos(d_0(t)\lambda) \right] , \tag{3.208}$$

and it follows that

$$\nu_t(\lambda, t) = \frac{4 d_0(t) \dot{d}_0(t)}{3\pi\lambda^2} \left[\lambda d_0(t) \cos\left(\lambda d_0(t)\right) - \sin\left(\lambda d_0(t)\right) \right] . \tag{3.209}$$

The radial and vertical velocity components are then found by differentiating (3.207) such that

$$\begin{aligned} \hat{u}_0 &= -\int_0^\infty \lambda \nu_t(\lambda, t) e^{-\lambda \hat{z}} J_1(\lambda \hat{r}) \, \mathrm{d}\lambda \,, \\ \hat{v}_0 &= -1 - \int_0^\infty \lambda \nu_t(\lambda, t) e^{-\lambda \hat{z}} J_0(\lambda \hat{r}) \, \mathrm{d}\lambda \,, \end{aligned} \tag{3.210}$$

using the fact that the derivative of J_0 is $-J_1$.

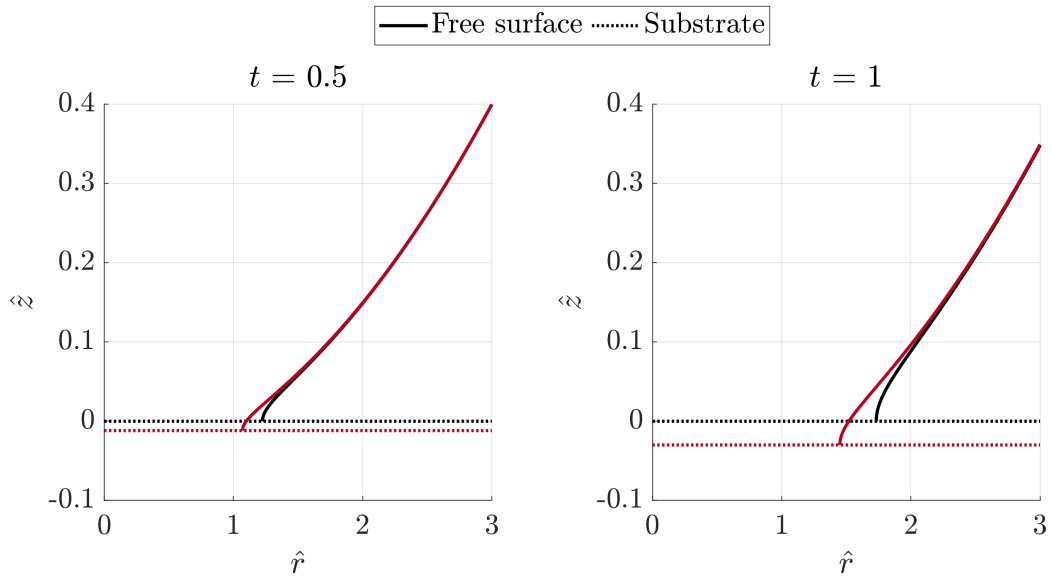

Figure 3.20: Leading-order solutions for the free surface location in the outer region $\hat{z} = \epsilon \hat{h}_0(\hat{r}, t)$ given by (3.206) (solid lines), alongside the substrate location $\hat{z} = -\epsilon w_0(t)$ (dotted lines). The black lines denote the stationary substrate case and the red lines denote the moving substrate case (with $w_0(t)$ given by (3.16)).

3.3.2.4 Solution for the pressure

From the leading-order Bernoulli equation (3.2), the leading-order pressure is given by

$$\hat{p}_0(\hat{r}, \hat{z}, t) = -\int_0^\infty \nu_{tt}(\lambda, t) e^{-\lambda \hat{z}} J_0(\lambda \hat{r}) \, \mathrm{d}\lambda \,. \tag{3.211}$$

By differentiating (3.209) with respect to t, we find that $\nu_{tt}(\lambda t)$ is given by

$$\begin{aligned} \nu_{tt}(\lambda, t) = \frac{4}{3\pi\lambda^2} \Big[& \lambda d_0(t) \cos\left(\lambda d_0(t)\right) \left(\dot{d}_0(t)^2 + d_0(t) \ddot{d}_0(t) \right) \\ & - \sin\left(\lambda d_0(t)\right) \left(\left(\lambda^2 d_0(t)^2 + 1\right) \dot{d}_0(t)^2 + d_0(t) \ddot{d}_0(t) \right) \Big]. \end{aligned} \tag{3.212}$$

3.3.3 Inner region

In this three-dimensional setting, the inner region represents a torus-shaped region surrounding the turnover curve. As in the two-dimensional case, we substitute the inner variables

$$r = \epsilon d(t) + \epsilon^3 \tilde{r}, \quad z = -\epsilon^2 w(t) + \epsilon^3 \tilde{z},$$
$$\phi = \epsilon^2 \left[\dot{d}(t) \tilde{r} - \epsilon w_t(t) \tilde{z} + \tilde{\phi} \right], \quad h = -\epsilon^2 w(t) + \epsilon^3 \tilde{h}, \quad p = \frac{1}{\epsilon^2} \tilde{p},$$

into (3.173)-(3.179) and expand $(\tilde{\phi},\, \tilde{h},\, \tilde{p}) = (\tilde{\phi}_0,\, \tilde{h}_0,\, \tilde{p}_0) + o(1)$ as $\epsilon \to 0$. By the argument presented in Moore (2014) [62], the leading-order inner problem is quasi-two-dimensional, and that by replacing $\tilde{x}$ with $\tilde{r}$, we recover the corresponding two-dimensional governing equations (3.71)-(3.76) to leading-order. Therefore the leading-order solutions for the complex velocity potential, complex velocity, free surface location and pressure are given by (3.86), (3.87), (3.89) and (3.92) respectively. Although the spatially dependent terms of the leading-order solutions in the inner region are the same as the two-dimensional case, the time-dependent terms $d_0(t)$, $\dot{d}_0(t)$ and $J(t)$ will differ.

3.3.3.1 Matching with the outer region

As was the case in two-dimensions, we determine the unknown asymptotic jet thickness $J(t)$ by matching the leading-order solutions for the velocity potential in the outer and inner regions via the intermediate variable technique. For simplicity, we match the solutions applied onto the substrate, so that $\hat{z} = \tilde{z} = 0$. First, we express the outer variables in terms of the inner variables,

$$\hat{r} = d(t) + \epsilon^2 \tilde{r}, \quad \hat{\phi} = \epsilon \left[\dot{d}(t)\tilde{r} + \tilde{\phi} \right],$$

and then use capital letters to denote an intermediate variable, defining

$$\hat{r} = d(t) + \epsilon^{\alpha} R, \quad \hat{\phi} = \epsilon^{\alpha - 1} \left[\dot{d}(t) R + \Phi \right], \tag{3.213}$$

where we anticipate the matching by taking $0 < \alpha < 1$, as was found in §3.2.4.4. We then need to re-express the leading-order solutions for the velocity potentials in terms of the intermediate variables and match their expansions as $\epsilon \to 0$ for $R = O(1)$.

We first need to find the solution for $\hat{\phi}_0$ on the contact set. Substituting the solution for χ (3.201) into (3.197), with the solution for $d_0(t)$ given by (3.204), the displacement potential along the contact set (where $\hat{r} < d_0(t)$) is

$$\Upsilon_0(\hat{r}, 0, t) = \frac{2}{3\pi} \int_{\hat{r}}^{d_0(t)} \frac{\sigma(\sigma^2 - d_0(t)^2)}{\sqrt{\sigma^2 - \hat{r}^2}} \, \mathrm{d}\sigma = -\frac{4}{9\pi} \left(d_0(t)^2 - \hat{r}^2 \right)^{3/2}, \tag{3.214}$$

and by differentiating (3.214) with respect to t we hence find $\hat{\phi}_0$ along the contact set to be

$$\hat{\phi}_0(\hat{r}, 0, t) = -\frac{4 d_0(t) \dot{d}_0(t)}{3\pi} \sqrt{d_0(t)^2 - \hat{r}^2}. \tag{3.215}$$

Substituting the intermediate variables (3.213) into (3.215) and expanding as $\epsilon \to 0$ yields the local expansion of the outer solution tending towards the turnover curve as

$$\Phi \sim -\dot{d}_0(t) R - \frac{4}{3\pi} \epsilon^{1-\alpha/2} d_0(t) \dot{d}_0(t) \sqrt{2 d_0(t)} \sqrt{-R}. \tag{3.216}$$

As the velocity potential in the inner region is the same as the two-dimensional case (replacing $\tilde{x}$ with $\tilde{r}$), we know from §3.2.4.4 that the far-field expansion for Φ from the inner region is given by

$$\Phi \sim -\dot{d}_0(t)R - 4\epsilon^{1-\alpha/2}\dot{d}_0(t)\sqrt{\frac{J(t)}{\pi}}\sqrt{-R}, \tag{3.217}$$

so hence by matching the expansions (3.216) and (3.217), we conclude that

$$J(t) = \frac{2d_0(t)^3}{9\pi} = \frac{2}{\sqrt{3}\pi}(t - w_0(t))^{3/2}, \tag{3.218}$$

where for the second equality we substituted in the solution for $d_0(t)$ given by (3.204). We see here that the displacement of the membrane directly reduces the thickness of the jet compared to the cases where the membrane is fixed.

In Figure 3.21 we plot the solutions for the jet thickness $J(t)$. By comparing to the two-dimensional case in Figure 3.11, we see how the thickness of the splash sheet in the axisymmetric setting is less than half of that in the two-dimensional case, and that the substrate motion here still decreases the thickness of the splash sheet, which is clearly seen when $w_0(t) > 0$ in (3.218).

3.3.4 Splash sheet region

The splash sheet is the three-dimensional analogue of the jet regions in the two-dimensional impact case, and it composes of a thin sheet of fluid emanating from the turnover curve across the substrate at high velocity. As we discussed in §3.3.3 that the inner region is quasi-two-dimensional, we use the same scalings as the jet for the splash sheet, such that

$$\begin{gathered} r = \epsilon\bar{r}, \quad z = -\epsilon^2 w(t) + \epsilon^3\bar{z}, \\ u = \frac{1}{\epsilon}\bar{u}, \quad v = -\dot{w}(t) + \epsilon\bar{v}, \quad h = \epsilon^3\bar{h}, \quad p = \epsilon\bar{p}. \end{gathered} \tag{3.219}$$

Then, expanding $(\bar{u},\, \bar{v}, \bar{h},\, \bar{p},\, \bar{w}) = (\bar{u}_0,\, \bar{v}_0, \bar{h}_0,\, \bar{p}_0,\, \bar{w}_0) + o(1)$ as $\epsilon \to 0$, by a similar argument to the two-dimensional case in §3.2.5 (see Moore (2014) [62] for details), the governing equations in the splash sheet are

$$\bar{u}_{0t} + \bar{u}_0\bar{u}_{0\bar{r}} = 0, \tag{3.220}$$

$$\bar{h}_{0t} + \bar{u}_0\bar{h}_{0\bar{r}} + \left(\bar{u}_{0\bar{r}} + \frac{1}{\bar{r}}\bar{u}_0\right)\bar{h}_0 = 0. \tag{3.221}$$

As the flow is irrotational, we have that $\bar{u}_{\bar{z}} = O(\epsilon^4)$, such that $\bar{u}_0$ is independent of $\bar{z}$. Subsequently, by the continuity equation, we have $\bar{v}_0 = -\bar{z}(\bar{u}_{0\bar{r}} + \bar{u}_0/\bar{r})$.

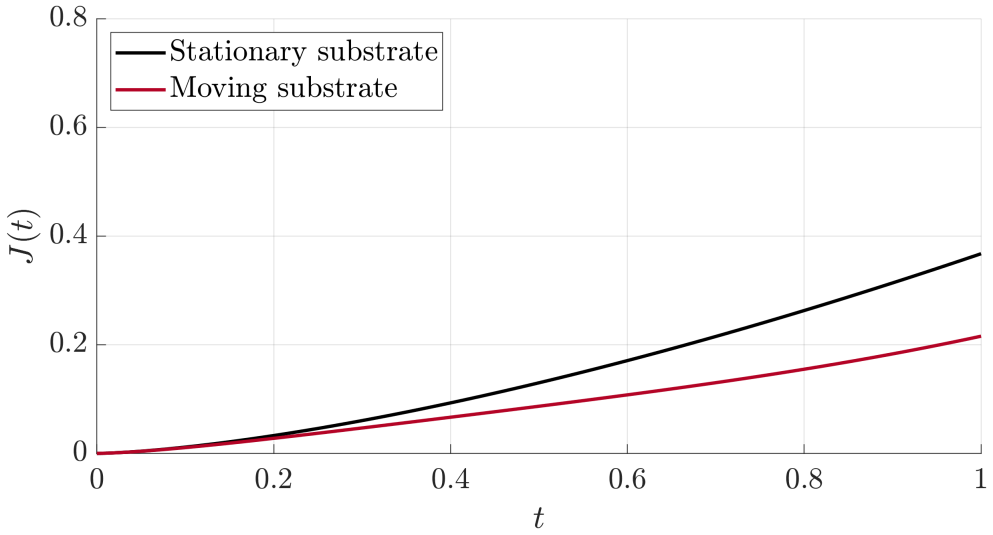

Figure 3.21: Solutions for the asymptotic jet thickness, $J(t)$, given by (3.218).

In the same manner as the two-dimensional case, the governing equations (3.220)-(3.221) can be solved via the method of characteristics. The boundary conditions are applied at $\bar{r} = d_0(\tau)$, which are applied to match with the inner region solution such that

$$t = \tau, \quad \bar{r} = d_0(\tau), \quad \bar{u}_0(d_0(\tau), \tau) = 2\dot{d}_0(\tau), \quad \bar{h}_0(d_0(\tau), \tau) = J(\tau). \tag{3.222}$$

As (3.220) is identical to (3.120) in the two-dimensional case (exchanging $\bar{x}$ for $\bar{r}$), we have that the solution is given by the characteristic parameter ξ such that

$$t = \tau + \xi, \quad \bar{r} = 2\dot{d}_0(\tau)\xi + d_0(\tau), \quad \bar{u}_0 = 2\dot{d}_0(\tau). \tag{3.223}$$

However, the governing equation for $\bar{h}_0$ in this case has an additional term, such that the characteristic equation is given by

$$\frac{\partial \bar{h}_0}{\partial \xi} = -\left(\frac{2\dot{d}_0(\tau)}{2\dot{d}_0(\tau)\xi + d_0(\tau)} + \frac{2\ddot{d}_0(\tau)}{2\ddot{d}_0(\tau)\xi - \dot{d}_0(\tau)} \right) \bar{h}_0. \tag{3.224}$$

Integrating (3.224) and applying the boundary condition (3.222) at $\xi = 0$, and finally substituting $\xi = t - \tau$, we have that the splash sheet solutions are given by

$$\bar{u}_0 = 2\dot{d}_0(\tau), \quad \bar{h}_0 = \frac{J(\tau) d_0(\tau) \dot{d}_0(\tau)}{\Big(d_0(\tau) + 2\dot{d}_0(\tau)(t-\tau)\Big)\Big(\dot{d}_0(\tau) - 2\ddot{d}_0(\tau)(t-\tau)\Big)} \tag{3.225}$$

with

$$\bar{r} = 2\dot{d}_0(\tau)(t - \tau) + d_0(\tau), \tag{3.226}$$

where $0 < \tau \leq t$. Similar to the two-dimensional case, the leading-order pressure is then found from the leading-order Bernoulli equation (3.174) to be

$$\bar{p}_0 = \left(\ddot{w}_0(t) - \dot{w}_0(t) \left(\bar{u}_{0\bar{r}} + \frac{1}{\bar{r}} \bar{u}_0 \right) \right) \left(\bar{h}_0 - \bar{z} \right), \tag{3.227}$$

such that when the velocity and acceleration of the substrate are zero, we have $\bar{p}_0 = 0$, in which case the pressure in the splash sheet would be $O(\epsilon^2)$.

The evolution of the free surface of the splash sheet $\bar{h}_0$ for the two example cases are shown in Figure 3.22, for t ranging from $= 0$ to 1, where the solid lines denote the free surface location and the dashed lines plot the evolution of the jet root $\bar{h}_0(d_0(t), t) = J(t)$ (which are plotted beyond $t = 1$ for visualisation purposes). Once again it is clear that the substrate motion causes the splash sheet to grow radially and vertically at a slower rate than the stationary substrate case.

3.3.5 Outer-outer region

The final region to resolve is the outer-outer region, which contains the portion of the droplet above the outer region and away from the point of contact with the substrate. As with the two-dimensional case, we expect the bulk of the droplet to remain mostly unaffected by the impact process in this early time regime.

To find the outer-outer scalings, we find the far-field behaviour of the displacement potential Υ_0 as $\hat{x}^2 + \hat{z}^2 \to \infty$. We first write the displacement potential (3.193) in terms of the function χ defined in (3.194) to give

$$\Upsilon_0(\hat{r}, \hat{z}, t) = \int_0^{d_0(t)} \chi(\sigma, t) \underbrace{\int_0^\infty \sin(\lambda\sigma) e^{-\lambda\hat{z}} J_0(\lambda\hat{r}) \, \mathrm{d}\lambda}_{I} \, \mathrm{d}\sigma \,,$$

where we have labelled the integral I to be the term that depends on $\hat{r}$ and $\hat{z}$. We introduce variables $0 \leq R < \infty$ and $0 \leq \theta < \pi/2$, such that

$$\hat{r} = R\sin(\theta), \quad \hat{z} = R\cos(\theta),$$

and substitute these into the integral I to find

$$I = \int_0^\infty \sin(\lambda\sigma) e^{-R\cos(\theta)\lambda} J_0(R\sin(\theta)\lambda) \, \mathrm{d}\lambda \,.$$

We now employ Laplace's method for approximating integrals [42] to find the asymptotic behaviour of I as $R \to \infty$. The dominant contribution from the integral will be

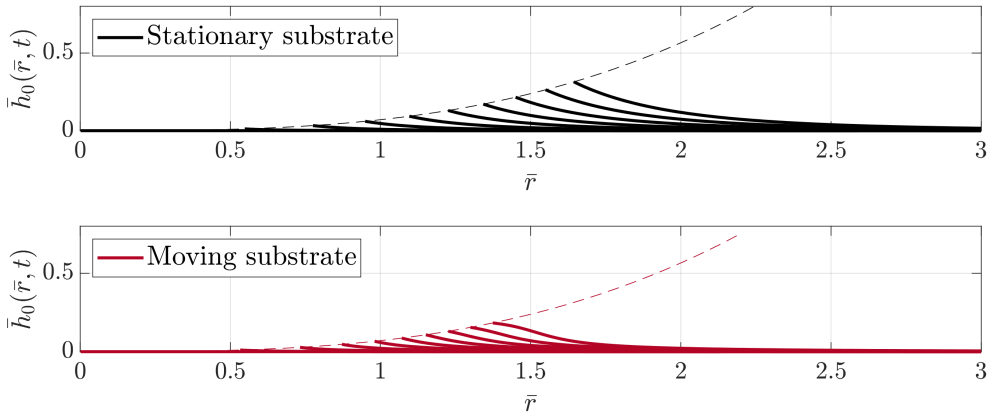

Figure 3.22: Leading-order solutions for the free surface location in the jet regions given by $\bar{z} = \bar{h}_0(\bar{r}, t)$ from (3.130) (solid lines). The lines are plotted in equal temporal steps from $t = 0$ to $t = 1$. The dashed lines plot the evolution of the point $\bar{h}_0(d_0(t), t) = J(t)$.

near $\lambda = 0$, where the exponential term is at its maximum. We therefore introduce δ such that $0 < 1/R \ll \delta \ll 1$ as $R \to \infty$, and split the range of integration by

$$I = I_1 + I_2 = \left(\int_0^{\delta} + \int_{\delta}^{\infty} \right) \sin(\lambda\sigma) e^{-R\cos(\theta)\lambda} J_0(R\sin(\theta)\lambda)\, \mathrm{d}\lambda\,,$$

where I_2 will be exponentially small compared to I_1 as $R \to \infty$. For I_1, we first expand $\sin(\lambda\sigma) \sim \lambda\sigma$ in the integrand as $\delta \ll 1$, then substitute $s = R\cos(\theta)\lambda$ to find

$$I_1 \sim \frac{\sigma}{R^2\cos^2(\theta)} \int_0^{R\delta\cos(\theta)} s e^{-s} J_0(\tan(\theta)s)\, \mathrm{d}s \sim \frac{\sigma}{R^2\cos^2(\theta)\left(1+\tan(\theta)^2\right)^{3/2}},$$

where we replaced the upper limit of the integrand with ∞, introducing only exponentially small errors. Therefore, substituting back into the $\hat{r}$ and $\hat{z}$ variables, we find that the asymptotic expansion for Υ_0 as $\hat{r}^2 + \hat{z}^2 \to \infty$ is

$$\begin{aligned} \Upsilon_0 &\sim \frac{\hat{z}}{(\hat{r}^2+\hat{z}^2)^{3/2}} \int_0^{d_0(t)} \sigma\chi(\sigma,t)\, \mathrm{d}\sigma \\ &= \frac{\hat{z}}{(\hat{r}^2+\hat{z}^2)^{3/2}} \cdot \frac{2}{\pi} \int_0^{d_0(t)} \sigma^2 \left(\frac{1}{3}\sigma^2 - (t - w_0(t)) \right) \mathrm{d}\sigma = -\frac{G(t)\hat{z}}{(\hat{r}^2+\hat{z}^2)^{3/2}}, \end{aligned} \tag{3.228}$$

where we define $G(t)$ by

$$G(t) = \frac{2d_0(t)^3}{3\pi}\left((t - w_0(t)) - \frac{3d_0(t)^2}{10} \right) = \frac{4d_0(t)^5}{45}, \tag{3.229}$$

which is found by substituting $d_0(t) = \sqrt{3(t - w_0(t)}$ from (3.204). From this, we readily find the far-field limit of $\hat{\phi}_0$, such that

$$\hat{\phi}_0 = -\hat{z} + \frac{\partial \Upsilon_0}{\partial t} \sim -\hat{z} - \frac{\dot{G}(t)\hat{z}}{(\hat{r}^2+\hat{z}^2)^{3/2}} \text{ as } \hat{r}^2 + \hat{z}^2 \to \infty, \tag{3.230}$$

and for the free surface $\hat{h}_0(\hat{r},t)$, by the kinematic boundary condition (3.189) on the free surface for $\hat{z}=0$, we have

$$\hat{h}_0(\hat{r},t) \sim \frac{1}{2}\hat{r}^2 - t - \frac{G(t)}{\hat{r}^3} \text{ as } \hat{r}\to\infty. \tag{3.231}$$

Recalling that the outer variables are defined by $\hat{r}=r/\epsilon$, $\hat{z}=z/\epsilon$, $\hat{\phi}=\phi/\epsilon$, $\hat{h}=h/\epsilon^2$, then the far-field limits (3.230) and (3.231) motivate defining the outer-outer variables as,

$$\phi = -z+\epsilon^3\Phi, \quad h(r,t) = 1\pm\sqrt{1-r^2} - \epsilon^2 t + \epsilon^5 H_{\pm}(r,t), \quad p=\epsilon P(r,z,t), \tag{3.232}$$

where the $\pm$ in the free surface denotes either the top or bottom half of the droplet, and we have the initial conditions $\Phi(r,z,0)=0$ and $H_{\pm}(r,0)=0$. Interestingly, these perturbations are one order of magnitude smaller than their two-dimensional counterparts in §3.2.6. This is because the velocity potential now has a $3/2$ singularity at the origin, as opposed to a square-root singularity as was the case in §3.2.6.

We then expand $(\Phi,\, H_{\pm},\, P) = (\Phi_0,\, H_{\pm 0},\, P_0) + o(1)$ as $\epsilon\to 0$, which results in the following boundary value problem within the sphere $z=h(r,0)$,

$$\frac{\partial^2\Phi_0}{\partial r^2} + \frac{1}{r}\frac{\partial\Phi_0}{\partial r} + \frac{\partial^2\Phi_0}{\partial z^2} = 0, \qquad \text{for } r^2+(z-1)^2\le 1, \tag{3.233}$$

$$\frac{\partial\Phi_0}{\partial t} = -P_0, \qquad \text{for } r^2+(z-1)^2\le 1, \tag{3.234}$$

$$\Phi_0 = 0, \qquad \text{for } r^2+(z-1)^2 = 1, \tag{3.235}$$

$$\frac{\partial H_{\pm 0}}{\partial t} \mp \frac{r}{\sqrt{1-r^2}}\frac{\partial\Phi_0}{\partial r} - \frac{\partial\Phi_0}{\partial z} = 0, \qquad \text{for } r^2+(z-1)^2 = 1, \tag{3.236}$$

$$\tag{3.237}$$

with the matching conditions

$$\Phi_0 \sim -\frac{\dot{G}(t)z}{(r^2+z^2)^{3/2}} \text{ as } r^2+z^2\to 0, \quad H_{-0}\sim -\frac{G(t)}{r^3} \text{ as } r\to 0. \tag{3.238}$$

We observe that Φ_0 has a unique solution given by

$$\Phi_0(r,z,t) = \frac{\dot{G}(t)(r^2+(z-1)^2-1)}{2(r^2+z^2)^{3/2}}, \tag{3.239}$$

which can readily be verified satisfies Laplace's equation (3.233). The radial and vertical velocities are hence given by $u\sim\epsilon^3 U_0$, $v\sim -1+\epsilon^3 V_0$, where

$$U_0 = \frac{\partial\Phi_0}{\partial r} = -\frac{\dot{G}(t)r(r^2+z^2-6z)}{2(r^2+z^2)^{5/2}}, \tag{3.240}$$

$$V_0 = \frac{\partial\Phi_0}{\partial z} = -\frac{\dot{G}(t)\left(r^2(z+2)+(z-4)z^2\right)}{2\left(r^2+z^2\right)^{5/2}}. \tag{3.241}$$

Substituting U_0 and V_0 into the leading-order kinematic boundary condition on the free surface (3.236), and integrating with respect to t results in the free surface location given by

$$H_{\pm 0}(r,t) = \pm \frac{G(t)}{2\sqrt{2}\sqrt{1-r^2}\left(1 \pm \sqrt{1-r^2}\right)^{3/2}}. \tag{3.242}$$

Finally, the leading-order Bernoulli's equation (3.234) gives the solution for the pressure

$$P_0(r,z,t) = -\frac{\partial \Phi_0}{\partial t} = \frac{\ddot{G}(t)(1-r^2-(z-1)^2)}{2(r^2+z^2)^{3/2}}. \tag{3.243}$$

Given that $G(t) = 4d_0(t)^5/45$, and that $d_0(t) = \sqrt{3(t-w_0(t))}$, we can see that the displacement of the substrate acts to decrease the velocity and free surface perturbations, and the pressure, in the outer-outer regions.

The leading-order pressure in the outer-outer region, ϵP_0, from (3.243) is shown in Figure 3.23 at time $t = 0.5$, where the stationary substrate case is shown for $r < 0$ and the moving substrate case for $r > 0$. By comparing to the two-dimensional case in Figure 3.13, we can see how the pressure decays away from the point of contact much faster in the axisymmetric case, as now we have stronger 3/2 singularity at the origin in the pressure as opposed to the square-root singularity that we had in two-dimensions. Due to the downwards acceleration of the substrate at $t = 0.5$, we can see how the pressure in the moving substrate case is lower than the stationary substrate case, as expected.

3.3.6 Pressure on the substrate

As in the two-dimensional case, to find the hydrodynamic force required for solving (2.33), we need to find the solution for the pressure on the substrate, which here we derive in each relevant asymptotic region as well as deriving an additive composite expansion.

Recall from (3.211) that in the outer region, the leading-order pressure is given by $\hat{p}_0 = -\partial^2 \Upsilon_0/\partial t^2$. Given the solution for Υ_0 on the contact set (3.214), the leading-order outer pressure on the substrate is given by

$$\begin{aligned} \hat{p}_0(\hat{r},0,t) &= \frac{4}{9\pi}\frac{\mathrm{d}^2}{\mathrm{d}t^2}\left[(d_0(t)^2-\hat{r}^2)^{3/2}\right] \\ &= \frac{4}{3\pi}\frac{\dot{d}_0(t)^2\left(2d_0(t)^2-\hat{r}^2\right)+d_0(t)\ddot{d}_0(t)(d_0(t)^2-\hat{r}^2)}{\sqrt{d_0(t)^2-\hat{r}^2}}, \end{aligned} \tag{3.244}$$

where we note that the pressure has a square-root singularity at the turnover curve $\hat{r} = d_0(t)$, which is also present in the two-dimensional solution (3.151).

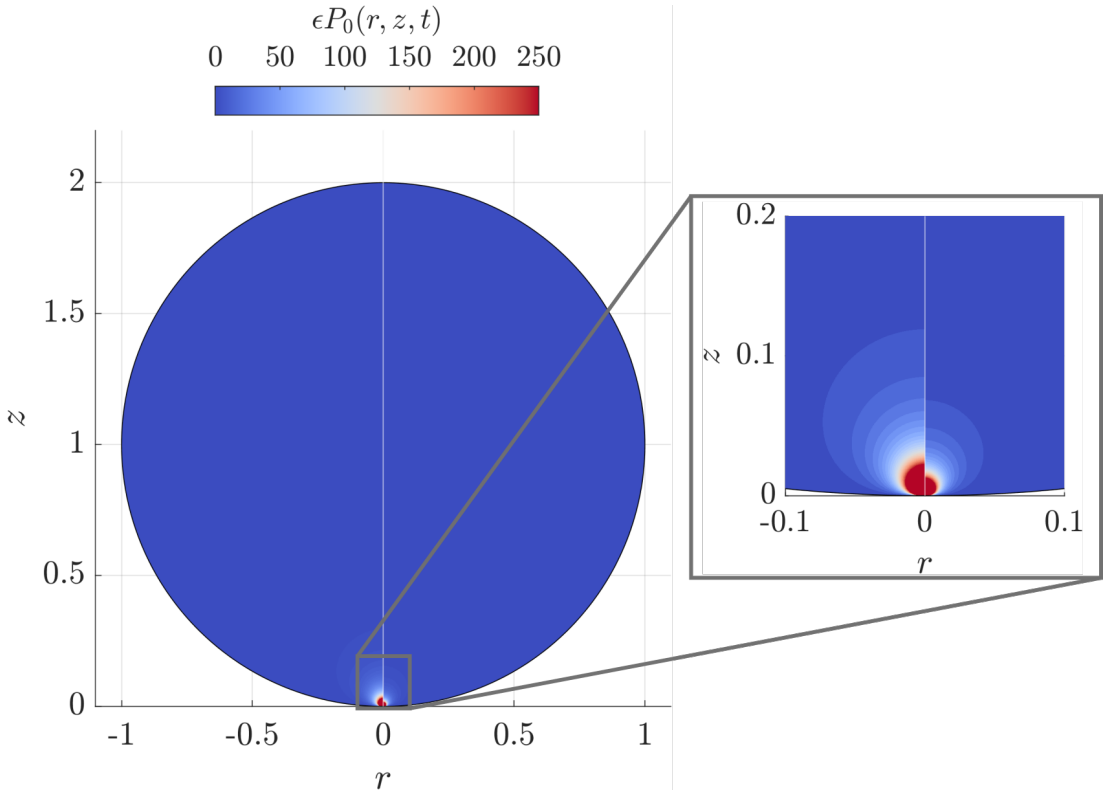

Figure 3.23: Leading-order solution for the pressure in the outer-outer region (3.243), where the stationary substrate case is plotted for $r < 0$ and the curved moving substrate case for $r > 0$. The inset shows the pressure singularity close to the origin.

We found in §3.3.3 and §3.3.4 that the inner and splash-sheet regions are quasi-two-dimensional. This means that the leading-order pressure on the substrate in these two regions will be identical to the two-dimensional case in §3.2.7, replacing $\tilde{x}$ with $\tilde{r}$ in (3.92) and $\bar{x}$ with $\bar{r}$ in (3.153). Again, the outer-outer region does not touch the substrate so we do not have a contribution from there.

By the same argument as §3.2.7, we find pressure is dominated by the outer and inner regions, and is negligible in the splash sheet by comparison. This motivates us to derive an additive composite expansion based on the outer and inner regions using an intermediate variable technique. Following from the matching conducted in §3.3.3.1, here choosing $\alpha = 1/2$, we define an intermediate variable $\hat{r} = d(t) + \epsilon^{1/2}R$. Substituting this into the leading-order solution for the pressure in the outer region (3.244) and expanding for $\epsilon \to 0$ with $R = O(1)$ gives,

$$\hat{p}_0(d(t) + \epsilon^{1/2}R, 0, t) = \frac{2\sqrt{2}d_0(t)^{3/2}\dot{d}_0(t)^2}{3\pi\epsilon^{1/4}\sqrt{-R}} + O(\epsilon^{1/4}),$$

where $R < 0$. We then define the overlap pressure by expressing the expansion in the

$O(1)$ variables and retaining the leading-order term, so that

$$p_{\text{overlap}}(r,t) = \frac{2\sqrt{2}d_0(t)^{3/2}\dot{d}_0(t)^2}{3\pi\sqrt{\epsilon}\sqrt{\epsilon d_0(t) - r}} \text{ for } 0 \le r < \epsilon d_0(t). \tag{3.245}$$

Therefore an additive composite solution for the pressure along the substrate is given by

$$\begin{aligned} p_{\text{comp}}(r,t) = H(\epsilon d_0(t) - r)\left[\frac{1}{\epsilon}\hat{p}_0(r/\epsilon, 0, t) - p_{\text{overlap}}(r,t)\right] \\ + \frac{1}{\epsilon^2}\tilde{p}_0(r/\epsilon^3 - d_0(t)/\epsilon^2, 0, t), \end{aligned} \tag{3.246}$$

where H is the Heaviside step function; and $\hat{p}_0$, $\tilde{p}_0$ and p_{overlap} are defined by (3.244), (3.152) and (3.246) respectively. As the outer pressure in both the two-dimensional and axisymmetric cases have square-root singularities at the turnover point/curve, the composite pressure $p_{\text{comp}}(r,t)$ looks similar to its two-dimensional counterpart shown in Figure 3.14. In a similar fashion to Figure 3.15, in Figure 3.24 we show the evolution of the composite pressure $p_{\text{comp}}(r,t)$ with solid lines, plotted with equal temporal spacing from $t = 0.05$ to 1. The dashed lines show the evolution of the maximum pressure, given by (3.93) (which we again plot for t beyond 1 for visual clarity). As expected, we can see how the pressure on moving substrate is substantially lower than the stationary substrate case.

3.3.7 Force on the substrate

In the axisymmetric coordinate system, the force on the substrate (2.35) is given by

$$F(t) = 2\pi \int_0^L rp(r, -\epsilon^2 w(t), t)\,\mathrm{d}r\,, \tag{3.247}$$

where the 2π factor accounts for the angular integral and we again assume that $L \gg \epsilon$. The outer, inner and jet regions all contain the surface of the substrate, so the pressure in these three regions contribute to the total force on the substrate.

Due to the presence of the r-term in the integral, the contribution from the outer region in this case will be $O(\epsilon)$, with an $O(\epsilon^2)$ contribution from the inner region and an even smaller $O(\epsilon^3)$ contribution from the splash sheet. Given this, the leading-order solution for the force $F(t) \sim \epsilon F_0(t)$ is again given by integrating the pressure along the outer region such that

$$\begin{aligned} F_0(t) &= 2\pi \int_0^{d_0(t)} \hat{r}\hat{p}_0(\hat{r}, 0, t)\,\mathrm{d}\hat{r} = \frac{8}{9}\int_0^{d_0(t)} \hat{r}\frac{\mathrm{d}^2}{\mathrm{d}t^2}\left[(d_0(t)^2 - \hat{r}^2)^{3/2}\right]\mathrm{d}\hat{r} \\ &= \frac{8}{45}\frac{\mathrm{d}^2}{\mathrm{d}t^2}\left(d_0(t)^5\right) = \frac{8}{9}d_0(t)^3\left(d_0(t)\ddot{d}_0(t) + 4\dot{d}_0(t)^2\right), \end{aligned} \tag{3.248}$$

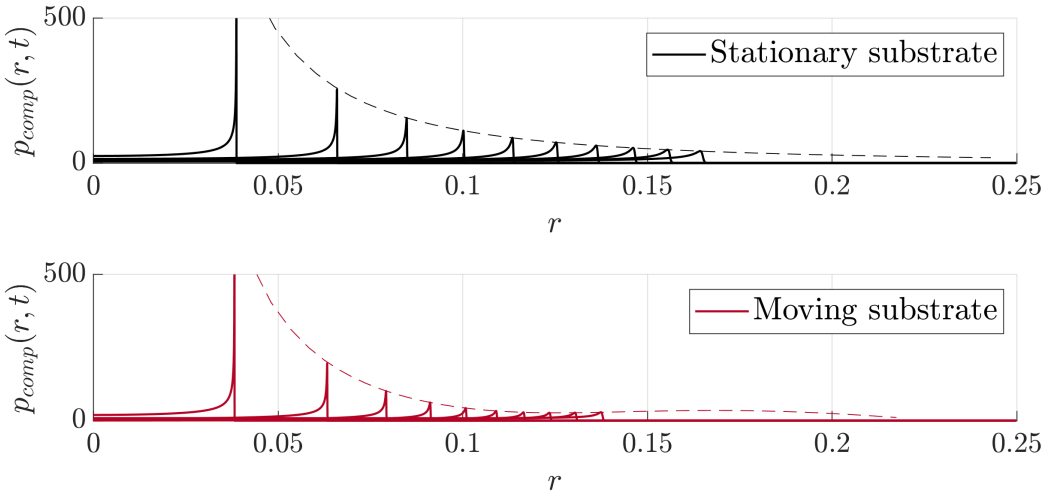

Figure 3.24: Temporal evolution of the composite pressure on the substrate $p_{\text{comp}}(x,t)$ (3.246), plotted with solid lines in equal intervals from $t = 0.05$ to 1. The dashed lines plot the evolution of the maximum pressure given by (3.93).

where $\hat{p}_0(\hat{r},0,t)$ is given by (3.244). As long as $\ddot{w}_0(0)$ is finite, we hence find that $F_0(0) = 0$. This is in contrast to the two-dimensional case, where we found $F_0(0) = 2\pi$. This difference is accounted for by the presence of the $\hat{r}$-term force integral in the axisymmetric setting.

While this gives the leading-order force, similar to the analysis conducted for the two-dimensional case in §3.2.8, we will also directly integrate the composite expansion for the pressure, $p_{\text{comp}}(r,t)$, to find what we refer to as the composite force, $F_{\text{comp}}(t)$. As this is an additive composite expansion, we can consider the contributions from each term of the expansion separately, and sum their contributions at the end, having already found the outer contribution to be $\epsilon F_0(t)$.

As the inner region is quasi-two-dimensional, the solution for the pressure along the substrate (3.152) is parameterised by the same parameter σ as was considered in the two-dimensional case. Hence we again define $c(t)$ such that $r = \epsilon d_0(t) + \epsilon^3 \tilde{r} = 0$ when $\sigma = -\log(c(t))$, which is given implicitly by (3.159). The contribution from the inner term is therefore

$$\begin{aligned} F_{\text{inner}}(t) &= 2\pi\epsilon^3 \int_{-d_0(t)/\epsilon^3}^{\infty} (\epsilon d_0(t) + \epsilon^3 \tilde{r}) \frac{1}{\epsilon^2} \tilde{p}_0(\tilde{r}/\epsilon^3 - \epsilon d_0(t), 0, t)\, \mathrm{d}\tilde{r} \\ &= \frac{8\epsilon^4 \dot{d}_0(t)^2 J(t)^2 c(t)}{\pi} \left[\frac{\pi d_0(t)}{\epsilon^2 J(t)} - \frac{1}{3} c(t)^2 - 2c(t) - 2\log(c(t)) + 1 \right], \end{aligned} \tag{3.249}$$

where in practice, (3.159) has to be solved numerically to find $c(t)$. Lastly, the

contribution from the overlap pressure, $p_{\text{overlap}}(r,t)$, given by (3.245), is

$$\begin{aligned} F_{\text{overlap}}(t) &= 2\pi \int_0^{\epsilon d_0(t)} r p_{\text{overlap}}(r,t)\,\mathrm{d}r = 2\pi\epsilon \int_0^{d_0(t)} \frac{2\sqrt{2}d_0(t)^{3/2}\dot{d}_0(t)^2\hat{r}}{3\pi\sqrt{d_0(t)-\hat{r}}}\,\mathrm{d}\hat{r} \\ &= \frac{16\sqrt{2}}{9}\epsilon d_0(t)^3\dot{d}_0(t)^2. \end{aligned} \tag{3.250}$$

Therefore, combining (3.248), (3.249) and (3.250), the composite force is given by

$$\begin{aligned} F_{\text{comp}}(t) = \frac{8}{9}\epsilon d_0(t)^3 &\left(d_0(t)\ddot{d}_0(t) + (4-2\sqrt{2})\dot{d}_0(t)^2\right) \\ &+ \frac{8\epsilon^4\dot{d}_0(t)^2J(t)^2c(t)}{\pi}\left[\frac{\pi d_0(t)}{\epsilon^2 J(t)} - \frac{1}{3}c(t)^2 - 4c(t) - 2\log(c(t)) + 1\right]. \end{aligned} \tag{3.251}$$

Note again that $F_{\text{comp}}(t)$ is not an asymptotic expansion for $F(t)$, but the result of directly integrating the composite pressure across the substrate. This means that if we expand $F_{\text{comp}}(t)$ to leading-order as $\epsilon \to 0$ then we should be left with $\epsilon F_0(t)$. As was conducted in the two-dimensional case, expanding $c(t) \sim c_0(t)$ we expand $c(t) \sim c_0(t)$, where $c_0(t)$ is given by (3.163). Given this, we expand $F_{\text{inner}}(t)$ to leading-order, finding

$$\begin{aligned} F_{\text{inner}}(t) &\sim \frac{8\epsilon^4\dot{d}_0(t)^2J(t)^2}{\pi}\cdot\frac{2}{3\epsilon^3}\left(\frac{\pi d_0(t)}{J(t)}\right)^{3/2} = \frac{16\epsilon\dot{d}_0(t)^2d_0(t)^{3/2}\sqrt{\pi J(t)}}{3} \\ &= \frac{16\sqrt{2}}{9}\epsilon d_0(t)^3\dot{d}_0(t)^2, \end{aligned}$$

where we substituted the solution for $J(t)$ from (3.218). This means that $F_{\text{inner}}(t) \sim F_{\text{overlap}}(t)$ as $\epsilon \to 0$, and we confirm that $F_{\text{comp}}(t) \sim \epsilon F_0(t)$ as $\epsilon \to 0$.

As we will see in later chapters, as in the two-dimensional case, we find that the composite force $F_{\text{comp}}(t)$ agrees more favourably with numerical simulations for intermediate times than the leading-order solution $F_0(t)$.

In Figure 3.25, we show the force for the two imposed substrate cases, where the dashed lines denote the leading-order force $F_0(t)$ and the solid lines denote the composite force $F_{\text{comp}}(t)$. We see here that the force on the substrate in the axisymmetric case is significantly different to the two-dimensional case shown in Figure 3.16. In particular, both the leading-order force $F_0(t)$ and composite force $F_{\text{comp}}(t)$ are initially zero, and grow in time. In constrast, the leading-order force in the two-dimensional case for the stationary substrate was equal to 2π for all time. For the moving substrate case, we can see again how the motion of the substrate significantly affects the evolution of the force curve.

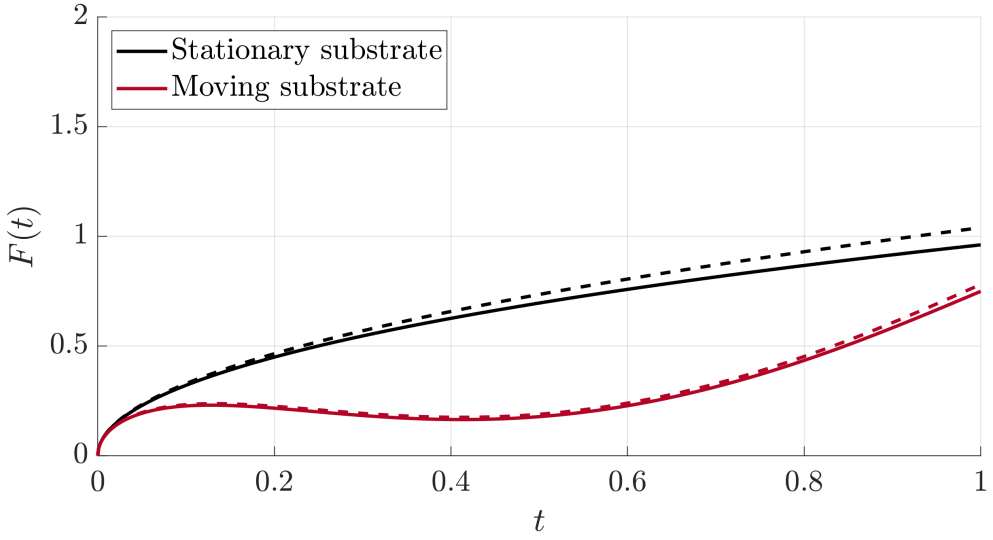

Figure 3.25: Solutions for the force on the substrate. The dashed lines show the leading-order force $F_0(t)$ (3.248), while the solid lines show the composite force $F_{\text{comp}}(t)$ (3.251).

3.3.8 Energy distribution

We return again to studying the distribution of kinetic energy, $E_K^*(t^*) = \rho_l^* R_d^{*3} V^{*2} E_K(t)$, throughout the droplet. As in §3.2.9, we transform the problem into a frame moving upwards at the initial droplet speed, denoting the moving frame variables with a $'$, giving

$$r = r', \quad z = z' - \epsilon^2 t, \quad (u,\, v) = (u', v' - 1), \quad \phi = \phi' - z' + \epsilon^2 t. \tag{3.252}$$

In this axisymmetric case, the kinetic energy within a region Γ is given by

$$E_{K,\Gamma}(t) = 2\pi \iint_\Gamma \frac{1}{2} |\boldsymbol{\nabla}\phi'|^2 r' \,\mathrm{d}r' \,\mathrm{d}z' = \pi \oint_{\partial\Gamma} \phi' \boldsymbol{\nabla}\phi' \cdot \hat{\mathbf{n}} \,\mathrm{d}S\,, \tag{3.253}$$

where for the second equality we applied Green's first identity, with $\partial\Gamma$ being the boundary of Γ, $\hat{\mathbf{n}}$ the outward unit normal for $\partial\Gamma$ and $\mathrm{d}S$ the surface element.

By a similar argument to the two-dimensional case, for the outer region we consider a region in the $(\hat{r}, \hat{z})$ plane bounded by a quarter circle region radius R, centred on the origin. This means $\partial\Gamma$ is the union of the quarter-circle arc of radius R, and two lines of length R along the $\hat{r}$ and $\hat{z}$ axes respectively. Given the far-field expansion of $\hat{\phi}_0$ from (3.230), for any fixed ϵ, we know that $\phi' = O(1/R^2)$ and $\boldsymbol{\nabla}\phi' \cdot \hat{\mathbf{n}} = O(1/R^3)$ as $R \to \infty$, meaning the contribution from the quarter-circle is $O(1/R^4)$. Along the vertical line on the $\hat{z}$ axis from $\hat{z} = 0$ to $\hat{z} = R$, we have that $\boldsymbol{\nabla}\phi' \cdot \hat{\mathbf{n}} = 0$ by symmetry,

so this line does not contribute to the kinetic energy. Along the $\hat{r}$ axis, we have that $\hat{\phi}_0 = 0$ for $\hat{r} > d_0(t)$, and for $\hat{r} < d_0(t)$ we have from (3.215) that

$$\phi' = \epsilon\hat{\phi}_0 + O(\epsilon^2) = -\frac{4\epsilon d_0(t)\dot{d}_0(t)}{3\pi}\sqrt{d_0(t)^2 - \hat{r}^2} + O(\epsilon^2),$$

and from the kinematic boundary condition (3.188) we have

$$\boldsymbol{\nabla}\phi' \cdot \hat{\mathbf{n}} = -\left(1 - \dot{w}_0(t)\right) + O(\epsilon).$$

Therefore as we take the radius of the quarter-circle $R \to \infty$, it follows that the leading-order solution for the kinetic energy in the outer region is given by

$$\begin{aligned} E_{K,\text{outer}}(t) &= \frac{4\epsilon^3 d_0(t)\dot{d}_0(t)}{3}(1 - \dot{w}_0(t))\int_0^{d_0(t)} \hat{r}\sqrt{d_0(t)^2 - \hat{r}^2}\,\mathrm{d}\hat{r} + O(\epsilon^4) \\ &= \frac{4\epsilon^3}{9} d_0(t)^4 \dot{d}_0(t)(1 - \dot{w}_0(t)) + O(\epsilon^4). \end{aligned} \tag{3.254}$$

The solution for the inner region in §3.3.3 was found to be quasi-two-dimensional, and thus by a similar argument for the two-dimensional energy in §3.2.9, we find that the kinetic energy in the inner region is asymptotically smaller than in the outer.

Given that the inner solutions are quasi-two-dimensional, to find the flux of energy entering the splash sheet $Q(t)$, we need to multiply the two-dimensional energy flux (3.169) about the circumference of the turnover curve at $r = \epsilon d(t)$, such that

$$Q(t) = 4\pi\epsilon d_0(t)\dot{d}_0(t)^3 J(t) + O(\epsilon^2),$$

By integrating the flux (taking into account the ϵ^2 time scaling), and using the solution for $J(t)$ from (3.218), we have the kinetic energy in the splash sheet to be

$$E_{K,\text{splash-sheet}}(t) = \frac{8}{9}\epsilon^3 \int_0^t d_0(\tau)^4 \dot{d}_0(t)^3\,\mathrm{d}\tau + O(\epsilon^4). \tag{3.255}$$

Finally for the outer-outer region, we have $(u', v') = O(\epsilon^3)$ across a region with an $O(1)$ volume, meaning $E_{K,\text{outer-outer}}(t) = O(\epsilon^6)$ and is hence negligible compared to the contributions from the outer and splash sheet regions. Therefore, to leading-order, the kinetic energy is transferred into the outer and splash-sheet regions, giving a total kinetic energy from (3.254) and (3.255) to be

$$E_{K,\text{droplet}}(t) = \frac{4\epsilon^3}{9}\left[d_0(t)^4\dot{d}_0(t)(1 - \dot{w}_0(t)) + 2\int_0^t d_0(\tau)^4\dot{d}_0(t)^3\,\mathrm{d}\tau\right] + O(\epsilon^4). \tag{3.256}$$

For the case of a stationary substrate, where $w(t) = 0$ and $d_0(t) = \sqrt{3t}$ from (3.204), it follows that

$$E_{K,\text{outer}}(t) = 2\sqrt{3}\epsilon^3 t^{3/2} + O(\epsilon^4), \tag{3.257}$$

$$E_{K,\text{splash-sheet}}(t) = 3\sqrt{3}\epsilon^3 \int_0^t \sqrt{\tau}\,\mathrm{d}\tau + O(\epsilon^4) = 2\sqrt{3}\epsilon^3 t^{3/2} + O(\epsilon^4). \tag{3.258}$$

As with the two-dimensional scenario, we have that in the stationary substrate case, that half of the kinetic energy of the droplet is distributed into the splash-sheet and the other half is within the outer region. However in the two-dimensional case, the kinetic energies grew linearly in time, whereas for this axisymmetric case, we have a $t^{3/2}$ time-dependence.

In Figure 3.26, we plot the kinetic energy in the outer region $E_{K,\text{outer}}(t)$ with solid lines and the kinetic energy in the splash sheet $E_{K,\text{jets}}(t)$ with dashed lines. As discussed above, we can see how the energies in the stationary case are equal, with variation between the two regions clear in the moving substrate case.

3.3.9 Summary

In this section, we have applied Wagner theory to the impact of a three-dimensional, axisymmetric droplet onto a flat substrate that can move in the vertical direction. Although the substrate is less general than that considered in §3.2, the three-dimensional hydrodynamic model is more directly applicable to real-world scenarios than its two-dimensional counterpart. We identified a number of key differences between the axisymmetric and two-dimensional solutions. One was that the outer-outer region experiences perturbations of a smaller asymptotic order, due to a stronger singularity in the pressure from the outer region. We also found how the force on the substrate follows a substantially different trend compared to the two-dimensional case, which will mean we can expect the solutions for the substrate position in the spring-supported plate case to differ. Finally, we found that the kinetic energy in the droplet grows with a $t^{3/2}$ time dependency, as opposed to linearly in two-dimensions.

3.4 Conclusion

In this chapter we have presented an analytical framework to study droplet impact onto deformable substrates, both in two-dimensional and an axisymmetric setting, by employing inviscid Wagner theory. We found that the problem breaks down into four distinct asymptotic regions during this time, in which we resolved the velocity,

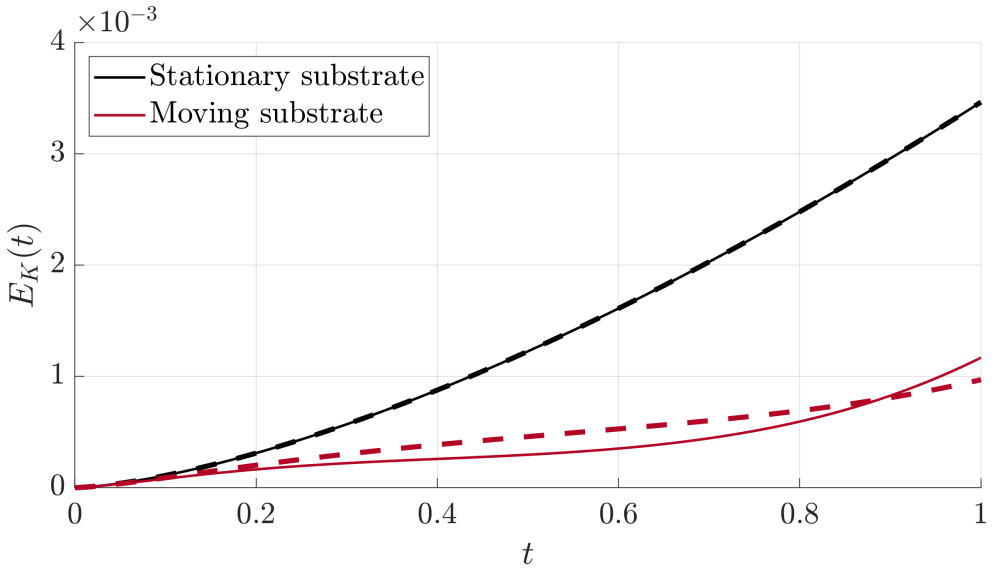

Figure 3.26: Evolution of the kinetic energy in the droplet against time,, where the solid lines denote the kinetic energy in the outer region (3.254) and the dashed lines denote the energy in the splash sheet (3.255).

free surface and pressure in each individually, as well as constructing a composite expansion for the pressure on the substrate between the outer and inner regions. As well as this, we also found the leading-order solutions for the force on the substrate, which will be used in Chapter 5 to find the solution for the spring supported plate, as well as analysing the distribution of kinetic energy throughout the droplet.

The model allows us to quantitatively understand the effect the substrate deformation have on the dynamics of the droplet. We found how the spreading of the droplet upon impact can be slowed or accelerated due to the motion of the substrate, both due to its velocity and curvature. The amount of fluid that is transferred into the resulting jets/splash sheet that emanate across the substrate is also substantially affected by the substrate motion, which at later times may determine whether these break up into a splash (and could be verified with fully three-dimensional simulations). We found that the distribution of pressure throughout the droplet can be significantly affected by the substrate motion, which will ultimately play an important role in determining the fluid-structure interaction between the droplet and the substrate in Chapters 5 and 6. Finally, we have quantified how the distribution of kinetic energy throughout the droplet is changed when the substrate deforms, in particular how much energy is transferred into the jets/splash sheet. As discussed by Howland et al. (2016) [46], understanding this energy distribution at early times is key in understanding the resulting splash suppression mechanism that they observed.

This is an effect that is currently out of reach of experimental measurement, and we will discuss in later chapters the evolution of this energy distribution once we model the fluid-structure interaction.

This analytical model relies on a number of assumptions in addition to those laid out in Chapter 2, specifically, we assumed the influence of the viscosity, surface tension, gravity and the surrounding gas were negligible to leading-order. We also focused on finding leading-order asymptotic expansions in time, where we let $\epsilon \to 0$ for $t^* = (\epsilon^2 R_d^*/V^*)t$. Because of these assumptions, we simplified the governing equations, and it allowing us to find analytical solutions that would have been impossible otherwise. However, we do know that these neglected effects can have an important role to play in certain regimes. As observed by Thoroddsen (2003) [90], in high velocity droplet impact experiments, a bubble of air can become entrapped inside the bubble as it impacts, due to the small dimpling of the bottom of the droplet as the air pressure below becomes higher. This of course would alter the early time dynamics that we have discussed here, and in particular, how the droplet would no longer make contact at the centre of the substrate. This pre-impact air cushioning effect has been widely studied [38, 39, 63], and it is possible to incorporate it into the Wagner model we have presented here. The surrounding air is also the key mechanism into how the droplet splashes at later times, so in order to develop a full model of splashing, the air must be incorporated.

Within the framework of the analytical model alone, it is impossible to validate our assumptions that these effects can be neglected, as this requires solving the full governing equations and comparing to our asymptotic approximations. To this end, in the next chapter we will present an alternative approach to modelling this system using direct numerical simulations. These will solve the full set of governing equations presented in Chapter 2, and allow us to validate the analytical model and assess the effects of the physical processes we neglected. In addition, these direct numerical simulations will allow us to study intermediate timescales that are out of reach of the analytical model (i.e. where $\epsilon = O(1)$). These simulations are extremely computationally expensive in comparison to the analytical model presented here, so conducting this cross-validation will allow us to understand when the analytical model can be accurately used as a cheaper alternative to direct numerical simulations.

Chapter 4

Direct numerical simulations

The analytical model derived in the previous chapter relied on a series of assumptions about the physical processes of the system, neglecting the influence of the viscous forces, surface tension, gravity and the surrounding gas, and only retaining the terms due to the inertia of the liquid. These assumptions were based on a scaling analysis to find the dominant contributions to the governing equations, however it is impossible to then assess the effects these neglected features would have on the flow within the framework of the analytical model. In addition, we made leading-order asymptotic expansions to study the early times of the impact, meaning the higher-order terms in the expansions that were neglected would become significant at later times, limiting the temporal scope of the model. There are two options for assessing the validity of the assumptions made by the analytical model. The first is to compare to real-world experiments, which is ultimately one of the eventual aims of any mathematical modelling process. Although this is possible to a certain extent, the fast time and small spatial length scales of droplet impact problems mean experimental studies for these physical processes are still limited. With high-speed imaging techniques, the interface of the droplet can be tracked in time in order to validate quantities such as the turnover curve and free-surface location, as was conducted by Howland et al. (2016) [46]. However imaging the emergence of the turnover curve at the time scales where the analytical model is valid is a significant challenge. To measure the velocity distribution inside the droplet would involve placing either markers or dyes inside the fluid, which is practical for larger scale experiments, but significantly more complex for millimetric droplets. Unfortunately, there is currently no feasible way to measure the pressure inside the droplet. Although pressure sensors could in theory be placed on the substrate to produce measurements in the respective regions, it would be practically difficult to get readings from multiple points along it to find the pressure

distribution. Lastly, the two-dimensional analytical model has no clear real-world analogue that would be appropriate to compare results to for this purpose.

As the analytical model is derived by neglecting terms in the governing equations presented in Chapter 2, a second validation option is to compare the predictions of the analytical model to numerical solutions found by solving the full Navier-Stokes equations. The advantage of doing this is clear, as it would provide full solutions for the velocity, pressure and interface location throughout the system which can be directly compared to the corresponding values from the analytical model. Of course, the Navier-Stokes equations are a notoriously difficult set of non-linear partial differential equations to solve, and for the best part of the last century this has only been possible in certain idealised situations. However, the exponential increase in computing power over the last few decades, alongside significant research in algorithmic design, have allowed finding numerical solutions for the full Navier-Stokes equations a reality. For our specific application, we are interested in direct numerical simulations (DNS) for gas-liquid multiphase flow problems. Although some authors refer to DNS as simulations that fully resolve turbulent flow, we take the definition of of DNS to be that of Trggvason et al. (2011) [91], which are "*simulations of unsteady flow containing a non-trivial range of scales, where the governing equations are solved using sufficiently fine grids so that all continuum time- and length-scales are fully resolved*". By carrying out DNS, we provide a thorough cross-validation case to assess the regimes of validity of the analytical model which otherwise would not be possible without advanced experimental setups.

Besides their capacity to cross-validate the analytical model, the DNS also allow us to study longer timescales out of reach of the analytical model. As discussed in Chapter 3, the basis of the analytical model was to study the early times of impact, where the bulk of the droplet continues to fall unaffected by the substrate, and deformations in the liquid-gas interface are only significant near the point of contact. We hence expect the analytical model to break down at more intermediate timescales once the entire droplet has begun to deform due to the impact. The DNS allow us to study an indefinite timescale of the impact process, limited only by time and computational resources. In addition, the analytical model is split into four distinct asymptotic regions, such that deriving global composite solutions for the entire domain would be a substantial mathematical undertaking. For the DNS, we solve for the dynamics of the entire system at once, including the interaction between the liquid and gas over multiple length scales.

The trade-off with conducting DNS is that it typically requires a substantial amount of computational resources to resolve the system at the required time- and length-scales, which is particularly acute in droplet impact systems where there are multi-scale features that evolve at vastly different time-scales. As a numerical method, to infer the effects varying different parameters have hence requires running a large number of individual simulations, which further adds to their cost. This is a stark contrast to analytical models where often these trends can either be evaluated exactly from a formula, or solved numerically as part of a system with much fewer degrees of freedom than full DNS.

In this chapter, we will detail the methodology we have adopted to conduct DNS to model droplet impact onto deformable substrates. We start by reviewing the current available numerical methods for conducting DNS of two-phase flow systems. We then provide a brief overview the general framework we choose to conduct these, namely the *Basilisk* (http://basilisk.fr/) volume-of-fluid solver, and lead on to detailing the specific implementation we use for our simulations. We then perform an extensive validation study for our implementation to ensure the accuracy and robustness of the numerical scheme. We finally summarise and lay out how the DNS will be used in the later chapters to model two specific cases of deformable substrates.

4.1 Numerical methods for two-phase flows

The earliest examples of computational fluid dynamics (CFD) date back to the 1930's [87], relying on neglecting terms and linearising the Navier-Stokes equations to yield the linearised potential flow equations (much like the analytical model in Chapter 3). It was not until the marker-and-cell (MAC) method was developed by Harlow and Wench (1965) [35] that numerical solutions for the full Navier-Stokes equations in two-phase flow were first executed. Since then, alongside the significant rise in the power of computing, various numerical methods for simulating two-phase flows have emerged. Particularly in the last decade, simulating three-dimensional, two-phase, multi-scale flows is now a common practice that would have been far out of the reach of the early practitioners of CFD.

For the purposes of this thesis, we define two-phase flow systems to be those where the two fluid phases are immiscible, as opposed to multiphase systems where mixing can occur. The main additional challenge two-phase flow modelling presents lies in accurately resolving the interface where the two fluid phases meet. In the analytical model, we neglected the stresses along the interface, resulting in what is known as

a free surface. However for the DNS, we retain the normal stresses due to surface tension, so thus for the context of the DNS, we will not refer to the interface as a free surface. The flow needs to satisfy boundary conditions, such as continuity of velocities and stresses along the interface, whose location in turn needs to be solved for as part of the problem. Typically, the discontinuity of the density and viscosity of the two fluid phases across the interface has been a limiting factor when conducting two-phase flow simulations, which is a problem for simulating cases ubiquitous in nature such as water-air systems.

In recent years, many distinct methods have been developed for simulating two-phase flows. For the purposes of our specific application of droplet impact, the method of choice at the very least must fulfil the following requirements:

1. The method must be able to resolve a rapidly changing interface with multi-scale features. As we saw in Chapter 3, these droplet impact systems exhibit rapid topological changes at the early times of impact, with regions of high curvature on a much smaller length scale to the bulk of the droplet that evolve rapidly.

2. The two-phase systems we are interested in (e.g. water-air) have a high contrast in density and viscosity between the phases, and the method of choice must be able to handle the large jumps in these fluid properties across the interface.

3. As the size of the droplets is typically on a millimetric scale, we expect surface tension to be an important factor in the dynamics, at least at intermediate times once the early stages considered by the analytical model have passed. Hence the method needs to accurately determine the surface tension forces along the interface, which requires knowing the normal and curvature of the interface to high-resolution.

Fulfilling any one of these requirements is a considerable task to overcome when developing a numerical method for two-phase flow, and it is only in recent years that the research area has matured enough that multiple methods exist that can satisfy at least some of these requirements. In the following, we will briefly review the existing numerical methods for simulating two-phase flow, and weigh up their features in order to determine the most appropriate method for our study. For more comprehensive reviews on the topic, we refer the reader to Scardovelli and Zaleski (1999) [80] and Tryggvason et al. (2011) [91].

One of the main distinctions between methods is whether they consider the interface as sharp (i.e. an infinitesimally thin boundary between the two phases), or diffuse (i.e. spanning a finite width with mixing of phases between). The diffuse interface approach seeks to reflect the fact that, at the molecular scale, the interface is not sharp and molecules can diffuse between the two phases. These diffuse interfaces are well described using phase separation models, based on the Cahn-Hilliard or Allen-Cahn equations [1]. In contrast, sharp interface methods assume the length scale of the problem is large enough the size of the diffuse interface is comparatively small, justifying approximating the interface with an infinitesimal line. For our purposes, we assume that the diffuse width of the interface is small enough compared to the length scale of the droplet that a sharp interface model is sufficient to accurately predict the behaviour of the interface, and the interested reader is directed to Anderson et al. (1998) [1] for a review on diffuse interface methods.

Most numerical methods for two-phase flows fall into three categories when considering the spatial discretisation: grid-free, moving-grid and fixed-grid. Grid-free methods involve tracking the trajectories of individual fluid volumes in a Lagrangian frame of reference, negating the need for a discretised Eulerian grid. Popular examples of such methods include particle-in-cell (Harlow (1964) [34]), smoothed-particle-hydrodynamics (Monaghan (1992) [61]) and molecular dynamics simulations [33]. These methods are inherently heavily parallelisable, and recent advances in graphics processing units (GPUs) hardware have made these attractive methods as more particles are able to be simulated than ever before. Although not grid-free, the Lattice-Boltzmann method [13] is another very popular method that, instead of solving the Navier-Stokes equations, relies on simulating the fluid as a system of collision processes based on kinetic theory. However these methods struggle to satisfy the density and viscosity jump conditions across the interface [80], and even at the millimetric scale of droplets, these methods can be prohibitively expensive in comparison to alternative methods which assume the fluids are continuous.

Moving- and fixed-grid methods both rely on a spatial discretisation in an Eulerian frame of reference, and are used to solve the Navier-Stokes equations on this grid. Moving-grid methods are those where the grid moves with the interface, such that there is always a clear divide between the regions occupied by each fluid. The advantage of this is that the Navier-Stokes equations can be solved separately in each region without having to deal with the jump in density or viscosity, which is referred to as a two-fluid formulation. The limiting factor to these methods is how much the interface deforms. As illustrated in Scardovelli and Zaleski (1999) [80], even

relatively small deformations of the interface can result in significant distortions in the computational grid. Typically, the domain will need to regularly be remeshed to respond to these distortions, which is an incredibly costly process computationally. Another disadvantage of moving-grid methods is that topological changes, such as fluid break-up or coalescence, cannot occur naturally. This is because the point of break-up/coalescence is a singularity in the interface, and the grid would have to become infinitesimally refined close to that region in order to resolve the process. Thus moving-grid solvers modelling systems where break-up and coalescence occur have to employ methods to artificially alter the interface close to the point of singularity.

In contrast, fixed-grid methods are those where the underlying grid structure is fixed, commonly with squares and cubes in two- and three-dimensions respectively, although other geometries, such as triangulation, are possible. In these cases, the interface cuts through the grid cells as it moves, hence there is no longer a clear distinction between the two regions of fluid as with moving-grid methods. Because of this, fixed-grid methods typically solve the same global conservation laws across the entire domain, which is referred to as a one-fluid formulation. Note that the "fixed" in fixed-grid refers only to the underlying structure of the orthogonal vectors that make up the grid. Fixed-grids can be adaptively refined during the simulations by equally splitting up cells into smaller cells of the same shape, and in reverse, coarsening groups of small cells into larger ones. The main challenge of fixed-grid methods is ensuring the interface is accurately resolved even as it passes through the different grid cells.

Another distinguishing feature between most methods is whether they are "interface-tracking" or "interface-capturing", and both fixed-grid and moving-grid methods can fall into either of these categories. Interface-tracking algorithms rely on a Lagrangian description of the interface, whilst solving the rest of the flow system on the fixed Eulerian grid. A common interface-tracking technique is the marker-and-cell (MAC) method [35], which involves placing markers on the interface and advecting these with the flow in time. The interface is then found by fitting a high-order polynomial to the marker points, which is a continuous representation of the interface that can be resolved even at sub-grid resolutions. An advantage of interface-tracking techniques is that they provide a natural framework for modelling additional physical processes that occur at the interface, such as the existence of surfactants or electrical charges. However, as noted by Scardovelli and Zaleski (1999) [80], if there are differences in the density and viscosity between the fluids, then there will be scales in the velocity and pressure field much smaller than the grid that will not be well resolved. For this reason, interface tracking techniques perform best when the fluid properties of

each phase are identical, such as when tracking a passive dye inserted into a fluid to visualise the flow. Interface-tracking algorithms are hence often used alongside other interfacial methods for this purpose.

Instead of explicitly tracking the interface, interface-capturing techniques work by introducing a scalar indicator function into the system which denotes which phase any given cell belongs to. The interface is then "captured" (often referred to as reconstructed) using this indicator function. Interface-capturing methods mainly differ by their choice of indicator function, and the two most popular are the level set and volume-of-fluid methods. For a more extensive review of interface capturing methods, see Mirjalili et al. (2017) [59].

Level set methods were popularised by Osher and Sethian (1988) [67] as a method for determining the dynamics of interfaces that appear in a number of different systems. The method is popular not just for CFD applications, but also in computer graphics and image processing. As the name indicates, the method involves defining a level set function $\phi(\mathbf{x}, t)$, which is defined to be the signed distance from the point $\mathbf{x}$ to the closest point on the interface. Subsequently, the curve $\phi = 0$ denotes the location of the interface, where $\phi < 0$ in one fluid and $\phi > 0$ in the other. This makes for a smooth representation of the interface, where the normal $\mathbf{n} = \boldsymbol{\nabla}\phi/|\boldsymbol{\nabla}\phi|$ and the curvature $\kappa = \boldsymbol{\nabla} \cdot \mathbf{n}$ of the interface can be computed to high accuracy, which is essential for determining the surface tension. The level set function is evolved in time by solving an advection equation given by

$$\frac{\partial \phi}{\partial t} + \mathbf{u} \cdot \boldsymbol{\nabla}\phi = 0.$$

Unfortunately, ϕ loses its signed distance property after this advection step, so needs to be re-initialised at each timestep. As detailed by Mirjalili et al. (2017) [59], the most direct approach to re-initialise ϕ is to first determine the interface location at $\phi = 0$, and then find the signed-distance from each other point in the domain to find ϕ everywhere else. However this is a prohibitively expensive process, with complexity $O(N^3)$ for a domain with N cells. Instead, alternative methods are typically adopted to re-initialise ϕ, such as that of Sussman et al. (1994) [86], who proposed a PDE based initialisation. The issue with these alternative methods is that the re-initialisation step typically moves the interface from its original location, resulting in the scheme no longer being mass conserving. Although improvements have since been made to reduce this mass loss, such as that of du Chéné et al. (2008) [23], the simplicity of the level set method is subsequently lost by requiring the use of these

complex re-initialised schemes, and have since become less popular in comparison to the alternatives.

The decline of level set methods in recent years has coincided with the rise of volume-of-fluid methods (VOF). In contrast to level set methods, VOF methods use a scalar field, $c(\mathbf{x}, t)$, such that $c = 1$ for cells in the first fluid, $c = 0$ in the second and $0 < c < 1$ in cells that are cut by the interface. The scalar c is hence referred to as the volume fraction, as it measures the volume of the first fluid that fills a given cell. The volume fraction is then used to define the density and viscosity of a given cell via

$$\rho(c) = \rho_1 c + \rho_2(1 - c),$$
$$\mu(c) = \mu_1 c + \mu_2(1 - c),$$

where ρ_i and μ_i are the density and viscosity of the first ($i = 1$) and second ($i = 2$) fluids. The continuity equation for the density of the fluid hence becomes a continuity equation for c,

$$\frac{\partial c}{\partial t} + \boldsymbol{\nabla} \cdot (c\mathbf{u}) = 0.$$

Because of this, unlike their level set counterparts, VOF methods are inherently mass conserving. This, however, comes at the cost of no longer having a smooth solution for the interface. The volume fraction c alone only indicates how much fluid is in a given cell, which is not sufficient to give a unique solution for the interface location in that cell. Instead, VOF methods have to reconstruct the interface by comparing each cell to its neighbours, and using this to construct the unit normal to the interface. In general, the resulting interface is discontinuous between cells, which poses a significant challenge when determining the curvature of the interface for accurate surface tension calculations.

It is clear that the choice of a particular numerical method involves balancing the respective advantages and disadvantages of said method compared to the alternatives. Motivated by this, hybrid approaches which combine aspects from different methods have been developed in order to mitigate the drawbacks of any one method. A popular hybrid method is the coupled-level set and volume-of-fluid method (CLSVOF) (Sussman & Puckett (2000) [85]). The aim of CLSVOF is to utilise the level set method for accurate computation of normals and curvature whilst using the VOF method to ensure the scheme is mass conserving. This results in a more accurate scheme than using level set or VOF on their own, however this comes at an increase in computational cost due to the additional computations of using both schemes.

As noted by Mirjalili (2017) [59], it is difficult to achieve efficient load-balancing when parallelising CLSVOF schemes due to the presence of operations required for both the VOF and the level set methods. Overall, hybrid methods should be a clear choice over other methods due to their increased accuracy, however the difficulty of implementation and increased computational cost means it is often more practical to accept the disadvantages of the individual methods, and instead devote resources to minimising the effects these have on the output of the simulations.

Implementing any of the aforementioned methods from scratch is a significant software engineering endeavour, requiring a substantial amount of time and effort to produce a package that is both accurate and efficient from a numerical standpoint, as well as ensuring that the code base is resusable and scalable. Because of this, most studies using these methods are carried out by building upon existing software implementations. From the standpoint of a scientific computing practitioner, the choice of which numerical method to use needs to be balanced with the quality of the existing implementations of that method. This choice often comes down to the resources available to the individual. For example, the *COMSOL Multiphysics* package [20] is a popular choice for many practitioners, as it boasts a wealth of different numerical solvers contained within a well maintained graphical user interface. However, the licensing costs of such software are often a prohibitive factor, in particular when one is concerned about the reproducibility of results for the wider research community. In addition, such closed-source software packages can be difficult to customise, which can be a barrier to research that seeks to push the boundaries of existing numerical methods. Because of this, open-source software packages such as *oomph-lib* [37], *OpenFOAM* [47] and *Gerris/Basilisk* [75, 77], are popular amongst research communities, as their accessibility provides fertile ground for collaboration and customisation by directly changing the source code. However a common downside to open-source software packages is that they lack the financial support that commercial software enjoys, often being maintained by users volunteering their spare time, and less commonly by users employed to do so. This often means that developmental progress in the software can be slower and with fewer resources to employ software testers, code bugs are more common. Many open-source packages mitigate this by supporting a wide network of contributors and users who can divide the workload and ensure the code base is well maintained.

Amongst the existing numerical methods and software packages, the VOF implementation in *Basilisk* [77] (the successor to *Gerris* [75]), stands out as a clear choice

to satisfy the aims of our research. *Basilisk* is a free and open-source software package for the solution of partial differential equations, with a specific focus on using the VOF method to solve a wide range of interfacial flow problems. The Navier-Stokes solvers in *Basilisk* are second-order accurate in space and time (including surface tension forces), as well as supporting adaptive mesh refinement and efficient load-balancing for large scale parallelisation. In addition, *Basilisk* has an active global community of both contributors and users, and its success as a software package is supported by over 150 peer-reviewed journal articles that make use of *Basilisk* over the last seven years. *Basilisk* is implemented in the *C* programming language [79], which for the last fifty years has been one of the most popular languages for high-performance computing due to its fast execution speeds, efficient memory allocation and numerous libraries. This makes *Basilisk* scripts heavily customisable and any of the subroutines supported by *C*, such as the *LAPACK* linear algebra package [2], can be utilised. For these reasons, the *Basilisk* VOF solver hence satisfies our earlier detailed requirements for a numerical method, whilst also providing a well established and supported software framework for conducting our DNS. In the following section, we will go into more detail on the VOF implementation in *Basilisk* and how we can utilise it for our purposes.

4.2 The *Basilisk* volume-of-fluid solver

Basilisk was introduced by Popinet (2015) [77], and is built upon its predecessor *Gerris*, which was first presented by Popinet (2003) [75] as a tree-based adaptive solver for the incompressible Euler equations, and was then extended in Popinet (2009) [76] to solve the full Navier-Stokes equations including surface tension. In this section, we provide a brief overview of the implementation of the VOF solver *Basilisk* uses to solve the Navier-Stokes equations with surface tension, summarising the methods detailed in the aforementioned articles and the *Basilisk* website [6], to which the reader is directed for a more comprehensive exposition.

The *Basilisk* framework is flexible enough that the user is free to choose their own non-dimensionalisation. For consistency, in the following discussion on the details of the *Basilisk* VOF solver, we will use the non-dimensionalisation that was presented in Chapter 2. These non-dimensional governing equations were presented in their two-fluid form. However VOF methods solve the one-fluid formulation of the problem, where the separate values for velocity, $\mathbf{u}_i$, and pressure, p_i, in each fluid phase are replaced with global variables, $\mathbf{u}$ and p. In addition, we define a volume fraction c,

such that $c = 1$ in the liquid and $c = 0$ in the gas (referred to as fluid 1 and 2, respectively). Setting the time scaling parameter $\epsilon = 1$, the one-fluid formulation of the governing equations (2.26)-(2.27) are

$$\rho(c)\left(\frac{\partial \mathbf{u}}{\partial t} + (\mathbf{u}\cdot\boldsymbol{\nabla})\mathbf{u}\right) = -\boldsymbol{\nabla}p + \boldsymbol{\nabla}\cdot(2\mu(c)\boldsymbol{D}) + \mathbf{F}, \tag{4.1}$$

$$\frac{\partial \rho}{\partial t} + \boldsymbol{\nabla}\cdot(\rho(c)\mathbf{u}) = 0, \tag{4.2}$$

$$\boldsymbol{\nabla}\cdot\mathbf{u} = 0, \tag{4.3}$$

where $\boldsymbol{D}$ is the rate of strain tensor, defined as $D_{ij} = (1/2)(\partial u_i/\partial x_j + \partial u_j/\partial x_i)$, and $\mathbf{F}$ collects the additional forcing terms. For our case, these will be due to surface tension and gravity, such that $\mathbf{F}$ is defined by

$$\mathbf{F} = \sigma\kappa\delta_s\mathbf{n} - \frac{\rho(c)}{\mathrm{Fr}^2}\hat{\mathbf{n}}_z, \tag{4.4}$$

where in this case $\sigma = 1/\mathrm{We}$ and δ_s is a Dirac distribution centred on the interface. The density $\rho(c)$ and viscosity $\mu(c)$ vary between the phases, which are defined in terms of the volume fraction c by

$$\rho(c) = \rho_1 c + \rho_2(1-c), \tag{4.5}$$

$$\mu(c) = \mu_1 c + \mu_2(1-c), \tag{4.6}$$

where we choose $\rho_1 = 1$, $\rho_2 = \rho_R$, $\mu_1 = 1/\mathrm{Re}$ and $\mu_2 = \mu_R/\mathrm{Re}$, recalling the definition of the density and viscosity ratios (2.2). In practice, spatial filtering is used to distribute the jump in density and viscosity values over multiple grid cells, which can improve the convergence of the algorithm when these jumps are large. Given this, the conservation of mass equation (4.2) is replaced with

$$\frac{\partial c}{\partial t} + \boldsymbol{\nabla}\cdot(c\mathbf{u}) = 0, \tag{4.7}$$

which determines how the volume fraction evolves in time.

4.2.1 Temporal discretisation

By introducing a finite timestep Δt, the problem is discretised by denoting variables with a subscript k to be evaluated at time $t = k\Delta t$, and introduce a second-order accurate staggered in time discretisation of the governing equations (4.1), (4.3) and

(4.7) to be

$$\rho_{k+\frac{1}{2}}\left[\frac{\mathbf{u}_{k+1}-\mathbf{u}_k}{\Delta t}+(\mathbf{u}_{k+\frac{1}{2}}\cdot\boldsymbol{\nabla})\mathbf{u}_{k+\frac{1}{2}}\right]=-\boldsymbol{\nabla}p_{k+\frac{1}{2}} + \boldsymbol{\nabla}\cdot\left[\mu_{k+\frac{1}{2}}(\mathbf{D}_k+\mathbf{D}_{k+1})\right]+\mathbf{F}_{k+\frac{1}{2}}, \tag{4.8}$$

$$\boldsymbol{\nabla}\cdot\mathbf{u}_{k+1}=0, \tag{4.9}$$

$$\frac{c_{k+\frac{1}{2}}-c_{k-\frac{1}{2}}}{\Delta t}+\boldsymbol{\nabla}\cdot(c_k\mathbf{u}_k)=0. \tag{4.10}$$

This system is simplified using the time-splitting projection method [14], by defining an auxiliary field $\mathbf{u}_*$ as the Helmholtz-Hodge decomposition of $\mathbf{u}_{k+\frac{1}{2}}$ by

$$\mathbf{u}_*=\mathbf{u}_{k+1}+\frac{\Delta t}{\rho_{k+\frac{1}{2}}}\boldsymbol{\nabla}p_{k+\frac{1}{2}}. \tag{4.11}$$

The idea of projection methods is to first solve for the auxiliary vector field $\mathbf{u}_*$, which does not satisfy the incompressibility condition, and then use the pressure term to "project" this auxiliary velocity onto the space of divergence-free vector fields, as $\mathbf{u}_{k+1}$ does satisfy the incompressibility condition. Substituting $\mathbf{u}_{k+1}$ from (4.11) into the momentum equation (4.8) gives,

$$\rho_{k+\frac{1}{2}}\left[\frac{\mathbf{u}_*-\mathbf{u}_k}{\Delta t}+\mathbf{u}_{k+\frac{1}{2}}\cdot\boldsymbol{\nabla}\mathbf{u}_{k+\frac{1}{2}}\right]=\boldsymbol{\nabla}\cdot\left[\mu_{k+\frac{1}{2}}(\mathbf{D}_k+\mathbf{D}_*)\right]+\mathbf{F}_{k+\frac{1}{2}}, \tag{4.12}$$

where by taking the divergence of (4.11), the fractional pressure is found by solving a version of Poisson's equation,

$$\boldsymbol{\nabla}\cdot\left[\frac{\Delta t}{\rho_{k+\frac{1}{2}}}\boldsymbol{\nabla}p_{k+\frac{1}{2}}\right]=\boldsymbol{\nabla}\cdot\mathbf{u}_*. \tag{4.13}$$

At each timestep, the scheme first advects the volume fraction to find $c_{k+\frac{1}{2}}$ from (4.10), then solves (4.12) for $\mathbf{u}_*$, which allows the calculation of divergence of $\mathbf{u}_*$ to determine the pressure from (4.13) and finally project $\mathbf{u}_*$ to find $\mathbf{u}_{k+1}$ from (4.11). In the following subsections, we summarise how each of these steps are carried out using quadtree spatial discretisation, which is more extensively detailed in Popinet (2003) [75].

4.2.2 Spatial discretisation

Basilisk (and *Gerris*) discretise space using a graded quadtree partitioning (octree in three-dimensions). As we will not be studying three-dimensional problems in this thesis, here we only discuss the quadtree partitioning. The left of Figure 4.1 shows an

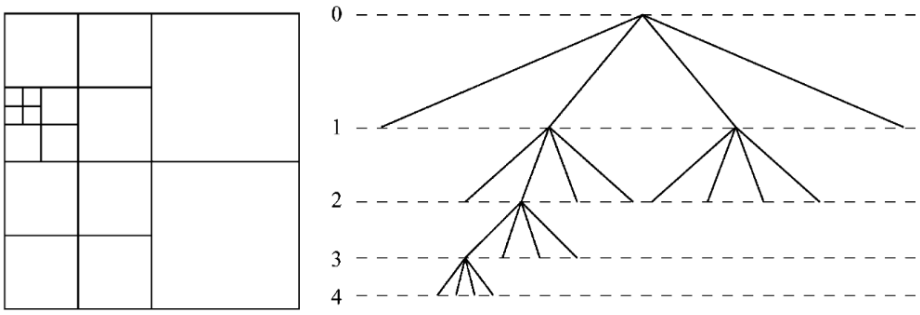

Figure 4.1: Example of a quadtree discretisation (left) and the corresponding tree representation (right). Source: Popinet (2003) [75].

example of a quadtree discretisation, sourced from Popinet (2003) [75]. Each square is referred to as a cell, where any cell may be the parent of four children, such that the child cells are made by splitting the parent cell into four. This relationship is represented by the tree structure on the right of Figure 4.1. The root cell is the base of this tree, and the *leaf* cells are those without any children. The level of a cell is defined by starting with 0 at the root cell, and adding one as you progress down the tree, as depicted in Figure 4.1. A cell is coarser than another if its level is lower, and vice versa with finer cells. Constraints are set on the structure such that adjacent cells (either meeting at a face or a vertex) cannot differ by more than one level.

Interfacial flow problems are often multi-scale, with small regions of rapid topological change in contrast with large regions where the flow is close to steady. The quadtree structure allows for high levels of refinement in the regions of interest, while keeping other regions coarser. This significantly reduces the number of degrees of freedom required to accurately represent the flow compared to uniform discretisations. However, the discretisation of spatial derivatives becomes more complex, as the derivatives in a particular cell depends on the levels of its neighbours. We will not detail them here, and refer the reader to Popinet (2003) [75] for a detailed derivation on the discretisation of the gradient function in a quadtree grid. The quadtree grid structure allows for efficient load-balancing when parallelising simulations, as neighbouring grid cells in the domain will be stored close to each other in memory.

4.2.3 Volume-of-fluid advection

The first step in the scheme is to solve the advection equation (4.10) for the volume fraction to find $c_{k+\frac{1}{2}}$. Recall that c gives the fraction each cell is filled by fluid 1, where the interfacial cells are those such that $0 < c < 1$. Thus although c can be used to indicate which cells contain the interface, it does not alone tell us the shape

of the interface. VOF methods attempt to find the interface through piecewise linear segments in each cell, which is found using the piecewise linear interface construction (PLIC) method [4]. The key simplification of PLIC is that the interface does not have to be continuous, such that neighbouring line segments do not need to meet. *Basilisk* generalises the PLIC method in order to work on quadtree grids, where neighbouring cells may be different in size. The PLIC algorithm is divided into two parts: reconstruction and propagation.

In the reconstruction step, a linear function for the interface in each cell is found, represented by the equation

$$\mathbf{m} \cdot \mathbf{x} = \alpha,$$

where $\mathbf{m}$ is the normal to the interface, $\mathbf{x} = (x, y)$ and $\alpha \in \mathbb{R}$. Thus $\mathbf{m}$ and α uniquely determine the equation for the linear interface passing through the given cell. A version of the Mixed-Youngs-Centred (MYC) implementation [5] is used to find $\mathbf{m}$ by constructing a finite difference scheme using the value of c in neighbouring cells, in which the implementation in *Basilisk* takes into account the quadtree structure where the refinement level of the interface may vary across cells. Once $\mathbf{m}$ is known, α is uniquely determined by ensuring the interfacial area entrapped by the line is equal to c.

The propagation step involves determining $c_{k+\frac{1}{2}}$ by advecting the interface according to (4.10). This is done by using the reconstructed interface from the previous step to accurately determine the volume flux through each cell and using the fact that $\mathbf{u}_k$ is divergence free, which is detailed by Popinet (2009) [76]. Given the solution for $c_{k+\frac{1}{2}}$, the density $\rho_{k+\frac{1}{2}}$ and viscosity $\mu_{k+\frac{1}{2}}$ are then found from (4.5)-(4.6).

4.2.4 Multigrid solver for the Poisson-Helmholtz equation

The scheme involves multiple steps where a version the Poisson-Helmholtz equation needs to be solved on the spatial domain. Here we will detail how the Poisson-Helmholtz solver in *Basilisk* is implemented, with more extensive details given in [75, 77]. First consider the general form of the Poisson-Helmholtz equation,

$$\boldsymbol{\nabla} \cdot (\alpha \boldsymbol{\nabla} a) + \lambda a = b, \tag{4.14}$$

where α, a and b are scalar fields and λ is a real constant. It is assumed that α, λ and b are known, and (4.14) needs to be solved for a. The solver is an iterative scheme, so it is assumed that we have a good initial guess $\tilde{a}$ for a, writing $a = \tilde{a} + \delta a$, where δa is the unknown error term. In practice, $\tilde{a}$ is usually taken to be the value of a from the

previous timestep. Given that (4.14) is linear in a, we can write the left-hand side as $\mathcal{L}(a)$ for a linear operator $\mathcal{L}$, such that

$$\mathcal{L}(a) = b \iff \mathcal{L}(\delta a) = b - \mathcal{L}(\tilde{a}) = R, \tag{4.15}$$

where R is referred to as the residual of δa. To find a from (4.15), the relaxation operator of $\mathcal{L}$, denoted by $\mathcal{R}$, is used to find δa, which is then added to $\tilde{a}$ to find a better guess, and which is then repeated process until the residual satisfies $|R| < \epsilon$, for some tolerance ϵ. However doing this for the entire grid at once is computationally expensive, so instead *Basilisk* uses multilevel acceleration to speed up this process. The multilevel hierarchy is defined such that the *multilevel* $\mathcal{M}_l$ of *depth* l is the set of cells that are either level l, or are leaf cells of level smaller than l. An example of such a multilevel hierarchy is shown in Figure 4.2, sourced from Popinet (2003) [75].

Using this multilevel hierarchy, the solution is found using the "V-cycle" multigrid technique. First, the residual on $\mathcal{M}_L$, denoted R_L, is found. This relies on discretising $\mathcal{L}$, taking into account the quadtree structure, as detailed in Popinet (2003) [75]. The residual is then recursively determined on the lower levels, where R_l is defined as the volume weighted average of R_{l+1} from the child cells, until R_0 is found. On the coarsest level $\mathcal{M}_0$, δa is then found via Jacobi or Gauss-Seidel relaxation techniques, given R_0. This value of δa is then used as the initial guess at the next finest level, repeating the process until we find δa on $\mathcal{M}_L$. Given this, the guess $\tilde{a}$ is updated by adding δa, and the whole process is repeated until $|R_L| < \epsilon$. By default, the algorithm has a tolerance of $\epsilon = 10^{-3}$, applies the relaxation methods 4 times per level, and restricts the maximum number of iterations of the V-cycle to 100. The user is free to change these options to either improve accuracy or decrease run-time, noting that lowering the tolerance will typically require more V-cycles to reach convergence.

The algorithm detailed in this subsection is used in various steps of the Navier-Stokes solver, in particular for finding the auxiliary velocity field $\mathbf{u}_*$ and the pressure $p_{k+\frac{1}{2}}$, setting the values of a, b, α and λ accordingly.

4.2.5 Surface tension term

As discussed in §4.1, accurately resolving the surface tension term $(\sigma\kappa\delta_s\mathbf{n})_{k+\frac{1}{2}}$ from (4.4) has historically been one of the most difficult aspects of applying VOF methods to surface tension driven flows. This is because in order to determine the curvature, κ, we need accurate estimations of the spatial derivatives of the interface. For level set methods, this is simple as the representation of the interface is continuous. However for VOF the reconstructed interface is not continuous between grid cells, which makes

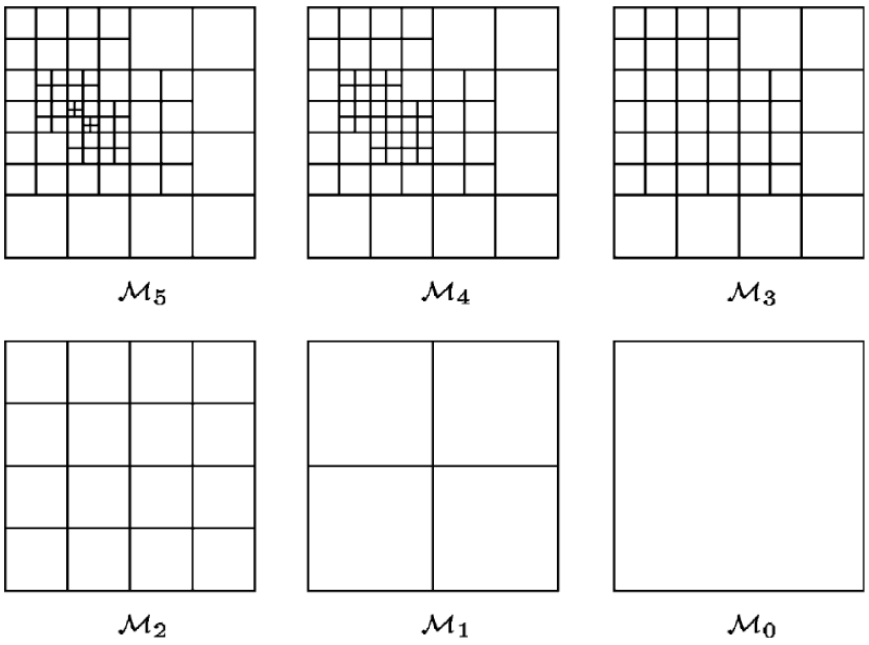

Figure 4.2: Example of a multilevel hierarchy for maximum level 5. Source: Popinet (2003) [75].

it difficult to find smooth solutions for κ. However, Popinet (2009) [76] developed a second-order accurate method for determining the surface tension term using height-functions, which is also implemented within *Basilisk*. Here we will briefly review how this algorithm works, and direct the reader to the work of Popinet (2009) [76] for more details.

First, the surface tension term is approximated using the continuum-surface-force (CSF) approach of Brackbill et al. (1992) [11],

$$\sigma\kappa\delta_s\mathbf{n} \approx \sigma\kappa\boldsymbol{\nabla}c, \quad \kappa = \boldsymbol{\nabla}\cdot\tilde{\mathbf{n}}, \text{ with } \tilde{\mathbf{n}} = \frac{\boldsymbol{\nabla}c}{|\boldsymbol{\nabla}c|}. \tag{4.16}$$

A common test-case for surface tension implementations is to test them on a stationary droplet in equilibrium, in which classical VOF implementations suffered from so-called parasitic currents due to errors in the curvature estimation. In this case of equilibrium, the momentum equation (4.8) with the CSF approximation reduces to

$$\boldsymbol{\nabla}p_{k+\frac{1}{2}} = \sigma\kappa(\boldsymbol{\nabla}c)_{k+\frac{1}{2}},$$

where Renardy & Renardy (2002) [78] noted that it is only possible to recover exact equilibrium so long as the discrete approximations of both gradient operators are compatible and that the curvature κ is constant. The first condition is ensured

by finding the cell-centred pressure gradient by averaging the face-centred pressure gradients.

The second condition depends on the accuracy of the curvature estimations. The implementation in *Basilisk* uses a hierarchical algorithm which uses different methods depending on how curved the interface is in comparison to the grid size. The first of these methods is the height-function formulation. This method aims to find the curvature either in the x or y direction, depending on the steepness of the interface. For the curvature in y, a 3×7 (resp. 7×3 for curvature in x) stencil centred on the cell where the curvature is to be evaluated is considered. Then a discrete approximation of the interface height $y = h(x)$ (resp. $x = h(y)$) is found by adding the volume fractions in each of the columns (resp. rows). Given h, the curvature is estimated as

$$\kappa = \frac{h''}{(1 + h'^2)^{3/2}},$$

where the derivatives are found using second-order accurate finite difference approximations. The choice between whether the curvature in x or y is used depends on the normal direction of the interface in the particular cell. The height-function method is accurate so long as the radius of curvature of the interface is much larger than the size of the cell. If this is not so, then instead the curvature is estimated by fitting a parabola through the interface local to the point and analytically differentiating the resulting equation for the parabola.

In practice, the height function curvature is numerically inexpensive to compute, and for most cases is sufficient to give a good approximation for the curvature, with the parabola fitting only needed local to regions with small radii of curvature. The overall algorithm has been shown to be second-order accurate in estimating the curvature of circular interfaces at various radii in Popinet (2009) [76].

4.2.6 Momentum equation solution

By re-arranging (4.12), the auxiliary velocity is found by solving,

$$\frac{\rho_{k+\frac{1}{2}}}{\Delta t}\mathbf{u}_* - \boldsymbol{\nabla}\cdot\left[\mu_{k+\frac{1}{2}}\mathbf{D}_*\right] = \boldsymbol{\nabla}\cdot\left[\mu_{k+\frac{1}{2}}\mathbf{D}_k\right] + \mathbf{F}_{k+\frac{1}{2}} + \rho_{k+\frac{1}{2}}\left[\frac{\mathbf{u}_k}{\Delta t} - \mathbf{u}_{k+\frac{1}{2}}\cdot\boldsymbol{\nabla}\mathbf{u}_{k+\frac{1}{2}}\right], \quad (4.17)$$

where the right-hand side only depends on quantities at timesteps k and $k+\frac{1}{2}$. In the previous subsections, we discussed how $\rho_{k+\frac{1}{2}}$, $\mu_{k+\frac{1}{2}}$ were found from the updated volume fraction $c_{k+\frac{1}{2}}$, and that we then also know $\mathbf{F}_{k+\frac{1}{2}} = (\sigma\kappa\delta_s\mathbf{n})_{k+\frac{1}{2}} - \rho_{k+\frac{1}{2}}\mathbf{n}_z/\mathrm{Fr}^2$. The final unknown on the right-hand side is the advection term $\mathbf{u}_{k+\frac{1}{2}}\cdot\boldsymbol{\nabla}\mathbf{u}_{k+\frac{1}{2}}$, which is estimated using the Bell-Colella-Glaz (BCG) second-order unsplit upwind scheme

[8]. The BCG scheme is only stable for CFL numbers less than 1, meaning we must have $\max(|\mathbf{u}|)\Delta t/\Delta x < 1$, where $\max(|\mathbf{u}|)$ is the maximum absolute value of velocity and Δx is the width of the smallest grid cell (i.e. at maximum refinement level).

Collecting all of this together, (4.17) is a vectorised version of the Poisson-Helmholtz equation, so can be solved using the multigrid solver detailed in §4.2.4 to find the solution for the auxiliary velocity $\mathbf{u}_*$.

4.2.7 Projection step

The final step in the scheme is to solve (4.13) for $p_{k+\frac{1}{2}}$. The divergence of the $\mathbf{u}_*$ is first calculated on the quadtree grid to find the right-hand-side, and then the multigrid Poisson-Helmholtz solver detailed in §4.2.4 is applied to find $p_{k+\frac{1}{2}}$. Lastly, the velocity $\mathbf{u}_{k+1}$ is found by re-arranging (4.11) and solving

$$\mathbf{u}_{k+1} = \mathbf{u}_* - \frac{\Delta t}{\rho_{k+\frac{1}{2}}} \boldsymbol{\nabla} p_{k+\frac{1}{2}}. \tag{4.18}$$

This final step is called the projection step, as it projects the auxiliary velocity $\mathbf{u}_*$ onto the space of divergence-free velocities.

4.2.8 Adaptive mesh refinement

One of the most advantageous features of *Basilisk* is adaptive mesh refinement (AMR). This is the process in which the quadtree grid described above can be refined in places of interest, and vice versa with coarsening. We can choose to refine with respect to criteria based how much different quantities are changing in certain areas, such as the velocity or the volume fraction. This involves estimating the error in the specific quantity on the current grid resolution, and determining if these errors are more than some set tolerance. The adaptivity process begins by finding all leaf cells which satisfy the refinement criteria, and subsequently refines these cells by splitting them into four. This is recursively repeated with the new leaf cells until every cell satisfies these refinement criteria. In the next step, all of the parents of the leaf cells are checked, and those that do not satisfy the refinement criteria are coarsened (i.e. their child cells are removed). Any new cells created through this refinement/coarsening process will need to be re-initialised. For the newly coarsened cells, the values are simply taken to be the volume weighted average of their previous children. For the newly refined cells, in order to achieve local conservation of momentum and vorticity, the newly refined cell is linearly interpolated from its parent cell and its gradients. More

detail onto the algorithms used in the adaptivity are found in Popinet (2003) [75] and Popinet (2015) [77].

After the adaptive step, there is no guarantee that the velocity is divergence-free anymore, hence a projection step is needed. To save computational costs, the adaptive mesh refinement is done on the auxiliary velocity field $\mathbf{u}_*$, before (4.13) is solved for $p_{k+\frac{1}{2}}$, hence negating the need for an additional projection step.

Adaptive mesh refinement means the total number of degrees of freedom within a simulation is significantly reduced compared to using a uniform grid. For example, a simulation conducted with a uniform grid at level 13 (i.e. one that has 2^{13} grid cells per dimension) would have approximately 67,000,000 grid cells in total. For the cases we will present in the following sections, our use of adaptive mesh refinement means the simulations typically have around 100,000 grid cells at any given time. This amounts to a 95% reduction in the number of degrees of freedom required to resolve the system, requiring significantly less memory and substantially reduced run times in comparison to using a uniform grid.

Now that we have covered the general features of the *Basilisk* volume of fluid solver, in the next section we move on to discussing the specific setups we use for conducting DNS for droplet impact systems.

4.3 Stationary substrate setup

In this thesis, we study both two-dimensional and axisymmetric droplet impact scenarios. Fortunately, *Basilisk* has subroutines (basilisk.fr/src/axi.h) that make the development of an axisymmetric scheme near identical to a two-dimensional scheme, so for brevity in the following we only discuss the two-dimensional setup, pointing out any components which needed special consideration to convert to the axisymmetric case. We start by detailing the setup for the case of impact onto a stationary substrate. In the later subsections, we will consider two different methods for extending this setup to consider substrate motion.

The domain is set to be a square, with side length W, such that the bottom and left edges lie along the x and z axes respectively. The setup for $W = 6$ is depicted in Figure 4.3. To be consistent with the non-dimensionalisation presented in Chapter 2, the droplet is initialised by setting the volume fraction $c = 1$ inside a circle with radius 1, centred on $x = 0$, $z = 1+H$, where H is the distance from the bottom of the droplet to the substrate. For the rest of the domain we set $c = 0$ to denote the gas phase. The velocity (u, v) and pressure p are initialised to be zero everywhere, apart from

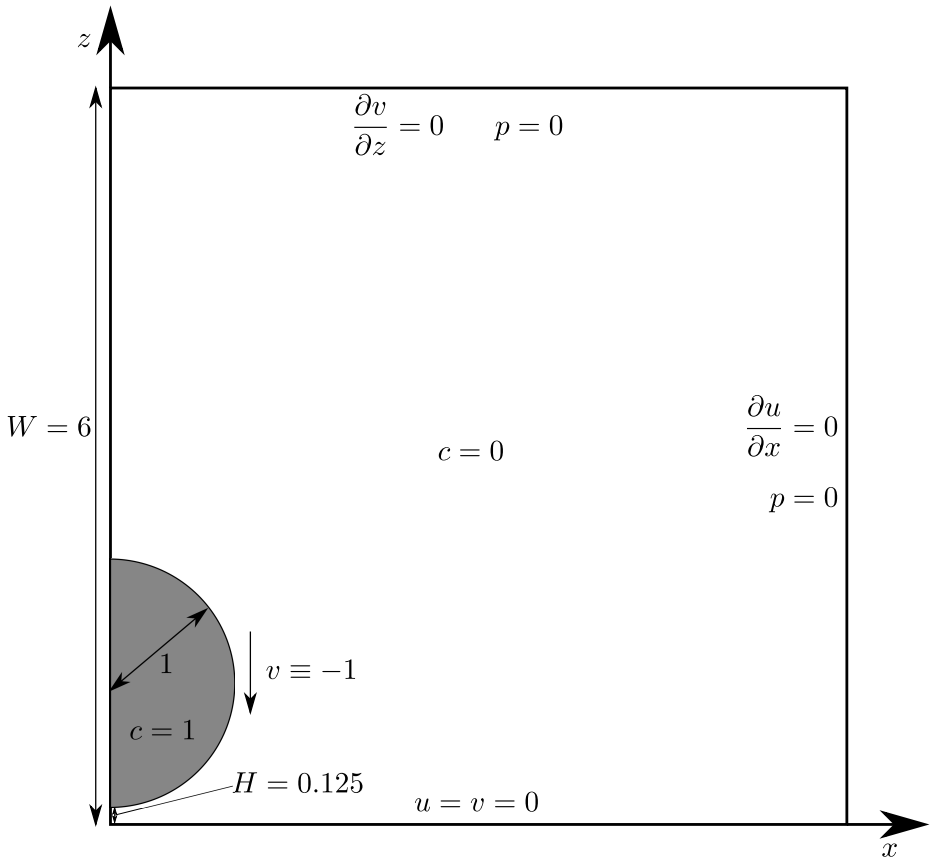

Figure 4.3: Setup of the simulation for impact onto a stationary substrate at the initialisation step, for a computational domain size $W = 6$ and initial droplet height $H = 0.125$.

inside the droplet where $v \equiv -1$. This initial condition is technically not consistent with the surface tension term in (4.4), however the first projection step will correct the pressure field to ensure for a well-defined initial condition. The simulations are initialised at time $t = -H$, such that $t = 0$ is the time the droplet would impact were the gas not present, consistent with the definition of t from Chapter 2. In practice, the droplet will make contact at some time $t > 0$ due to the air cushioning effects of the gas.

The bottom boundary is taken to be the substrate, so we apply no-slip and impermeability boundary conditions resulting in $u = v = 0$. As discussed in Chapter 2, we select to enforce a constant 90° contact angle on any contact point between the two fluids and the substrate. Along the top and right boundaries, we set the far-field boundary conditions that $p = 0$ and $\partial_n \mathbf{u} = 0$, where ∂_n denotes the partial derivative in the outward normal direction to the boundary. The left boundary is given symmetric boundary conditions, such that the normal derivative of all quan-

tities are zero there, which is applied by default in the axisymmetric setup by the *Basilisk* subroutines.

For a given maximum level of refinement M, the quadtree grid is initialised to be at level M in a region of width 0.04 around the droplet interface. For later times, adaptive mesh refinement is used to refine regions where the velocity and interface location are changing rapidly. We set the maximum timestep of the simulations to be $\Delta t = 10^{-4}$, however as the scheme for resolving the surface tension is explicit in time, the timestep is also enforced to be smaller than the oscillation period of the smallest capillary wave, such that

$$\Delta t \leq \sqrt{\frac{\rho_m \Delta_M^3}{\pi \sigma}},$$

where $\rho_m = (\rho_1 + \rho_2)/2$ and Δ_M is the width of the grid cells at level M. To increase the accuracy of the simulation, the tolerance for the Poisson solver is set to be 10^{-5}, instead of the default value of 10^{-3}. Given this stricter tolerance, the maximum number of iterations for the Poisson solver is set to 300, rather than the default value of 100.

At regular timesteps, the hydrodynamic force applied to the substrate is determined by numerically integrating the pressure and the viscous stress along the bottom boundary using the trapezoidal rule. To ensure accuracy for this quantity, the cells along the bottom boundary are kept at the maximum refinement level M. Note that here the integrand differs depending on if we are considering the two-dimensional or axisymmetric case.

Several additional details are worth noting in order to ensure a robust computational setup. First, due to the high contrast in densities and viscosities across the interface, spatial filtering is used to smooth out the jump across multiple grid cells, as detailed in Popinet (2009) [76]. Secondly, the nature of VOF schemes means that the interface is allowed to break up and produce smaller droplets and bubbles. Any droplets or bubbles produced with diameters typically smaller than 16 level M grid cells are deemed nonphysical and are dynamically removed, with the exception of the entrapped gas bubble we expect to see near the point of contact. As will be discussed in the validation section (§4.5), we find that the area/volume of the droplet at the chosen resolution level used for the stationary substrate results only changes by approximately 0.003% throughout the course of the simulation, meaning the scheme is still sufficiently mass conserving even with this droplet/bubble removal. Finally, it has been observed in other studies, such as Philippi et al. [74], that numerical instabilities in the Poisson solver can cause the pressure values to spuriously fluctuate between

timesteps, thus resulting in the hydrodynamic force values to vary artificially. When considering the fluid-structure interaction cases later, these spikes in the force can be problematic and potentially cause a breakdown in the resulting numerical scheme for the substrate position. To prevent this, we use a peak-detection algorithm [92] to identify numerical spikes and smooth out the resulting force. This algorithm works by determining the standard deviation of the force from a set number of previous timesteps, and identifies a non-physical spike if it significantly deviates from the previous force values. In these cases, the force is taken to be a weighted average of the previous forces in order to avoid polluting the scheme with these non-physical force values.

Typically, the simulations are executed until the turnover point surpasses the initial droplet radius, at which point we are far beyond the early times considered by the analytical model. From the analytical model, we saw from (3.54) that the turnover point in the two-dimensional case evolves as $d_0(t) = 2\sqrt{t}$, whereas for the axisymmetric case from (3.204) we have $d_0(t) = \sqrt{3t}$. This means we can expect the droplet spreading of the two-dimensional case to be faster than the axisymmetric case, and we thus end the simulation earlier when needed.

Due to the high number of grid cells, it is impracticable both in terms of storage and run-time to save all of the available data generated by a simulation, so we make informed choices about what data to output and how frequently it is outputted. Global quantities, such as the force on the substrate, the volume of the droplet and the number of grid cells, are outputted at every timestep, as they require a minimal amount of memory to store. At a lower frequency (typically at time intervals of 10^{-3}), we output the location of the interface, which is given as a sequence of line segments through the relevant grid cells, as well as the values of the pressure and stress along the substrate. At even lower frequencies, we output the data across the entire domain, which includes the velocity, pressure and volume fraction in every grid cell. Typically these data files are $\approx$ 10 MB in size for level 13 simulations, hence writing these to the hard drive takes a non-negligible amount of time meaning we output them at a low frequency (at time intervals of 10^{-2}). Post-processing with MATLAB is used to analyse the quantities which are not directly extractable from the simulation, such as the turnover point location. We will discuss details on how the individual post-processing techniques are conducted within the discussions of the relevant results.

4.4 Deformable substrate consideration

Having detailed the setup for a stationary substrate, we now turn our attention to how we implement substrate motion into the DNS. Considering immersed solid boundaries in a flow is one of the oldest problems in CFD, dating back to the original simulations modelling aerofoils [87], and *Basilisk* has subroutines for embedding such solid boundaries into a domain. The immersed boundary method of Peskin (2002)[73] has become one of the most popular methods for modelling the motion of an elastic body immersed into a fluid, which couples a Lagrangian description of the body to an Eulerian description of the surrounding flow. Unfortunately, embedding a boundary into a two-phase flow is a significant challenge, as the triple-contact point (where liquid, gas and substrate meet) is very difficult to accurately resolve. Because of this, the embedded boundary subroutines in *Basilisk* are only available to cases where a single phase meets the boundary, which is not sufficient for our purposes as we expect both the liquid and the gas to meet the substrate. Because of this, we consider two different strategies which allow us to simulate droplet impact onto a moving substrate without having to use embedded boundary methods.

4.4.1 Moving frame setup

The issue of the triple contact points means we cannot embed a boundary inside the computational box, however we can have such a point along the boundaries of the computational domain, which stay in place throughout the simulation. This motivates us to consider a moving frame of reference, such that the substrate always lies along the bottom boundary of the domain. In the case where the substrate is deformable, this would only be possible by deforming the resulting geometry spatially, to map the non-flat substrate onto the boundary. However in the case where the substrate remains rigid, i.e. $w(x,t) = w(t)$, with a horizontal width L, this is possible by a simple shift in the vertical direction of the position, velocity and accelerations. Specifically, we define the moving frame coordinate system by

$$\mathbf{x}' = (x',\, z') = (x,\, z + w(t)), \quad \mathbf{u}' = (u',\, v') = (u,\, v + \dot{w}(t))\,, \tag{4.19}$$

where quantities with a prime $'$ are taken to be in the moving frame. Given this, the momentum equation (4.1) is transformed to be

$$\rho'(c')\left(\frac{\partial \mathbf{u}'}{\partial t} + (\mathbf{u}' \cdot \boldsymbol{\nabla})\mathbf{u}'\right) = -\boldsymbol{\nabla} p' + \boldsymbol{\nabla} \cdot (2\mu'(c)\mathbf{D}') + \mathbf{F}', \tag{4.20}$$

$$v' = 0 \text{ on } x' \leq L,\, z' = 0, \tag{4.21}$$

where the forcing term now has an additional component due to the substrate acceleration,

$$\mathbf{F}' = \kappa'\sigma\delta_s\mathbf{n} + \rho'(c')\left(\ddot{w}(t) - \frac{1}{\mathrm{Fr}^2}\right)\hat{\mathbf{n}}_z, \tag{4.22}$$

with all other governing equations remaining the same besides introducing the prime notation. Note how this is almost identical to the stationary setup considered before, with the main change being the additional forcing term due to the acceleration of the substrate. However, the boundary conditions on the computational domain need to also be transformed in order to take the moving frame into account. Specifically, we apply a mixed condition along the bottom boundary, with $v' = 0$ for $x' \leq L$ and $v' = \dot{w}(t)$ for $x' > L$, as well as specifying that $v' = \dot{w}(t)$ along the right-hand boundary. The point $x' = L$ on the bottom boundary must be treated with care in order to avoid singularities where the boundary condition changes. To prevent this, we ensure that L is large enough such that the wetted part of the bottom boundary never surpasses L. The bottom of the substrate lies outside of the computational domain, and as discussed in Chapter 2, we assume the gas there remains at atmospheric pressure and exerts no viscous stress on the substrate. We keep the condition that $\partial v/\partial z = 0$ along the top boundary the same, as this is still consistent with the moving frame formulation. The resulting computational setup for $L = 2$ is shown in Figure 4.4.

The implementation of the simulation is then mostly identical to the stationary substrate case, with the addition of updating the boundary conditions and acceleration terms at each timestep to take into account the motion of the substrate. However, care must be taken when imposing the velocity of the substrate, as high values of $\dot{w}(t)$ will induce a substantial amount of flow close to the far boundaries which can lead to a breakdown of the solution. For the practicality of our studies, the induced motion of the substrate is typically small in comparison to the droplet velocity and this issue does not arise. During post-processing, the resulting solutions in the original frame of reference can be simply found from (4.19).

The method of changing the frame of reference to map the substrate onto the computational boundary becomes significantly more complicated once the substrate is deformable, i.e. w depends on x as well as t. This is because the resulting change of frame would deform the z-coordinate with respect to x, meaning that the moving frame would no longer be a linear transformation of the original frame. Implementing the system in this deformed frame would be a substantially greater challenge, as the spatial derivatives would have to be adjusted at the fundamental level of the solver,

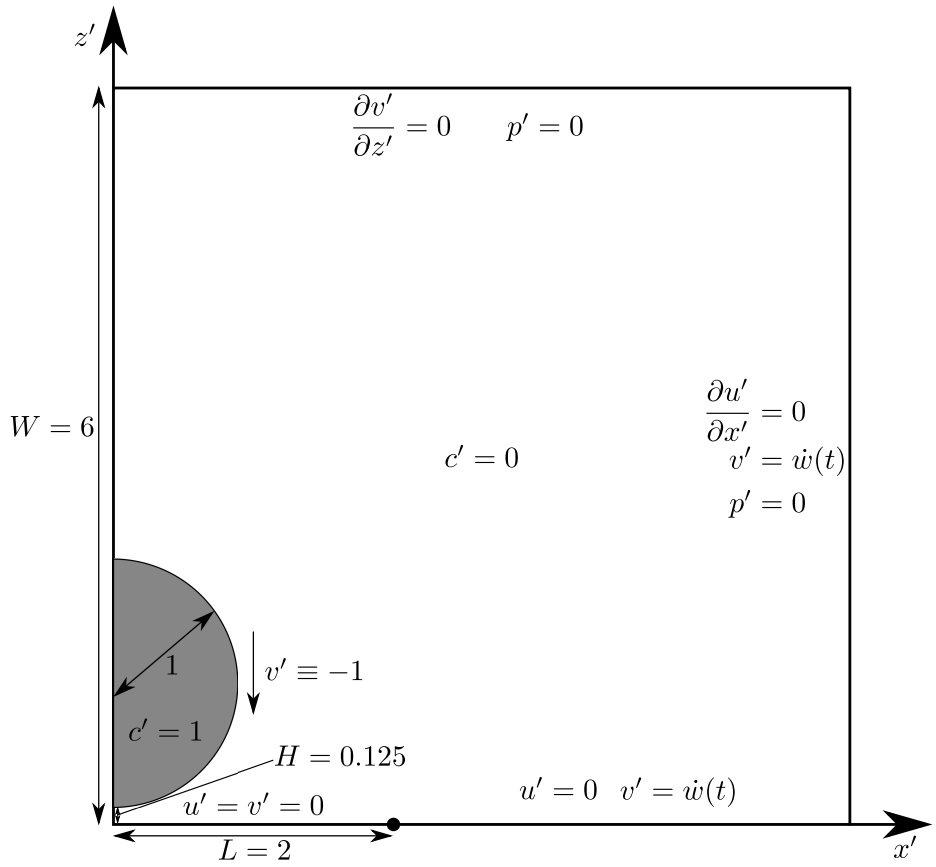

Figure 4.4: Setup of the simulation for impact onto a rigid, moving substrate at the initialisation step, within the moving frame formulation. The computational domain is of size $W = 6$, with a substrate width $L = 2$ and initial droplet height $H = 0.125$.

as well as redefining how quantities such as the surface tension are calculated. In addition, the extra acceleration terms would not only depend on w, but also the pressure and velocities, so care would need to be taken when adding in the acceleration terms to ensure the accuracy of the scheme. However, implementing this change of frame method for a deformable substrate would be a valuable extension for the two-phase flow community, as it would allow the simulation of more general fluid-structure interactions problems while negating the need for embedded boundaries. The extension of the moving frame formulation to consider deformable substrates is beyond the scope of this thesis, so instead we utilise a simpler alternative method to model the deformable substrate case, which we detail in the following subsection.

4.4.2 Linearised boundary setup

Recall that the no-slip and no-flux boundary conditions on the substrate are applied at $z = -w(x, t)$. The difficulty here is that these boundary conditions are applied

on a non-flat boundary that moves in time, which is not directly possible without using embedded boundary methods that are currently not supported for two-phase *Basilisk* simulations. To resolve this, we make the assumption that $w(x,t)$ is small enough that we can linearise this boundary condition, and instead apply it onto the line $z = 0$ for all times. This drastically simplifies the problem, as we can consider the square domain from the stationary substrate setup, with the only change being that we now have the boundary condition that $v = -\partial w/\partial t$ for $x \leq L$ on the bottom boundary. Apart from updating this boundary condition at every timestep, the implementation is then identical to the stationary substrate setup. This method was employed in Howland et al. (2016) [46], where experiments and *Basilisk* simulations were conducted to study droplet impact onto silicone gels. By using this method, they found that even with small substrate deformations, the simulations predicted that the ejection speeds and internal pressure of the droplet were significantly lower than the rigid case, which qualitatively reflected what was observed by their corresponding experiments.

Although the results of Howland et al. (2016) [46] give us good motivation for employing this approach for our simulations, the simplicity of the method comes at a number of costs relating to the accuracy of the solution. The most apparent is that we are no longer applying the boundary conditions along the substrate, which means the simulations are in a fundamentally different geometry to the original problem. The effect of this discrepancy increases when the displacement of the membrane increases, so it will be important to monitor the size of w, to ensure it remains small for the cases we study. Another consequence of this method is that by applying a finite fluid velocity along the substrate, we will inevitably lose or gain fluid mass through that boundary, meaning the scheme is no longer mass conserving. The amount of mass loss/gain will depend on $\partial w/\partial t$, so again we would expect the best results when the substrate displacement is small. We will quantify the extent of this mass loss/gain effect in the following validation section, and discuss how we take it into account when interpreting our results.

Despite the drawbacks, this linearised boundary method still allows us to encapsulate the effects that the substrate motion has on the flow. As long as the substrate deformation is relatively small, the linearised boundary condition should be sufficiently close to true substrate location, and the velocity of the substrate should then in turn alter the dynamics of the flow. As was seen in Howland et al. (2016) [46], substantial decreases in the droplet pressure can be observed by allowing the sub-

strate to deform. In using this method, we will keep in mind its limiting factors and discuss their potential impact on our results.

4.5 Numerical validation

One of the reasons for us choosing to conduct DNS was to cross-validate analytical model from Chapter 3, which relied on a series of assumptions about the system that are not made in the DNS framework. Before doing this, we need to conduct an extensive validation effort to confirm the results of the DNS are independent of the computational parameters we have chosen. The main parameter of interest in this regard is the maximum level of refinement, as this determines the required resolution to be imposed for mesh-independent results. In this endeavour, we will test the outputs of the simulations for refinement levels higher and lower than the level we intend to use for our results in the following chapters. This way, we can validate the scheme by showing how the results for key quantities become independent once we increase the level beyond a certain point. We have also conducted validation tests to ensure that the solution is independent of increasing the size of the computational domain (adjusting the refinement level accordingly) and the initial height of the droplet, however we will not detail these here for brevity.

Throughout this section, we will focus on validating a series of time-dependent quantities in which we have analytical solutions for in Chapter 3, and we will show the predictions of the analytical model for these quantities alongside the DNS throughout this validation. Note, however, that this analytical framework is tailored towards modelling the early times of impact, in which we go beyond with the DNS. The exact timescale this covers is not well-defined, however we know that once the turnover point/curve reaches the initial radius of the droplet (i.e. $\epsilon d(t) = 1$ in Figure 3.1), then the asymptotic structure of the analytical solution breaks down. In particular, the outer region would be the same size as the outer-outer, and the flow entering the inner regions would change direction. Therefore, any analytical solutions plotted in this section will only be shown up until the time where the turnover point/curve reaches the initial droplet radius.

Considering the three setups detailed above (appropriate for modelling stationary substrates, rigid moving substrates and curved moving substrates respectively), we focus on showing the mesh dependence of a number of physical quantities that are relevant to the modelling problem we wish to solve. For all of these cases, we consider a computational domain width of $W = 6$, with an initial droplet height of $H = 0.125$,

with a minimum refinement level of 5. We then vary the maximum refinement level from 10 to 14, with our intention to show that level 13 is sufficient for our purposes. For clarity, recall that a level m cell has a width equal to $W/2^m$, and if the grid were uniform at level m, would have $\lfloor 2^m/W \rfloor$ cells per unit droplet radius. So the minimum level 5 corresponds to 5 cells per unit radius, whereas levels 10 to 14 correspond to 170 to 2730 cells per unit radius respectively. In later chapters, we vary the size of the domain W, and in which cases we adjust the maximum of level of refinement accordingly in order to keep the same number of cells per unit droplet radius.

In the following, we focus on validating time-dependent quantities of the system across the entire simulation timescale. For this purpose, we compare the results from the level 10-13 simulations with a reference level 14 simulation, confirming that our level 13 results are insensitive to further mesh refinement. To this end, we define a discrete L_2-norm error metric between a level m simulation and the reference level 14 simulation. Let $f_m(t)$ be some time-dependent quantity of a simulation with maximum level $m < 14$, then we define the discrete L_2-norm of the difference between $f_m(t)$ and $f_{14}(t)$ across the full simulation timescale to be

$$||f_m - f_{14}||_2 = \sqrt{\frac{1}{K}\sum_{k=0}^{K}(f_m(t_k) - f_{14}(t_k))^2}, \tag{4.23}$$

where t_k is the discretised time value and K is the total number of timesteps. Although the L_2-norm of a specific level is not informative in isolation, by comparing these values for each maximum refinement level, we hope to see numerical convergence as m increases.

4.5.1 Stationary substrate validation

We first focus on validating the case where the substrate is stationary, as this will be an important control benchmark to compare the moving substrate cases to. Here we test the scheme to ensure the geometrical properties of the system are consistent with existing analytical and experimental studies for droplet impact. The simulations were run from $t = -0.125$ to $t = 0.625$ in both the two-dimensional and axisymmetric settings. A snapshot of two-dimensional simulation at $t = 0.275$ for maximum refinement level 13 is shown in Figure 4.5, where the left-hand side shows the volume fraction (mirrored from the simulation setup for visual clarity), and the right-hand side shows the refinement level. It is clear from this figure how the adaptive grid is fine close to the droplet interface, as well as in other regions where the air flow has

caused large velocities. We can also see how the grid is coarsened in regions where the dynamics are slower, such as the centre of the droplet and the air sufficiently far away. For this snapshot of the simulation, there were 96,280 grid cells in total, whilst there would have been 67,108,864 cells were the grid uniform at level 13. This exemplifies the strength of adaptive mesh refinement in reducing the number of degrees of freedom whilst still resolving relevant details to high accuracy.

As the moving substrate cases were built upon from the stationary substrate setup, it is important here to ensure the droplet itself has been accurately resolved by the scheme. For this purpose, we focus on the evolution of a particular point on the droplet, namely the horizontal position of the turnover point (or turnover curve in the axisymmetric setting), $d(t)$. In the analytical model from Chapter 3, this quantity is defined to be the point at which the droplet interface becomes vertical and ejects fluid across the substrate. This definition is valid for early times, however at the later times captured by the DNS, the interface can become non-vertical once the turnover point has surpassed the initial droplet radius. Therefore a definition that is valid for a larger timescale is the point on the interface with the maximum curvature (excluding the tip of the jet/splash sheet and the entrapped bubble). In order to find the evolution of the turnover point from the DNS, we conduct post-processing on the outputs of the droplet interface location, which are a series of non-continuous line segments. At early times when the turnover region only contains a few grid cells, the estimate of the curvature can become noisy, even with *Basilisk*'s highly-accurate curvature schemes (see §4.2.5). Because of this, we opt to define the turnover point in the DNS as the left-most point on the interface below the centre of the droplet (excluding the entrapped bubble). This allows us to accurately resolve the turnover point at early times, meaning we can directly compare to the analytical model during the times we expect its predictions to be most valid. However, this does mean we only have DNS solutions for this quantity up until the time where the turnover point surpasses the radius of the bulk of the droplet.

In Figure 4.6, we show the validation study for the turnover point/curve, with Figure 4.6a showing the turnover point $d_m(t)$ for the two-dimensional case and Figure 4.6b showing the turnover curve in the axisymmetric case. The colours depict the maximum refinement level, m, and the black dashed lines show the analytical solutions from (3.54) and (3.204). The vertical dashed lines denote the time where the analytical models predict the turnover point exceeds the initial droplet radius, and hence we stop plotting the analytical solution after those times. The insets illustrate the L_2-norm error between the solutions with maximum level m and the reference

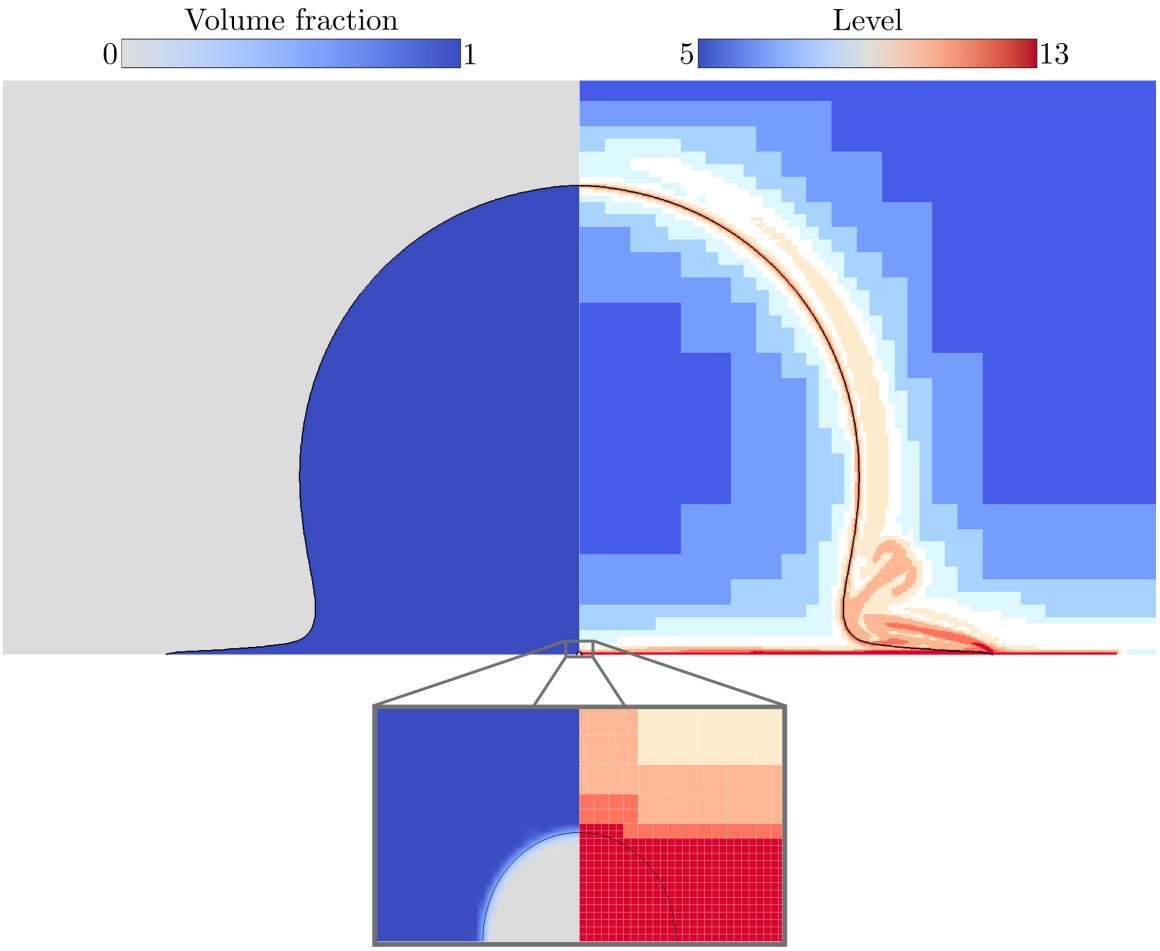

Figure 4.5: Snapshot close to the droplet for the DNS for a two-dimensional impact case onto a stationary substrate, taken at $t = 0.275$, for maximum refinement level 13. The left-hand side shows the volume fraction (mirrored in x for visual clarity), while the right-hand side shows the level of mesh refinement. The bottom panel shows a zoomed in view of the entrapped bubble, with the grid structure on the right-hand side shown in white alongside the colour plot for the refinement level.

level 14. The L_2-norm of each case shows how there is a strong convergence for $d_m(t)$ as m is increased, with level 13 becoming visually indistinguishable from the reference level 14 on the plots. In addition, the numerical results agree well with the analytical solutions up to around $t = 0.2$, at which point the horizontal extent of the turnover point/curve is $\approx 80\%$ of the initial droplet radius. This is much later than we anticipate the analytical model to be valid for, given the early-time assumptions made in Chapter 3, which gives encouragement for the results of the analytical model. Overall Figure 4.6 gives evidence that the spreading behaviour of the well resolved at our choice of maximum refinement level $m = 13$.

Of course the turnover point/curve tracks just a single point on the interface,

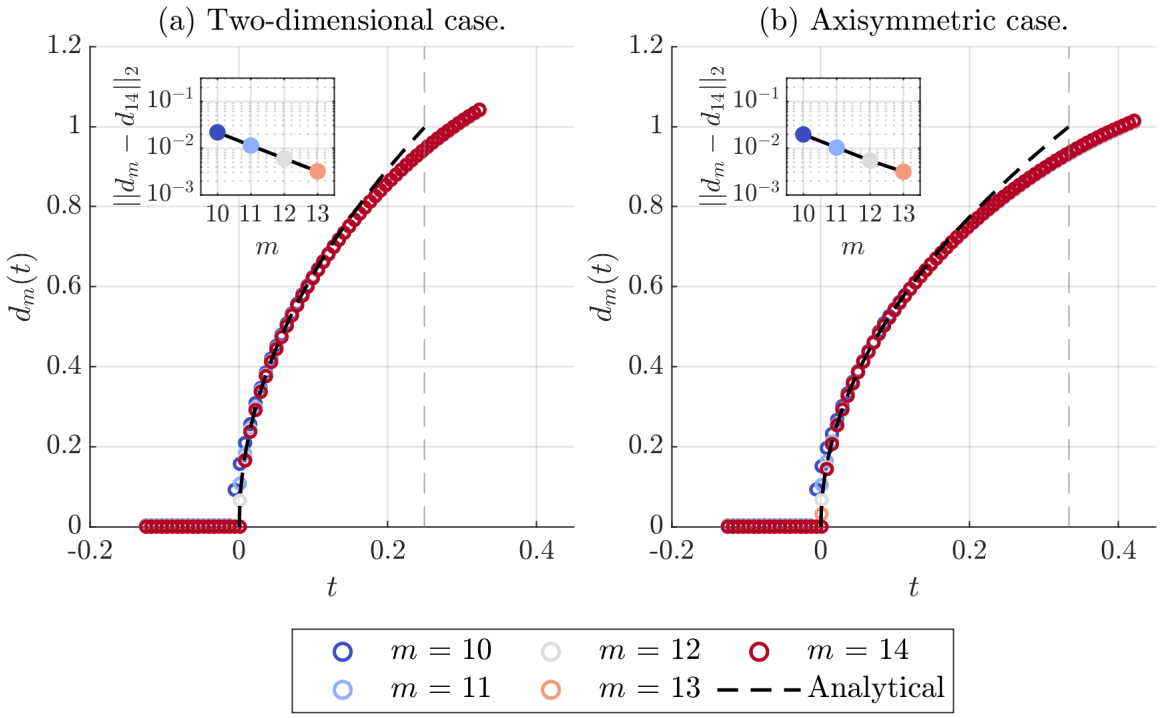

Figure 4.6: Numerical solutions for the turnover point $d_m(t)$ at maximum refinement level m varied between 10 and 14, for the two-dimensional (left) and axisymmetric (right) cases with a stationary substrate. The black dashed lines show the analytical solutions given by (3.54) and (3.204). The insets illustrate the L_2-norm (defined in (4.23)) of the difference between solutions with maximum level m and the reference maximum level 14 results.

and the advantage of the DNS is that we readily have access to the location of the entire interface at any given time. Thus other geometrical features of the system, such as the location of the jet-tip or the height of the top of the droplet, could also be used to validate the simulations in the same fashion. Although we do not conduct this validation here for brevity, we will briefly discuss one more geometrical feature, namely the entrapped bubble. From experimental studies such as Thoroddsen et al. (2003) [90], we expect the droplet to deform at its base at it approaches the substrate due to the build up of the air pressure, resulting in the droplet contacting off-centre and entrapping a small bubble of air. This bubble is initially elongated along the boundary, and eventually contracts to form a stable half-sphere on the centre point. By imaging the impact of high speed water drops of diameter 4 mm onto solid surfaces, Thoroddsen et al. (2003) [90] found that the radius of this entrapped bubble after contraction was typically around 50 μm, which is only 2.5% of the initial droplet radius. Because of these small scales, accurately resolving these entrapped air bubbles within a numerical simulation is a significant technical task. However

doing so provides good stress-test for the robustness of the scheme for resolving the multi-scale features of the system.

The entrapped bubble is visible in the inset of Figure 4.5, which was taken from a level 13 simulation. From the inset it can be seen that the entrapped bubble in this case has a radius of around 13 cells, which is ≈ 0.009 times smaller than the droplet radius, which is on the same order of magnitude as the size of the bubbles observed by Thoroddsen et al. (2003) [90]. Therefore, despite how from Figure 4.6 we see that the coarser simulations manage to predict the turnover point evolution well, we cannot expect them to resolve the entrapped bubble for lower refinement levels. For example, a bubble with the radius shown in Figure 4.5 would be equal to the width of ≈ 3.5 level 11 cells. This would be too coarse of an interface for accurate surface tension calculations and therefore we could not resolve the entrapped bubble dynamics with this refinement level.

Whilst we dynamically remove artificially small droplets and bubbles which pollute the scheme, we do ensure that the entrapped bubble remains when possible. Overall, the entrapped bubble is not one of the focuses of this thesis, and there are a number of cases where we choose to remove the entrapped bubble in order to ensure our scheme is robust. The first is the case we discussed above, when the chosen refinement level is too coarse to accurately resolve the bubble. In these cases, rather than reflecting true physics, the presence of the bubble is instead a numerical artefact, which typically acts to create regions of spuriously high pressure along the interface due to the poorly resolved surface tension balance. The second case where we choose to remove the entrapped bubble is when we are considering the linearised boundary setup. As previously discussed, in this setup we impose a non-zero flux condition on the bottom boundary, and the result is that the entrapped bubble loses volume as the substrate initially moves downwards. The result is that the entrapped bubble becomes artificially small, causing large pressure variations due to the under-resolved surface tension forces on the bubble interface. Therefore we choose to remove the entrapped bubble in these cases to mitigate this effect. Ultimately, this breaks the mass conservation of the scheme by replacing the gas phase with liquid in this region, however this is only a small amount compared to the overall size of the droplet, and we already expect to lose some mass by using the linearised boundary setup. However we find that we do not need to remove the bubble for the moving frame setup, as in that case we do apply a no-flux condition at the substrate which allows for a well-resolved entrapped bubble similar to the stationary substrate setup.

As the above discussed features are related to the geometry of the droplet, it is natural that they would converge with increasing grid resolution. In the following two subsections, we will focus on non-geometric properties of the flow, showing that increasing grid refinement still results in numerical convergence of these properties. We in turn validate the moving frame and linearised boundary formulations detailed in §4.4, but continue to use the stationary substrate both in order to strengthen the validation and provide comparisons to the moving substrate cases.

4.5.2 Moving frame validation

Having provided support that the stationary substrate setup gives robust predictions for the geometry of the droplet, we move on to validating the results of the moving frame setup given in §4.4.1. For these cases, the substrate is taken to be rigid, such that $w(x,t) = w(t)$. The fluid-structure interaction problem we will consider in Chapter 5 relies on coupling the substrate motion with the force exerted on the substrate from the fluid phases, so here we focus on validating that the force converges as the maximum level of refinement is increased.

To validate the moving frame setup, we need to impose the substrate motion with a given solution for $w(t)$. This imposed motion is for robust testing, and in Chapter 5 we will consider true fluid-structure interaction. In order to emulate the types of substrate motions we see in Chapter 5, we keep the substrate stationary up until $t = 0$, and then impose an oscillatory substrate motion for $t > 0$ given by the equation

$$w(t) = a(1 - \cos(\omega t) + t^2), \tag{4.24}$$

where we let $a = 0.00125$ and $\omega = 12$, which is plotted in Figure 4.7 for both the two-dimensional and axisymmetric cases. Alongside the DNS solutions for the force, we will also plot the corresponding analytical solutions, in which we have the leading-order and composite force for the two-dimensional case given by (3.158) and (3.162) respectively, and their axisymmetric counterparts by (3.248) and (3.251).

We present the two-dimensional validation cases in Figure 4.8, in the same format as the turnover point validation cases in Figure 4.6, where the insets show the L_2-norm error for F_m given by (4.23). Here we can see how the solution for the force on the substrate experiences a significant amount of noise in comparison to the geometrical quantities studied in §4.5.1. As previously mentioned, this is due to the temporal instabilities in the Poisson solver for the pressure, as was observed in Philippi et al. (2016) [74]. However, from the figures we can see how these instabilities are reduced as the maximum refinement level is increased, and from the L_2-norm error plots we

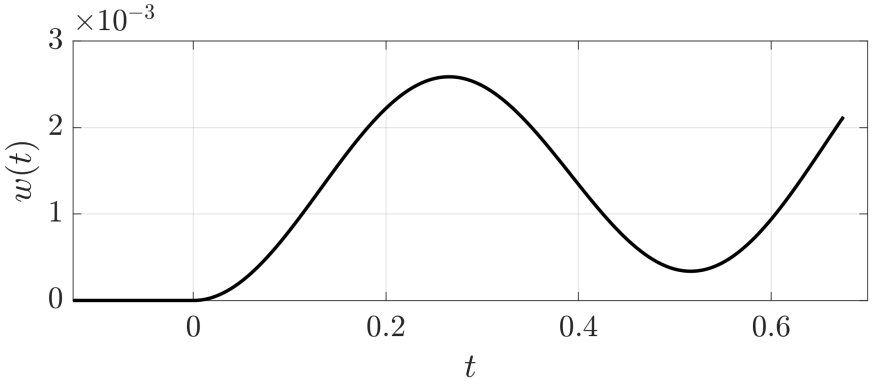

Figure 4.7: Imposed rigid substrate motion, where $w(t) = 0$ for $t < 0$ and $w(t)$ is given by (4.24) for $t > 0$, for $a = 0.00125$ and $\omega = 12$.

still see a strong convergence in the values of $F_m(t)$ as m is increased. By comparing Figure 4.8a and 4.8b, we see how the force reacts to the acceleration of the substrate, experiencing oscillations that are not present in the stationary substrate case. By comparing the DNS solutions to their analytical counterparts, it is clear how the leading-order force (shown with black dashed lines) fails to match the trend as well as the composite force (shown with black solid lines). This is particularly true in the stationary substrate setup, where the leading-order solution predicts the force is constant for all time which is clearly not reflected by the DNS. We found that the contributions to the force from the viscous stress was around 10^{-5} times smaller than from the pressure. From this, combined with the knowledge of the close agreement between the DNS and analytical solutions for the turnover point in Figure 4.6, we can infer that these differences are due to the analytical solution over-predicting the pressure on the substrate. We will return to this in the following section when discussing the linearised boundary validation.

Similarly, in Figure 4.9, we show the axisymmetric validation cases for the same imposed substrate motion. The force in the axisymmetric case differs from the two-dimensional case as it is small at the point of impact, and then grows as the droplet spreads. We discussed this difference in the context of the analytical model in §3.3.7, and it is due to the radial term that appears in the force integral given by (3.247). The noise in the solution for the axisymmetric case appear to be slightly more pronounced than in the two-dimensional case. However, from the L_2-norm errors we can still see how the values of $F_m(t)$ converge as we increase the refinement level, although not as strongly as in the two-dimensional case. Encouragingly, the analytical solutions for the force seem to agree better with the DNS for these cases in comparison to Figure 4.8. This could have been expected by the fact that, in the stationary case,

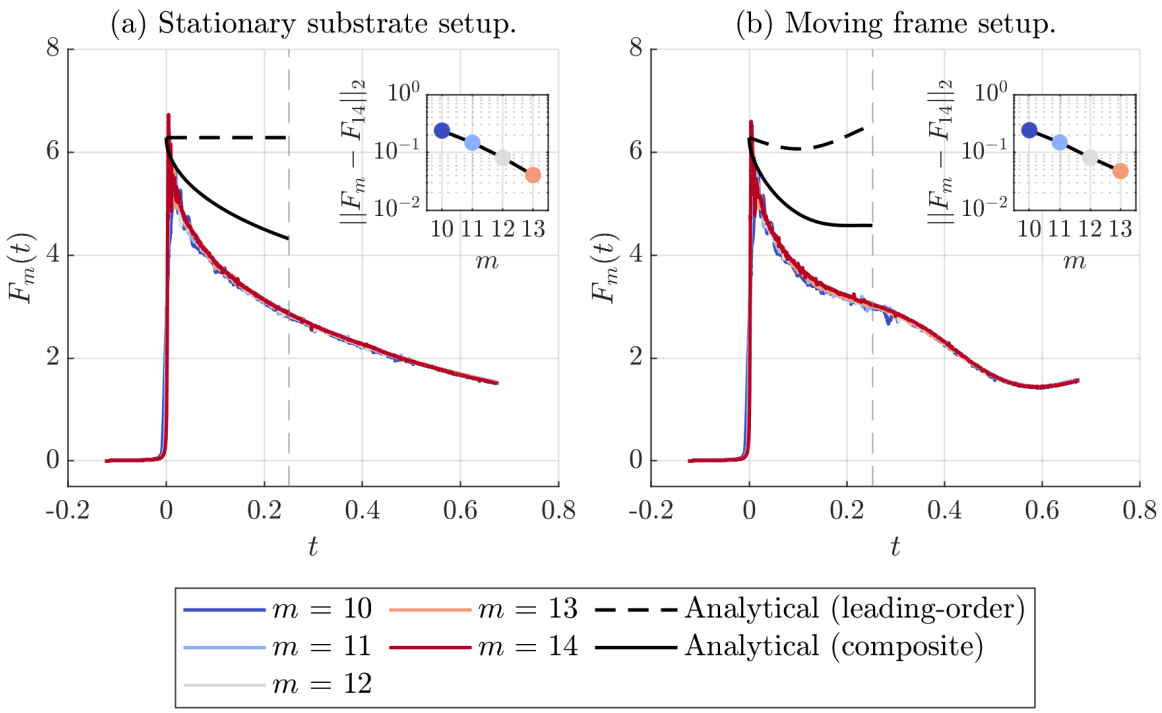

Figure 4.8: Numerical solutions for the force on the substrate $F_m(t)$ in the two-dimensional case, where the maximum refinement level m is varied between 10 and 14, where (a) shows the stationary substrate setup and (b) the moving frame setup with imposed substrate motion shown in Figure 4.7. The black dashed and solid lines show the leading-order and composite analytical solutions, given by (3.158) and (3.162) respectively. The insets illustrate the L_2-norm (defined in (4.23)) of the difference between solutions with maximum level m and the reference maximum level 14 results.

the two-dimensional leading-order solution predicted the force to be constant in time. This is naturally a surprising result, and from Figure 4.8 we saw that instead the force exhibits a sharp jump upon impact, which then decreases in time. For the axisymmetric case, the analytical solutions predict that the force is initially 0, due to the radial term in force integral dominating the pressure singularity. Due to this, the force values from the DNS and analytical solutions agree better at early time than the two-dimensional case. We also again see that the composite solution agrees with the DNS much better than the leading-order solution at more intermediate times. The composite solution may compare more favourably, as it takes into account the forcing from the inner region, which grows in size as the droplet spreads and hence has a more significant contribution to the force at later times.

Overall, the validation results in Figures 4.8 and 4.9 show a clear convergence for the force values in both the stationary substrate and the moving frame setups, and we

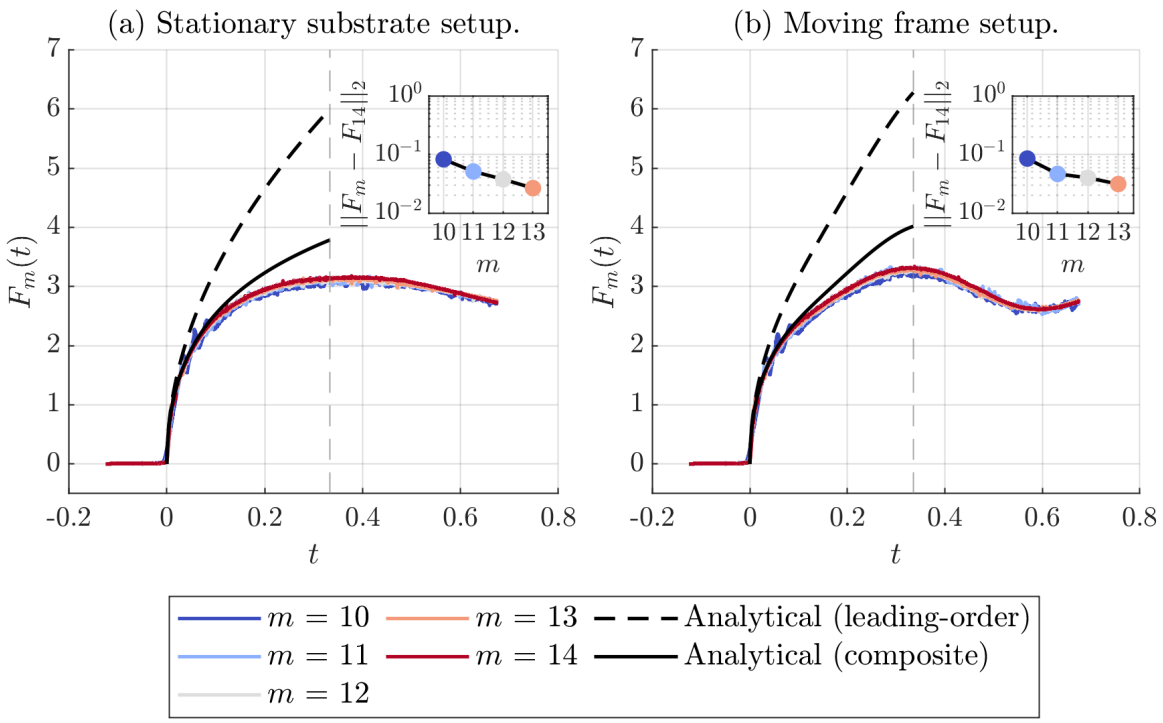

Figure 4.9: Numerical solutions for the force on the substrate $F_m(t)$ in the axisymmetric case, where the maximum refinement level m is varied between 10 and 14, where (a) shows the stationary substrate setup and (b) the moving frame setup with imposed substrate motion shown in Figure 4.7. The black dashed and solid lines show the leading-order and composite analytical solutions, given by (3.248) and (3.251) respectively. The insets illustrate the L_2-norm (defined in (4.23)) of the difference between solutions with maximum level m and the reference maximum level 14 results.

can see that taking the maximum refinement level of $m = 13$ is sufficient to capture the evolution of the force. We found good agreement with the analytical solutions in the axisymmetric case, however the comparisons for the two-dimensional case were less favourable.

4.5.3 Linearised boundary validation

The linearised boundary setup detailed in §4.4.2 allows us to simulate deformable substrate cases, where w no longer has to be rigid. For the purposes of our results in Chapter 6, we focus only on the two-dimensional case. As before, we validate the method by imposing the motion of the substrate, where we will consider a full fluid-structure interaction in Chapter 6. We let $w(x, t) = 0$ for $t < 0$, and then for $t \geq 0$, we allow the substrate to oscillate in the same time dependent manner as depicted in

Figure 4.7, but now varying spatially such that

$$w(x,t) = a(1 - \cos(\omega t) + t^2)\left(1 - \frac{x^2}{L^2}\right), \tag{4.25}$$

where we again have $L = 2$, but for this case we let $a = 0.05$, $\omega = 4$, and the spatial variation is such that $w(x,t) = 0$ at $x = L$. These parameters are chosen less for their physical applicability, and more to demonstrate the effects substrate motion has on the solution, and to allow us to make use of the analytical solutions presented in Appendix A for substrates given by quadratic polynomials in x.

The fluid-structure interaction considered in Chapter 6 relies on coupling the pointwise position of the substrate with the pressure and the viscous stress of the fluid at that point. As the pressure is usually the dominating contribution to this, we focus here on validating the value of the pressure evaluated along a specific point on the substrate, namely at the origin, which we denote $p_m(0,t)$ for maximum refinement level m.

The validation for the pressure in the stationary setup and the linearised boundary setup are shown in Figure 4.10, with the same format as the previous validation plots, showing the analytical solution for the pressure from (3.151) in black dashed lines. In the analytical model, the pressure at the origin is infinite at the point of impact, which in practice we do not expect to happen. However, this does indicate that the initial pressure here should be high, and we plot the pressure with a semi-log plot for visual clarity. It can be seen from both figures that the pressure peaks in levels 10 and 11 are much lower than the higher levels, which indicates how we need higher refinement levels to accurately resolve the initial impact times. As noted before, the pressure values are prone to temporal fluctuations, which can be seen clearly for all of numerical results here. These can be particularly acute in interfacial regions, which is why we chose to remove the entrapped bubble for these cases. However, this removal process can still leave artefacts in the pressure which pertain for later times. For both cases, the pressure decreases after impact, with good agreement in the DNS solutions for levels 12-14. Note that from the solutions for the force presented in Figure 4.8, we expect the analytical solution to over-predict the pressure, which is seen in the stationary substrate case in Figure 4.10a. For the moving substrate case presented in Figure 4.10b, it seems that the analytical solution follows the DNS solution much more closely. We can infer then that the pressure in the DNS is not responding to the substrate motion as much as anticipated. This could be accounted for by recalling that we are applying the kinematic boundary condition along $z = 0$, rather than $z = -w(x,t)$, so we expect the response from the pressure to be less than

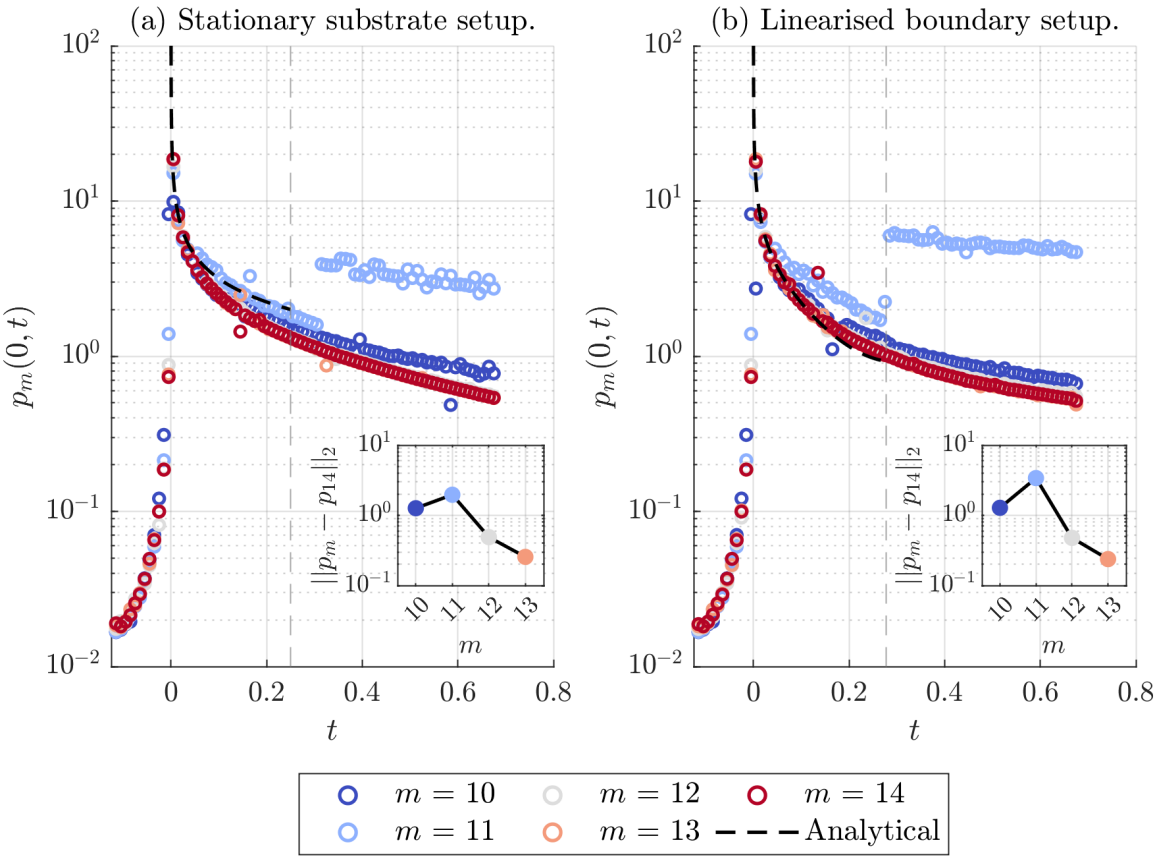

Figure 4.10: Numerical solutions for the pressure at the origin, $p_m(0,t)$, at maximum refinement level m varied between 10 and 14, where (a) shows the stationary substrate setup and (b) the linearised boundary setup with imposed substrate motion given by (4.25). The black dashed lines show the analytical solution given by (3.151).

would be the case if the boundary condition were applied along the substrate. This is an inherent limitation of the linearised boundary method and is only mitigated by ensuring the substrate deformation is as small as possible. Overall we do see that the pressure has a response to the substrate motion, and the inset plots show that we have reached numerical convergence for the chosen level 13 simulations.

As discussed earlier, another limiting factor of the linearised boundary setup is that it involves imposing a non-zero vertical velocity at the bottom boundary, which will lead to loss or gain of fluid mass as the substrate deforms. In order to assess the extent of this, we define $a_m(t)$ to be the area of the liquid phase at time t for the maximum refinement level m simulation, and then define the ratio between the change in droplet area and its initial area, $R_m(t)$ to be

$$R_m(t) = \frac{a_m(t) - \pi}{\pi}, \tag{4.26}$$

where π is the initial droplet area. For an exactly mass-conserving simulation, $R_m(t)$ should be 0 for all time. In the analytical model, the leading-order solution for the jet predicts that it has an infinite radial extent, which we know in practice cannot be true. So for an imposed solution given by (4.25), we derive an analytical approximation for the droplet area at time t by integrating the liquid flux through the boundary from $x = 0$ up to $x = d_0(t)$, where $d_0(t)$ is given by (3.51), such that

$$R_{\text{analytical}}(t) = -\frac{a}{\pi}\int_0^t (2\tau + \omega\sin(\omega\tau))d_0(\tau)\left(1 - \frac{d_0(\tau)^2}{3L^2}\right)\mathrm{d}\tau\,, \tag{4.27}$$

for $t > 0$. We can also determine the maximum amount of area lost by assuming that the entire plate is wetted for all time, and integrate $w_t(x,t)$ from $x = 0$ to L to find

$$R_{\max}(t) = -\frac{2aL}{3\pi}\int_0^t 2\tau + \omega\sin(\omega\tau)\,\mathrm{d}\tau\,. \tag{4.28}$$

Given this, in Figure 4.11 we plot the area ratio $R_m(t)$ for both stationary and linearised boundary setup with the imposed substrate solution given by (4.25), noting the difference in the vertical axes limits for each case. For the stationary setup, the area is conserved well for levels 12 and above, with much of the area change being the initial removal of the entrapped bubble and the later removal of the non-physical droplets that break off the end of the jets when the refinement level is too low. However for the linearised boundary setup, it is clear that the droplet is losing mass due to the substrate motion. The trend of this area ratio lies between the analytical approximation (4.27), which under-predicts the mass loss, and the maximum loss solution (4.28). As expected, increasing the refinement level in these cases does not prevent this from happening, as it is an inherent consequence of the scheme we have implemented. Overall, the area of the droplet varies by approximately 9% of its origin size, which would naturally be higher if we increase the magnitude of the substrate deformation. This limitation of the linearised boundary method can hence only be minimised by ensuring the substrate deformation is not too high, and in Chapter 6 we keep this mass loss in mind when interpreting results from the DNS.

The validation studies presented in this section show that choosing a maximum level of refinement of $m = 13$ is sufficient to capture the relevant quantities from the DNS needed for the results in Chapters 5 and 6. In these cases the width of the computational domain was $W = 6$. We will ensure that $W = 6 \times 2^n$ for later simulations, for some integer $n \geq 0$, with maximum refinement level $m = 13 + n$, to ensure the spatial resolution stays the same.

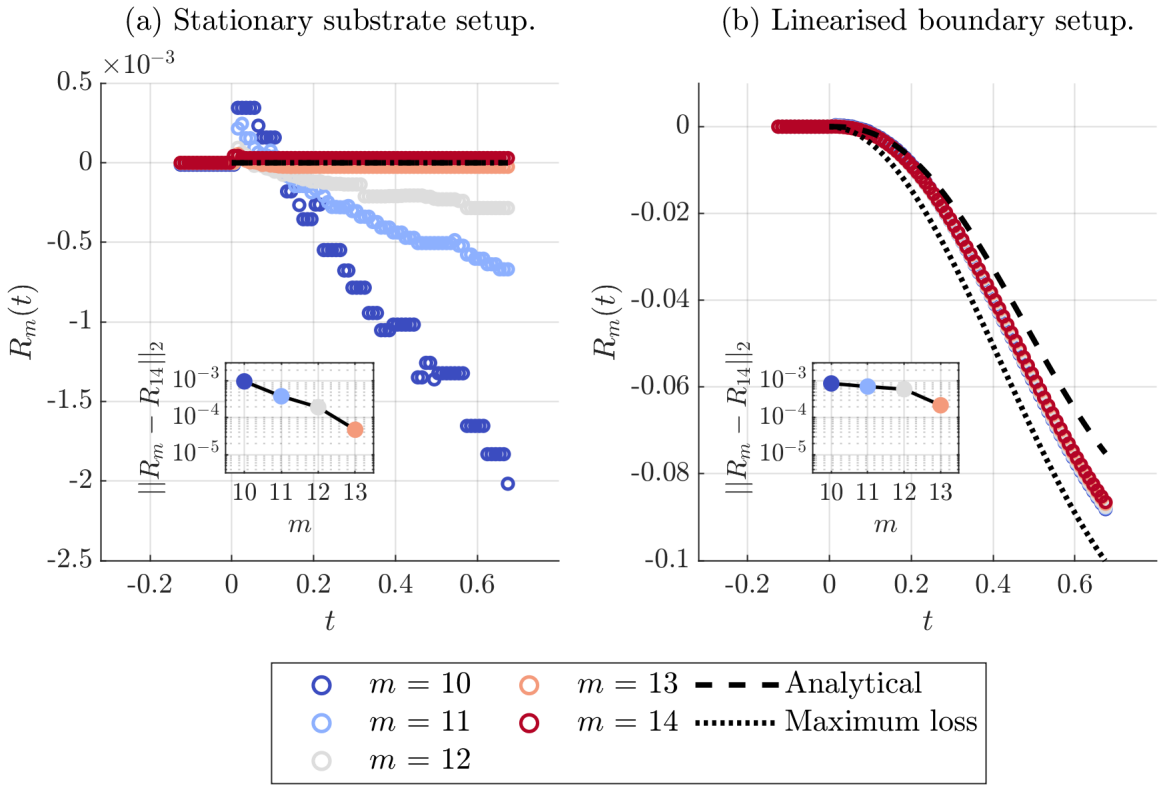

Figure 4.11: Numerical solutions for the area ratio of the droplet, $R_m(t)$, defined in (4.26), at maximum refinement level m varied between 10 and 14, where (a) shows the stationary substrate setup and (b) the linearised boundary setup with imposed substrate motion given by (4.25). The black dashed lines show the analytical solution given by (4.27), and the black dotted lines shown the maximum mass lost given by (4.28). The insets illustrate the L_2-norm (defined in (4.23)) of the difference between solutions with maximum level m and the reference maximum level 14 results.

Other chosen parameters of the system include the initial height of the droplet, the size of the computational domain and the tolerance of the Poisson solver. Overall, these quantities tend to have diminishing returns as they are increased (or decreased for the tolerance), so we will leave out a more detailed discussion of these parameters here for brevity. Overall, the numerical validation in this section lead us to the conclusion that the DNS schemes we have implemented are robust and are thus confident in using them in the later chapters for modelling impact onto deformable substrates. Furthermore, we have a clear understanding of the sources of errors, which will assist us in the interpretation of future results.

4.6 Fluid-structure interaction

The validation cases studied in the previous section involved imposing a pre-determined substrate motion, and validating that the flow reacted to this motion appropriately. In practice, the aim of this thesis is to study the fluid-structure interaction between the fluids and the substrate, such that the motion of the substrate depends on the flow, and vice versa. This interaction depends on the governing equations we use to couple these together, in which we consider different forms between Chapters 5 and 6. Hence we forgo the validation for the fluid-structure interaction until their relevant chapters, as this will first require us to validate the numerical schemes used to find the substrate motion in the absence of the fluid.

4.7 Summary

In this chapter, we have presented the methodology we will use to conduct direct numerical simulations of droplet impact onto deformable substrates. Within this, we have two strategies for modelling the motion of the substrate. The first is a moving frame setup, where we transform the reference frame of the simulation to one that is moving with the substrate, which is only valid for the case where the substrate is rigid. The alternative method relies on linearising substrate boundary conditions onto the flat computational boundary, which we have shown accurately predicts the pressure in the flow despite resulting in the mass of the droplet to no longer be conserved. We then provided a thorough validation study demonstrating the accuracy and robustness of our numerical scheme.

In the later chapters, the DNS will provide important cross-validation for the analytical model at early times, enabling us to assess the effects of the forces neglected by the analytical model. In addition, the DNS provides us with a framework to study the intermediate time-scales of the problem, once the droplet spreading across the substrate has become significant.

Chapter 5

Droplet impact onto a spring-supported plate

In the previous chapters, we presented both an analytical and a computational framework to model the fluid-structure interaction between the impact of a high speed droplet and a movable substrate. Within the respective chapters, we assumed the displacement of the substrate from its initial position remained small in comparison to the droplet size throughout the impact process. Besides that assumption, the position of the substrate was left as an unknown, and the methodologies were sufficiently general such that we can use them to model a variety of different fluid-structure interaction problems. Within the following two chapters, we will consider two separate fluid-structure interaction setups modelling the response the substrate has to the impacting droplet. This will allow us to gain insight into a range of physical applications, as well as cross-compare the results of the analytical and computational models to assess their predictive capabilities.

5.1 Spring-supported plate

For this chapter, we will consider the impact of a high-speed droplet onto a spring-supported plate, as first discussed in Chapter 2. For this case, the substrate is a rigid plate of dimensionless radius L, and is supported below by a Hookean spring and a linear dashpot. The axisymmetric analytical model presented in §3.3 was restricted to rigid substrates, which makes it applicable to the spring-supported plate case. Therefore, for brevity, in this chapter we will restrict ourselves to axisymmetric setups, although we note that the two-dimensional setups considered in Chapters 3 and 4 are also applicable to this problem. The model and results of this chapter are based on the results published by Negus et al. (2021) [65].

In this spring-supported plate model, the Hookean spring provides an elastic response to substrate displacement and the dashpot provides a viscous damping response. Although the geometric setup for this problem is idealised, many real-world fluid-structure interaction problems have these elastic and damping responses. One example is the impact of a droplet onto a leaf, which is common both during rain and in pesticide dispersal. In the study of Gart et al. (2015) [27], droplets were impacted onto cantilever beams in experiments inspired by situations where raindrops impact onto the end of leaves. The effects of the vibration frequency and damping of the beam affect the displacement, torque and bending energy of the beam throughout the process were measured. In addition, the tip of the oscillating beam was modelled as a damped harmonic oscillator, which yielded close experimental agreement despite the full beam equation not being taken into account. The governing equation (2.33) for the plate displacement we use for our spring-supported plate model is equivalent to that which Gart et al. (2015) [27] used to model the displacement of the tip of the beam. Therefore, although our model does not describe the full cantilever setup considered by Gart et al. (2015) [27], we will be able to gain insight into the effects the elastic and dampening components of the system have on the droplet at early times using this simple model.

In the following, we will be comparing predictions of both the analytical model (where $\epsilon \ll 1$) and the DNS (where $\epsilon = 1$). For consistency in our results, we will re-scale the time variable in our analytical solutions to match with the DNS, and we will only refer to quantities with the $\epsilon = 1$ time scaling. The axisymmetric analytical model is presented in §3.3, and the DNS will make use of the moving frame setup detailed in §4.4.1.

5.2 Solution for the plate displacement

Recall from Chapter 2 that the plate displacement (taking $\epsilon = 1$) at $z = -w(t)$ satisfies

$$\alpha\ddot{w}(t) + \beta\dot{w}(t) + \gamma w(t) = F(t), \quad w(t_0) = \dot{w}(t_0) = 0, \tag{5.1}$$

where $F(t)$ is the force exerted on the plate from above and the three dimensionless parameters are given by

$$\alpha = \frac{M^*}{\rho_l^* R_d^{*3}}, \quad \beta = \frac{c^*}{\rho_l^* V^* R_d^{*2}}, \quad \gamma = \frac{k^*}{\rho_l^* V^{*2} R_d^*}, \tag{5.2}$$

to which we refer to as the mass ratio, the damping factor and the stiffness factor, as they measure the relative strength of the mass of the plate, damping factor of

the dashpot and the stiffness of the spring in (5.1). For all of the cases studied in this chapter, we will consider a spherical droplet comprising of a liquid of density $\rho_l^* = 998$ kgm^{-3}, with initial radius $R_d^* = 1$ mm and downwards speed $V^* = 5$ ms^{-1}, such is typical for raindrops. We take the plate radius $L^* = 2R_d^* = 2$ mm, which is sufficiently large such that the extent of the splash sheet in the DNS remain on the plate. Therefore the mass ratio α, damping factor β and stiffness factor γ are completely determined by the mass of the plate M^*, the damping factor of the dashpot c^* and the stiffness of the spring k^*. The focus of this chapter is to determine the effects that these three components of the plate-spring-dashpot system have on the dynamics of the droplet. As this is an idealised toy model, we will focus on varying the dimensionless parameters α, β and γ to study regimes where the richest fluid-structure interaction is observed. In our parameter studies, we will draw back to the dimensional quantities to discuss the physical application of our results. As the droplet has a millimetric length scale, we will express the spring constant k^* in Newtons-per-millimetre to better understand the amount of force needed to compress the spring on these length scales.

For the analytical model, in §3.3.7 we derived two expressions for the force $F(t)$, which we will make use of for solving (5.1). The first is the leading-order force $F_0(t)$ given by (3.248), and the second is the composite force $F_{\text{comp}}(t)$ given by (3.251). Recall that the composite force was derived by directly integrating the composite solution for the pressure $p_{\text{comp}}(r,t)$ along the substrate, and thus tends towards the leading-order solution as $t \to 0$. However note that during the validation for the DNS in Chapter 4, we found from Figure 4.9 that the composite force agrees more favourably with the DNS solution at intermediate times, so we will therefore make use of both solutions and study the timescales in which each one is more appropriate. Both expressions for the force depend non-linearly on the leading-order acceleration of the substrate, $\ddot{w}_0(t)$. Because of this, the plate equation (5.1) with α, β, $\gamma = O(1)$ cannot be solved exactly even within the framework of the analytical model, and will need to be solved numerically. The resulting equation is a non-linear implicit ODE, which we solve using MATLAB's implicit, variable order differential equation solver, *ode15i*. For the timescales considered in this chapter, typically these numerical solutions are found within a few seconds on 1 CPU per set of plate parameters, which makes the analytical model solutions orders of magnitude faster to solve than the DNS solutions. However, for certain parameter regimes, leading-order solutions for $w(t) \sim w_0(t)$ can be found by making use of the leading-order force $F_0(t)$. To this

end, by substituting (3.248) into (5.1), the asymptotic solutions for $w(t)$ can be found from

$$\tilde{\alpha}\ddot{w}(t) + \tilde{\beta}\dot{w}(t) + \tilde{\gamma}w(t) \sim \frac{\mathrm{d}^2}{\mathrm{d}t^2}\left[(3(t - w(t)))^{5/2}\right], \tag{5.3}$$

where $\tilde{\alpha} = 8\alpha/45$, $\tilde{\beta} = 8\beta/45$ and $\tilde{\gamma} = 8\gamma/45$.

As *Basilisk* makes use of the *C* programming language, pre-built differential equation solvers compatible with the DNS implementation do exist, such as the *GSL library* or *Basilisk*'s own *Runge-Kutta solvers*. However, as (5.1) is relatively simple to discretise, we chose to implement our own finite difference scheme. We choose a constant timestep size $\Delta t = 10^{-4}$, and at every discrete timestep $t_k = t_0 + k\Delta t$, we directly integrate the pressure and viscous stress along the substrate using the trapezoidal rule to find the force, $F(t_k)$. We then discretise (5.1) to find $w(t_{k+1}) \approx w_{k+1}$ using the following explicit second-order scheme

$$w_{k+1} = \Delta t^2 F(t_k) + \left(2\alpha - \Delta t^2\gamma\right) w_k - \left(\frac{\alpha - \Delta t\beta/2}{\alpha + \Delta t\beta/2}\right) w_{k-1}, \tag{5.4}$$

Given this, the boundary conditions on the computational domain and the global acceleration at time t^k are updated by approximating the time derivatives of w by

$$\dot{w}(t) \approx \frac{w_{k+1} - w_{k-1}}{2\Delta t}, \quad \ddot{w}(t) \approx \frac{w_{k+1} - 2w_k + w_{k-1}}{\Delta t^2}. \tag{5.5}$$

Throughout the simulations, we ensure that the timestep used by the VOF solver is no greater than our chosen plate timestep $\Delta t = 10^{-4}$.

Having developed the two methods for solving (5.1) to find the plate displacement, we are ready to find the solutions for the full fluid-structure interaction problem with both methodologies for specific values for the plate parameters, α, β, γ.

5.3 Stationary plate comparison

We start by comparing the results of a specific set of substrate parameters to the case where the plate is held stationary. This will allow us to make a detailed analysis on the entire system, and to observe the effects the plate motion has on the fluid. In addition, we will also compare the solutions of the two adopted modelling techniques, inferring the timescales in which the analytical model and the DNS are in agreement. For the moving plate case, we choose the plate parameters such that the mass ratio $\alpha = 2$, the damping factor $\beta = 0$ and the stiffness factor $\gamma = 20$. These parameters were chosen as they represent a case where we observed a rich fluid-structure interaction within the system, such that there are clear differences between the moving plate case and the

stationary plate case. These parameters represent a plate of mass $M^* = 1.996 \times 10^{-6}$ kg, which is approximately half of the mass of the droplet, whilst the dimensional spring constant is $k^* = 0.499$ N/mm. As the mass of the plate is lower than that of the droplet, the momentum transfer from the droplet should allow the plate to considerably displace on the length scale of the droplet. However the stiffness of the spring should act to slow this motion after a certain level of displacement, hence we expect to see a rich interaction between the droplet and the plate in this scenario. For this section we will focus on the differences between these two cases, and we will provide a more extensive study on the effects each of the plate parameters have on the dynamics in §5.4.

The solution for the plate displacement at $z = -w(t)$, as well as the derivatives $\dot{w}(t)$ and $\ddot{w}(t)$, for the moving plate case are shown in Figure 5.1. The blue solid lines denote the DNS solutions, the red dashed lines denote the analytical solutions making use of the leading-order force $F_0(t)$ and the red dotted lines denote the analytical solutions making use of the composite force $F_{\text{comp}}(t)$. The DNS solutions are plotted from $t = t_0 = -0.125$ to $t = 0.675$. In a similar manner to the validation cases from Chapter 4, we only plot the analytical solutions up until the point the turnover curve $r = d_0(t) = 1$. As the two analytical cases have different predictions for the plate displacement, the turnover curve evolution is in turn different for each case, and therefore the time where $\epsilon d_0(t) = 1$ is different for each case. This occurs at $t \approx 0.41$ in the moving plate case making use of the leading-order force and at $t \approx 0.39$ in the moving plate case using the composite force. The vertical dashed and dotted lines in Figure 5.1 denote these respective times for each case. Note that in the stationary plate case, we have $d_0(t) = \sqrt{3t}$, so the turnover curve reaches $r = 0.5$ at $t = 1/3 \approx 0.33$ in the stationary plate case.

For Figure 5.1, that the plate experiences an initial strong downwards acceleration once the droplet impacts at $t = 0$. The elasticity of the spring will work against this acceleration, and from the plot of $-\ddot{w}(t)$, we find that the plate begins to accelerate upwards by $t \approx 0.5$. This is reflected in how the downwards velocity, $-\dot{w}(t)$, begins to decrease in magnitude at these later times. At early times (for $t \lesssim 0.025$), both of the analytical solutions agree well with the DNS, which is most clear on the plot for $-\ddot{w}(t)$. However for more intermediate times (from $t \gtrsim 0.05$), the analytical solution using the leading-order force agrees with the DNS less favourably than the analytical solution using the composite force. In fact, we have excellent agreement between the DNS and the composite force case right up until $t \approx 0.39$, at which point the turnover curve reaches the initial droplet radius. Even though this time marks the upper limit

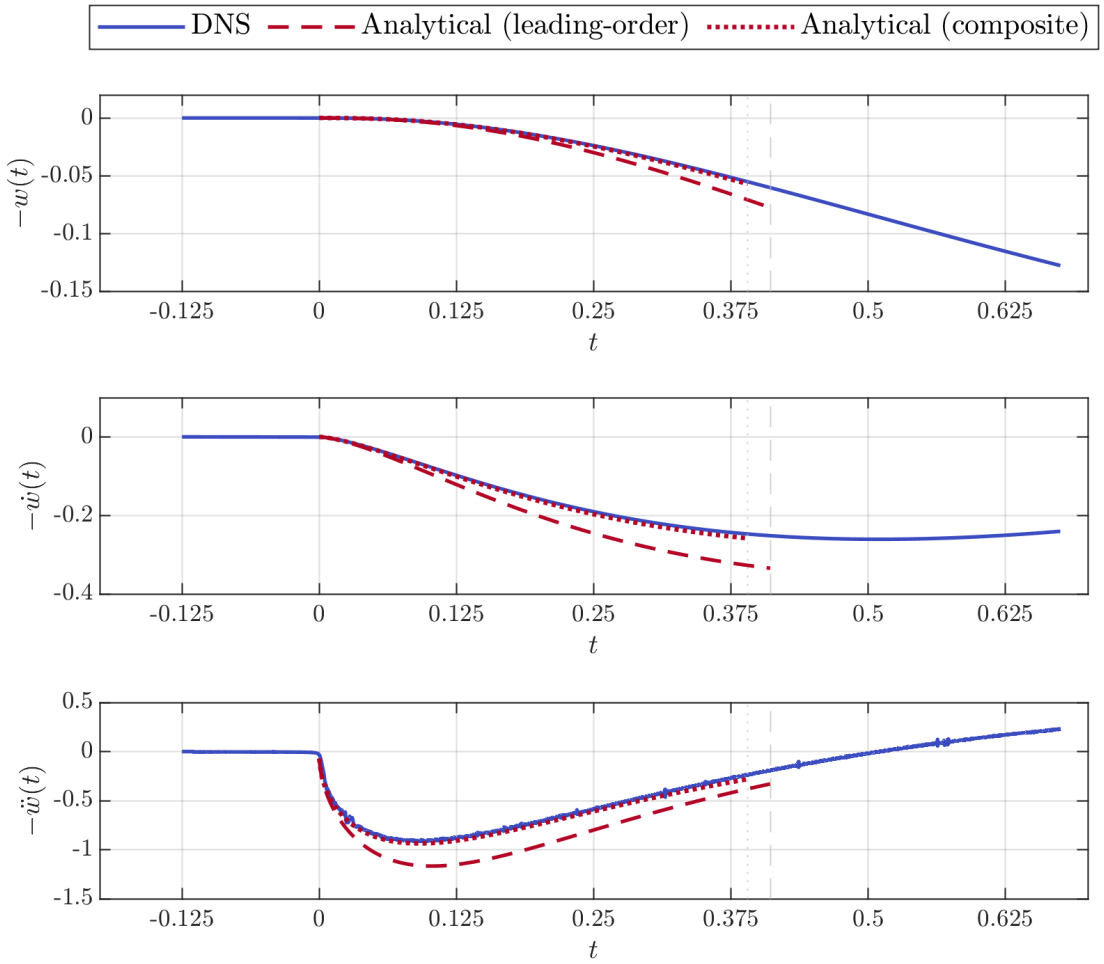

Figure 5.1: Solution for the plate displacement at $z = -w(t)$ and its time derivatives for $(\alpha, \beta, \gamma) = (2, 0, 20)$. The DNS solutions are denoted by blue solid lines, the analytical solution using the leading-order force given by (3.248) are shown with red dashed lines and the analytical solution using the composite force given by (3.251) are shown with red dotted lines.

of where we can use the analytical solution, we would typically expect its accuracy to break down much earlier, as the analytical model relies on assuming the outer region is much smaller than the overall droplet radius. Given this, the agreement between the DNS and the analytical solution using the leading-order force is still good, with the analytical solution capturing the overall trend of the displacement curves.

To fully understand the nature of the fluid-structure interaction, it is essential to know the hydrodynamic force exerted on the plate, $F(t)$. In Figure 5.2, we plot the solution for the force $F(t)$, showing the stationary plate case in Figure 5.2(a) and the moving plate case in Figure 5.2(b). In the same manner as Figure 5.1, the blue solid lines denote the DNS solutions, whilst the two different analytical solutions are

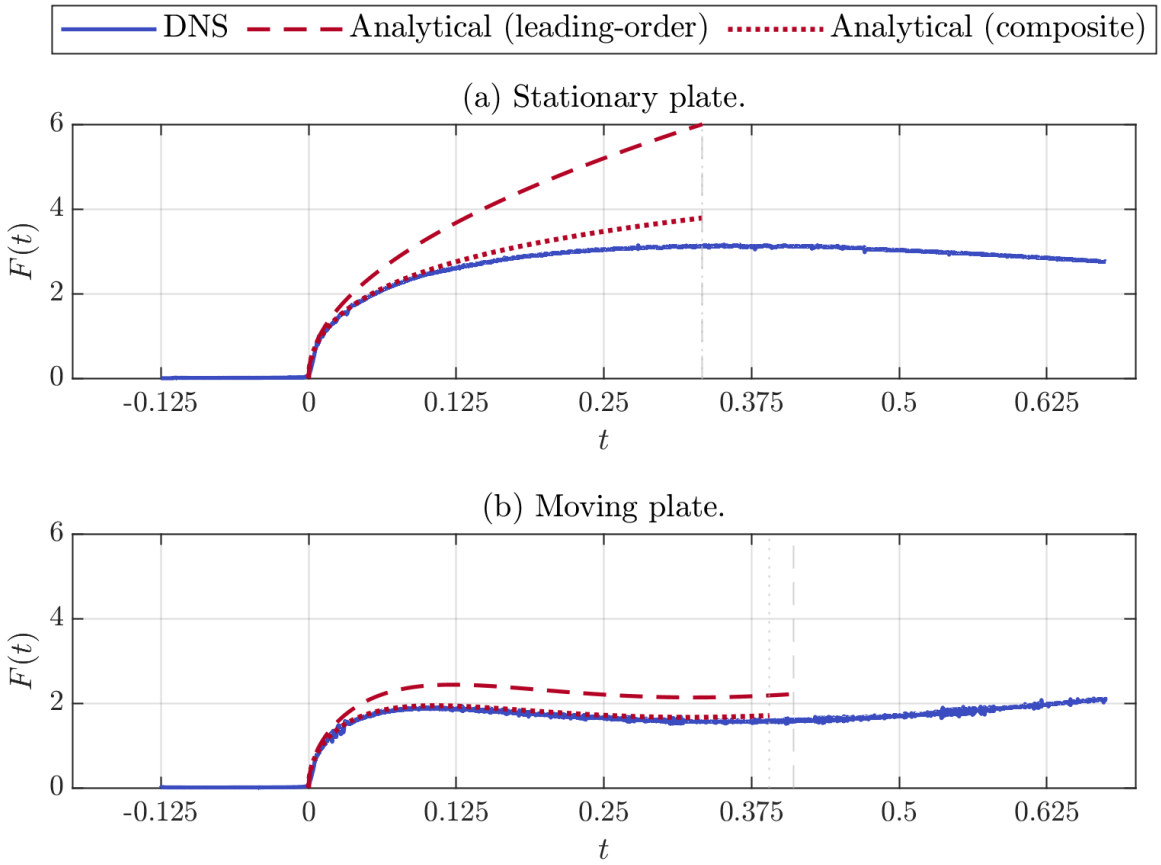

Figure 5.2: The hydrodynamic force on the plate, where the blue lines denote the DNS solutions, the red dashed lines denote the leading-order analytical force given by (3.248) and the red dotted lines denote the composite analytical force given by (3.251). Figure 5.2(a) shows the case where the plate is stationary, and Figure 5.2(b) shows the moving plate case for $(\alpha, \beta, \gamma) = (2, 0, 20)$.

denoted by red dashed and dotted lines respectively.

In the stationary plate case, the DNS solution predicts that the force experiences an initial growth stage, up until around $t \approx 0.35$ where the force begins to decrease monotonically. At early times, when the acceleration of the substrate is low, the force in the moving plate case is not noticeably different to the stationary substrate case. However by $t \approx 0.125$, the force in the moving plate case is noticeably lower, due to the strong downwards acceleration of the plate that can be seen in Figure 5.1. Eventually, once the acceleration changes direction at around $t \approx 0.5$, the force in the moving plate case then begins to increase, whilst the force in the stationary plate case is still monotonically decreasing. It is clear by comparing the force in Figure 5.2(b) and the plate displacement solutions in Figure 5.1 that there is a strong coupling between the motion of the plate and the hydrodynamic force. When comparing

the analytical solutions to the DNS in Figure 5.2, both analytical solutions agree well with the DNS at early times for $t \lesssim 0.025$. However, we again see how the two analytical solutions diverge from each other at more intermediate times, with the composite force case following the DNS solution more closely. Interestingly, the analytical solutions seem to diverge more from the DNS solution in the stationary plate case in comparison to the moving plate case. This may be due to fact that, as we will see later, the impact process is slowed down in the moving plate case compared to its stationary counterpart, therefore the early time assumptions of the analytical model are valid for a more extended period of time in the moving plate case. Given this, we still have very good agreement between the DNS and the analytical solution using the composite force up until about $t \lesssim 0.125$ in both stationary and moving plate cases. Recall that the leading-order force solution only considers contributions from the outer region, whereas the composite force was found by directly integrating the composite solution for the pressure between the outer and inner regions. The fact that the composite force case follows the DNS more closely suggests that the influence the inner region has on the force becomes significant relatively early on in the droplet impact process, and is worth retaining in the solution used for the force in order to extend the temporal scale in which the analytical model can accurately be used.

Given the clear differences in the force between the stationary and moving plate cases, it is worth investigating how the properties of the fluid phase as a whole are affected by the plate motion. The most direct quantities that determine the force are the pressure and viscous stress along the substrate. These quantities are both present in the DNS, but the viscous stress is absent from the analytical model due to its neglect of viscosity. However, we found that typically the viscous stress along the substrate in the DNS was $\approx 10^5$ times smaller than the pressure, and was prone to noise due to the small length-scales. Therefore we can conclude that the pressure along the plate provides the dominant contribution to the force in the DNS, so in Figure 5.3, we plot the pressure along the plate in both the stationary and moving plate cases, where we plot the pressure from $t = 0.025$ up to $t = 0.275$ at regular temporal intervals of 0.05. Due to the better agreement found by using the composite force in Figure 5.2, we only show the analytical solution for the composite pressure $p_{\text{comp}}(r, t)$ (given by (3.246)). The DNS solutions are plotted with blue solid lines, and the analytical solutions in red dotted lines. Lines plotted at later times are shown in lighter colours for visual clarity.

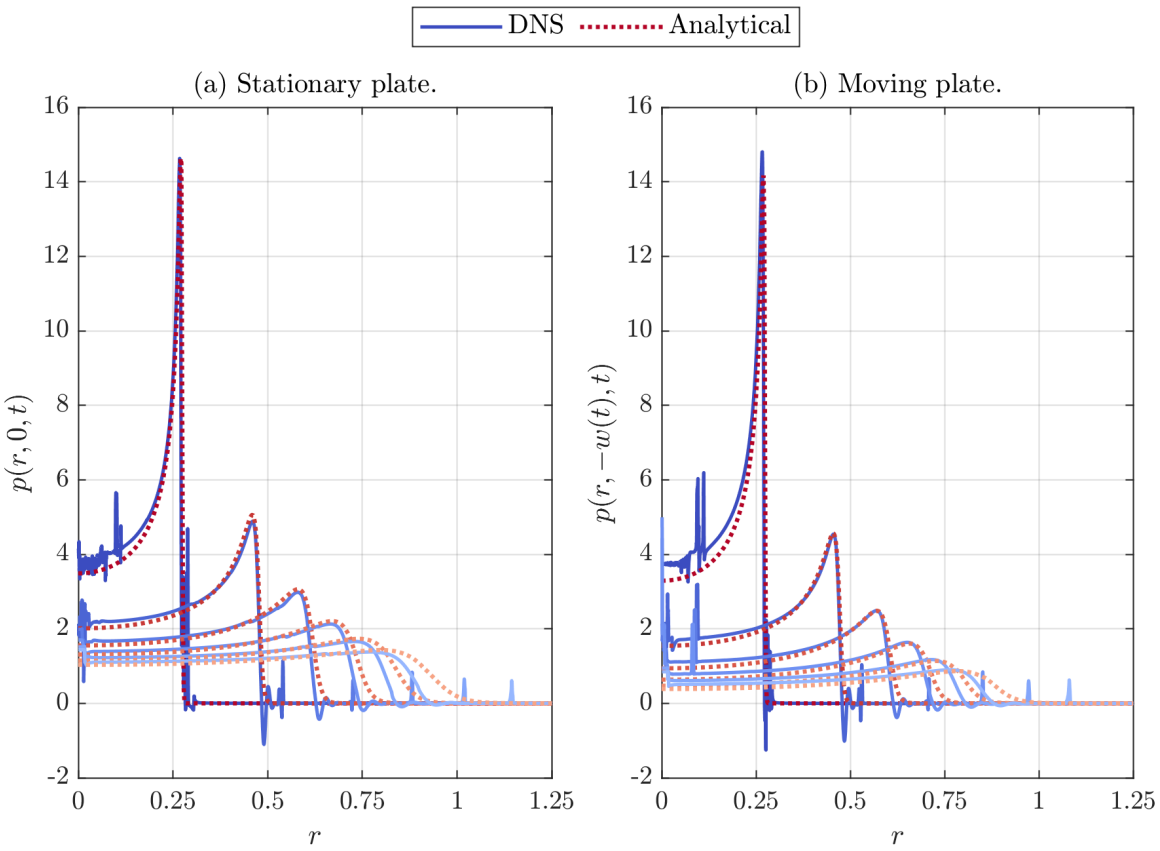

Figure 5.3: The pressure on the plate, where the blue lines denote the DNS solutions, and the red dotted lines denote the composite pressure given by (3.246). The solutions are plotted from $t = 0.025$ to 0.275 in regular temporal intervals, with the lighter colours denoting later times. Figure 5.3(a) shows the case where the plate is stationary, and Figure 5.3(b) shows the moving plate case for $(\alpha, \beta, \gamma) = (2, 0, 20)$.

By comparing the stationary and moving plate cases in Figure 5.3, we find that for the early times, the pressure is mostly unaffected by the plate motion, which is reflected by the force in Figure 5.2 for $t \lesssim 0.025$. At later times, the peak in the pressure in the moving plate case is lower, as well as the radial extent of the pressure peak being smaller due to the slower evolution of the turnover curve. Overall this makes it clear why the force in the moving plate case in Figure 5.2(b) is lower than in the stationary plate case for $t \leq 0.275$. By focusing on the DNS solutions, we observe that there are typically two spatial regions at each timestep where the solution experiences numerical noise. The first is close to the origin, which is due to the presence of the entrapped gas bubble. Although from Figure 4.5 we showed that this entrapped bubble is well-resolved geometrically, it still represents a small volume in comparison to the size of the entire droplet. Typically this entrapped bubble emerges from a region of initially high pressure upon impact, and thus the combination of

the small length scale and high pressures result in the observed numerical noise. The second region that experiences noise is typically to the right of the pressure peak, and by investigating snapshots of the DNS, we found this to align with the tip of the splash sheet. This peak occurs due to the cells close to the tip which are a mix of both fluid phases, and are therefore prone to fluctuations in pressure due to the surface tension. Numerical fluctuations in pressure such as these are common for volume-of-fluid simulations, such was observed by Philippi et al. (2016) [74] in their DNS for droplet impact onto a solid surface using *Gerris* (the predecessor to *Basilisk*). Increasing the spatial resolution of the simulations could reduce some of these numerical fluctuations by resolving the entrapped bubble and splash sheet to a higher degree. However, as the force is determine by integrating the pressure across the entire plate, these small regions of numerical noise have a minimal effect on the solution for the force at our chosen level of refinement, as was seen in the numerical validation presented in Figure 4.9.

At early times, we observe from Figure 5.3 that the analytical solutions agree well with the DNS in the vicinity of the pressure peaks. Close to the origin, the analytical solution typically under-predicts the DNS solution. This under-prediction may be due to the analytical model not taking into account the initial build up of pressure close to the origin prior to impact due to the presence of the gas. At more intermediate times, the analytical solution typically disperses out to a larger radial extent than the DNS, with a slower decay of pressure tending towards the splash sheet. This is reflected in Figure 5.2, where for $t \gtrsim 0.125$ the analytical solution typically over-predicts the solution for the force in comparison to the DNS. As we will see in Figure 5.7, this may be also due to the fact the analytical model predicts the radial extent of the turnover curve to be greater than what we actually see in the DNS.

The differences in the pressure along the plate between the two cases shown in Figure 5.3 motivates us to analyse how the pressure across the entire droplet is affected by the plate motion. Although we have the solution for the pressure in each the individual region of the analytical model, we would need to construct a global composite solution for the pressure to find the solution everywhere. However, we do readily have access to this data for the DNS. In Figure 5.4 we show the global distribution of pressure from the DNS at a series of times. The left-hand sides of each sub-figure show the stationary plate case, while the right-hand sides shows the moving plate case, where the pressure scales are adjusted in each sub-figure to reflect the dynamically changing pressure. The vertical placement of the snapshots are adjusted to take into account the moving plate case, where the position of the plate is

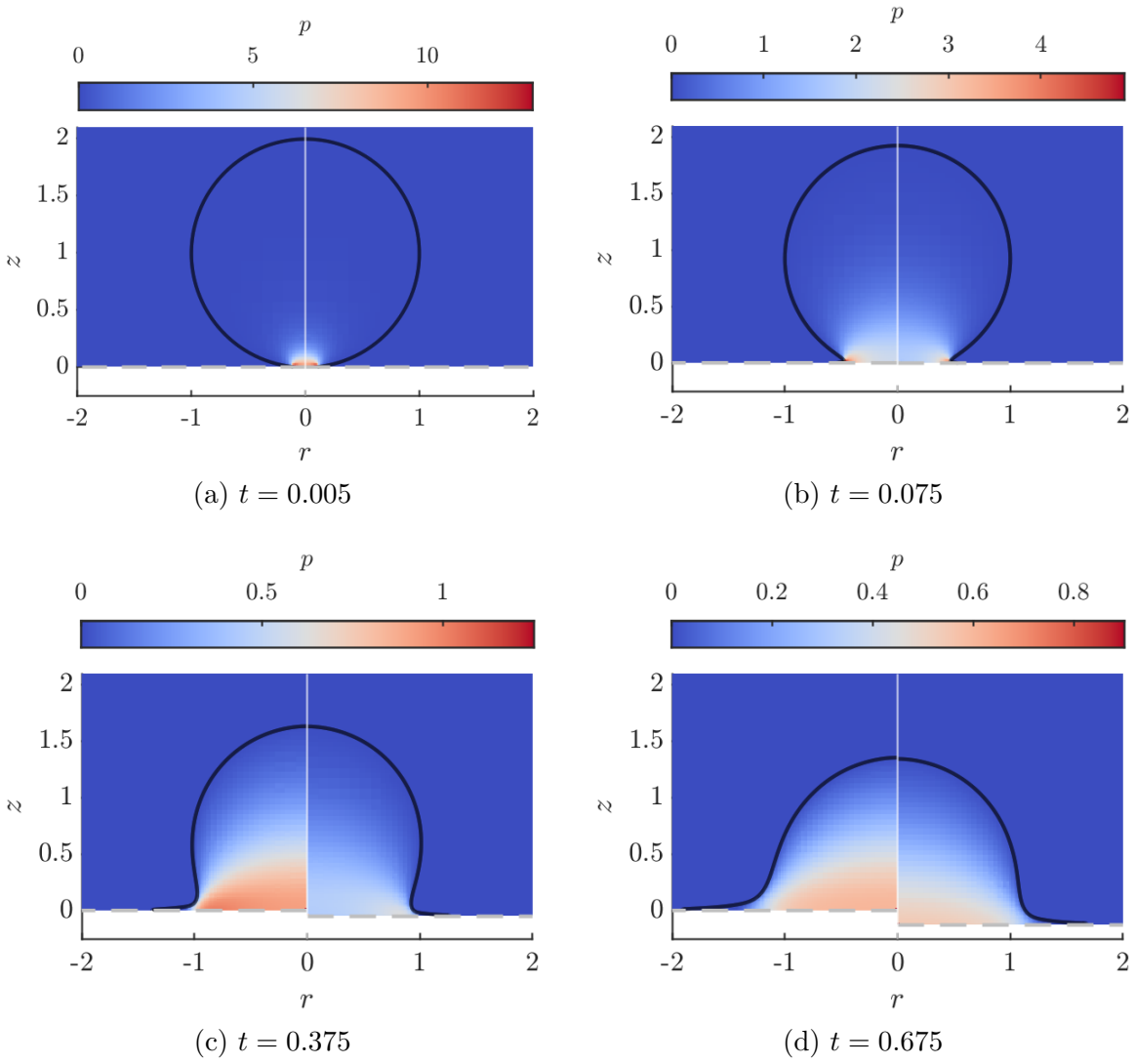

(a) $t = 0.005$ (b) $t = 0.075$

(c) $t = 0.375$ (d) $t = 0.675$

Figure 5.4: Snapshots of the pressure distribution predicted by the DNS, where the left-hand side of each sub-figure denotes the stationary plate case and the right-hand side of each sub-figure denotes the moving plate case for $(\alpha, \beta, \gamma) = (2, 0, 20)$. The snapshots for the moving plate case are displaced downwards to reflect the position of the plate.

denoted by the dashed horizontal grey lines. Figure 5.4(a) shows the pressure shortly after impact, where we note that the stationary and moving plate cases are visually indistinguishable as the plate acceleration is still low. At $t = 0.075$, depicted in Figure 5.4(b), the plate displacement is still small, however minute differences in pressure close to the turnover region can be seen, indicating the downwards acceleration of the plate is beginning to affect the droplet. At the intermediate time of $t = 0.375$, shown in Figure 5.4(c), we observe that the pressure in the moving plate case is significantly lower than the stationary plate case, as the downwards acceleration of the plate has

reduced the pressure in comparison to the stationary plate case. For the final timestep of the simulation at $t = 0.675$, shown in Figure 5.4(d), the pressure difference between the two cases has reduced, as at this time we found from Figure 5.1 that the plate is now accelerating upwards. Overall from the four snapshots shown in Figure 5.4, we can see that the plate motion has a strong effect on the global pressure distribution within the droplet, which is then in turn coupled back to the plate motion via the hydrodynamic force $F(t)$ in (5.1).

The preceding figure shows that there is a rich coupling between the pressure distribution in the droplet and the plate motion. Recall that the fluid-structure interaction happens via the kinematic boundary condition at the plate (2.28), which enforces that the fluid velocity matches the velocity of the plate along the plate surface. We observe that when the plate is moving downwards, the resulting pressure in the droplet decreases, and vice-versa when the plate moves upwards. Overall this reflects the amount of work the plate is doing on the droplet. When the plate is moving downwards, this will be lower than the stationary substrate case, and similarly when the plate is moving upwards, this work is increased. Although there is a strong coupling between the pressure and the plate motion, the pressure is a quantity that is difficult to measure experimentally and it is not clear from analysing the pressure alone the overall effect of the plate motion on the droplet dynamics. One quantity of particular interest is the location of the droplet interface. Most experimental studies of droplet impact are focused on capturing the interface location via imaging techniques, such as laser interferometry and high-speed photography; see, for example, Pepper et al. (2008) [72] and Fudge et al. (2021) [25]. The velocity of the droplet can also be inferred from the evolution of the interface, and changes in the interface ultimately determine whether or not the droplet eventually splashes.

Although we can find the location of the entire interface using both the analytical model and the DNS, it is more conducive to first start by comparing the evolution of the turnover curve. Recall that this is defined to be the point where the interface turns over and ejects fluid across the substrate. Within the analytical model, the leading-order radial position of the turnover curve is at $r = d_0(t)$, where from (3.204) we have $d_0(t) = \sqrt{3(t - w_0(t))}$. The vertical height of the turnover curve above the plate is $H(t)$, where from (3.90), $H(t) = (1+4/\pi)J(t)$ with $J(t)$ given by (3.218). We find the turnover curve location from the DNS in the post-processing stage, where we locate the interface line segment with the minimum radial extent, excluding the entrapped bubble and the upper-half of the droplet. Given this, the radial position of the turnover curves are shown in Figure 5.5 for both stationary and moving plate

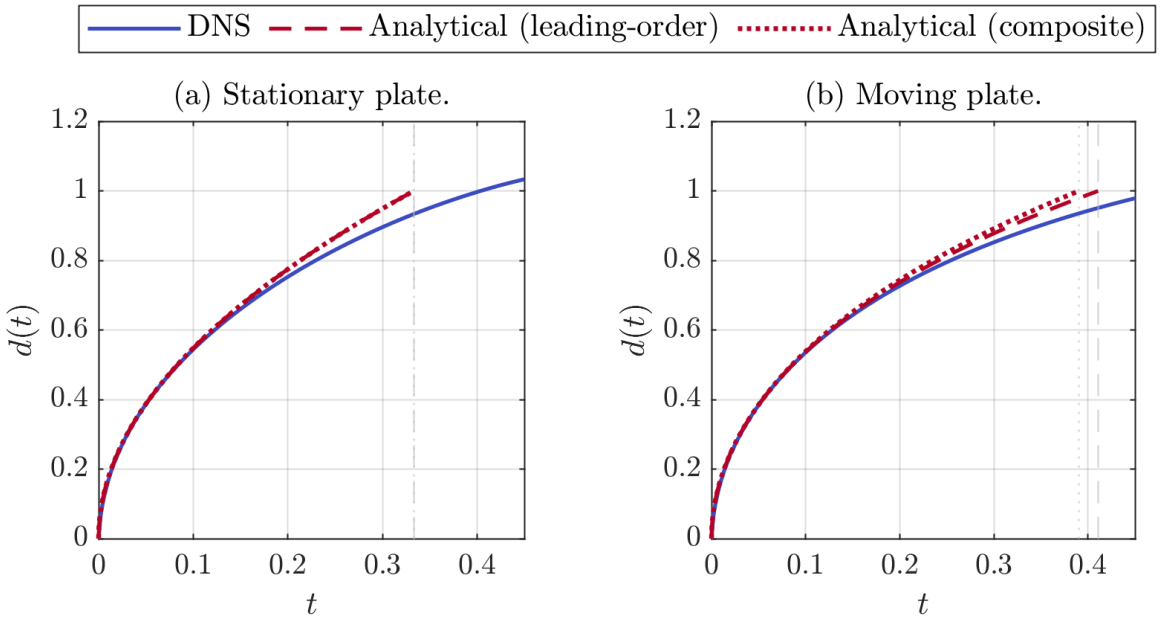

Figure 5.5: Radius of the turnover curve, where the blue lines denote the DNS solutions, the red dashed lines denote the analytical solution (3.204) where the leading-order force has been used to find the plate displacement, and the red dotted lines denotes the analytical solution using the composite force. Figure 5.5(a) shows the case where the plate is stationary, and Figure 5.5(b) shows the moving plate case for $(\alpha, \beta, \gamma) = (2, 0, 20)$.

cases. As before, we denote the DNS solutions with solid blue lines, whilst the analytical solutions using the leading-order force are denoted by red dashed lines, and the analytical solutions using the composite force are denoted by red dotted lines.

By comparing the stationary and moving plate cases in Figure 5.5, we conclude that the radius of the turnover curve evolves more slowly in the moving plate case. This was expected from the analytical model, as we have from (3.204) that $d_0(t) = \sqrt{3(t - w_0(t))}$, such that the downwards displacement of the plate acts to lower the value of $d_0(t)$ in comparison to the stationary plate case. As discussed in §3.3.2.2, the turnover curve must evolve more slowly in the moving plate case in order to conserve mass, as there is a finite volume of fluid below the plane the plate initially lies in. Overall, both analytical solutions have very close agreement with the DNS solution for $t \lesssim 0.2$, and begin to over-predict the solution for later times. This may be caused by the finite liquid viscosity in the droplet present in the DNS slowing down the spreading of the droplet at a faster rate than predicted by the analytical model, which neglects viscous effects.

Similarly, in Figure 5.6, we show the height of the turnover curve, $H(t)$, for the

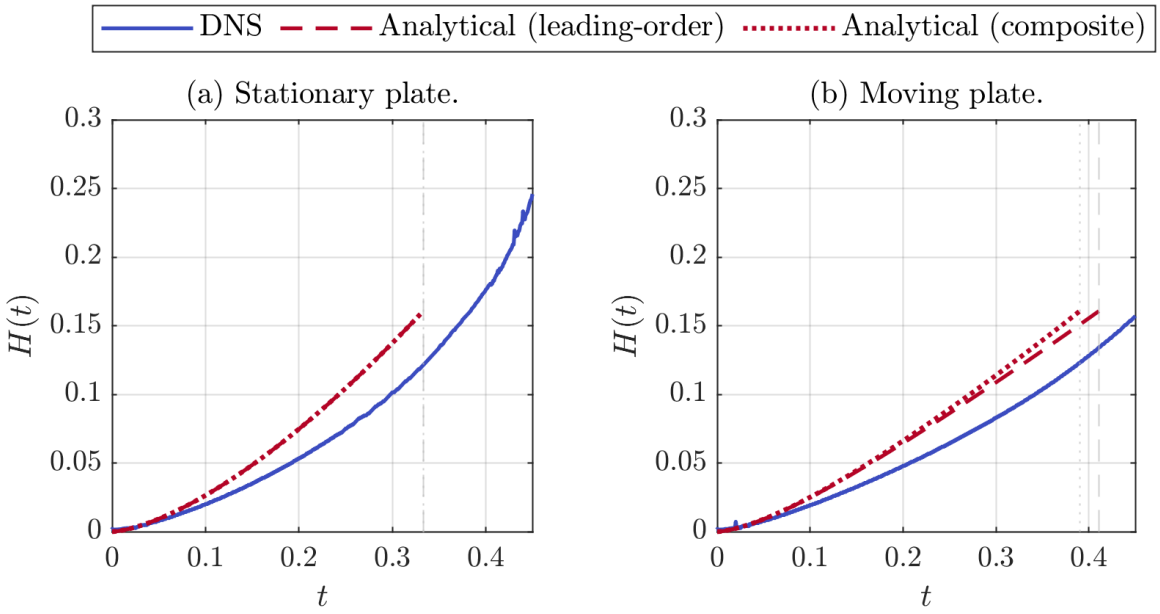

Figure 5.6: Height of the turnover curve above the plate, where the blue lines denote the DNS solutions, the red dashed lines denote the analytical solution (3.90) where the leading-order force has been used to find the plate displacement, and the red dotted lines denotes the analytical solution using the composite force. Figure 5.6(a) shows the case where the plate is stationary, and Figure 5.6(b) shows the moving plate case for $(\alpha, \beta, \gamma) = (2, 0, 20)$.

stationary and moving plate cases, where the analytical solution is given by (3.90). From the DNS solutions, it is clear that the height of the turnover curve is substantially reduced in the moving plate case for $t \gtrsim 0.35$. This, alongside the slower radial evolution of the turnover curve, show that the splash sheet in the moving plate case will be ejected more slowly and with a lower thickness. This could relate to the splashing suppression mechanism discussed by Howland et al. (2016) [46], because if the splash sheet is slower and contains a smaller amount of fluid, it will be less likely to break up into a splash. The analytical solutions for $H(t)$ in Figure 5.6 agree less favourably with the DNS than the solutions for the turnover curve radius. This discrepancy could be due to the analytical model not accounting for the surface tension, which has a significant role in determining the shape of the splash sheet as it emerges from the turnover curve at early times.

Having identified changes in the turnover point position in Figures 5.5 and 5.6, we can investigate further by plotting the interface local to the turnover curve in order to understand the effect the plate motion has on the interface. For the DNS, this amounts to plotting the interface line segments in a small region close to the already identified turnover curve position. For the analytical solution, we have three

different asymptotic regions that meet at the turnover curve. The turnover curve is approached from above in the outer region, tending towards the small inner region local to the turnover curve, in which we then tend towards the splash sheet as we extend radially outwards from the inner region along the plate. To find the free surface local to the turnover region, we construct a piecewise composite solution across these three regions. For the upper part of the free surface, we can match the outer and inner region solutions to find a composite solution for the upper half. For the lower part, we can match the inner and splash sheet solutions. As the outer solution meets the substrate at the turnover curve by the Wagner condition, and the splash sheet emanates radially from the turnover curve, we do not need to match the outer and splash sheet regions and can hence construct a piecewise composite solution.

We plot the interface location local to the turnover curve in Figure 5.7 for both the stationary and moving plate cases. The curves are plotted for $t = 0.005$, $t = 0.07$, $t = 0.135$ and $t = 0.2$, with later times plotted in lighter colours. Recall that the analytical model predicts that the splash sheet emerges immediately at the time of impact, and has an infinite radial extent. This is a consequence of the analytical model neglecting surface tension and viscosity, and in practice the splash sheet emerges shortly after the time of impact with a finite radial extent. This can be seen at the earliest time solutions at $t = 0.05$, where we find that the splash sheet has yet to emerge in the DNS solutions. At time $t = 0.07$, the splash sheet has emerged in the DNS solutions, and we note how the analytical solutions follow the DNS closely local to the turnover curve. As expected, the agreement breaks down as we extend outwards radially, as the analytical solutions predict the splash sheet extends infinitely. At later times, the analytical solutions tend to over-predict the radial and vertical position of the turnover curve. This may be a consequence of neglecting the surface tension effects, which have a stronger influence in the small length scales local to the turnover curve. Although we observe that the vertical position of the interface is lower in the moving plate case due to the plate displacement, we know from Figure 5.6 that the height of the turnover curve above the plate for $t \lesssim 0.2$ is largely unaffected by the plate motion.

From Figure 5.6, we observe that the substrate motion affects the height of the turnover curve more significantly for $t \gtrsim 0.3$. At these more intermediate times, we know from Figures 5.5 and 5.6 that the analytical solution begins to diverge from the DNS as the turnover curve approaches and exceeds the initial droplet radius. Given this, in Figure 5.8 we plot just the DNS solutions for the interface at times $t = 0.25$, $t = 0.425$ and $t = 0.6$. As before, lighter colours denote later times, and

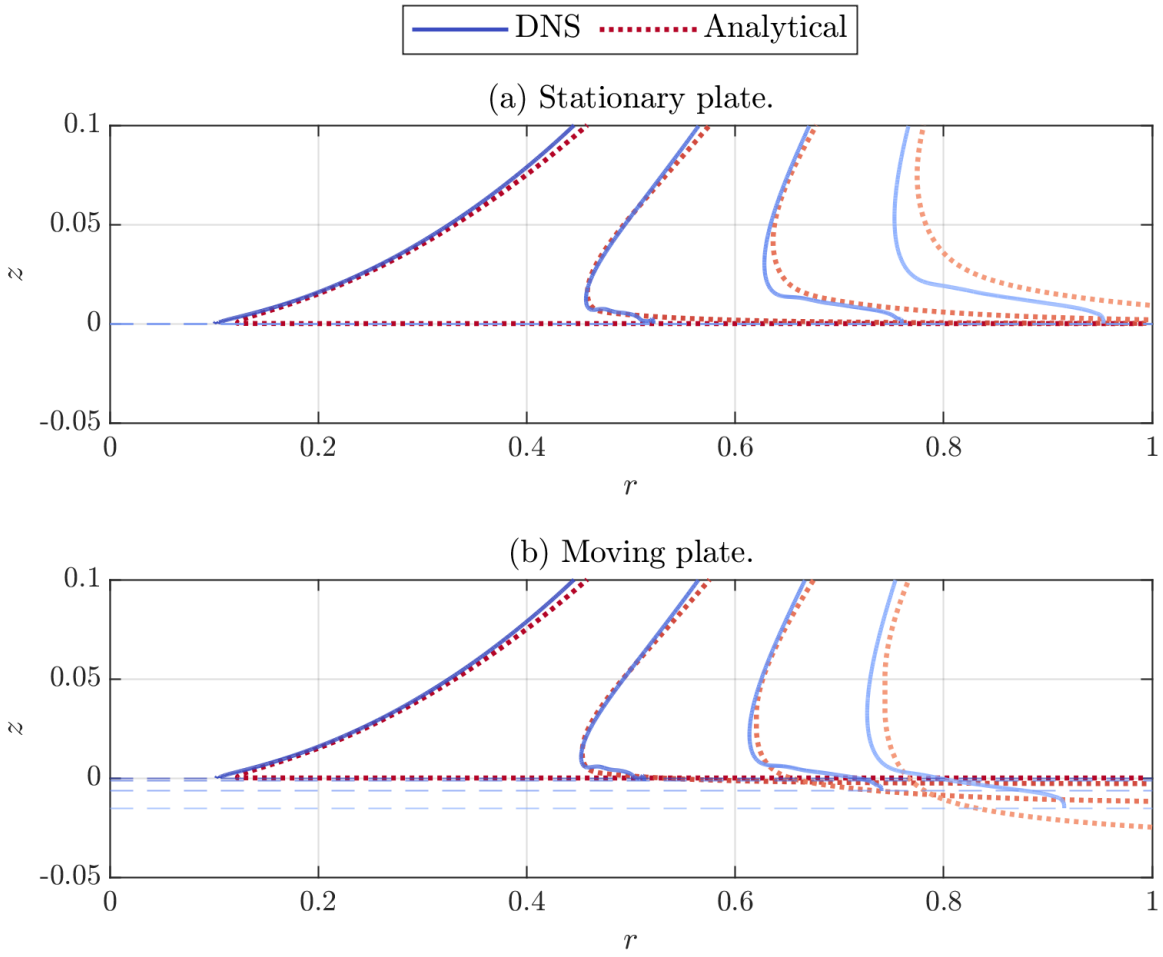

Figure 5.7: Interface of the droplet, where the blue lines denote the DNS solutions and the red dashed lines denote the analytical solutions. The lines are plotted for $t = 0.005$, 0.07, 0.135 and 0.2, with the lighter line colour denoting later times. Figure 5.7(a) shows the stationary plate case and Figure 5.7(b) shows the moving plate case for $(\alpha, \beta, \gamma) = (2, 0, 20)$.

the horizontal dashed lines denote the location of the plate. For $t = 0.25$, the vertical displacement of the plate is still relatively small, but it is clear that the radius of the turnover curve is smaller in the moving plate case. This effect is amplified at later times, where the radial extent of both the turnover curve and the tip of the splash sheet is significantly smaller in the moving plate case. By referring back to Figure 5.4, we find that the bulk of the droplet interface is largely unaffected by the substrate motion at these later times, so we can conclude that the plate motion predominantly acts to slow down the initial spreading and ejection of the splash sheet of the droplet. This behaviour is similar to the experimental findings of Howland et al. (2016) [46], in which it was found that the bulk of the droplet was unaffected by the stiffness of

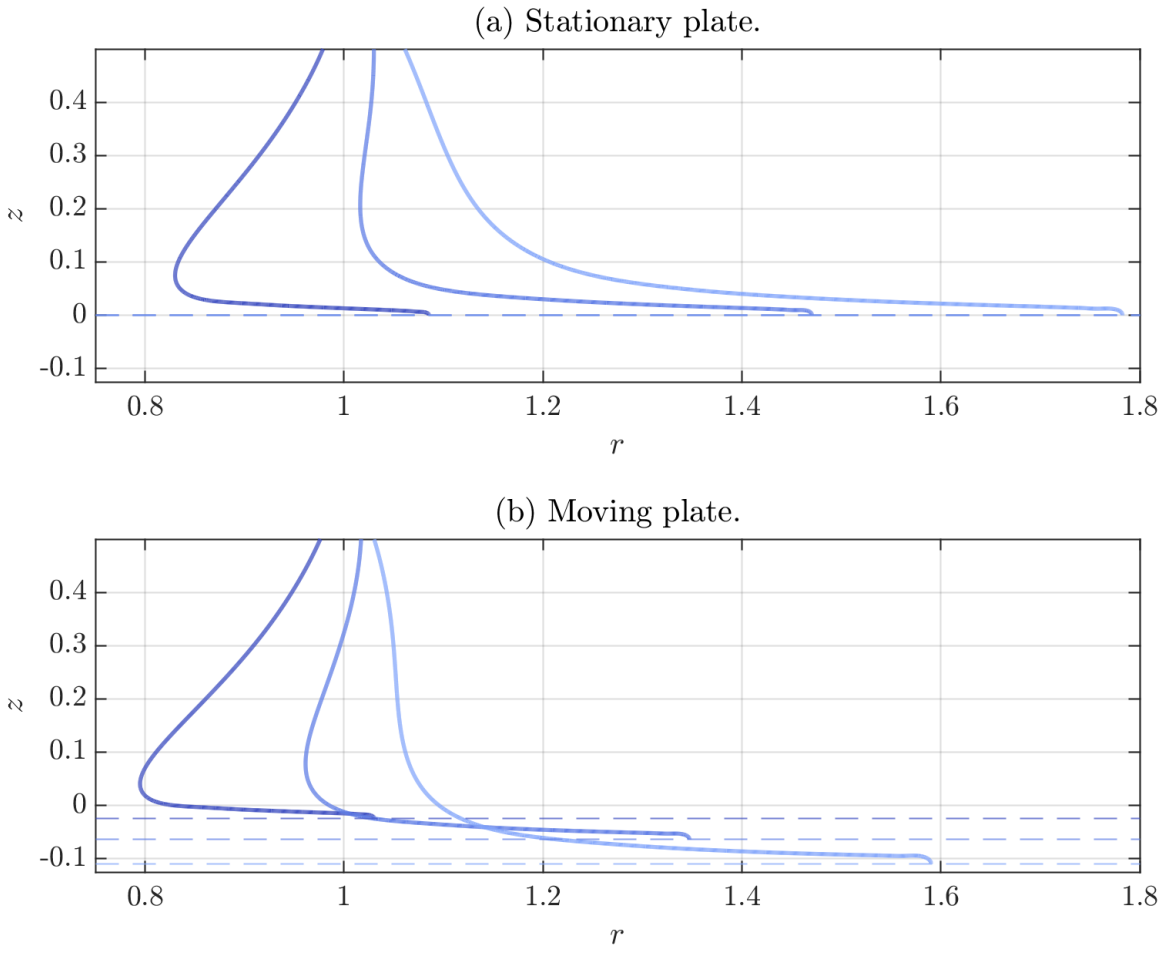

Figure 5.8: DNS solutions for the interface of the droplet for $t = 0.25$, 0.425 and 0.6, where the lighter lines denote later times. The horizontal dashed lines denote the position of the plate. Figure 5.8(a) shows the stationary plate case and Figure 5.8(b) shows the moving plate case for $(\alpha, \beta, \gamma) = (2, 0, 20)$.

the substrate, and differences between cases are isolated to the ejection of the lamella at early times.

In this subsection, we have focused on comparing the differences between a specific plate-spring-dashpot setup to the case where the plate is stationary, allowing us to focus on the fine details of the predictions from both of our presented modelling techniques. We have found how the acceleration of the moving plate changes the internal pressure distribution of the droplet, which is ultimately coupled to the plate motion via the exerted hydrodynamic force. We then saw how the plate motion acts to slow down the spreading of the droplet across the plate, localising changes in the droplet interface close to the substrate. This provides insight into the splash-suppression mechanism discussed by Howland et al. (2016) [46], where it was found

that droplets are less likely to splash when impacting more compliant substrates.

By utilising the composite solution for the force (3.251), we found that the predictions of the analytical model closely follow the results of the DNS for the plate displacement, hydrodynamic force, pressure and turnover curve radius up until around $t = 0.25$, at which point the turnover curve radius was approximately 0.8 times the initial droplet radius. This is an encouraging result for the validity of the analytical model at times far beyond what would have typically been expected. We saw from Figures 5.6 and 5.7 that the analytical model is less effective at predicting the evolution of the splash sheet, at which point surface tension effects become more dominant. Overall the close agreement of the analytical model and DNS for the relevant quantities and timescales is encouraging, in particular as the computational cost of finding the analytical solutions is significantly smaller than the DNS.

The results presented in this section represent only one particular plate-spring-dashpot setup. In order to fully understand the mechanisms involved in the fluid-structure interaction between the droplet and the plate, we need to study a wide range of plate parameters and compare the effects each of these have on the studied droplet impact dynamics.

5.4 Plate parameter comparisons

Recall that the plate-spring-dashpot system is characterised by three dimensionless parameters. The mass ratio, $\alpha = M^*/(\rho_l^* R_d^{*3})$, is proportional to the ratio between the mass of the plate and the mass of the droplet, with $\alpha = 4\pi/3$ representing the case where their masses are equal. The damping factor, $\beta = c^*/(\rho_l^* V^* R_d^{*2})$ represents the strength of the damping provided by the dashpot and the stiffness factor $\gamma = k^*/(\rho_l^* V^{*2} R_d^*)$ represents the stiffness of the spring. Increasing each of these parameters acts to lessen the magnitude of the plate displacement upon impact, however they individually represent different physical processes of the plate-spring-dashpot system.

In order to determine the influence each of these parameters have on the dynamics of the system, we need to conduct an extensive parameter study, varying the values of α, β and γ across many orders of magnitude. Given that the DNS typically takes around 24 CPU hours to resolve per set of parameters, it would take a large amount of computational resources to conduct this parameter study with the DNS alone. Fortunately, in the previous section we found numerical evidence of very good agreement between the analytical model and DNS solutions for times $t \lesssim 0.25$ for

particular quantities, where the radius of the turnover curves reached ≈ 0.8 times the initial droplet radius. As the analytical solutions are found in a matter of seconds per set of parameters, we opt to use the analytical model to conduct this extensive parameter study. Then, the results of the analytical parameter sweep can be used to identify regimes of interest that we can target for DNS in order to study the later times in which the analytical solution break down.

In the following, we will conduct three different parameter studies, where for each we vary one of the plate parameters α, β or γ, whilst keeping the other two fixed. This allows us to isolate the effects each parameter has on the dynamics, with the aim of measuring how a selection of key quantities at a specific time differ as we vary each of these parameters in turn. To this end, we choose a test time $t_c = 1/12 \approx 0.083$, such that the analytical model predicts the turnover curve radius $d_0(t_c) = \sqrt{3t_c} = 0.5$ in the stationary plate case. From the previous section, we found that the analytical model and DNS solutions agreed well up until the turnover curve radius reached around 0.8. Therefore the time $t_c = 1/12$ is chosen as we expect the analytical model to agree well will the DNS solutions at time time. At t_c, we save the radius of the turnover curve $d_0(t_c)$, the radial speed of the turnover curve, $\dot{d}_0(t_c)$; the height of the turnover curve above the plate, $H(t_c)$; and kinetic energies in the outer region, $E_{K,\text{outer}}(t_c)$, and the splash sheet region, $E_{K,\text{splash}}(t_c)$. These quantities give us an insight into how the plate motion affects the interface close to the plate, as well as an indication into the distribution of the kinetic energy across the droplet. For each parameter sweep, we test 500 different cases, varying one of α, β or γ across different orders of magnitude.

5.4.1 Mass ratio

We start by varying the mass ratio, α, whilst setting both the damping factor and stiffness factor to zero, i.e. $\beta = \gamma = 0$, and solving (5.1) numerically, making use of the composite force $F_{\text{comp}}(t)$. This allows us to isolate the effects the plate mass has on the dynamics in the absence of both the spring and the dashpot. For this case where $\beta = \gamma = 0$, we can find an implicit solution for the leading-order displacement $w_0(t)$ from (5.3) given by

$$w_0(t) = \tilde{\alpha}^{2/3} f\left(\frac{t}{\tilde{\alpha}^{2/3}}\right), \text{ where } f(\xi) + \frac{1}{3} f(\xi)^{2/5} = \xi, \tag{5.6}$$

where recall $\tilde{\alpha} = 8\alpha/45$. Although we need to solve the algebraic equation for $f(\xi)$ numerically, this only needs to be done once across a wide enough range of ξ to find the asymptotic solutions for $w_0(t)$ for our desired range of α.

In Figure 5.9, we plot $d_0(t_c)$, $\dot{d}_0(t_c)$, $H(t_c)$, $E_{K,\text{outer}}(t_c)$ and $E_{K,\text{splash}}(t_c)$ at time $t_c = 1/12$ for α ranging from 10^{-2} up to 300. The solid lines denote the numerical solutions gained by solving (5.1) using the composite force, and the dotted lines denote the asymptotic solutions found by using the leading-order solution (5.6). The horizontal dashed lines indicate the stationary plate values, and the vertical lines denote the parameters we select for the DNS as shown in Figure 5.10. We find from Figure 5.9 that as α is increased, the moving plate solutions all approach the stationary substrate values. This is due to the fact that, in the absence of the elasticity from the spring, the plate motion slows down as α is increased. Typically by $\alpha = 100$, representing a plate approximately 24 times heavier than the droplet, these representative quantities are largely unaffected by the plate motion. On the other hand, as we make α smaller, we find that these quantities become significantly lower than their stationary plate values, e.g. the speed of the turnover point at t_c is around a third of the size of the stationary case when $\alpha = 10^{-2}$. For physical context, when $\alpha = 10^{-2}$, the plate has a mass that is around 0.2% of the mass of the droplet. In these cases where $\alpha \ll 1$, the plate mass is so low that it requires a very small amount of momentum transfer to be moved from its initial position, and thus the droplet spreading is drastically slowed due to the droplet receiving less force back from the plate. Of note in these cases is how the distribution of the kinetic energy between the outer and splash sheet regions differ. Even though the energy in both the outer and splash sheet regions are lower than the stationary case, we in fact have more energy entering the splash sheet than the outer region (where they both have an equal amount in the stationary case). It is interesting then that even though the droplet is receiving less energy overall, the energy it is receiving is being transferred more into the splash sheet than the outer region. The asymptotic solutions, denoted by the dotted lines, follow the trends of the numerical solutions very closely in Figure 5.9, although they are systematically lower. This is because the asymptotic solution makes use of the leading-order force, which we from Figure 5.2 is higher than the composite force. Because the force is higher, the plate will displace to a greater degree and therefore $d_0(t)$ and $H(t)$ will be lower.

All of the fluid quantities shown in Figure 5.9 monotonically increase with α, so we select five different cases equally spaced in the logarithmic space of α for DNS. Recall that the DNS makes use of the moving frame formulation presented in §4.4.1, in which the acceleration of the fluid globally is incremented by the plate acceleration. We found that for $\alpha \lesssim 2$ the plate acceleration was typically strong enough that the DNS struggled to converge to a valid solution due to finite flow velocities being

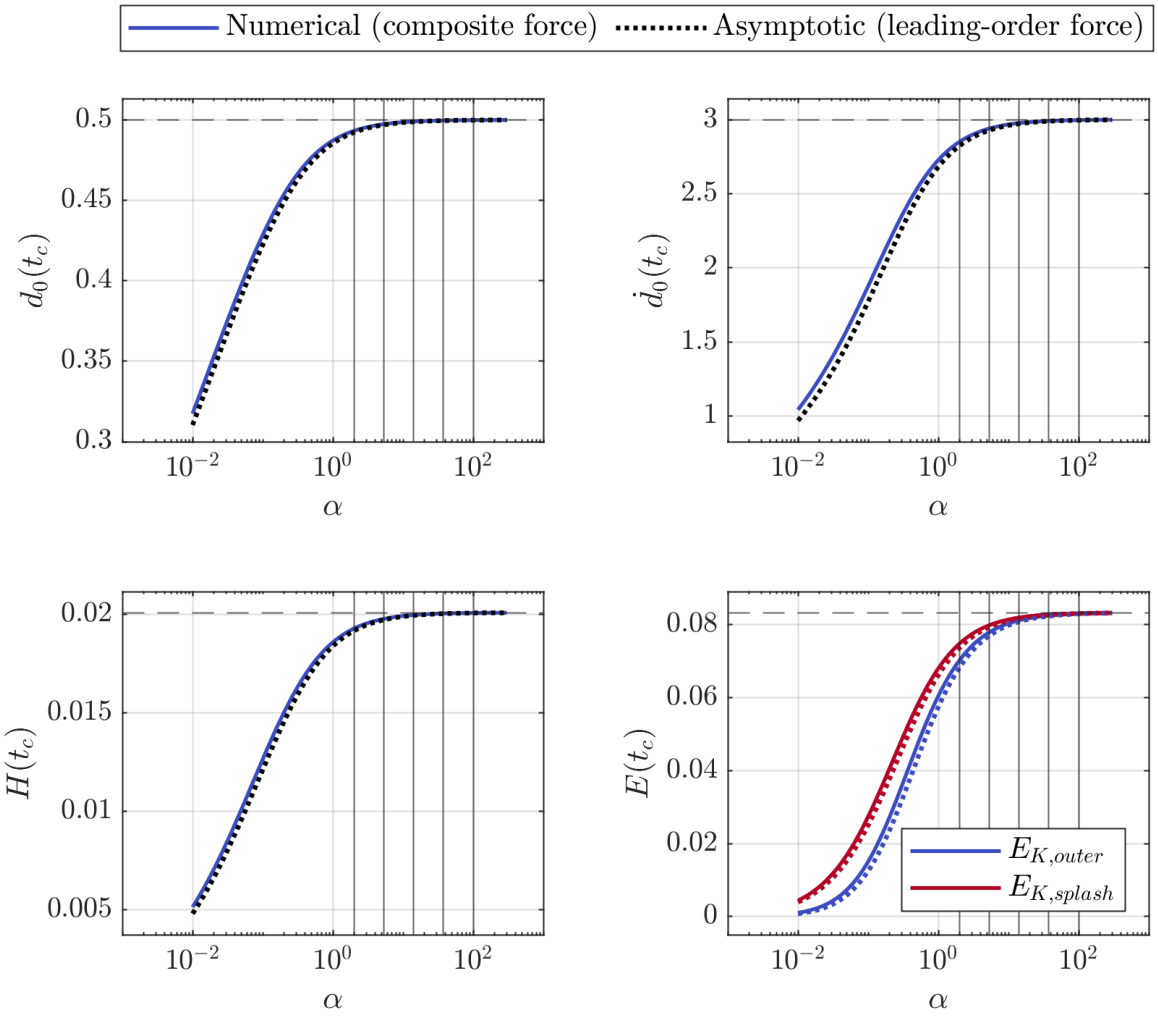

Figure 5.9: Analytical solutions for the turnover curve radius $d_0(t_c)$ and velocity $\dot{d}_0(t_c)$, given by (3.204), the turnover curve height $H(t_c)$, given by (3.90) and the kinetic energies $E_{K,\text{outer}}(t_c)$ and $E_{K,\text{splash}}(t_c)$, given by 3.254 and (3.255), for time $t_c = 1/12$. For all cases, the damping factor $\beta = 0$, the stiffness factor $\gamma = 0$, and α ranges from 10^{-2} up to 300. The horizontal dashed lines denote the stationary plate solutions and the vertical lines denote the parameters tested with the DNS and plotted in Figure 5.10.

induced close to the far-field boundaries. For this reason, we tested values of $\alpha = \{2, 5.318, 14.14, 36.61, 100\}$ for the DNS, which are denoted by vertical lines in Figure 5.9.

The DNS solutions for the plate displacement and force are shown in Figure 5.10, where the line colours are plotted from blue to red as α increases, with the black line denoting the force for the stationary plate case. We can clearly see that as α increases, the plate displaces to a lesser degree, which is reflective of the plate being heavier and therefore requiring more force to move. Subsequently, we can conclude

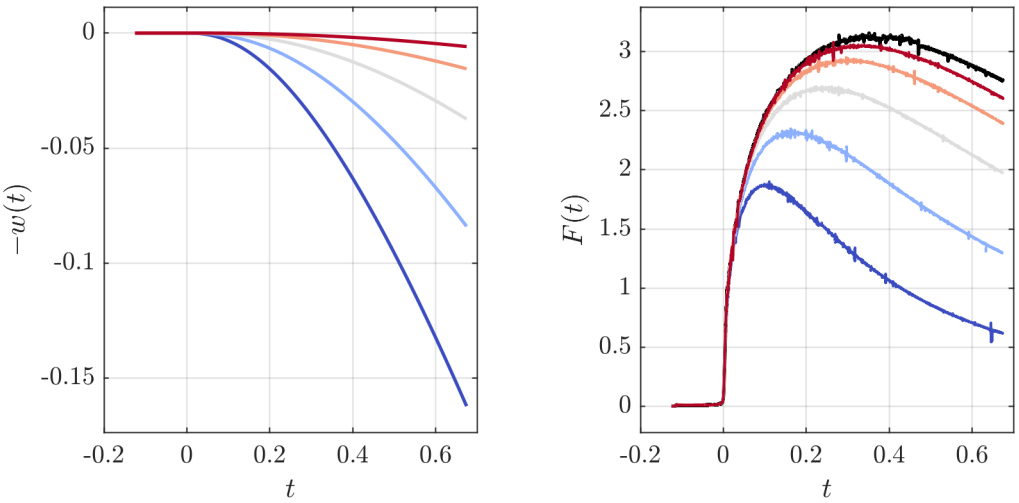

Figure 5.10: DNS solutions for the plate displacement and the force on the substrate for $\beta = \gamma = 0$, with α ranging from 2 (blue line) to 200 (red line), with the stationary plate solution shown in black. The values of α plotted are shown by the vertical lines in Figure 5.9.

that the hydrodynamic force monotonically decreases as α decreases. In the absence of damping or elasticity, the vertical motion of the plate in these cases essentially acts to slow down the impact process of the droplet, as the force it experiences upon impact is reduced when α becomes smaller.

In order to illustrate the difference in the spreading behaviour as α increases, in Figure 5.11, we show snapshots of the DNS at $t = 0.675$ for both the $\alpha = 2$ and $\alpha = 100$ moving plate cases. By comparing the location of the interfaces, we note that the droplet in the $\alpha = 100$ case has spread further along the plate than the $\alpha = 2$ case, as well as how the upper-most part of the droplet has fallen a greater vertical distance with respect to the plate. We can also see how the radial velocity in the splash sheet, $u(r, z, t)$, is greater in the $\alpha = 100$ case than it is in the $\alpha = 2$ case. We can infer from Figure 5.11 that the speed of the splash sheet is reduced in the cases where the substrate is allowed to displace by a greater degree, which could relate to the splash suppression mechanism discussed by Howland et al. (2016) [46].

By analysing the results of the analytical model in Figure 5.9, and the DNS results from Figure 5.10 and 5.11, we observe that the mass of the plate interacts with the droplet by slowing down its vertical motion. Specifically, by making the plate lighter, it displaces to a greater degree, and thus the initial spreading process of the droplet is slowed down.

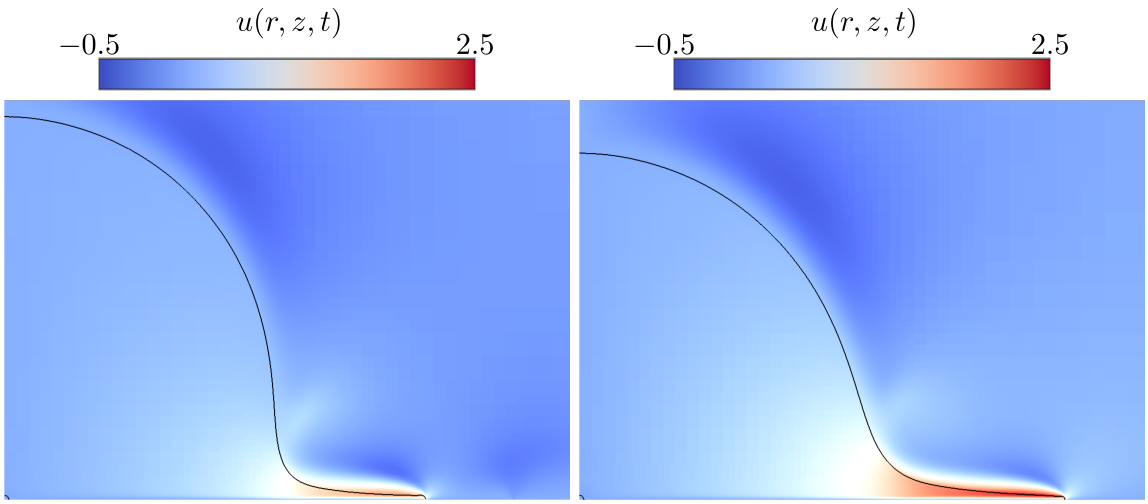

(a) $\alpha = 2$ (b) $\alpha = 100$

Figure 5.11: Snapshots of the radial velocities from the DNS at $t = 0.675$, for the moving plate cases where $\beta = \gamma = 0$, and either $\alpha = 2$ (Figure 5.11(a)) or $\alpha = 100$ (Figure 5.11(b)).

5.4.2 Stiffness factor

In the previous subsection, we studied setups where the plate is not supported by a spring or a dashpot. Real-world substrates typically do have additional features which resist motion from forcing, and commonly this can be modelled by an elastic response, which in our model is provided by the Hookean spring. As discussed previously, the experimental study of Gart et al. (2015) [27] studied the impact of droplets onto cantilever beams inspired by the phenomena of rain droplets impacting onto leaves, in which the end of the cantilever beam could be modelled as a damped harmonic oscillator.

The strength of the elastic response from the spring is measured by the stiffness factor, $\gamma = k^*/(\rho^* V^{*2} R_d^*)$, where k^* is the spring constant with units Newtons per metre. When a harmonic oscillator governed by (5.1) in the absence of forcing or damping (i.e. $F(t) = \beta = 0$) is displaced from equilibrium, it will exhibit oscillations about the equilibrium point with angular frequency $\omega = \sqrt{\gamma/\alpha}$. Therefore, for any fixed mass ratio α, increasing the stiffness factor will increase the frequency of these oscillations. In our case, the plate is in equilibrium at $t = t_0$, and is initially displaced from equilibrium due to the hydrodynamic forcing $F(t)$. Increasing the stiffness of the spring will make it more difficult to displace the plate, so we expect that increasing γ will reduce the plate displacement as well as increase the frequency at which it oscillates.

For high stiffness values, the frequency of these oscillations will be high enough that we expect the plate to vibrate with a time period on the scale of the early impact times. Experimental studies involving impact onto vibrating substrates include the work of Weisensee et al. (2017) [95], where droplets were impacted onto superhydrophic substrates oscillating with frequencies up to 100 Hz. Although the vibrations of these substrates were forced, they did reveal how the imposed vibrations drastically affected the later time spreading and bouncing of the droplet, and could change the amount of time the droplet was in contact with the substrate. In terms of mathematical modelling, Khabakhpasheva & Korobkin (2020) [49] utilised axisymmetric Wagner theory to model the high-speed impact of a droplet onto a vibrating substrate. By increasing the frequency of the forced oscillations, they found that the solution for the splash sheet could become singular and break down to what they refer to as a splash, consistent with the definition of splashing used by Pegg et al. (2018) [71]. The vibration of the substrate was shown to cause oscillations in the pressure along the substrate, which is consistent with our findings from Figures 5.3 and 5.4. In addition, they modelled the fluid-structure interaction between a droplet and a spring-supported plate governed by (5.1) in the absence of damping using the leading-order solution for the force (3.248). They concluded that the break-down of the splash sheet due to the vibrations was not possible for the spring-supported plate, and could only happen when the oscillations were forced. In this subsection we extend on the findings of Khabakhpasheva & Korobkin (2020) [49] by utilising the composite force solution for the force (3.251), which we have shown provides better agreement with DNS, as well as investigating later timescales using the DNS.

To study the effects that the elasticity has on the droplet dynamics, for this subsection we fix the mass ratio $\alpha = 2$ and damping factor $\beta = 0$, and vary the stiffness factor γ from 10^{-1} up to 10^{7}. For small values of γ, the leading-order solution for the plate displacement from (5.3) will be the $\gamma = 0$ solution given in (5.6). For $\gamma \gg 1$, the leading-order solution for $w_0(t)$ will be

$$w_0(t) = \frac{135\sqrt{3}}{4}\left(\frac{\tilde{\alpha}}{\tilde{\gamma}^5}\right)^{1/4} g\left(\sqrt{\frac{\tilde{\gamma}}{\tilde{\alpha}}}t\right), \text{ where } g(\xi) = \int_0^{\xi} \tau^{1/2}\sin(\xi-\tau)\,\mathrm{d}\tau\,, \qquad (5.7)$$

where recall that $\tilde{\gamma} = 8\gamma/45$. Similar to (5.6), here we only have to solve for $g(\xi)$ once for a large enough range of ξ in order to find the leading-order solutions for $w_0(t)$ for all of the desired values of γ.

In Figure 5.12 we plot the analytical solutions for $d_0(t_c)$, $\dot{d}_0(t_c)$, $H(t_c)$, $E_{K,\text{outer}}(t_c)$ and $E_{K,\text{splash}}(t_c)$ at time $t_c = 1/12$, with 500 different cases of γ ranging from 10^{-1}

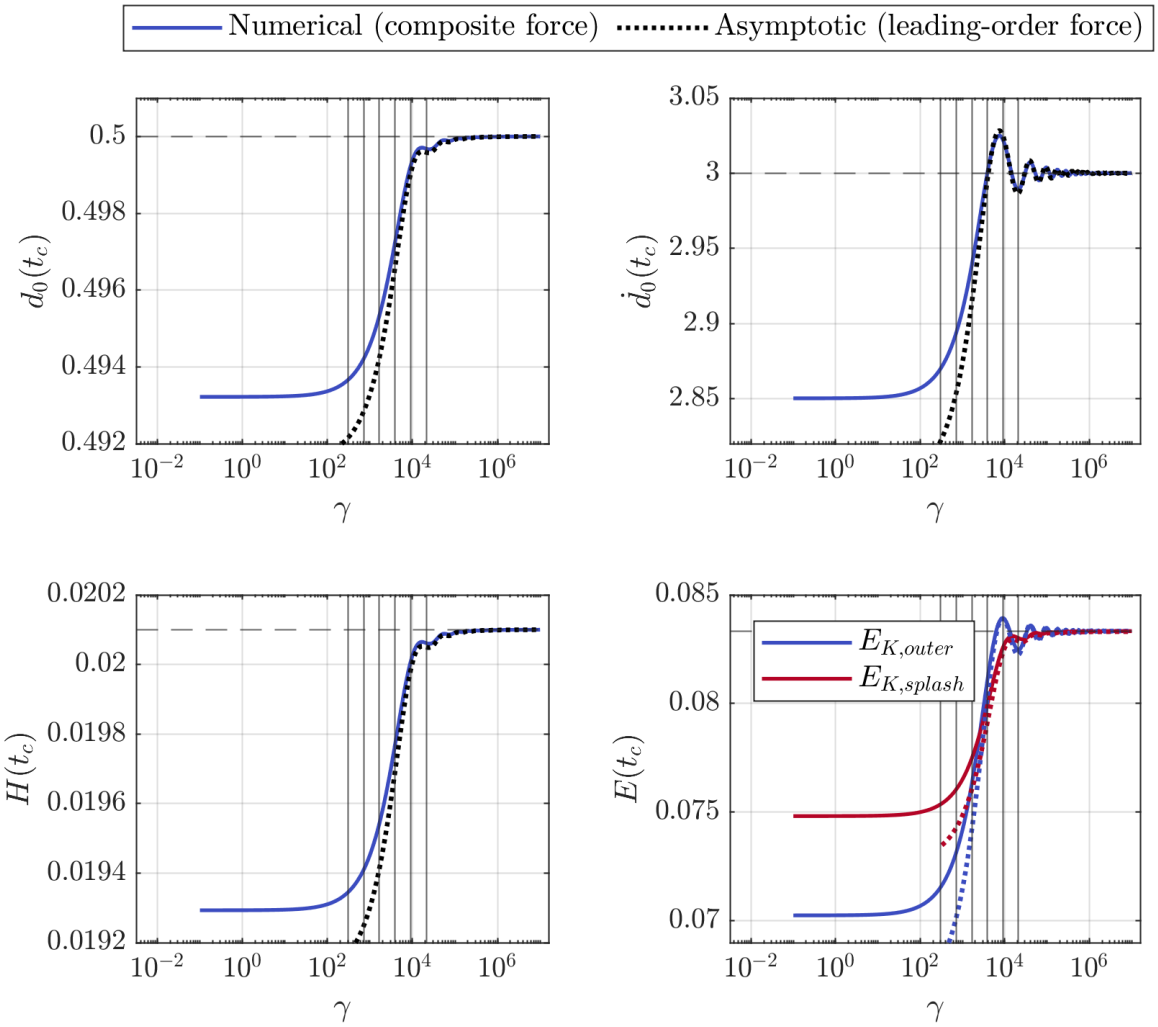

Figure 5.12: Analytical solutions for the turnover curve radius $d_0(t_c)$ and velocity $\dot{d}_0(t_c)$, given by (3.204), the turnover curve height $H(t_c)$, given by (3.90) and the kinetic energies $E_{K,\text{outer}}(t_c)$ and $E_{K,\text{splash}}(t_c)$, given by 3.254 and (3.255), for time $t_c = 1/12$. For all cases, the mass ratio $\alpha = 0$, the damping factor $\beta = 0$, and γ ranges from 10^{-1} up to 10^7. The horizontal dashed lines denote the stationary plate solutions and the vertical lines denote the parameters tested with the DNS and plotted in Figure 5.13.

up to 10^7. As was the case in Figure 5.9, the solid lines denote the solutions gained by numerically solving (5.1) using the composite force, the dotted lines denote the asymptotic solutions found using (5.7) for $\gamma \gg 1$, the horizontal dashed lines denote the stationary plate solutions and the vertical lines denote the parameters selected for the DNS shown in Figure 5.13.

From Figure 5.12, we find that, as $\gamma \to 0$, the solutions approach the case where the spring is absent, which for $\alpha = 2$, is shown by the left-most of the vertical

lines in Figure 5.9. Similarly, for large $\gamma \gtrsim 10^6$, the solutions converge onto the stationary plate solutions, in which case the high stiffness of the spring prevents the plate from moving enough to have a noticeable effect on the droplet. The quantities monotonically increase as γ goes from 10^{-1} up until to approximately 9000, which is a similar behaviour to what we observed for increasing the mass ratio in Figure 5.9, and represents how increasing the stiffness reduces the amount the plate displaces. For physical context, the spring constant when $\gamma = 10^{-1}$ is $k^* \approx 2.5 \times 10^{-3}$ N/mm, which is weak enough to provide little resistance when being compressed on the millimetric droplet scale. For $\gamma = 9000$, the spring constant is $k^* \approx 224$ N/mm, which means there is a very strong resistance to compression on the millimetric droplet scale. Once $\gamma \gtrsim 9000$, we begin to see non-monotonic behaviour in the solutions, in particular how the speed of the turnover curve at $t = t_c$ is greater than the stationary plate value for $\gamma = 9000$ (penultimate vertical line), and is less than the stationary plate value for $\gamma = 21000$ (final vertical line). Correspondingly, the distribution of kinetic energy between the outer region and splash sheet also changes between these cases. The asymptotic solution, given by (5.7), assumes that $\gamma \gg 1$, and we observe that the asymptotic solutions follow the numerical solutions well in Figure 5.12 once $\gamma \gtrsim 10^4$.

The non-monotonic behaviour of these analytical solutions for high values of γ are better understood by determining the time-period of the plate oscillations. Recall that the time period of the plate in the absence of forcing is $T = 2\pi\sqrt{\alpha/\gamma}$. For $\alpha = 2$ and $\gamma = 9000$, the time period is $T_{9000} \approx 0.094$, and for $\gamma = 21000$ the time period is $T_{21000} \approx 0.061$. Given that $t_c = 1/12 \approx 0.083$, we have that the time periods of the oscillations for these values of γ are close to the test time t_c. This means that although the plate displacement is small for these cases, the plate acceleration will be high at $t = t_c$ due to the short time period of the oscillations. It is noteworthy that, despite the time period of the $\gamma = 21000$ case being very short, the fact that we restrict the timestep in both the DNS and analytical solutions to be at most $\Delta t = 10^{-4}$ means that we still capture the dynamics of these cases well.

To further investigate these effects, in Figure 5.13 we plot the DNS solutions for the values of γ denoted by the vertical lines in Figure 5.12, which are $\gamma = \{303.6, 708.5, 1653, 3857, 9000, 21000\}$. In the same manner as Figure 5.10, the line colours are such that the lowest γ value is plotted in blue, the highest plotted in red and the black line denotes the stationary plate solution. As expected, we find that increasing γ both decreases the amount the plate displaces, as well as increasing the frequency of the oscillations. The effect of the plate oscillations are clear from the

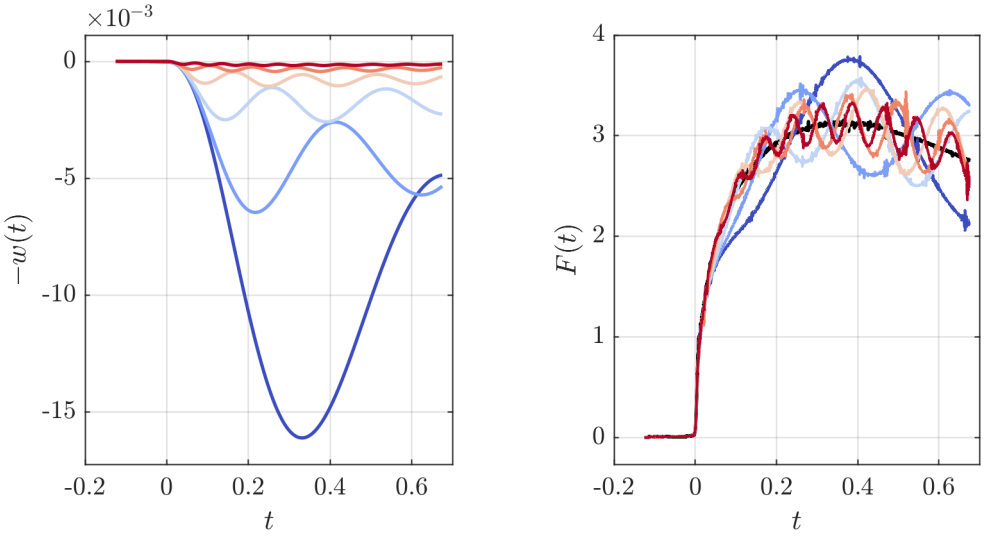

Figure 5.13: DNS solutions for the plate displacement and the force on the substrate for $\alpha = 2$, $\beta = 0$, with γ ranging from 303.6 (blue line) up to 21000 (red line), with the stationary plate solution shown in black. The values of γ plotted are shown by the vertical lines in Figure 5.12.

solutions for the force $F(t)$. For the lowest values of γ, the force experiences a low-frequency oscillation, which oscillates significantly above and below the stationary plate solution. As γ is increased, the frequency of the oscillations increase, but the solutions for the force deviate from the stationary plate case to a lesser degree. Even though the plate displacement for the highest γ case is very small (typically around 10^{-4}), the resulting force profile differs considerably from the stationary plate case due to the high frequency of the oscillations.

From Figure 5.12, we saw how the evolution of the turnover point, both in its radius and height, is affected by these oscillations for high values of γ. In particular for the higher values of γ, the turnover curve velocity at the time t_c experienced non-monotonic behaviour as γ increased. To explore this, in Figure 5.14, we plot the difference between the DNS solution for the turnover curve radius $d(t)$ and the stationary plate case $d_{\text{stat}}(t)$ for the three largest values of γ studied with the DNS. For early times, the solutions exhibit some numerical noise due to the turnover curve being not well resolved shortly after impact (see Figure 5.7 for context). However after roughly $t = 0.025$, the values of $d(t) - d_{\text{stat}}(t)$ exhibit temporal oscillations in line with the plate displacement oscillations that can be seen in Figure 5.13. For $\gamma = 3857$ and $\gamma = 9000$, despite the oscillations, the turnover curve radius is smaller than the stationary plate value, indicating that the plate displacement is still acting to slow down the spreading in these cases. However for $\gamma = 21000$, there is a period of time

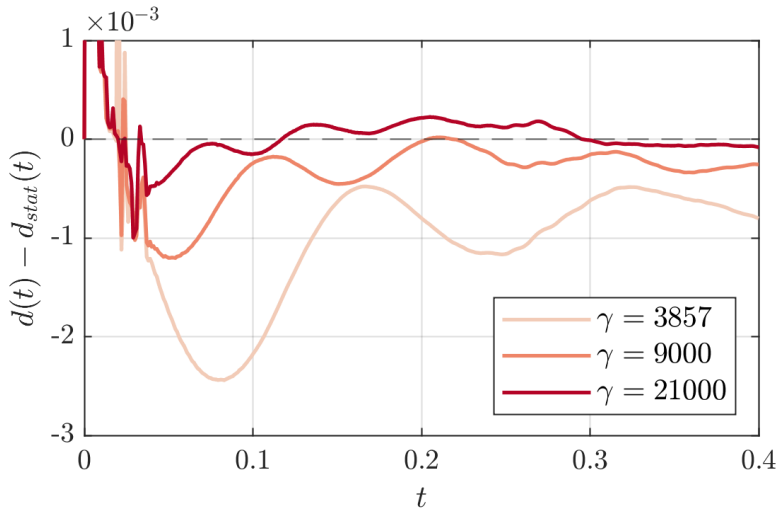

Figure 5.14: DNS solutions for the difference between the radial position of the turnover curve, $d(t)$, and the corresponding value in the stationary case, $d_{\text{stat}}(t)$, for $\alpha = 2$, $\beta = 0$ and $\gamma = \{3857, 9000, 21000\}$.

where the turnover curve radius is larger than the respective stationary plate value. This indicates that, despite the plate displacement being relatively small (around 10^{-4} for the $\gamma = 21000$ case), the high frequency oscillations of the plate in this case is acting to speed up the spreading of the droplet at certain times. Up until this point, the moving plate cases we have studied have been shown to decrease the rate the droplet spreads across the plate in comparison to the stationary plate case, which typically happens as the vertical motion of the substrate slows down the impact process. However in this case, the substrate deformation is small, and instead the plate exhibits high frequency vibrations. The dimensionless time-period of oscillation, $T_{21000} \approx 0.061$ corresponds to a dimensional time-period of $T^*_{21000} \approx 12.2$ μs, or a frequency of ≈ 81 kHz. This is much higher than the frequency of the vibrations studied by Weisensee et al. (2017) [95], which went up of 100Hz, however their experimental study was focused on much later times of impact. For the analytical framework for droplet impact onto oscillating substrates studied by Khabakhpasheva & Korobkin (2020), frequencies of up to ≈ 30 kHz were studied, so in this analysis we have extended the range of parameters studied for the spring-supported plate case.

Whereas from §5.4.1 we noted that the mass of the plate acts to slow down the spreading of the droplet in a reasonably monotonic way, in this subsection we have observed that the droplet has a more complex response to the elasticity. From Figure 5.12 we found that for most values of γ, decreasing the stiffness of the spring acts to slow down the droplet spreading, however we have seen that for very high values of

γ, the induced vibrations can instead have the opposite effect and actually promote a faster speed of spreading across the substrate.

5.4.3 Damping factor

The dashpot acts to resist the motion of the plate via viscous dissipation. When a damped harmonic oscillator governed by (5.1) for α, β, $\gamma > 0$ in the absence of forcing is displaced from equilibrium, it exhibits motion that is described as either under-, critical- or over-damped. Under-damping occurs when the oscillator exhibits oscillations due to the spring that decrease in magnitude due to energy losses from the damping. Critical-damping occurs when the damping is just strong enough to prevent the first oscillation to occur, so that the oscillator reaches equilibrium in the fasted possible time. Over-damping is when the damping factor is stronger than the critical value, and returns to equilibrium more slowly as the damping slows down the motion. In the following, we will study how the dynamics of the droplet change as the plate-spring-dashpot goes from being under-damped to over-damped by varying β. For this parameter study, we will fix $\alpha = 2$ and $\gamma = 100$, in which case the critical damping value is $\beta_c = 2\sqrt{\alpha\gamma} = 20\sqrt{2} \approx 28.28$. When $\beta = O(1)$, the plate equation (5.1) must be solved analytically. However when $\beta \gg 1$, we can find the leading-order solution for $w_0(t)$ from (5.3) to be

$$w_0(t) = \frac{45\sqrt{3}}{2\tilde{\beta}} t^{3/2}, \tag{5.8}$$

where recall that $\tilde{\beta} = 8\beta/45$.

In the same manner as Figures 5.9 and 5.12, in Figure 5.15 we show the analytical solutions for $d_0(t_c)$, $\dot{d}_0(t_c)$, $H(t_c)$, $E_{K,\text{outer}}(t_c)$ and $E_{K,\text{splash}}(t_c)$ at time $t_c = 1/12$ for β varying from $10^{-2}\beta_c$ to $10^4\beta_c$, where $\beta_c = 20\sqrt{2}$ is the critical damping value. The solid lines denote the solutions found from solving (5.1) numerically using the composite force, the dotted lines denote the solutions found by making use of the leading-order plate displacement (5.8) for $\beta \gg 1$, the horizontal dashed lines denote the corresponding values in the stationary plate case, and the vertical dashed lines denote the parameters selected for the DNS shown in Figure 5.16, with the exception of $\beta = 0$ which is not shown due to the logarithmic scaling of the plots. For physical context, the critical damping value β_c corresponds to a dashpot with damping factor $c^* \approx 0.141$ Ns/m. For physical context, typical shock absorbers used in cars can have damping coefficients from around $c^* = 8$ Ns/m up to around 1748 Ns/m [22]. For large values of β, we see from Figure 5.15 that the moving plate solutions tend

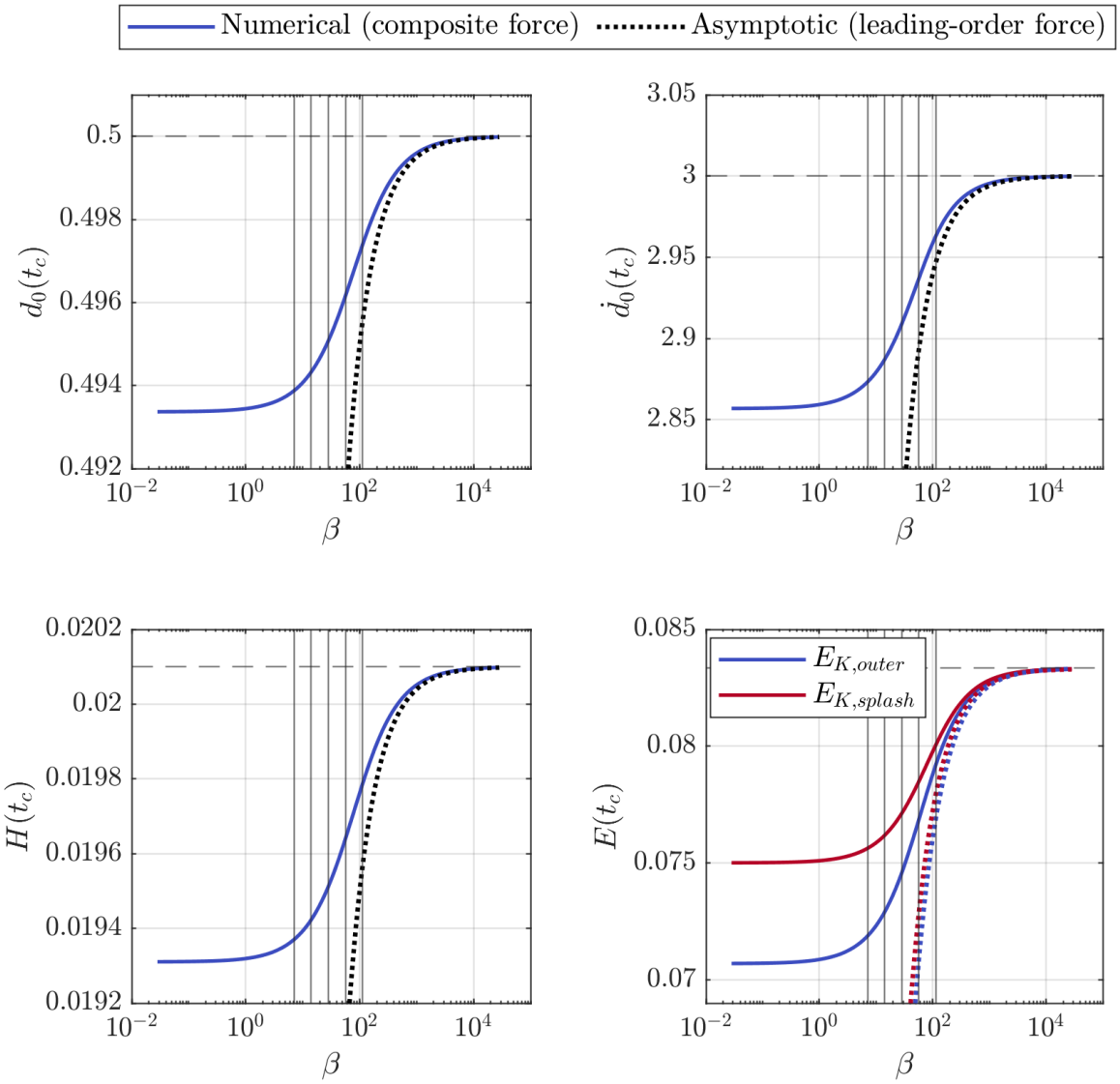

Figure 5.15: Analytical solutions for the turnover curve radius $d_0(t_c)$ and velocity $\dot{d}_0(t_c)$, given by (3.204), the turnover curve height $H(t_c)$, given by (3.90) and the kinetic energies $E_{K,\text{outer}}(t_c)$ and $E_{K,\text{splash}}(t_c)$, given by 3.254 and (3.255), for time $t_c = 1/12$. For all cases, the mass ration $\alpha = 2$, the stiffness factor $\gamma = 100$, and β ranges from $10^{-2}\beta_c$ up to $10^2\beta_c$, for the critical damping coefficient $\beta_c = 20\sqrt{2}$. The horizontal dashed lines denote the stationary plate solutions and the vertical lines denote the parameters tested with the DNS and plotted in Figure 5.16.

towards the stationary plate values, in which case the damping is so strong that the plate only moves a very small amount. We find that the asymptotic solutions determined by (5.8) agree well with the numerical solutions for $\beta \gtrsim 10^3$. As the asymptotic solution (5.8) is $\sim t^{3/2}$, we can conclude that the damping has removed the temporal oscillations for these large values of β. The turnover curve radius and

velocity, as well as its height, tend to decrease monotonically with β, indicating how reducing the damping causes the plate to displace more, and hence slow the spreading in the same manner as was seen in §5.4.1 for the mass ratio α. For small values of β, typically when $\beta \lesssim 10^{-1}\beta_c$, the solutions converge to a constant value as $\beta \to 0$. For these ranges, the damping effect is very weak, and the system is so under-damped that oscillations due to the spring are largely left unaffected by the dashpot.

The vertical lines in Figure 5.15 represent where $\beta = \{\beta_c/4,\ \beta_c/2,\ \beta_c,\ 2\beta_c,\ 4\beta_c\}$, and thus cover the regimes where the system transitions between being under-damped to over-damped. In Figure 5.16, we plot the solutions for the plate displacement and force from the DNS for these parameter values, in addition to the case where $\beta = 0$ for reference. In the same manner as Figure 5.10, β increases as the colours change from blue to red, with the critical damping case plotted in the lightest red colour, and the stationary plate case plotted in black. From the solutions for the plate displacement, we note that as β is increased, the oscillations which are present in the $\beta = 0$ case are gradually removed, with the plate displacing downwards monotonically for the over-damped cases. This effect is more apparent in the solutions for the force, where the cases with $\beta < \beta_c$ appear to experience a large oscillation about the stationary plate value. Similarly for the over-damped cases, the force solutions appear to be converging towards the stationary plate case solution. The critically damped case clearly resides in the middle of these two regimes, where the oscillations have been damped out, but the force has not yet converged to the stationary plate value.

In the previous subsection, we found that the elasticity effects from the spring can induce high frequency oscillations which, at certain timescales, can actually accelerate the spreading of the droplet in comparison to the stationary plate value. However the damping from the dashpot removes kinetic energy from the plate, and from Figure 5.16, we found that by introducing damping above or equal to the critical damping value, the oscillations of the substrate induced by the spring can be suppressed. Although the damping ultimately makes the plate more difficult to displace, it could be used as a mechanism to reduce the amount the plate vibrates in the cases where γ is very high.

5.4.4 Summary

In this section we have extensively studied the effects each of the three components of the plate-spring-dashpot system have on the dynamics of the droplet. When we decrease the mass of the plate, categorised by the mass ratio α, we found that the impact process is slowed down, as lighter plates are displaced to a greater degree

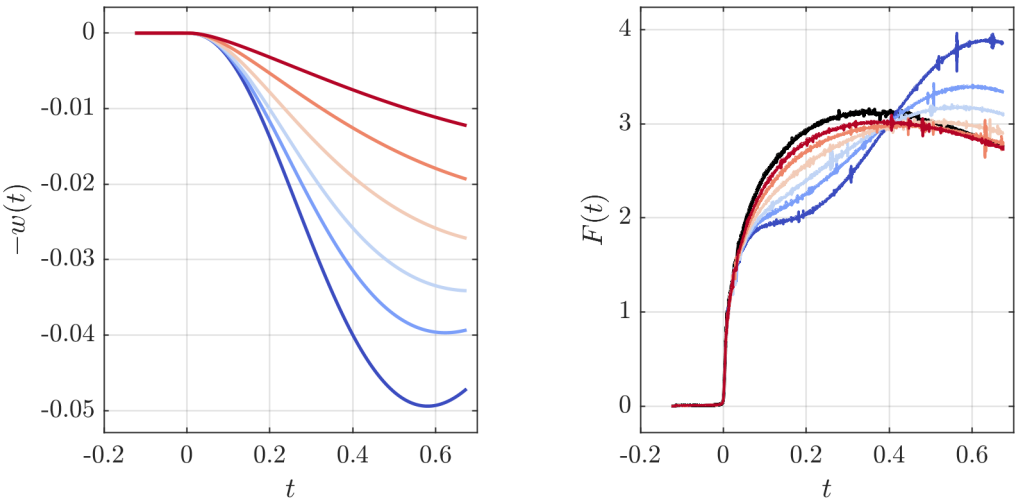

Figure 5.16: DNS solutions for the plate displacement and the force on the substrate for $\alpha = 2$, $\gamma = 100$, with β ranging from 0 (blue line) up to $4\beta_c$ (red line) where $\beta_c = 20\sqrt{2}$, with the stationary plate solution shown in black. The values of β plotted are shown by the vertical lines in Figure 5.15.

upon impact. The stiffness of the spring, categorised by the stiffness factor γ, induces oscillations in the plate as well as decreasing the amount the plate is displaced overall. We saw that for moderate values of γ, the stiffness acts to reduce the amount the plate displaces, and thus tends towards the stationary plate dynamics. However, we saw that springs with very high stiffnesses induce vibrations with time periods on the same timescale as the early spreading times for the droplet, and in these cases we found that how these vibrations can actually increase the rate of spreading as they rebound from the initial impact force. Finally, we saw how the dashpot, categorised by the damping factor β, acts to slow down the displacement of the plate, and that once the damping exceeds the critical damping threshold, the oscillations of the plate can be suppressed. Overall, by controlling these three parameters, see how the nature of the fluid-structure interaction between the droplet and the plate is significantly changed, and we have revealed the rich interplay between these physical effects.

5.5 Conclusion

Despite its simplicity, we have demonstrated that the plate-spring-dashpot model considered in this chapter exhibits a rich fluid-structure interaction between the droplet and the plate. We have identified that, by allowing the plate to move, the dynamics of the droplet impact can be significantly changed in comparison to the case where the droplet impacts a stationary plate. In particular, the downwards acceleration of

the plate upon impact acts to reduce the pressure inside the droplet, which in turn slows down the process which initialises the spreading of the droplet across the plate. By varying the mass of the plate, the stiffness of the spring and the strength of the dashpot, we have seen that there are a large range of responses the droplet can exhibit during the early times of impact.

As well as exploring the dynamics of this novel fluid-structure interaction problem, we have also investigated how the predictions of the analytical model presented in Chapter 3 and the direct numerical simulations presented in Chapter 4 compare to one another. We found that the analytical predictions for the plate displacement agreed extremely well with the DNS prior to the turnover curve reaching the initial droplet radius at approximately $t = 0.35$, as well as good agreement in the results of the turnover curve radius and the pressure and force on the plate up to around $t = 0.2$. Given this strong agreement, we used the analytical model to conduct a large parameter study of 1500 different plate setups across Figures 5.9, 5.12 and 5.15. This allowed us to determine the trends in the key quantities relating to the early time spreading of the droplet with minimal computational resources. To put this into context, each set of DNS took around 24 CPU hours to resolve across 8 CPUs, meaning testing the same number of parameters in the DNS would have required around 36,000 CPU hours. Instead, each numerical solution found using the analytical model took $\approx$ 5 seconds, meaning the entire parameter study required 2 CPU hours on a single CPU. The results of this parameter study were then used to make informed choices on which parameters of interest would be best to study using the DNS. For example, in Figure 5.12, we identified interesting behaviour in the turnover curve velocity at $\gamma = 21000$, which we then targeted for DNS which allowed us to see how the spreading in this case was actually faster than the stationary plate case at certain times. This exemplifies the strength of our methodology of employing both an approximate, computationally cheap analytical model in combination with computationally expensive yet highly accurate direct numerical simulations in order to explore the problem at a greater depth.

Despite the richness of the fluid-structure interaction studied in this chapter, the presented model is limited to rigid substrates. Many relevant real-world substrates of interest, such as leaves or soft subsrates for novel printing applications, exhibit not just vertical displacement upon impact, but also deformation and bending. In the next chapter, we will study a more complex model for the substrate that allows for deformation, specifically an elastic membrane under tension.

Chapter 6

Droplet impact onto an elastic membrane

In the previous chapter we studied the impact of a droplet onto a rigid substrate that could only displace vertically. However, a wide range of real world substrates can also experience bending deformations, which would not be taken into account in the framework presented in Chapter 5. For this chapter, we will study the impact of a two-dimensional droplet onto an elastic membrane, which has a finite bending stiffness and can be held under a range of tensions. In this two-dimensional setting, the membrane displacement (given by (2.36)) is equivalent to an Euler-Bernoulli beam with an additional term to take into account the tension. Throughout this chapter, we will refer back to the experimental work of Pepper et al. (2008) [72], who studied the impact of high-speed droplets onto elastic membranes under a variety of tensions. They found that droplet splashing could be reduced when the membranes were held under lower tensions, and measured that, in these cases, the lamella initially emerged more slowly when the tension was lower. This is also similar to the findings of Howland et al. (2016) [46], where droplets impacting onto silicon gels with lower stiffnesses were found to be less likely to splash. Although the presented model for the membrane in this chapter is more widely relevant as it takes into account these bending deformations, the direct experimental applicability is reduced as we consider a two-dimensional model. However our aim in this chapter is to provide insight into the physical mechanisms at play at the early times of these impact processes, and investigate how the fluid-structure interaction between the droplet and the membrane alters the dynamics at early times.

Recall from (2.36) that the displacement of the membrane from its initial position

$z = -\epsilon^2 w(x,t)$ is given by

$$\frac{\alpha}{\epsilon^2}\frac{\partial^2 w}{\partial t^2} - \epsilon^2\beta\frac{\partial^2 w}{\partial x^2} + \epsilon^2\gamma\frac{\partial^4 w}{\partial x^4} = p_i(x, -\epsilon^2 w(x,t), t) - \frac{2\mu_i}{\mathrm{Re}}\frac{\partial v_i}{\partial z}, \tag{6.1}$$

where $i = l$ where the membrane is wetted and $i = g$ where the membrane is unwetted, and the dimensionless parameters (α, β, γ) are given by

$$\alpha = \frac{\rho_m^*}{\rho_l^*}\delta, \quad \beta = \frac{T^*}{\rho_l^* R_d^* V^{*2}}, \quad \gamma = \frac{E^*}{3\rho_l^* V^{*2}}\delta^3, \quad \delta = \frac{\delta^*}{R_d^*}. \tag{6.2}$$

There are five dimensionless parameters in total that determine the physical setup of the membrane. The thickness ratio, δ, measures the ratio between the thickness of the membrane δ^* and the radius of the droplet R_d^*. Similarly, the dimensionless width $L = L^*/R_d^*$ is the ratio between the width of the membrane and the radius of the droplet. The derivation of the membrane equation (6.1) in Howell et al. [43] relies on assuming that $\delta \ll L$, so we will ensure throughout that we choose δ and L appropriately. This is consistent with the experimental study of Pepper et al. (2008) [72], where droplets were impacted onto membranes of thicknesses of approximately 12 μm with widths of a few centimetres. For any given thickness δ, the density factor α is proportional to the ratio between the density of the membrane ρ_m^* and the density of the liquid ρ_l^*. Similarly, for any given δ, the stiffness factor γ is proportional to the ratio between the Young's modulus of the membrane E^* and the inertial pressure scale $\rho_l^* V^{*2}$. Finally, the tension factor, β, is proportional to the tension applied through the membrane T^*, and does not depend on the thickness ratio δ. We take the membrane to be simply supported at its end points $x = \pm L$, and initially flat and stationary, giving the following boundary and initial conditions:

$$w = \frac{\partial w}{\partial x} = 0 \text{ at } x = \pm L, \quad w = \frac{\partial w}{\partial t} = 0 \text{ at } t = t_0. \tag{6.3}$$

Our presented model for an elastic membrane can be applied to a wide range of deformable substrates by varying each of the five dimensionless parameters. As we have assumed $\delta \ll L$, we must ensure that the thickness of the membrane is much less than its width, and it is typically easier to control the width of the chosen substrate over its thickness. Throughout this chapter, we take $L = 16$ (representing a membrane with total width $2L^* = 3.2$ cm). This value was chosen as it represents a membrane size that is large enough to be considered in a laboratory setup, whilst remaining small enough to prevent incurring substantial computational costs to simulate. Deformable substrates can also have a wide range of thicknesses, δ^*. For example, Saran wrap (the material in which Pepper et al. (2008) [72] studied droplet impact upon), has

a thickness of ≈ 10 μm, whilst materials such as rubber can be made into sheets of thicknesses upwards of a few centimetres. This means that, for our modelling, we may vary δ over a wide range, with the restriction of ensuring that $\delta \ll L$. However, the density of the membrane ρ_m^* typically lies within a smaller range when considering possible materials that can be used to make a deformable substrate. For example, low-density polyethylene (LDPE) has a density of approximately 900 kgm^{-3}, whilst steel has a density of approximately 7800 kgm^{-3}. This means that for any choice of δ, we can only vary α within a small range of around 1-2 orders of magnitude. On the other hand, the amount of tension T^* a material can undergo will depend on its tensile strength, which will depend on various properties of the physical substrate. Many real-world examples can withstand being held under a large amount of tension before snapping, such as sheets of rubber and latex. Finally, the Young's modulus E^* can vary substantially between different materials. Plastic materials such as rubber and LDPE can have Young's moduluii from approximately $0.01 - 0.1$ GPa, whilst highly stiff materials such as steel can have a Young's modulus of approximately 200 GPa. This means that for any fixed δ, we can vary the parameter γ by approximately three orders of magnitude.

We will start this chapter by detailing how we solve the PDE for the membrane position (6.1) within both the analytical model and the DNS. Given this, we will then select a particular set of membrane parameters in order to compare the predictions of each modelling technique for the dynamics of both the membrane and the impacting droplet. Then we will conduct an extensive parameter study in order to gain insight into the effects each of the above detailed membrane parameters have on the fluid-structure interaction between the droplet and the membrane.

6.1 Numerical solution for the membrane position

In Chapters 3 and 4, we derived an analytical model and a DNS setup for modelling the impact of a two-dimensional droplet onto a deformable substrate at a time and space dependent position $z = -\epsilon^2 w(x,t)$. In order to resolve the full fluid-structure interaction problem, we will need to solve the membrane equation (6.1), which will be coupled to the fluid via the stress terms on the right-hand-side. Given that the pressure term depends non-linearly on the membrane displacement, (6.1) is a non-linear, fourth-order in space and second-order in time PDE, and will need to be solved numerically. In §6.1.1-6.1.2, we will detail two different numerical schemes for

determining the membrane displacement using the analytical model, and in §6.1.3 we will detail the method used to resolve the membrane displacement in the DNS.

6.1.1 Normal modes method

In §3.2, we use the analytical modelling framework to find the leading-order solutions for hydrodynamic components of the system in terms of the leading-order membrane position, $w_0(x,t)$. Recall that for the analytical model, we neglect the influence of the surrounding gas, viscosity and surface tension, writing $p_l = p$ for brevity. Therefore in the analytical model, the membrane equation (6.1) reduces to

$$\frac{\alpha}{\epsilon^2}\frac{\partial^2 w_0}{\partial t^2} - \epsilon^2\beta\frac{\partial^2 w_0}{\partial x^2} + \epsilon^2\gamma\frac{\partial^4 w_0}{\partial x^4} = p(x, -\epsilon^2 w_0(x,t), t). \tag{6.4}$$

The first method we will consider for solving (6.4) is the normal modes method, which was previously applied to a similar problem of wave impact onto a beam by Korobkin (1998) [52]. The normal modes method proposes constructing a series solution for $w_0(x,t)$ of the form

$$w_0(x,t) = \sum_{n=1}^{\infty} a_n(t)\psi_n(x), \tag{6.5}$$

where

$$\psi_n(x) = \frac{\cos(k_n x)}{\sqrt{L}}, \quad k_n = \frac{\pi(2n-1)}{2L}, \tag{6.6}$$

and where k_n is the wavenumber, and each $\psi_n(x)$ is referred to as a *normal mode* which is a solution to the homogeneous form of the membrane equation (6.4) (where $p \equiv 0$). Therefore, the normal modes method decomposes the solutions of (6.4) as a series of modes, that spatially vary with $\psi_n(x)$ and have a time-dependent amplitude $a_n(t)$. The initial conditions for $a_n(t)$ as a result of (6.3) are hence

$$a_n(0) = \dot{a}_n(0) = 0 \text{ for } n \geq 1. \tag{6.7}$$

By multiplying the membrane equation (6.4) by $\psi_n(x)$ and integrating from $x = -L$ to L, we obtain after integrating by parts (using the boundary conditions (6.3)) the following ordinary-differential-equation for $a_n(t)$:

$$\ddot{a}_n(t) + \omega_n^2 a_n(t) = \frac{\epsilon^2}{\alpha\sqrt{L}}\int_{-L}^{L} p(x, -\epsilon^2 w(x,t), t)\cos(k_n x)\,\mathrm{d}x\,, \tag{6.8}$$

where ω_n is the angular frequency of the n^{th} mode when $p \equiv 0$, given by the dispersion relation

$$\omega_n^2 = \frac{\epsilon^4(\beta k_n^2 + \gamma k_n^4)}{\alpha}. \tag{6.9}$$

Given the dispersion relation (6.9), we can determine the phase and group velocity of each normal mode in time, given by

$$v_{\text{phase}}(k_n) = \frac{\omega_n}{\epsilon^2 k_n} = \sqrt{\frac{\beta + \gamma k_n^2}{\alpha}}, \quad v_{\text{group}}(k_n) = \frac{1}{\epsilon^2}\frac{\mathrm{d}\omega_n}{\mathrm{d}k_n} = \frac{\beta + 2\gamma k_n^2}{\sqrt{\alpha\,(\beta + \gamma k_n^2)}}. \tag{6.10}$$

For $\gamma > 0$, the solutions to (6.1) are dispersive, which means each normal mode has a different phase and group velocity. If the tension factor $\beta = 0$, then we have that $v_{\text{group}}(k_n) = 2v_{\text{phase}}(k_n)$. On the other hand, if the stiffness factor $\gamma = 0$, then the waves are non-dispersive, such that $v_{\text{phase}}(k_n) = v_{\text{group}}(k_n) = \sqrt{\beta/\alpha}$ for all values of n. Initially at $t = 0$, we have $w = w_t = 0$, but the analytical solution for the pressure will be infinitely large at $x = 0$. This means we expect the membrane to be initially displaced at $x = 0$ just after impact, and the waves will subsequently travel away from the origin towards the end of the membrane at the group velocities.

Following the method of Korobkin (1998) [52], we approximate the pressure p along the membrane with the leading-order asymptotic solution in the outer region, i.e.

$$p(x, -\epsilon^2 w(x,t), t) \sim \begin{cases} \dfrac{1}{\epsilon}\hat{p}_0(\hat{x}, 0, t), & |\hat{x}| < d_0(t), \\ \\ 0, & |\hat{x}| > \epsilon d_0(t), \end{cases} \tag{6.11}$$

where recall $\hat{x} = x/\epsilon$ and $\hat{p}_0$ is given by (3.69). For the remainder of this sub-section, we will write $d_0(t) = d$ for brevity. Following the method of Korobkin (1998) [52], we seek a series solution for the leading-order velocity potential in the outer region $\hat{\phi}_0$ (first introduced in §3.2.3) applied to the membrane. Taking the real part of (3.31) for $\zeta = \hat{x}$ for with $|\hat{x}| < d$, we have

$$\hat{\phi}_0(\hat{x}, 0, t) = -\sqrt{d^2 - \hat{x}^2}\left[1 - \frac{1}{\pi}\fint_{-d}^{d} \frac{m_t(s,t)}{\sqrt{d^2 - s^2}(s - \hat{x})}\,\mathrm{d}s\right], \tag{6.12}$$

and we then construct a series solution for $\hat{\phi}_0$ in terms of $\psi_n(x)$ by defining

$$\hat{\phi}_0(\hat{x}, 0, t) = \epsilon \sum_{n=1}^{\infty} q_n(t)\psi_n(\epsilon\hat{x}), \tag{6.13}$$

where $q_n(t)$ is given by the integral

$$q_n(t) = \frac{1}{\sqrt{L}}\int_{-d}^{d} \hat{\phi}_0(\hat{x}, 0, t)\cos(\epsilon k_n \hat{x})\,\mathrm{d}\hat{x}\,. \tag{6.14}$$

To determine $q_n(t)$, we first note that the series solution for $m(s,t)$, defined by (3.29), is

$$m(s,t) = \int_0^s \hat{w}_0(\xi,t)\,\mathrm{d}\xi = \sum_{m=1}^{\infty} \frac{a_m(t)}{\sqrt{L}} \int_0^s \cos(\epsilon k_m \xi)\,\mathrm{d}\xi = \frac{1}{\epsilon\sqrt{L}} \sum_{m=1}^{\infty} \frac{a_m(t)}{k_m} \sin(\epsilon k_m s),$$

which leads to

$$q_n(t) = \frac{1}{\sqrt{L}}(-g_n(t) + s_n(t)), \tag{6.15}$$

where

$$g_n(t) = \int_{-d}^{d} \sqrt{d^2 - \hat{x}^2}\cos(\epsilon k_n \hat{x})\,\mathrm{d}\hat{x} = \frac{\pi d}{\epsilon k_n} J_1(\epsilon k_n d). \tag{6.16}$$

Here, $J_n(\cdot)$ is the Bessel function of the first kind, and

$$\begin{aligned} s_n(t) &= \frac{1}{\pi}\int_{-d}^{d}\left(\sqrt{d^2-\hat{x}^2}\int_{-d}^{d}\frac{m_t(s,t)}{\sqrt{d^2-s^2}(s-\hat{x})}\,\mathrm{d}s\right)\cos(\epsilon k_n\hat{x})\,\mathrm{d}\hat{x} \\ &= \frac{1}{\epsilon\pi\sqrt{L}}\sum_{m=1}^{\infty}\frac{\dot{a}_m(t)}{k_m}\int_{-d}^{d}\int_{-d}^{d}\frac{\sqrt{d^2-\hat{x}^2}}{\sqrt{d^2-s^2}}\frac{\sin(\epsilon k_m s)\cos(\epsilon k_n\hat{x})}{s-\hat{x}}\,\mathrm{d}s\,\mathrm{d}\hat{x} \\ &= \frac{1}{\sqrt{L}}\sum_{m=1}^{\infty}\dot{a}_m(t)S_{mn}(t), \end{aligned} \tag{6.17}$$

where, from Korobkin (1998) [52], $S_{mn}(t)$ may be written in the form

$$S_{mn}(t) = \begin{cases} \dfrac{\pi d}{\epsilon(k_n^2-k_m^2)}[k_n J_0(\epsilon k_m d)J_1(\epsilon k_n d) - k_m J_0(\epsilon k_n d)J_1(\epsilon k_m d)], & \text{if } m \neq n, \\ \dfrac{\pi d^2}{2}[J_0^2(\epsilon k_n d) + J_1^2(\epsilon k_n d)], & \text{if } m = n. \end{cases}$$

Now, recalling that $\hat{p}_0 = -\partial\hat{\phi}_0/\partial t$ for $\hat{z} = 0$, the leading-order ODE (6.8) for $a_n(t)$ is given by

$$\ddot{a}_n(t) + \omega_n^2 a_n(t) = -\frac{\epsilon^2}{\alpha}\dot{q}_n(t). \tag{6.18}$$

Then, by defining a new dependent variable

$$b_n(t) = \frac{\dot{a}_n(t) + \epsilon^2 q_n(t)/\alpha}{\omega_n^2}, \tag{6.19}$$

and substituting $b_n(t)$ into (6.18), we are left with a system of first-order ODEs given by

$$\dot{a}_n(t) + \frac{\epsilon^2}{\alpha L}\sum_{m=1}^{\infty}\dot{a}_m(t)S_{mn}(t) = \omega_n^2 b_n(t) + \frac{\epsilon^2}{\alpha\sqrt{L}}g_n(t), \tag{6.20}$$

$$\dot{b}_n(t) = -a_n(t). \tag{6.21}$$

In practice, this system will need to be solved using numerical methods, so it is convenient to express (6.20)-(6.21) in the following vectorised form

$$\dot{\mathbf{a}}(t) = \left[\boldsymbol{I} + \frac{\epsilon^2}{\alpha L}\boldsymbol{S}(t)\right]^{-1}\left[\boldsymbol{\omega}^\top \cdot \mathbf{b}(t) + \frac{\epsilon^2}{\alpha\sqrt{L}}\mathbf{g}(t)\right], \tag{6.22}$$

$$\dot{\mathbf{b}}(t) = -\mathbf{a}(t), \tag{6.23}$$

where $\boldsymbol{I}$ is the identity matrix, $\mathbf{f}(t) = (f_1(t), f_2(t), \dots)$ for $\mathbf{f} = \mathbf{a}, \mathbf{b}, \boldsymbol{\omega}, \mathbf{g}$ and $\boldsymbol{S}(t)$ is a matrix with components $S_{mn}(t)$.

In addition, we have the solution for d, given by (3.51), which in series form is

$$\begin{aligned} t - \frac{d^2}{4} &= \frac{1}{\pi}\int_{-d}^{d} \frac{\hat{w}_0(s,t)}{\sqrt{d^2 - s^2}}\,\mathrm{d}s = \frac{1}{\pi}\int_{-\pi/2}^{\pi/2} w_0(\epsilon d\sin\theta, t)\,\mathrm{d}\theta \\ &= \frac{1}{\pi\sqrt{L}}\sum_{n=1}^{\infty} a_n(t)\int_{-\pi/2}^{\pi/2}\cos(\epsilon k_n d\sin\theta)\,\mathrm{d}\theta \\ &= \frac{1}{\sqrt{L}}\sum_{n=1}^{\infty} a_n(t) J_0(\epsilon k_n d) = \frac{1}{\sqrt{L}}\mathbf{a}(t)\cdot\boldsymbol{\Gamma}(t), \end{aligned} \tag{6.24}$$

where on the first line we have made the substitution $s = \epsilon d\sin\theta$, and on the final line we define $\boldsymbol{\Gamma}(t) = (J_0(\epsilon k_1 d), J_0(\epsilon k_2 d), \dots)$.

Note that throughout the system (6.22)-(6.24), the time variable t only appears explicitly in (6.24), whilst d appears explicitly throughout (as part of the argument for the Bessel functions). Hence, it is convenient to change the independent variable to d instead of t, following Korobkin (1998) [52]. This is only justified so long as $\mathrm{d}t\,/\,\mathrm{d}d > 0$, a condition we monitor in the numerical solution. However note that as part of our analysis in §3.2.3, we already assumed that $\dot{d}(t) > 0$ for all time in order to ensure stability, so this is an equivalent assumption. Hence, by writing $t = t(d)$, we can differentiate (6.24) to determine

$$\frac{\mathrm{d}t}{\mathrm{d}d} = Q(d, \mathbf{a}, \dot{\mathbf{a}}) = \frac{\sqrt{L}d + 2\mathbf{a}\cdot\boldsymbol{\Gamma}_d(d)}{2\sqrt{L} - 2\dot{\mathbf{a}}\cdot\boldsymbol{\Gamma}(d)}, \tag{6.25}$$

where $\boldsymbol{\Gamma}_d = -\epsilon(k_1 J_1(\epsilon k_1 d), k_2 J_1(\epsilon k_2 d), \dots)$. Therefore, changing the independent variable from t to d in (6.22)-(6.23) results in the system

$$\frac{\mathrm{d}\mathbf{a}}{\mathrm{d}d} = \mathbf{F}(d, \mathbf{b})Q(d, \mathbf{a}, \mathbf{F}(d, \mathbf{b})), \tag{6.26}$$

$$\frac{\mathrm{d}\mathbf{b}}{\mathrm{d}d} = -\mathbf{a}Q(d, \mathbf{a}, \mathbf{F}(d, \mathbf{b})), \tag{6.27}$$

where

$$\mathbf{F}(d, \mathbf{b}) = \left[\boldsymbol{I} + \frac{\epsilon^2}{\alpha L}\boldsymbol{S}(d)\right]^{-1}\left[\boldsymbol{\omega}^\top \cdot \mathbf{b}(d) + \frac{\epsilon^2}{\alpha\sqrt{L}}\mathbf{g}(d)\right], \tag{6.28}$$

with initial conditions

$$\mathbf{a}(0) = \mathbf{b}(0) = \mathbf{0}. \tag{6.29}$$

Once (6.26)-(6.27) have been solved for $\mathbf{a}(d)$ and $\mathbf{b}(d)$, (6.24) can then used to determine the time $t(d)$ as a function of d. Linear interpolation can then be used to find the values of $a_n(t)$ as a function of time given $t(d)$, which allows us to determine the membrane position given by (6.5).

Throughout the analysis in Chapter 3, numerous quantities of interest were found as functions of the membrane position, the turnover point $d(t)$ and its derivative $\dot{d}(t)$. We will detail how to determine a selection of these quantities in terms of the normal modes coefficients $\mathbf{a}(t)$ and $\mathbf{b}(t)$, which we will make use of in the following sections. First, the turnover point derivative $\dot{d}(t)$ is found by inverting (6.25), such that

$$\dot{d}(t) = \frac{1}{Q(d, \mathbf{a}, \mathbf{F}(d, \mathbf{b}))}. \tag{6.30}$$

From (3.98), the jet thickness $J(t)$ depends on the time derivative of the membrane, $w_t(x,t)$, which requires finding $\dot{\mathbf{a}}(t) = \mathbf{F}(d, \mathbf{b})$. Given this, from (3.98), we have

$$J(t) = \frac{\pi(1 - B(t))^2 d(t)}{8\dot{d}(t)^2}, \quad B(t) = \frac{1}{\sqrt{L}}\dot{\mathbf{a}}(t) \cdot \mathbf{\Gamma}(t). \tag{6.31}$$

As the leading-order pressure is given by $\hat{p}_0 = -\partial\hat{\phi}_0/\partial t$, we have from (6.12) that

$$\hat{p}_0(\hat{x}, 0, t) = -\epsilon \sum_{n=1}^{\infty} \dot{q}_n(t)\psi_n(\epsilon\hat{x}), \tag{6.32}$$

where $q_n(t)$ is found by re-arranging (6.19). The derivative of $q_n(t)$ cannot be found analytically using the solutions to the system (6.26)-(6.27), therefore $\dot{q}_n(t)$ must be found via numerical differentiation.

The final quantities of interest relevant for our results in the following sections are the energies in the outer and jet regions. The energy in the jets, given by (3.170), are found via numerical integration using the solutions for $d(t)$, $\dot{d}(t)$ and $B(t)$. For the energy in the outer region, we have from (3.167) that

$$\begin{aligned} E_{K,\text{outer}}(t) &= -\frac{\epsilon^2}{2}\int_{-d}^{d}\left(1 - \frac{\partial\hat{w}_0}{\partial t}\right)\hat{\phi}_0(\hat{x}, 0, t)\,\mathrm{d}\hat{x} \\ &= \frac{\epsilon^2}{2\sqrt{L}}\sum_{n=1}^{\infty}\dot{a}_n(t)\int_{-d}^{d}\cos(\epsilon k_n\hat{x})\hat{\phi}_0(\hat{x}, 0, t)\,\mathrm{d}\hat{x} - \frac{\epsilon^2}{2}\int_{-d}^{d}\hat{\phi}_0(\hat{x}, 0, t)\,\mathrm{d}\hat{x} \\ &= \frac{\epsilon^2}{2}\sum_{n=1}^{\infty} q_n(t)\left[\dot{a}_n(t) - \frac{2\sin(\epsilon k_n d)}{\sqrt{L}k_n}\right], \end{aligned} \tag{6.33}$$

where we substituted the series solutions for $w_0(x,t)$ and $\hat{\phi}_0(\hat{x}, 0, t)$ from (6.5) and (6.12) respectively.

6.1.1.1 Numerical scheme

The full system (6.26)-(6.27) involves an infinite number of normal modes and is continuous in the variable d. In order to find a numerical solution to the system, we first must truncate the series (6.5) to a finite number of normal modes N_M, resulting in a finite system of ODEs in d. After choosing a discrete step Δd, this system is then solved using MATLAB's medium-order differential equation solver, ode45. The values for Δd and N_M must be chosen with care, as will be detailed in the following.

The size of the step Δd should depend on the desired temporal resolution, which we denote as Δt. Following Korobkin (1998) [52], we can use (6.25) to motivate choosing $\Delta d = \min_{t \leq t_{\max}}(1/Q)\Delta t$, where $t_{\max}$ is the maximum value of t chosen for the numerical scheme. In general, Q depends on the solution $\mathbf{a}$, so we cannot know the value of $\min_{t \leq t_{\max}}(1/Q)$ *a priori*. Instead, we approximate this by noting that for the case of impact onto a rigid membrane, $\mathbf{a} = \mathbf{0}$ and $d = 2\sqrt{t}$, giving $Q = \sqrt{t}$. Therefore, we approximate $\min_{t \leq t_{\max}}(1/Q) \approx 1/\sqrt{t_{\max}}$, and choose

$$\Delta d = \frac{1}{\sqrt{t_{\max}}} \Delta t. \tag{6.34}$$

To determine the appropriate number of normal modes, we first note that the time period of the n^{th} mode in the homogeneous version of (6.20) (where $p \equiv 0$) is given by

$$T_n = \frac{2\pi}{\omega_n} = \frac{2\pi}{\epsilon^2} \sqrt{\frac{\alpha}{\beta k_n^2 + \gamma k_n^4}}, \tag{6.35}$$

which decreases as n increases. Hence for any discrete timestep Δt, in order to accurately resolve the temporal oscillations of all of the modes, for any given value of N_M, we set $\Delta t = t_{N_M}/q$, where $q \geq 1$ is an integer chosen to ensure that there are q timesteps to cover the N_M^{th} mode's oscillation period. Therefore, we can rearrange the time period equation (6.35) for the chosen value of Δt in order to find an upper bound on N_M, defined to be $N_\Delta(\Delta t)$, such that

$$N_M \leq N_\Delta(\Delta t) = \frac{1}{2} + \frac{L}{\pi \epsilon \sqrt{2\gamma}} \sqrt{\sqrt{4\gamma\alpha \left(\frac{2\pi}{q\Delta t}\right)^2 + \epsilon^4 \beta^2} - \epsilon^2 \beta}. \tag{6.36}$$

In general, the choice of q needs to be validated to ensure it is high enough for the scheme to converge to the correct solution. For the results presented in this chapter, we found that $q = 10$ was sufficient for all cases.

As the original formulation (6.5) depends on an infinite number of normal modes, we need to ensure we take N_M to be large enough to give an accurate solution for

the membrane displacement, whilst ensuring we satisfy the condition (6.36). After choosing a value of Δt, motivated by the desired temporal evolution to which we wish to resolve the system, we conduct the following algorithm:

1. Determine $N_\Delta(\Delta t)$ from (6.36), which is the maximum number of normal modes we can take for any given Δt.

2. Choose an initial $N_M < N_\Delta/2$. Then, solve the system (6.22)-(6.23) using MATLAB's ode45 solver, convert the solutions into a time-dependent system using (6.24), and finally find the solution for the leading-order membrane displacement $w_0(x,t)$ from (6.5).

3. Double the number of modes (such that $N_M \to 2N_M$), and solve for $w_0(x,t)$ again using the method in step 2.

4. Determine the absolute maximum value difference between the solutions found in steps 2 and 3. If this is less than some desired tolerance, tol, we conclude the solution has converged and stop the process.

5. Otherwise, we repeat steps 2-4 with the new value of N_M until we either reach convergence, or until $N_M > N_\Delta$. If this happens, then we let $\Delta t \to \Delta t/10$, and start again from step 1.

Eventually, this process should terminate at an accurate solution for $w_0(x,t)$, however we have found that certain sets of parameters require prohibitively small timesteps and high number of normal modes in order to converge, which we will discuss later. For all of the cases studied in this chapter, we set the tolerance to be $tol = 10^{-4}$, which is of the same order as the solutions found for the membrane displacement in §6.3.

Despite giving us an accurate solution for $w_0(x,t)$, the above algorithm does not guarantee us convergent solutions for all of the quantities relevant to the flow. One in particular is the leading-order pressure on the membrane, $\hat{p}_0(\hat{x},0,t)$, given by (3.151). The truncated series solution of (6.32) for $\hat{p}_0(\hat{x},0,t)$ will be finite for any finite value of N_M. However, we know from (3.151) that the leading-order pressure solution diverges at the turnover point $\hat{x} = d(t)$. This makes it difficult for the normal modes series solution to converge, as an infinite number of modes are required to resolve the divergent point. To exemplify this, we will study the speed of convergence the series solution (6.32) exhibits towards the exact solution (3.151) when the membrane

is stationary. In this case, we have $d(t) = 2\sqrt{t}$ and $\mathbf{a}(t) = \mathbf{0}$, so that (3.151) and (6.32) become

$$\hat{p}_0(\hat{x}, 0, t) = \frac{2}{\sqrt{d(t)^2 - \hat{x}^2}}, \tag{6.37}$$

$$\hat{p}_{N_M}(\hat{x}, t) = \frac{2\pi}{L} \sum_{n=1}^{N_M} J_0(\epsilon k_n d(t)) \cos(\epsilon k_n \hat{x}), \tag{6.38}$$

where we define $\hat{p}_{N_M}$ to be the truncated series solution for (6.32) with N_M modes. To analyse the error between the series solution and the exact solution, we choose a specific time t, and discretise $\hat{x}$ from 0 up to (but not including) d using M points. We then define the error at time t to be given by

$$\text{Error}(N_M) = \sqrt{\frac{1}{M} \sum_{m=1}^{M} \left(\frac{\hat{p}_0(\hat{x}_m, 0, t) - \hat{p}_{N_M}(\hat{x}_m, t)}{\hat{p}_0(\hat{x}_k, 0, t)} \right)^2}. \tag{6.39}$$

In Figure 6.1 we show the solutions for $\hat{p}_{N_M}$ for varying values of N_M, as well as the exact solution, plotted on a log-scale for visual clarity. We also show the error, where we take $\epsilon = 0.1$, $L = 16$, $t = 1/16$ and discretise $\hat{x}$ using $M = 10^4$ points. It is clear that a very high number of modes are needed to converge to a reasonable solution for the pressure. We can see visually that for up to $N_M = 8192$, the series solution does not capture the exact solution well. The error between the exact and series solution is above 1% even for $N_M = 131072$, which is a very high number of normal modes and would present a significant computational cost to resolve the full system with. The slow convergence of the pressure was discussed by Korobkin (1998) [52], where they showed that the coefficients $\dot{q}_n(t) = O(1/\sqrt{n})$ as $n \to \infty$. We plot the curve $\text{Error}(N_M) \sim 1/\sqrt{N_M}$ with a black dotted line in Figure 6.1, and we can see that the errors roughly follow this curve. As in practice the number of modes we can take are restricted by N_Δ (6.36), we will see later that this slow convergence means we cannot accurately resolve the pressure using the normal modes within a reasonable computational time.

Another example of a quantity which we wish to resolve for the following results is the energy in the outer region, $E_{K,\text{outer}}(t)$. For the stationary membrane case where $d(t) = 2\sqrt{t}$ and $\mathbf{a}(t) = \mathbf{0}$, the exact and series solutions from (3.167) and (6.33) are given by

$$E_{K,\text{outer}}(t) = \epsilon^2 \pi t, \tag{6.40}$$

$$E_{N_M}(t) = \frac{\epsilon \pi d(t)}{L} \sum_{n=1}^{N_M} \frac{1}{k_n^2} J_1(\epsilon k_n d(t)) \sin(\epsilon k_n d(t)). \tag{6.41}$$

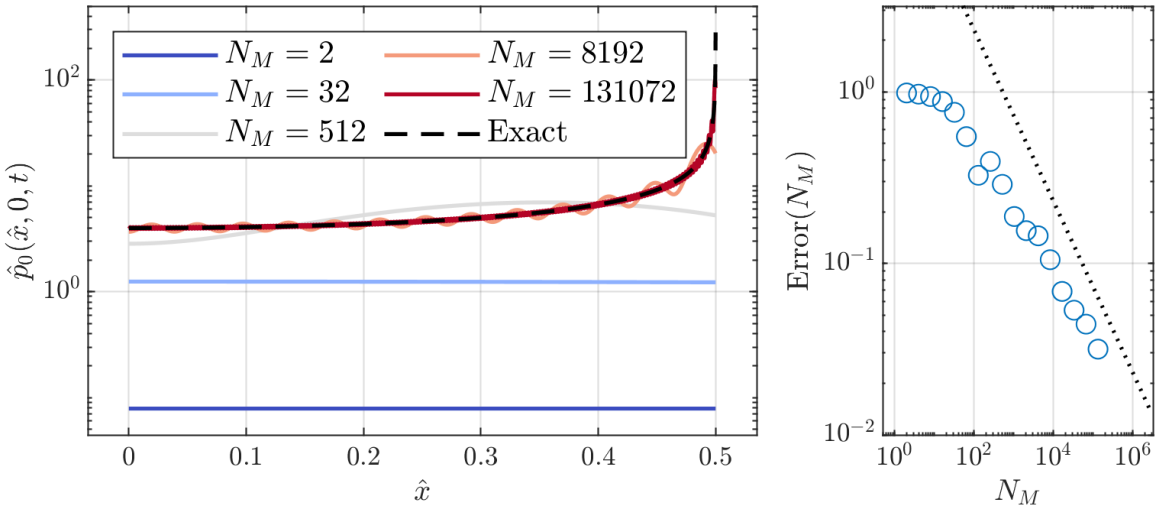

Figure 6.1: (Left): Comparison of the exact solution for the leading-order outer pressure on the membrane $\hat{p}_0$, given by (6.37), and the normal modes solutions $\hat{p}_{N_M}$, given by (6.38); the membrane is stationary, with $\epsilon = 0.1$, $t = 1/16$ and $L = 16$. (Right): Error values between $\hat{p}_0$ and $\hat{p}_{N_M}$, defined by (6.39). The black dotted line denotes a curve with the relation $\text{Error}(N_M) \sim 1/\sqrt{N_M}$.

For a uniform discretisation of time from 0 up to $t_{\max}$ with K points, we define the error to be

$$\text{Error}(N_M) = \sqrt{\frac{1}{K}\sum_{k=1}^{K}\left(\frac{E_{K,\text{outer}}(t_k) - E_{N_M}(t_k)}{E_{K,\text{outer}}(t_k)}\right)^2}. \tag{6.42}$$

In Figure 6.2 we plot the solutions for $E_{N_M}(t)$ for $\epsilon = 0.1$, $L = 16$ from $t = 0$ to 1 for various values of N_M, alongside the error values. The convergence here is faster than for the pressure, however we still require over $N_M = 1024$ normal modes in order for the error to be under 1%. As we will discuss later, this can present an issue in the cases where the parameters are such that N_Δ is small, meaning we would need to decrease the timestep considerably in order to converge to an accurate solution for $E_{K,\text{outer}}(t)$. The black dotted line denotes a curve with the relation $\text{Error}(N_M) \sim 1/(N_M)^{3/2}$, so we see that the solutions have a faster rate of convergence than the pressure solutions.

For the results presented in §6.2-6.3, with $L = 16$, the number of modes required to converge to a solution for $w_0(x, t)$ varied from $N_M = 4$ to $N_M = 122$. Once the final value of N_M has been chosen, the numerical scheme takes around 1 minute on 1 CPU to find the solution to (6.26)-(6.27). The process of finding the required values of Δt and N_M has to be repeated for each set of parameters, however we save these values for each parameter case in order to reduce computational time when re-running the scheme at later dates.

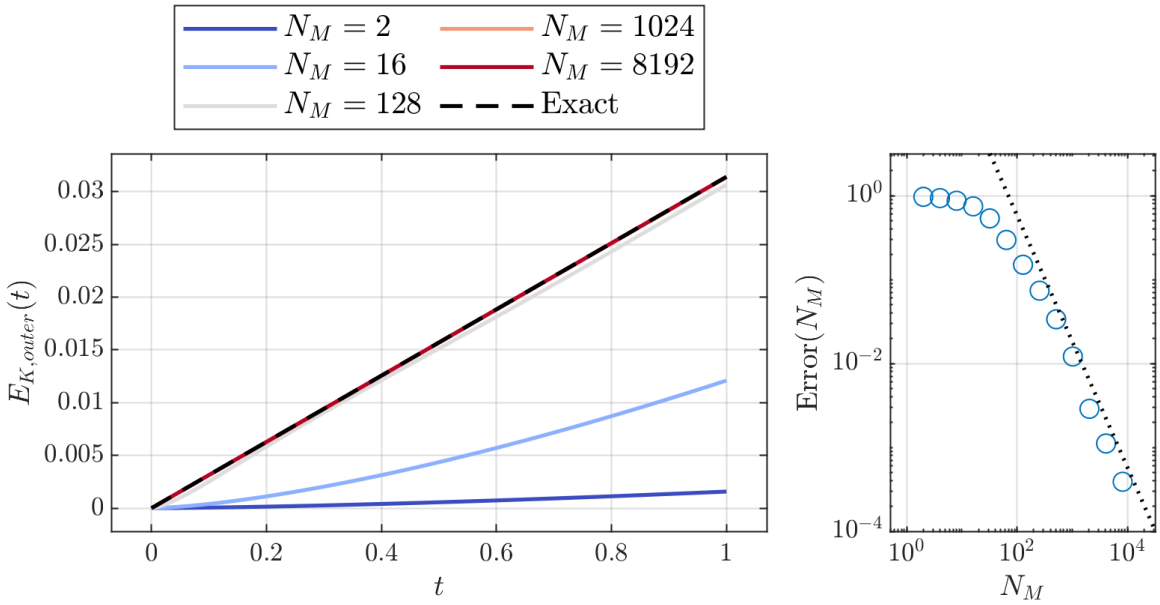

Figure 6.2: (Left): Comparison of the exact solution for the leading-order outer region energy $E_{K,\text{outer}}(t)$, given by (6.40), and the normal modes solutions $E_{N_M}(t)$, given by (6.41); where the membrane is stationary, with $\epsilon = 0.1$ and $L = 16$. (Right): Error values between $E_{K,\text{outer}}(t)$ and $E_{N_M}(t)$, defined by (6.42). The black dotted line denotes a curve with the relation $\text{Error}(N_M) \sim 1/(N_M)^{3/2}$.

As noted in Korobkin (1998) [52], one of the strengths of the normal modes method lies in choosing d as the independent variable. In the original variables, as $t \to 0$, we have $d = O(t^{1/2})$, $w_0 = O(t^{3/2})$, $w_{0t} = O(t^{1/2})$ and $w_{0tt} = O(t^{-1/2})$, so computational difficulties are faced as the contact region extends with a large velocity and the acceleration of the membrane is unbounded at early times. However, by considering d as the independent variable, then $t = O(d^2)$, $w_0 = O(d^3)$, $w_{0t} = O(d)$ and $w_{0tt} = O(d^{-1})$. This means the ODEs (6.26)-(6.27) are more regular at $d = 0$, and we can capture the early time deformations of the membrane to high accuracy. An additional advantage is that utilising the normal modes method reduces the number of degrees of freedom required to resolve the spatial dynamics. As we will discuss later for the DNS, for a membrane width of $L = 16$, the discrete grid size for the spatial dimension along the membrane is taken to be $\Delta x = 24/2^{15} \approx 7 \times 10^{-4}$, with 21,845 grid cells. Typically, we found that we needed at most 122 normal modes to converge to a solution in the results presented in §6.2-6.3, which represents approximately 180 times fewer degrees of freedom required to resolve the spatial dynamics.

A disadvantage of the normal modes method is the fact the convergence for certain quantities, such as the pressure, can be prohibitively slow given that, for any set of parameters, we have an upper bound on the number of normal modes we can

take, which was discussed previously by Korobkin (1998) [52]. Another potential limitation of the normal modes method is that it relies on approximating the pressure on the substrate with just the leading-order outer solution $\hat{p}_0(\hat{x}, 0, t)/\epsilon$ in (6.11). In Chapter 5, we found that the analytical solutions agreed with DNS much more closely when the composite solution for the pressure across the outer and inner regions was used to determine the force, rather than just the outer. We can anticipate similar behaviour for this case, where utilising the composite pressure derived in (3.156) may yield better agreement than just the outer pressure. Unfortunately, utilising the composite solution within the normal modes method means that we could not determine the coefficient $q_n(t)$ in (6.14) exactly, and would have to resort to numerical integration methods. Given this, the computational complexity of using the normal modes method would be increased, and make them equivalent in terms of complexity as solving the membrane equation (6.4) using a finite difference method.

6.1.2 Finite difference method

The previously discussed limitations of the normal modes method motivate considering using more direct methods to find the solution to the membrane equation (6.4). In this subsection we formulate an alternative method using a finite difference scheme. Not only is this method able to resolve the pressure to a higher accuracy than the normal modes method, but it also allows the use of the composite solution to the pressure (3.156), which we showed in Chapter 5 can yield closer agreement with the DNS versus using just the pressure from the outer region (of which the normal modes method is based on).

In the following, we discretise the membrane equation (6.4) using a finite difference scheme. It is known that explicit discretisations of hyperbolic PDEs are unstable, so we chose an implicit discretisation for the w dependent terms in the PDE. The scheme is second-order accurate in space and first-order in time, which we will detail in the following.

6.1.2.1 Discretisation of PDE

As the membrane position $w(x, t)$ is symmetric about $x = 0$, to save on computational costs, we consider the domain restricted to $0 \leq x \leq L$, and re-write the PDE system

(6.3)-(6.4) as

$$\alpha w_{tt} = \mathcal{L}(x,t) + p(x,t) \qquad \text{for } 0 \leq x \leq L, \tag{6.43}$$

$$w_x = w_{xxx} = 0 \qquad \text{at } x = 0, \tag{6.44}$$

$$w = w_{xx} = 0 \qquad \text{at } x = L, \tag{6.45}$$

$$w(x,0) = w_t(x,0) = 0 \qquad \text{for } 0 \leq x \leq L, \tag{6.46}$$

where

$$\mathcal{L}(x,t) = \beta w_{xx} - \gamma w_{xxxx}, \tag{6.47}$$

and we write $p(x, -\epsilon^2 w(x,t), t) = p(x,t)$ for brevity.

We discretise the spatial domain using N_F uniformly spaced points, and define $x_n = n\Delta x$, where $\Delta x = (N_F - 1)/L$, and discretise in time using a finite timestep Δt, defining $t^k = k\Delta t$. Subsequently, we let w_n^k approximate $w(x_n, t^k)$, and p_n^k approximate $p(x_n, -\epsilon^2 w(x_n, t^k), t^k)$. We define a scheme similar to that considered in Mitchell et al. (1980) [60] for the wave equation, such that

$$\alpha \left(\frac{w_n^{k-1} - 2w_n^k + w_n^{k+1}}{\Delta t^2} \right) = \frac{1}{4} \left(L_n^{k-1} + 2L_n^k + L_n^{k+1} \right) + p_n^{k-1}, \tag{6.48}$$

where L_n^k is a second-order spatial discretisation of $\mathcal{L}$ at $x = x_n$, defined by

$$L_n^k = \frac{\beta \left(w_{n-1}^k - 2w_n^k + w_{n+1}^k \right)}{\Delta x^2} - \frac{\gamma \left(w_{n-2}^k - 4w_{n-1}^k + 6w_n^k - 4w_{n+1}^k + w_{n+2}^k \right)}{\Delta x^4}. \tag{6.49}$$

If $p_n^k \equiv 0$ for all n and k, then (6.48) would be a second-order in time and space scheme. However, as determining p_n^k relies on knowing w_{tt} at $t = t^k$, we cannot resolve for p_n^k at t^k without solving a non-linear equation for w_n^{k+1}. Therefore we take p_n^{k-1} on the right-hand-side of (6.48) instead of p_n^k, which introduces an $O(\Delta t)$ error and reduces the scheme to be first-order in time.

We discretise the boundary conditions (6.44)-(6.45) using second-order accurate derivatives, and given that $w_{N_F - 1} = 0$, we do not need to solve for this point, and instead consider length $M = N_F - 1$ vectors for $W^k = (w_0^k, \ldots, w_{M-1}^k)$, $P^k = (p_0^k, \ldots, p_{M-1}^k)$, which results in a matrix form for (6.48) given by

$$AW^{k+1} = BW^k - AW^{k-1} + \frac{4\Delta x^4}{\gamma} P^{k-1}, \tag{6.50}$$

where A and B are banded matrices with two upper and lower diagonals representing the finite difference coefficients in (6.48). The second-order discretisation for the initial condition $w = w_t = 0$ then gives

$$W^0 = \mathbf{0}, \quad \frac{W^1 - W^{-1}}{2\Delta t} = \mathbf{0} \implies W^1 = W^{-1}, \tag{6.51}$$

and noting that $P^k = \mathbf{0}$ for $k \leq 0$, the initial condition for W^1 is hence

$$W^1 = \frac{1}{2} B W^0 = \mathbf{0}. \tag{6.52}$$

6.1.2.2 Numerical algorithm

The following numerical algorithm is used to solve the scheme (6.50) using MATLAB:

1. At timestep k, given P^{k-1} is known, we solve the matrix equation (6.50) for W^{k+1} using a MATLAB's banded matrix solvers.

2. We then determine the time derivatives at $t = t^k$ via

$$W_t^k = (W^{k+1} - W^{k-1})/2\Delta t, \quad W_{tt}^k = (W^{k-1} - 2W^k + W^{k+1})/\Delta t^2,$$

   and create linearly interpolated functions across $0 \leq x \leq L$ for $w(x, t^k)$, $w_t(x, t^k)$, and $w_{tt}(x, t^k)$ using W^k, W_t^k and W_{tt}^k.

3. Use a non-linear solver and global adaptive quadrature to find the leading-order turnover point $d_0(t^k)$ from (3.51) using the aforementioned interpolated function for $w(x, t^k)$, and then find $\dot{d}(t^k)$ from (3.53).

4. Solutions for $m_t(s, t^k)$ and $m_{tt}(s, t^k)$, defined by (3.29), are calculated for $0 \leq s < d(t^k)$ using trapezoidal integration. This allows the calculation of the quantities $A(t^k)$ (3.67) and $B(t^k)$ (3.98) using global adaptive quadrature in order to determine the outer pressure and jet thickness, respectively.

5. The composite solution for the pressure P^k is determined from (3.156), using trapezoidal rule to determine the outer pressure contribution from (3.151).

6. Repeat the steps 1-5 for $t = t^{k+1}$, until $t = t_{\max}$.

In order to compare to the direct numerical simulations, all of the results for §6.2 use $N_F = 21,845$ grid points with $\Delta t = 10^{-4}$. The computation time for $t_{\max} = 0.275$ on 1 CPU is typically around 3 minutes, which is about three times longer than the normal modes solutions take to compute.

As mentioned above, the finite difference method has the advantage of being compatible with the composite solution for the pressure (3.156), which has been shown to be more consistent with the numerical results from the DNS in Chapter 5. In addition, we expect to be able to resolve the solution for the pressure to a much higher degree of accuracy than the normal modes method, as discussed in §6.1.1.

The finite difference scheme is also unconditionally stable, which means that we can achieve arbitrary accuracy spatially, whereas the normal modes method is limited by the number of modes it can take for any given timestep Δt, such that $N_M < N_\Delta(\Delta t)$. However, as the discretisation for the finite difference scheme is uniform in space, the pressure profile can be poorly resolved at early times when $d_0(t^k)$ is only the size of a few grid points. This could be improved upon by considering a non-uniform discretisation in space, which would increase the complexity of the implementation. This issue is not present when using the normal modes method, as the normal mode scheme is regular at early times, as discussed previously. The finite difference method solution is also more computationally expensive than the normal modes method, as the number of grid points, N_F, is typically much larger than the required number of normal modes, N_M.

6.1.3 Direct numerical simulations

For the DNS, we take into account both the liquid viscosity and the gas phase properties, which were neglected from the analytical model. Therefore we solve the full membrane equation (6.1) for the membrane displacement. Within the linearised boundary setup detailed in §4.4.2, the membrane is taken to lie along the bottom boundary of the computational domain for $0 \leq x \leq L$ for all time. The membrane equation (6.1) is solved using a modified version of the finite difference scheme detailed in the previous subsection. The main difference is that, at the current timestep t^k, the pressure and viscous stress along the substrate are known, so we can use the current value of the pressure P^k in (6.50). We also have an additional source term in (6.50) due to the viscous stress. The scheme based on (6.50) is solved at regular timesteps $\Delta t = 10^{-4}$ using the DGBSV solver provided by the LAPACK linear algebra package, which makes use of the LU decomposition method to solve the banded matrix equation. Once W^{k+1} has been found, the vertical velocity boundary condition is updated by approximating the membrane velocity by $(W^{k+1} - W^{k-1})/(2\Delta t)$. The VOF grid for $x \leq L$ along the bottom boundary is held at the chosen maximum refinement level, and the number of finite difference grid points N_F is chosen such that Δx is equal to the width of the maximum refinement level VOF cell.

6.2 Model comparisons

We have established three different methods for solving the membrane equation (6.1) (two using the analytical model, and one within the DNS). Before we explore the

range of possible membrane setups, in this section we will focus on a single set of membrane parameters α, β, γ and compare the solutions found using each method. For this section, we will take the membrane to be a sheet of latex, with thickness $\delta^* = 1$ mm and width $2L^* = 32$ mm (such that $\delta = 1$ and $L = 16$). Latex has a density of $\rho_m^* = 1.1 \times 10^3$ kgm^{-3} and a Young's modulus of $E^* = 1.2$ MPa [9]. We will assume the sheet is not held under any tension, so we take $T^* = 0$. Given this, we have $(\alpha, \beta, \gamma) = (1.1, 0, 668)$. As the thickness and Young's modulus for this case are relatively low, we expect to the membrane to exhibit a reasonable amount of deformation in response to the droplet impact.

Similar to the results in Chapter 5, we will re-scale the time variable in the analytical model with the $\epsilon = 1$ scaling used by the DNS in order for us to compare the different models. We run the DNS from $t = t_0 = -0.125$ up to $t = 0.575$. As the membrane width is $L = 16$, we let the computational domain width be $W = 24$, and in order to retain the same spatial resolution that we concluded in §4.5 was sufficient for our studies, we set the maximum refinement level to be 15. For the analytical solutions, we run up until the point where the turnover point $d_0(t) = 1$, which in the stationary membrane case occurs at $t = 0.25$. In Figure 6.3, we compare the solutions for the membrane position at $z = -w(x, t)$ and the membrane velocity $-w_t(x, t)$ at times $t = 0$, $t = 0.01$ and $t = 0.1$. The DNS solutions are shown with solid blue lines, the analytical solutions using the normal modes method are shown with red dashed lines and the analytical solutions using the finite difference method are shown with red dotted lines.

As the analytical model neglects the influence of the surrounding gas, it predicts the membrane to be flat and stationary at $t = 0$, as depicted in Figure 6.3(a). However, for the DNS, the membrane displaces a small amount before impact due to the pressure build up in the surrounding gas. Shortly after impact at $t = 0.01$, shown in Figure 6.3(b), all of the solutions predict there to be a strong displacement in the membrane close to the origin, with wave-like displacement curves that decay in magnitude far from the origin. Because the membrane displaced before $t = 0$ in the DNS due to the gas, we see that the analytical solutions under-predict the initial displacement at $t = 0.01$ as they neglect the influence of the gas. It is clear that, in this particular physical setup, the pre-impact gas dynamics do have a role to play in the initial deformation of the membrane. Although this is not taken into account in our model, the pre-impact gas dynamics of a droplet impacting onto a membrane were considered analytically by Henman et al. (2021) [38], and could be incorporated into this modelling framework.

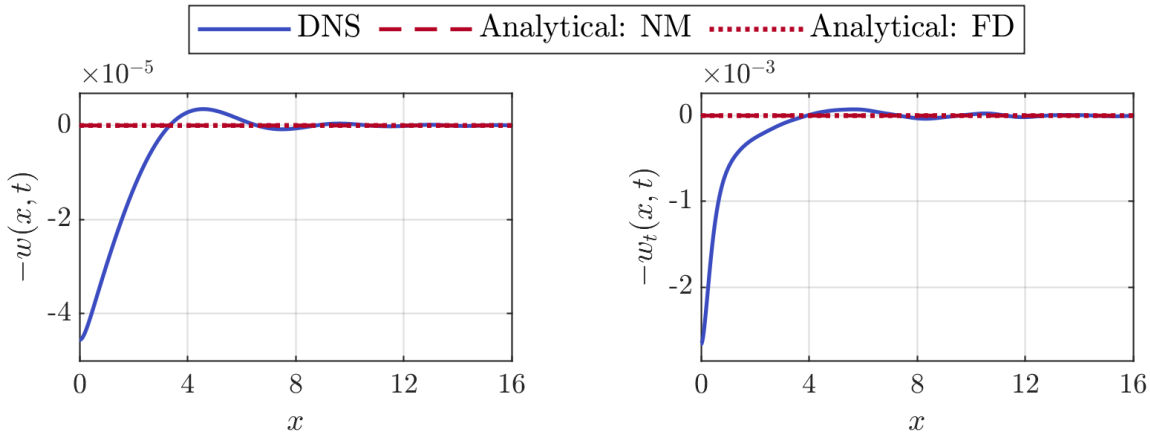

(a) $t = 0$

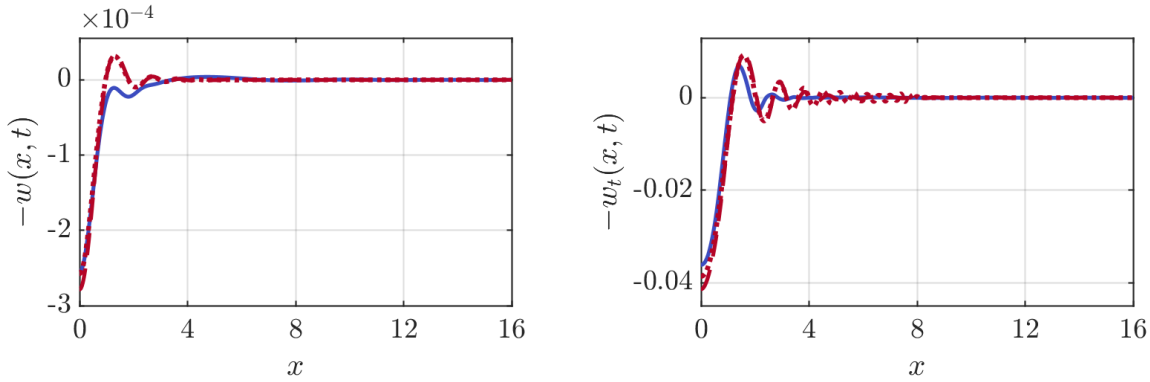

(b) $t = 0.01$

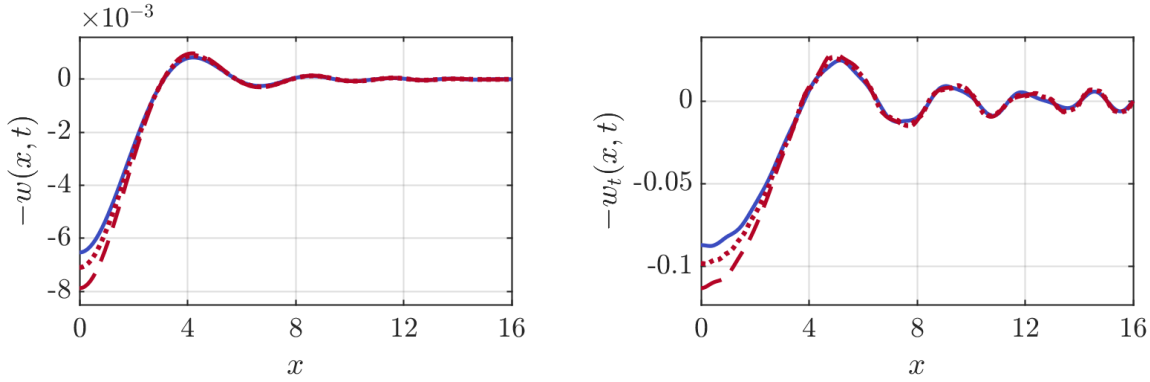

(c) $t = 0.1$

Figure 6.3: The position of the membrane at $z = -w(x,t)$ and its velocity $-w_t(x,t)$ when $(\alpha,\, \beta,\, \gamma) = (1.1,\, 0,\, 668)$. The blue lines denote the DNS solutions, the red dashed lines denote the analytical solutions using the normal modes (NM) method and the red dotted lines denote the analytical solutions using the finite difference (FD) method.

At the intermediate time of $t = 0.1$, shown in Figure 6.3(c), both analytical solutions agree well with the DNS along the majority of the membrane. Close to the

origin, we see that the normal modes method solution over-predicts the membrane displacement more than the finite difference method solution. Similar to our results from Chapter 5, this is likely due to the normal modes method only making use of the pressure from the outer region, whilst the finite difference method solution utilises the composite solution for the pressure. Recalling from Figure 3.14, we know that outer solution for the pressure diverges at the turnover point, hence over-predicting the pressure local to the turnover point compared to the composite solution. Therefore we can conclude that the inner region becomes more important to take into account when predicting the membrane displacement at these intermediate times.

From the plot of the velocity in Figure 6.3(b) at $t = 0.01$, we see that there are wave-packets travelling towards the end of the membrane. Because of the simply-supported boundary conditions, these waves will eventually be reflected back from the edge of the membrane. This is then clearly seen in the velocity plot in Figure 6.3(c) at $t = 0.1$, by which point the reflected waves have reached the centre of the membrane and hence interfere with the outgoing waves. This wave interference creates small wavelength ripples in the solution for the velocity; hence we can see how it is important to consider fine spatial discretisation to take this into account. For context, the normal modes solution for this case had $N_M = 40$ normal modes, meaning the group velocity (given by (6.10)) of the highest mode is $v_{\text{group}}(k_{N_M}) \approx 382$. At this speed, the waves reach the edge of the membrane at $t \approx 0.04$, and return to the centre of the membrane at $t \approx 0.08$, which is consistent with the wave interference seen in Figure 6.3(c). From Figure 6.3, we can conclude that both analytical solutions agree well with the DNS for the membrane displacement solution for this case, whilst representing a substantial reduction in the computational costs.

The membrane position is determined by the point-wise stress exerted onto the membrane from the fluid, given by the pressure and viscous stress on the right-hand-side of (6.1). The viscous stress is absent from the analytical model, and similar to our results from Chapter 5, we found that the viscous stress exerted on the membrane in the DNS was typically 10^5 times less than the pressure. This means that the pressure is the dominant contributing factor to the stress forcing the membrane displacement. To better understand the predictions from each model, in Figure 6.4, we plot the pressure along the membrane in equal temporal intervals from $t = 0.01$ up to $t = 0.12$, where lighter colours represent later times. On the top graph, the DNS solutions are shown with solid blue lines, and the analytical solutions using the finite difference method are shown in red dotted lines. On the bottom graph, the analytical solutions

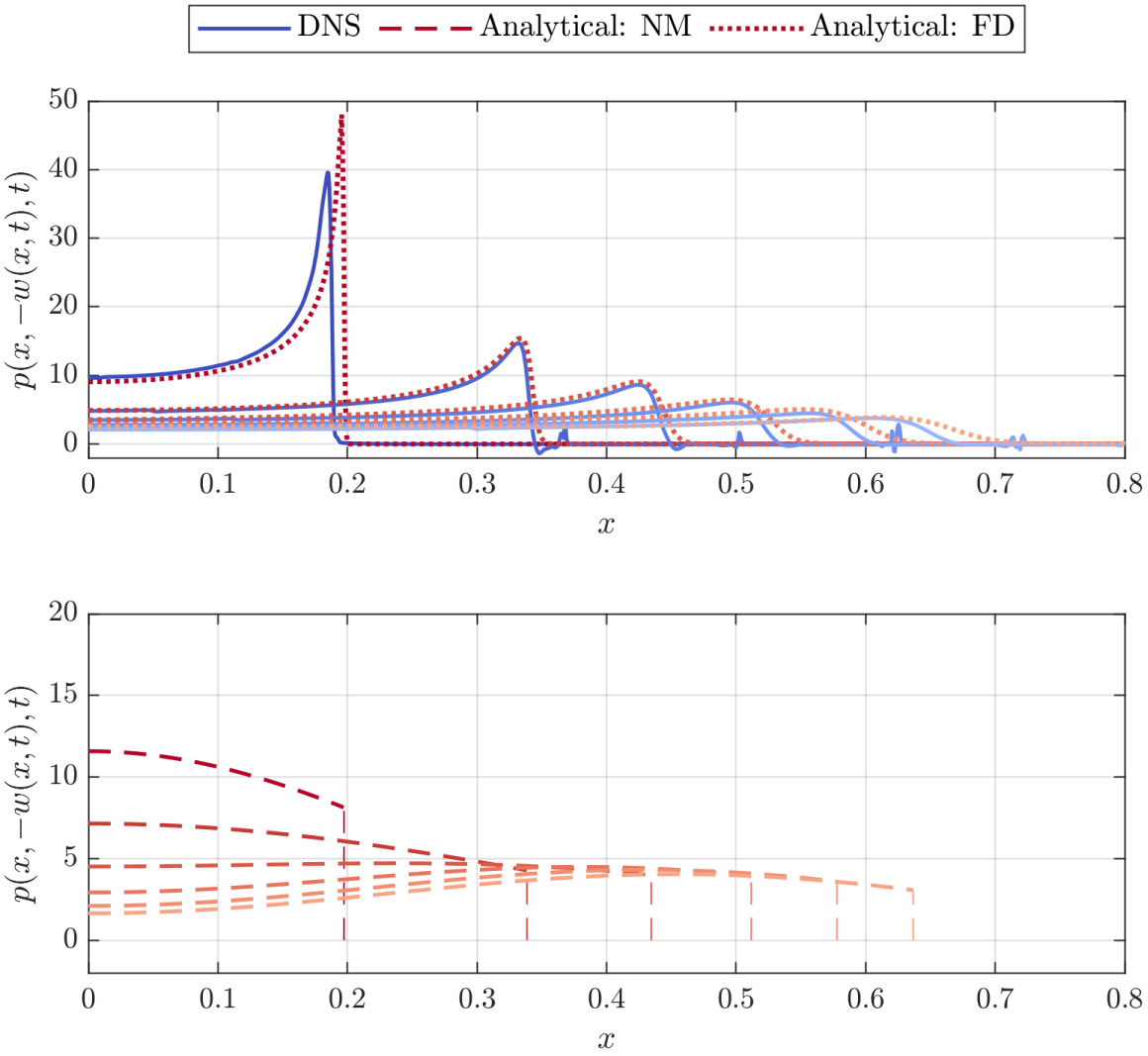

Figure 6.4: Pressure along the membrane for $(\alpha, \beta, \gamma) = (1.1, 0, 668)$ in equal temporal intervals from $t = 0.01$ up to $t = 0.12$, with lighter colours denoting later times. The top graph shows the DNS solution in solid blue lines and the analytical solutions using the finite difference (FD) method in red dotted lines. The bottom graph shows the analytical solutions using the normal modes method (NM) in red dashed lines.

using the normal modes method are shown with red dashed lines, with the pressure axis scaling adjusted for visual clarity.

Overall, the analytical solution using the finite difference method follows the DNS solutions much more closely than the normal modes. At the earliest time, there is a slight over-prediction of the pressure peak, and its horizontal location. However, at more intermediate times, the analytical solution follows the DNS closely, and at the later times we see that the solutions begin to diverge. This later time behaviour was also seen in the axisymmetric case in Chapter 5, and is likely due to the viscous

effects in the DNS reducing the pressure at later times. However the normal modes solutions fail to represent the pressure curves from the DNS at all. Referring back to Figure 6.1, we found that the normal modes solutions for the pressure require $N_M = O(10^6)$ in order to lie within 1% of the actual leading-order pressure. For this case, the normal modes solutions have $N_M = 40$, so this is far from being enough. For the chosen timestep of $\Delta t = 10^{-4}$, from (6.36) we know that the maximum number of normal modes that can be taken is 80. In order to have $N_M = O(10^6)$, we would need $\Delta t = O(10^{-12})$, which would be computationally intractable. It is clear that in order to resolve the pressure on the membrane using the analytical model, the finite difference method is the only tractable option.

Despite the series solution for the pressure from the normal modes comparing poorly to the DNS, we can still use it to approximate the maximum pressure along the substrate using the inner solution (3.93), where $\max(p(x,t)) \sim \dot{d}_0(t)^2/2$. In Figure 6.5, we compare the solutions for the maximum pressure along the substrate from the DNS (blue scatter points) alongside the analytical predictions using the normal modes method (red dashed line) and finite difference method (red dotted line). Both the analytical solutions follow the trend of the DNS curve very closely for $t > 0$. This is encouraging, in particular for the normal modes solution, as it shows that we can still use it to make quantitative predictions for some aspects of the pressure profile of the droplet along the membrane. From Figures 6.4 and 6.5, we can conclude that the appropriately chosen analytical solving method can be used to approximate the pressure distribution along the membrane to a high degree of accuracy for early times.

We now move onto studying the effects the membrane motion has on the interface of the droplet. To this end, we first focus on the horizontal position of the turnover point, $x = d(t)$, (with analytical solution given by (3.51)) for both the stationary and moving membrane cases, plotted in Figure 6.6. Both types of analytical solutions follow the DNS very closely up until the turnover point reaches $d(t) \approx 0.8$. At $t = 0.25$, where the analytical model predicts $d_0(t) = 1$ for the stationary membrane case, we find for the moving membrane case that $d_0(t) \approx 0.95$, so the membrane displacement has slowed down the turnover point spreading by $\approx 5\%$. This is similarly reflected in the DNS solution, where the equivalent reduction is around 2%.

In Figure 6.7, we plot the height of the turnover point, $H(t)$, with analytical solution given by (3.90). For this case, we find that the height of the turnover point has dropped by approximately 17% when comparing the stationary and moving membrane analytical solutions at $t = 0.25$, which is a significantly larger reduction than we saw for the horizontal position of the turnover point. Although the analytical and DNS

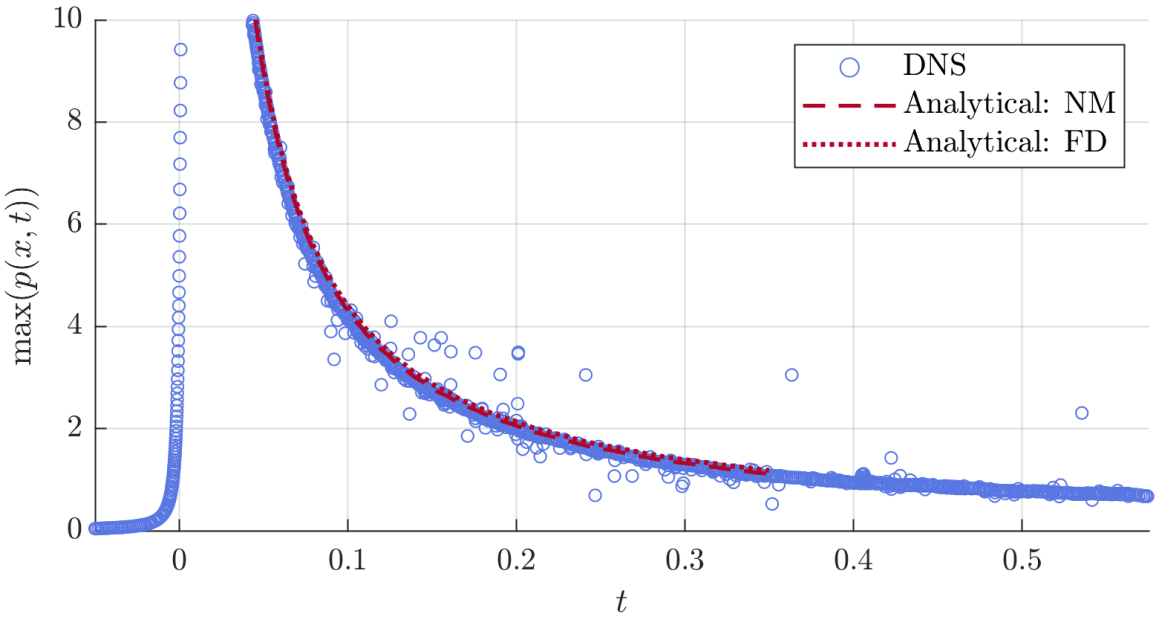

Figure 6.5: Maximum pressure along the membrane for $(\alpha, \beta, \gamma) = (1.1, 0, 668)$. The DNS solutions are shown with blue scatter points, whilst the analytical solutions (from (3.93)) are shown with red dashed (normal modes) and red dotted (finite difference) lines respectively.

solutions do not agree as well for the turnover height, we do also find that the turnover point height to have reduced by approximately 17% in the DNS case as well. This means that, even though the analytical solutions over-predict the evolution of the jet height, the relative differences between the stationary and moving membrane cases are well captured.

When interpreting data taken from the DNS for the moving membrane cases, it is worth recalling that, due to the nature of the linearised boundary setup considered in §4.4.2, we expect there to be mass lost through the bottom boundary as we apply a non-zero flux condition there. Therefore, it is important to assess to what extent this mass loss has effected the solutions gained from the DNS. To this end, in Figure 6.8, we plot the interface of the droplet taken from the DNS in equal temporal intervals from $t = 0.005$ up to $t = 0.575$, where Figure 6.8(a) shows the stationary substrate case and Figure 6.8(b) shows the moving membrane case. As we know from Figures 6.6 and 6.7, we expect only a relatively small reduction in the evolution of the turnover point between the two cases, which is reflected when comparing these points in Figure 6.8. However, we see that the horizontal extent of the jet in the moving membrane case has been significantly reduced at later times in comparison to the stationary membrane case, much more so than the reduction in the turnover point. This is

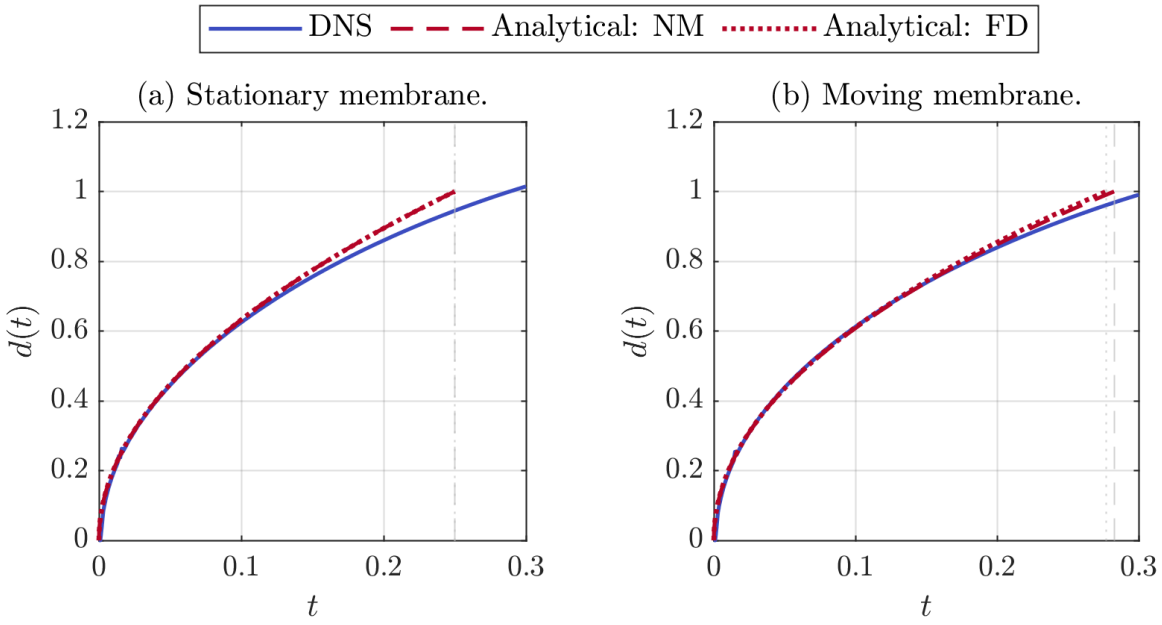

Figure 6.6: The horizontal position of the turnover point, $d(t)$, for the (a) the stationary membrane case and (b) the moving membrane case with $(\alpha,\ \beta,\ \gamma) = (1.1,\ 0,\ 668)$. The blue lines denote the DNS solutions, the red dashed lines denote the analytical solutions using the normal modes (NM) method and the red dotted lines denote the analytical solutions using the finite difference (FD) method (with analytical solution given by (3.51)).

likely due to the fact that, as the jet becomes very thin towards its tip, the non-zero flux boundary condition acts to remove fluid volume from the jets, effectively reducing the amount of mass it contains. Although this effect is relatively small at early times, at the last timestep, the jet tip position has reduced from $x = 2.41$ in the stationary membrane case to $x = 1.84$ in the moving membrane case, marking a 24% reduction. Given that the horizontal extent of the turnover point only reduced by approximately 5% in this case, we can infer that much of this reduction is due to the mass loss.

To quantify the extent of this mass loss, in Figure 6.9, we plot $R(t)$, defined in (4.26) to be the ratio between the change in droplet area and its initial area, for both the stationary and moving membrane case. Whilst the stationary case only lost around 10^{-3}% of its mass across the simulation timescale, the moving membrane case lost approximately 5% in total. As the mass is lost through the bottom boundary where the droplet makes contact with the membrane, we can infer from this that a substantial amount of the mass lost would have been through the jet, as at later times, the jet makes up a large portion of the contact set.

In this section we have focused on comparing the predictions of the DNS with those of the analytical model when the droplet impacts onto a thin sheet of latex,

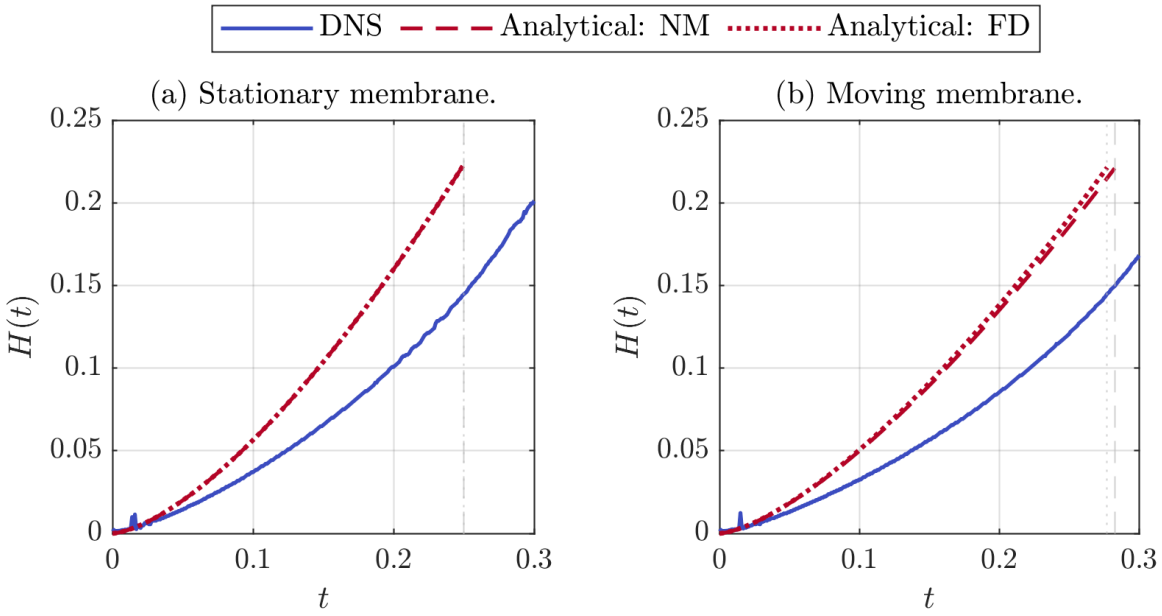

Figure 6.7: The height of the turnover point, $H(t)$, for the (a) the stationary membrane case and (b) the moving membrane case with $(\alpha, \beta, \gamma) = (1.1, 0, 668)$. The blue lines denote the DNS solutions, the red dashed lines denote the analytical solutions using the normal modes (NM) method and the red dotted lines denote the analytical solutions using the finite difference (FD) method (with analytical solution given by (3.90)).

using both the normal modes and finite difference method to resolve the membrane position with the analytical model. We found that the analytical model gives close agreement with the DNS solutions for the membrane position shortly after the time of impact, as well as the location of the turnover point and the maximum pressure on the membrane. We also found that the normal modes method is insufficient to resolve the pressure along the entire length of the membrane, which was noted by Korobkin (1998) [52].

The DNS solutions presented in this section took around 500 CPU hours to resolve, whilst the analytical solutions using the normal modes and finite difference methods took around 1 and 5 minutes respectively. Given the close agreement of the analytical and DNS solutions, this marks a substantial reduction in computational cost whilst retaining good accuracy at early times. In particular, the normal modes method only required $N_M = 40$ modes, whilst its finite difference based counterpart used $N_F = 21,845$ spatial grid points. This means the normal modes method requires much fewer degrees of freedom to resolve the spatial dynamics of the membrane. In addition, the normal modes method gave us insight into quantities such as the phase and wave velocity of the solutions, which would have had to be determined

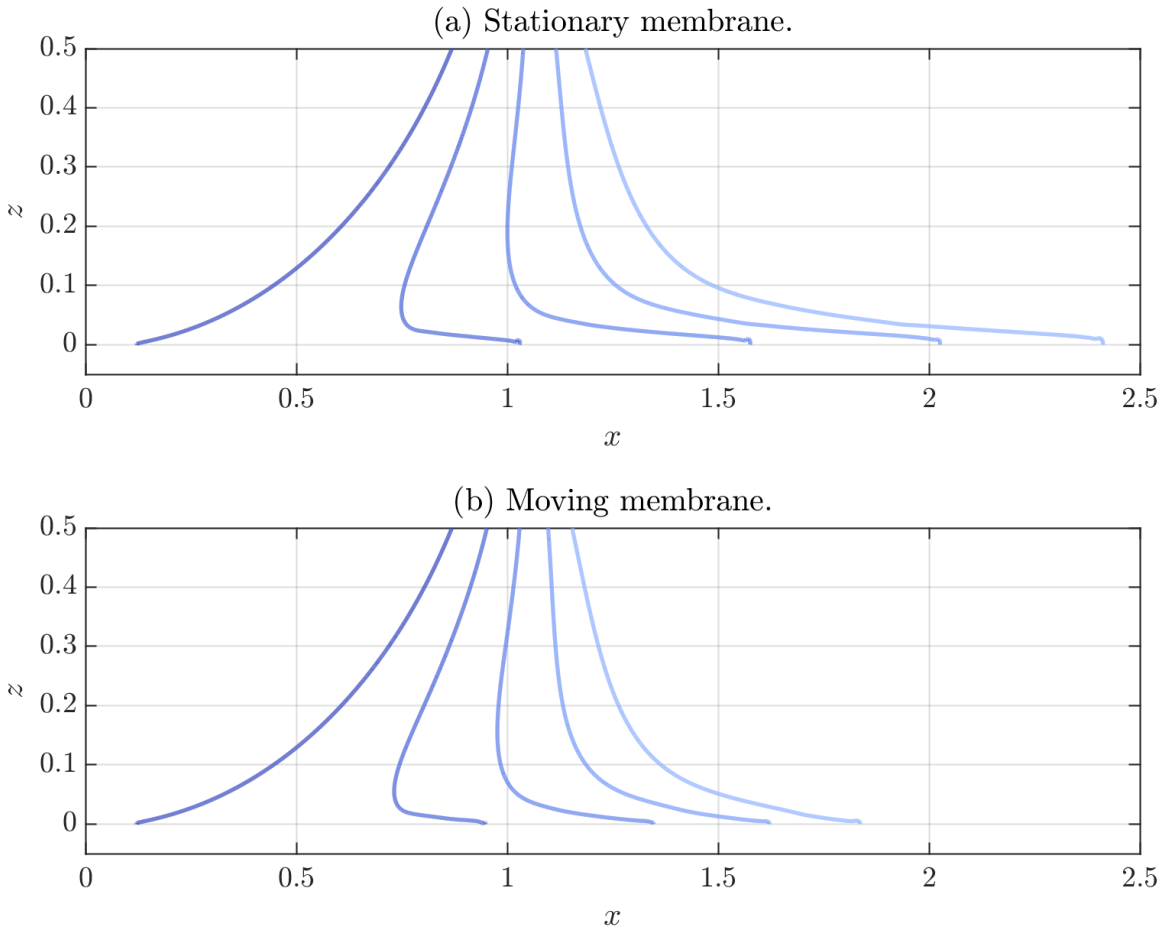

Figure 6.8: The interface of the droplet taken from the DNS, plotted in equal temporal temporal intervals from $t = 0.005$ up to $t = 0.575$, where lighter colours denote later times. Figure 6.8(a) shows the stationary membrane case whilst Figure 6.8(b) shows the moving membrane case with $(\alpha, \beta, \gamma) = (1.1, 0, 668)$.

numerically from the finite difference solution using discrete Fourier transformations. Having studied this one particular membrane setup in detail, in the following section we will conduct a parameter study to investigate the effects that membranes with different physical properties have on the dynamics of the system.

6.3 Membrane parameter comparisons

In the previous section, we extensively studied one particular membrane setup, which represented a sheet of 1 mm thick latex under no tension with a width of $L^* = 1.6$ cm. In this section, we will study how varying the material properties of the membrane alters the dynamics of the system. As previously detailed, there are five dimensionless parameters which determine the material properties of the membrane,

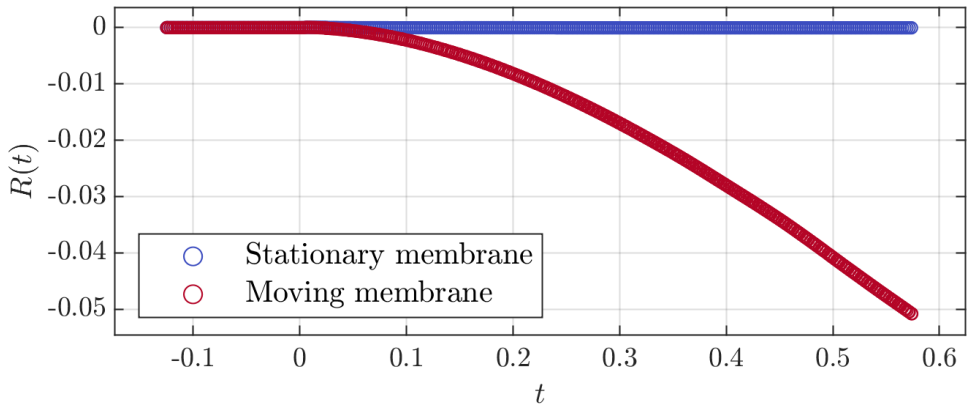

Figure 6.9: Area loss in the droplet, defined by (4.26), for the stationary membrane case (blue) and the moving membrane case (red) with $(\alpha, \beta, \gamma) = (1.1, 0, 668)$.

namely the width L, the thickness ratio δ, the density factor α, the tension factor β and the stiffness factor γ. For brevity, in this section we will keep the width at a constant value of $L = 16$. In addition, we will assume the density of the membrane is kept at the value for latex, such that $\rho_m^* = 1.1 \times 10^3$ kgm^{-3}. In the following, we will study the change in the dynamics when we independently vary the thickness ratio δ, the tension factor β and the stiffness factor γ.

In order to determine the influence each of these parameters have on the dynamics of the system, we need to conduct an extensive parameter study, varying the values of δ, β and γ. The DNS solutions gained from the previous section, with maximum refinement level 15, took around 500 CPU hours to resolve each, whereas the analytical solutions only require a few minutes to resolve. In the previous section, we found good agreement between the analytical and DNS solutions for the membrane at early times, as well as close agreement for the turnover point position and maximum pressure values. Given this, we can employ the same strategy we used in Chapter 5 to conduct a wide parameter study using the analytical model. This will help us to identify parameter regimes of interest which can then be targeted for DNS, which will allow us to study the later time behaviour of the process. For the DNS in this section, we will use a lower refinement level of 14, which typically reduced the CPU time to around 150 hours. This was done to reduce the computational time it took to obtain the results of the parameter studies, and from §4.5, we know that for the quantities we are interested in for these results, level 14 is sufficient to give us an accurate DNS solution. In particular, we know from Figure 4.11 that the amount of mass lost from the boundary is relatively insensitive to lowering the refinement level.

In the following, we will conduct three different parameter studies, where for each

we vary either the membrane thickness, stiffness or tension, whilst keeping the other material properties fixed. We will determine how a selection of key quantities related to the droplet dynamics at a specific time differ as we vary each of these properties in turn. To this end, we choose a test time $t_c = 1/16 = 0.0625$, such that the analytical model predicts the horizontal position of the turnover point is at $d_0(t_c) = 2\sqrt{t_c} = 0.5$ in the stationary membrane case. At this time, we know from Figure 6.6 that the analytical model agrees closely with the DNS solution for the turnover point position. For this parameter study, we opt to use the normal modes method to determine the analytical solutions. Not only is this method computationally faster than the finite difference method, but it also gives us additional insight into the membrane dynamics informing us into the number of normal modes that are excited during the process. At t_c, we save the horizontal position of the turnover point, $d_0(t_c)$; the height of the turnover point, $H(t_c)$; the maximum pressure on the membrane, $\max(p(x, t_c))$; and the kinetic energies in the outer region, $E_{K,\text{outer}}(t_c)$, and the jets, $E_{K,\text{jets}}(t_c)$. These quantities indicate the extent to which the membrane motion affects the emergence of the turnover point at early time, as well as how it affects the pressure and kinetic energy distribution in the droplet. In addition, we also save the number of normal modes required to reach convergence, N_M, and the corresponding phase and group velocities of the N_M^{th} mode, given by (6.10). These will give us an indication as to the wave forms of the membrane solutions, and the speeds at which they propagate outwards upon impact. For each parameter study, we test 100 difference cases, varying either δ, γ or β independently.

6.3.1 Membrane thickness

The thickness ratio $\delta = \delta^*/R_d^*$ represents the ratio between the thickness of the membrane and the radius of the droplet. We would typically expect thicker membranes to deform less upon impact due to fact that they would have more mass and therefore require more force to deform. For this section, we will assume the membrane is again made of latex and is not under tension, such that $T^* = 0$ (therefore $\beta = 0$) and that $E^* = 1.2$ MPa. Therefore, for fixed ρ_m^* and E^*, we have that $\alpha = 1.1\delta$ and $\gamma = 668\delta^3$.

For this section we will study the effects of varying the thickness ratio from $\delta = 0.125$ up to $\delta = 8$. The derivation of the membrane equation (6.1) assumes that the thickness of the membrane is much less than the width of the membrane. Therefore the $\delta = 8$ case is such that the membrane thickness is a quarter of the total width of the membrane, so increasing the thickness past this point would risk pushing outside of the bounds where the membrane equation is valid. In Figure 6.10, we plot the

normal modes solutions for $d_0(t_c)$, $H(t_c)$, $\max(p(x,t_c))$, $E_{K,\text{outer}}(t_c)$ and $E_{K,\text{jets}}(t_c)$ for δ varying from $\delta = 0.125$ to 8, where $t_c = 1/16$; as well as the number of modes required to reach convergence, N_M, and the phase and group velocities, $v_{\text{phase}}(k_{N_M})$ and $v_{\text{group}}(k_{N_M})$. Physically, this range covers membranes of thicknesses from 0.125 mm up to 8 mm.

The results in Figure 6.10 show that decreasing the membrane thickness δ for $\delta \leq 2$ acts to decrease the values of the turnover point horizontal position, turnover point height, maximum pressure and the kinetic energies. For the lowest value of $\delta = 0.125$, we see that the pressure value is less than half of the stationary membrane case, and the kinetic energies are each less than a quarter of the stationary membrane values. For small values of δ, the membrane will displace to a greater degree (i.e. $w_0(x,t)$ is greater). By analysing (3.51), (3.90), (3.93), (3.167) and (3.170), we can readily see how this is expected behaviour when the displacement is increased. For large values of δ, we expect the solutions to converge onto the stationary membrane values. There is a monotonic behaviour between δ and the turnover point location and height. It is apparent then that the thinner membranes, which will deform to a greater degree, act to slow down the spreading with thinner jets. Similarly, the maximum pressure is smaller in the lower δ cases, as the fact the membrane is more deformable acts to reduce the pressure, where the maximum pressure is under half of the stationary membrane value for $\delta = 0.125$. We also see there to be a significant reduction in the energy in both the outer region and jets as δ decreases. Interestingly, we see the monotonic behaviour in $E_{K,\text{outer}}(t_c)$ break down once $\delta \gtrsim 2$, where the energy in the outer region actually decreases for these higher values of δ. We can better understand this behaviour by studying the number of normal modes, N_M, required to reach convergence, plotted in Figure 6.10. From (6.36) (the formula for the maximum number of modes we can take, N_Δ), we expect $N_\Delta \sim \delta^{-1/2}$, which is captured in Figure 6.10. For $\delta \geq 2$, we have that $N_M \leq 28$. Referring back to the analysis of the accuracy of the energy solution in Figure 6.1, we find that the error between the exact and normal modes solution for $E_{K,\text{outer}}(t)$ when $N_M \leq 28$ is at least 50%, which could explain why these irregularities occur in Figure 6.10 for $\delta \geq 2$. As discussed in §6.1.1, this is an inherent feature of the normal modes method which makes it difficult to study the cases where the membrane parameters are large, as the condition that $N_M \leq N_\Delta$ prevents us from taking enough normal modes in the solution to have convergent solutions to certain quantities.

The vertical lines in Figure 6.10 denote the range of parameters which we select for studying using DNS, as we can see that there is a noticeable difference in the

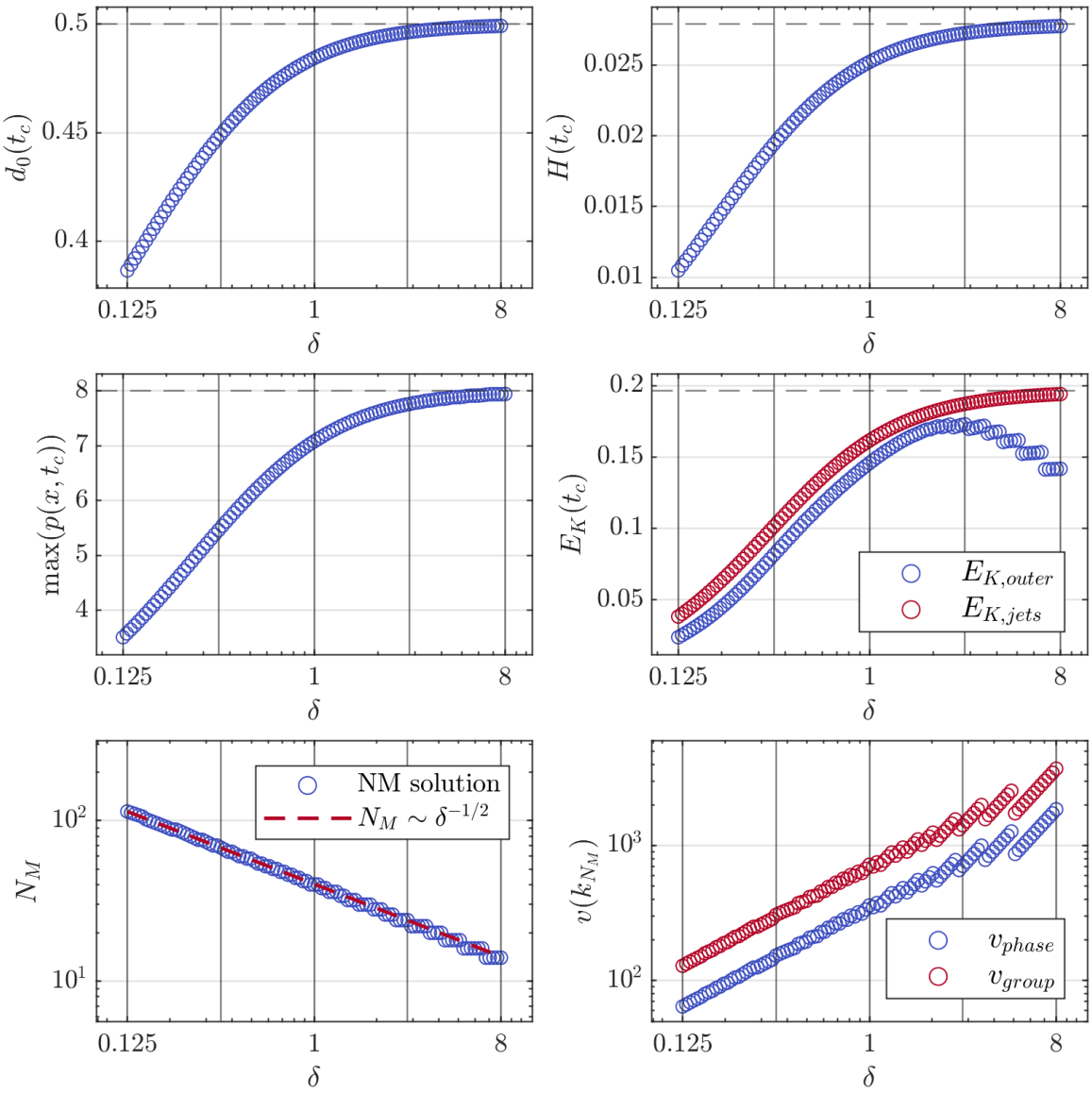

Figure 6.10: Normal modes solution for the turnover point horizontal position $d_0(t_c)$ (3.51), turnover point height $H(t_c)$ (3.90), maximum pressure $\max(p(x,t_c))$ (3.93), and the kinetic energies $E_{K,\text{outer}}(t_c)$ (3.167) and $E_{K,\text{jets}}(t_c)$ (3.170), for time $t_c = 1/16$; as well as the number of modes required to reach convergence, N_M, and the phase and group velocities, $v_{\text{phase}}(k_{N_M})$ and $v_{\text{group}}(k_{N_M})$, given by (6.10). For all cases, $\alpha = 1.1\delta$, $\beta = 0$ and $\gamma = 668\delta^3$. The horizontal dashed lines denote the stationary membrane solutions, and the vertical lines denote the parameters selected for DNS in Figure 6.11.

behaviour of the droplet in response to membrane across this range. In Figure 6.11, we plot the DNS solutions for the membrane position and velocity for the values of δ denoted by the vertical lines in Figure 6.10, at times $t = 0.1$, $t = 0.2$ and the final time value of $t = 0.575$. We clearly see how the membrane displaces to a greater degree

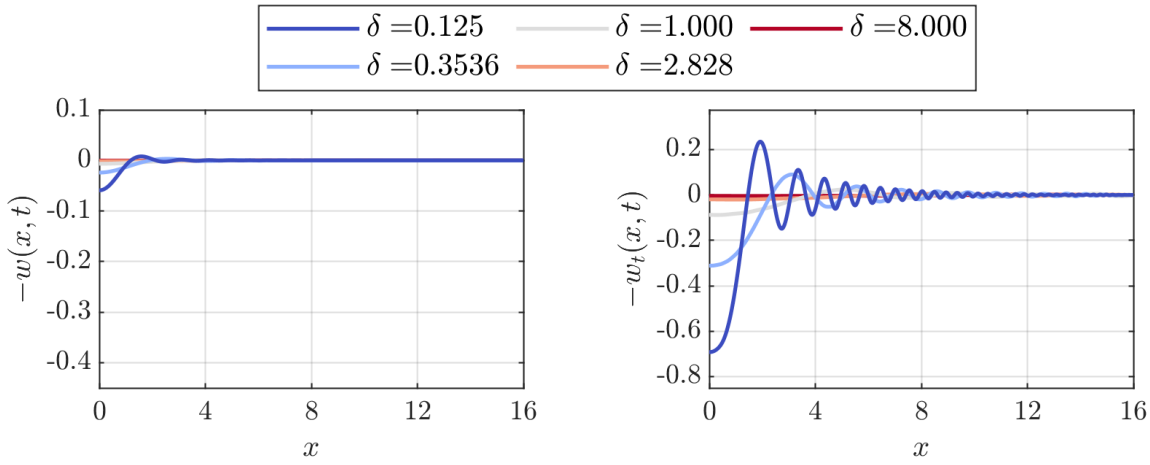

(a) $t = 0.1$

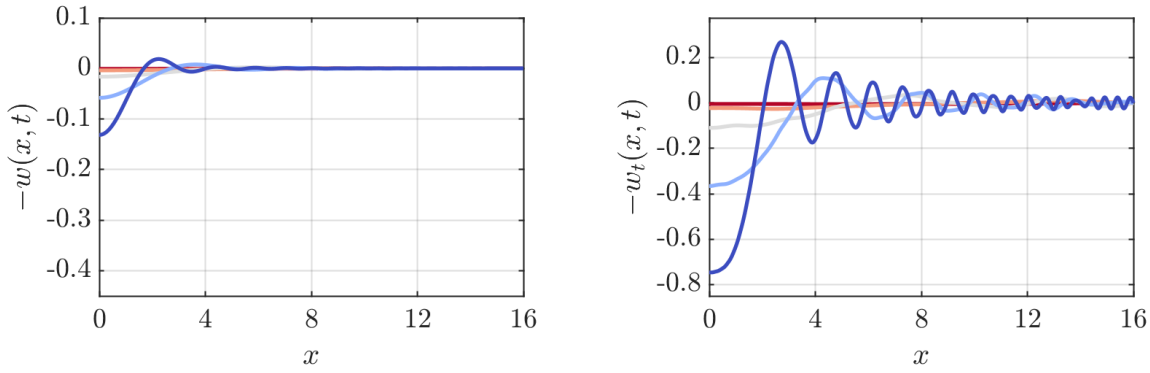

(b) $t = 0.2$

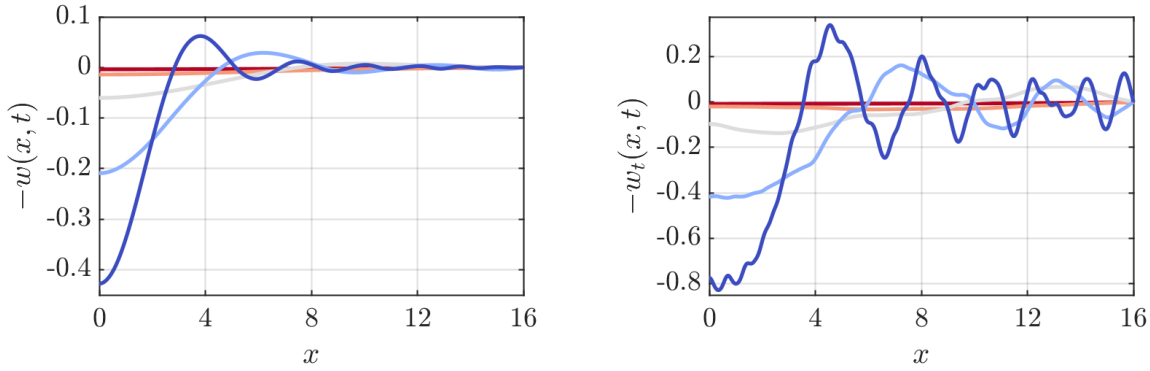

(c) $t = 0.575$

Figure 6.11: DNS solutions for the position of the membrane at $z = -w(x,t)$ and its velocity $-w_t(x,t)$ for $\alpha = 1.1\delta$, $\beta = 0$ and $\gamma = 668\delta^3$. The thickness ratio δ is varied from 0.125 to 8, with the colours changing from blue to red as δ is increased.

for smaller values of δ, which is as expected as the membranes in these cases require less force to displace. From Figure 6.10(a), we know from the normal modes solutions that the cases where δ is lower excite more normal modes (i.e. N_M is higher), which means the wave solutions will have a lower wavelength, which is clearly reflected in

the DNS solutions in Figure 6.11. For this case where $\beta = 0$, we have from (6.10) that the group velocity $v_{\text{group}}(k_n) = 2v_{\text{phase}}(k_n)$, which we plot in Figure 6.10 for $n = N_M$. The higher δ cases have a higher value of the phase/group velocity, meaning the waves travel outwards towards the edge of the membrane more quickly. This can be seen at $t = 0.2$ in Figure 6.11(b), where the waves reflected back from the edge of the membrane have not appeared to have affected the $\delta = 0.125$ case to a significant degree close to the origin, but have for the $\delta = 1$ case. The overall behaviour of the membrane solutions from Figure 6.11 is then that the smaller the membrane thickness, the more the membrane is displaced upon impact from the droplet, with the waves travelling from the origin will having a smaller wavelength and velocity.

To illustrate the effects the membrane motion has on the evolution of the droplet, in Figure 6.12 we plot the horizontal and vertical position of the turnover point, $d(t)$ and $H(t)$, from the DNS for the five different values of δ indicated with vertical lines in Figure 6.10, along with the stationary membrane case shown with black dotted lines. The lines are stopped at the times when $d(t) = 1$, which are denoted by vertical dotted lines. The trends shown by the analytical solutions in Figure 6.10 are well reflected by the DNS solutions, showing that the evolution of the horizontal and vertical positions of the turnover point are slowed down when the membrane thickness is decreased. From Figure 6.11, we can infer that this is due to the membrane experiencing a substantial displacement local to the droplet (where $x < 1$) when the thickness is lower, which thus slows down the initial spreading of the droplet upon impact.

The membrane motion according to (6.1) is driven by the pressure along the membrane, which is plotted in Figure 6.13 for the five different δ varying cases and the stationary membrane case at $t = 0.1$. There is a substantial reduction in the pressure due to the membrane motion, which was predicted by the analytical solutions given in Figure 6.10. As the pressure peak occurs close to the turnover point, we see that the horizontal location of the pressure peak has been reduced, following the trends in the turnover point seen in Figure 6.12. The pressure curves in Figure 6.13 exemplify the fluid-structure interaction between the droplet and the membrane; for lower values of δ, the membrane displaces to a greater degree, meaning the pressure impulse exerted onto the droplet is lower, causing the pressure to decrease in comparison to the higher δ cases. As the membrane displacement is driven by the pressure, the displacement is still greater in the lower δ cases despite this lower value of the pressure.

For any given material, we expected that thinner membranes would deform to a greater degree than thicker ones upon impact, which has been confirmed by the results of this subsection. When the membrane displaces to a greater degree, we

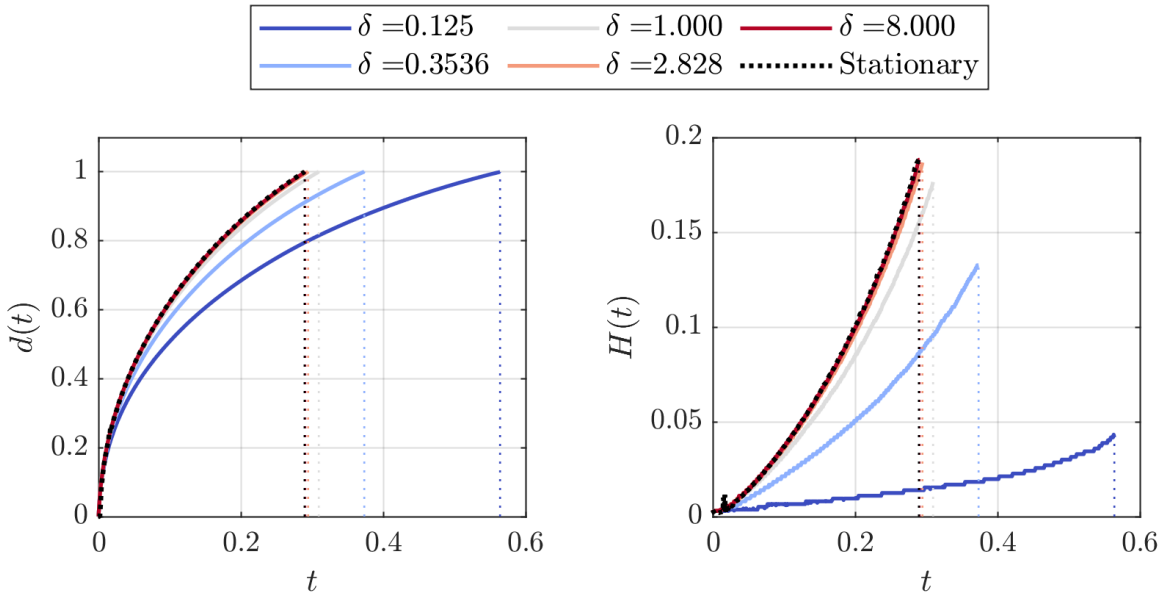

Figure 6.12: DNS solutions for the turnover point horizontal position $d(t)$ and vertical position $H(t)$, for $\alpha = 1.1\delta$, $\beta = 0$ and $\gamma = 668\delta^3$. The thickness ratio δ is varied from 0.125 to 8, with the line colours changing from blue to red as δ is increased, and the black dotted lines denote the stationary membrane solution. The vertical dotted lines denote the times at which $d(t) = 1$.

have seen that the droplet spreads more slowly across it, as it has lost some of its kinetic energy in deforming the membrane upon impact. This also acts to reduce the pressure inside the droplet, as seen in Figure 6.13. We have demonstrated in this subsection that varying the thickness of the membrane can have a strong influence on the dynamics both of the form the membrane displacement takes, as well as affecting the spreading behaviour of the droplet itself.

6.3.2 Membrane stiffness

In the previous subsection, the material properties of the membrane were kept constant, and only the thickness of the membrane was changed. In this subsection, we will set the thickness ratio at a constant value of $\delta = 0.125$ (such that $\alpha = 0.1375$), assume that the membrane is under no tension (i.e. $\beta = 0$), and vary the stiffness factor γ. The Young's modulus of solids can vary across many orders of magnitude, so we will vary γ from 1 up to 10^6 (where in this case $\gamma = 1.305$ for latex). In the same manner as Figure 6.10, in Figure 6.14 we plot the normal modes solutions for $d_0(t_c)$, $H(t_c)$, $\max(p(x, t_c))$, $E_{K,\text{outer}}(t_c)$ and $E_{K,\text{jets}}(t_c)$ for γ varying from $\gamma = 1$ to 10^6, where $t_c = 1/16$, as well as the number of modes required for convergence, N_M, and the corresponding phase and group velocities. For this case with δ fixed,

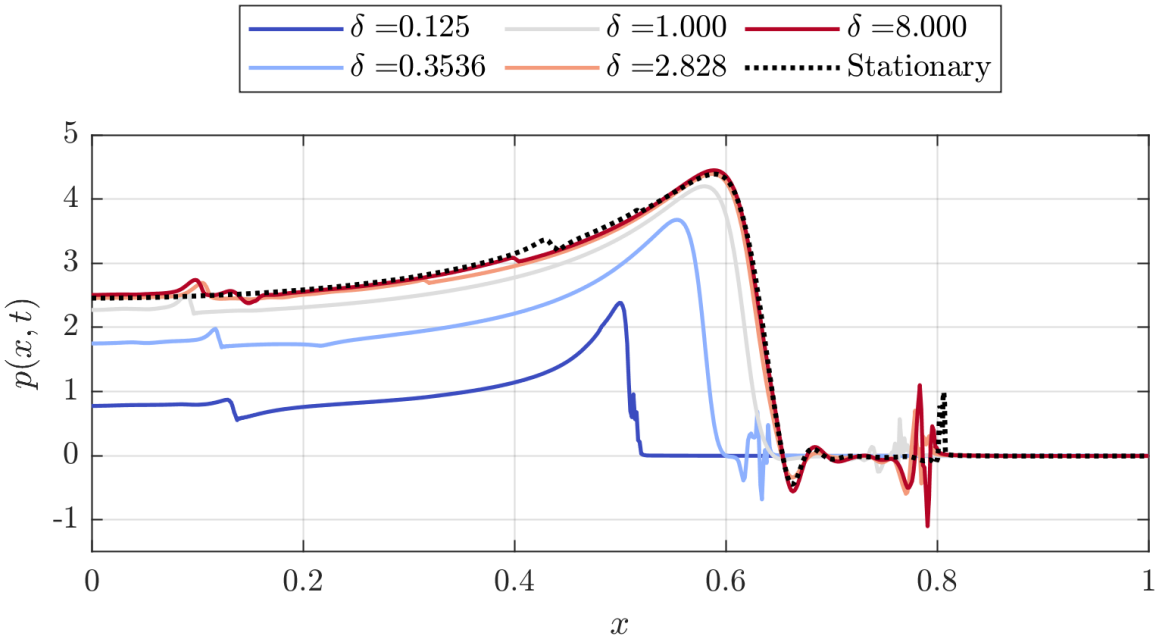

Figure 6.13: DNS solutions for the pressure on the membrane at $t = 0.1$, for $\alpha = 1.1\delta$, $\beta = 0$ and $\gamma = 668\delta^3$. The thickness ratio δ is varied from 0.125 to 8, with the line colours changing from blue to red as δ is increased, and the black dotted line denotes the stationary membrane solution.

from (6.36) we have that $N_\Delta = O(\gamma^{-1/4})$ as γ is varied, and as $\beta = 0$, we still have $v_{\text{group}}(k_n) = 2v_{\text{phase}}(k_n)$.

Similar to the membrane thickness, we expect that stiffer membranes will deform to a lesser degree due to providing more resistance to motion. Subsequently, in Figure 6.14 we see that the turnover point horizontal and vertical positions, $d_0(t)$ and $H(t)$, as well as the maximum pressure and energies are reduced for lower values of γ, as the membrane displacement is greatest in these cases. Once $\gamma \gtrsim 10^3$, we begin to see irregularities in the solutions and the monotonic behaviour breaks down, particularly for the maximum pressure and the energy in the outer region. Once $\gamma \geq 10^3$, from the plot of the number of modes, N_M, in Figure 6.14, we see that $N_M \leq 22$. Therefore, similar to the case with the membrane thickness in §6.3.1, we expect the kinetic energy in the outer region to poorly converge once $\gamma \geq 10^3$ as there are not a sufficient number of modes for the series solution to converge to the exact solution. Although there is also non-monotonic behaviour for the turnover point location and the maximum pressure, this is due to temporal oscillations in the turnover point solution. To demonstrate this, in Figure 6.15 we plot the normal modes solutions for $\dot{d}_0(t)$ for the five values of γ denoted by the vertical lines in Figure 6.14, along with the stationary membrane solution of $d_0(t) = 1/\sqrt{t}$. It can be seen

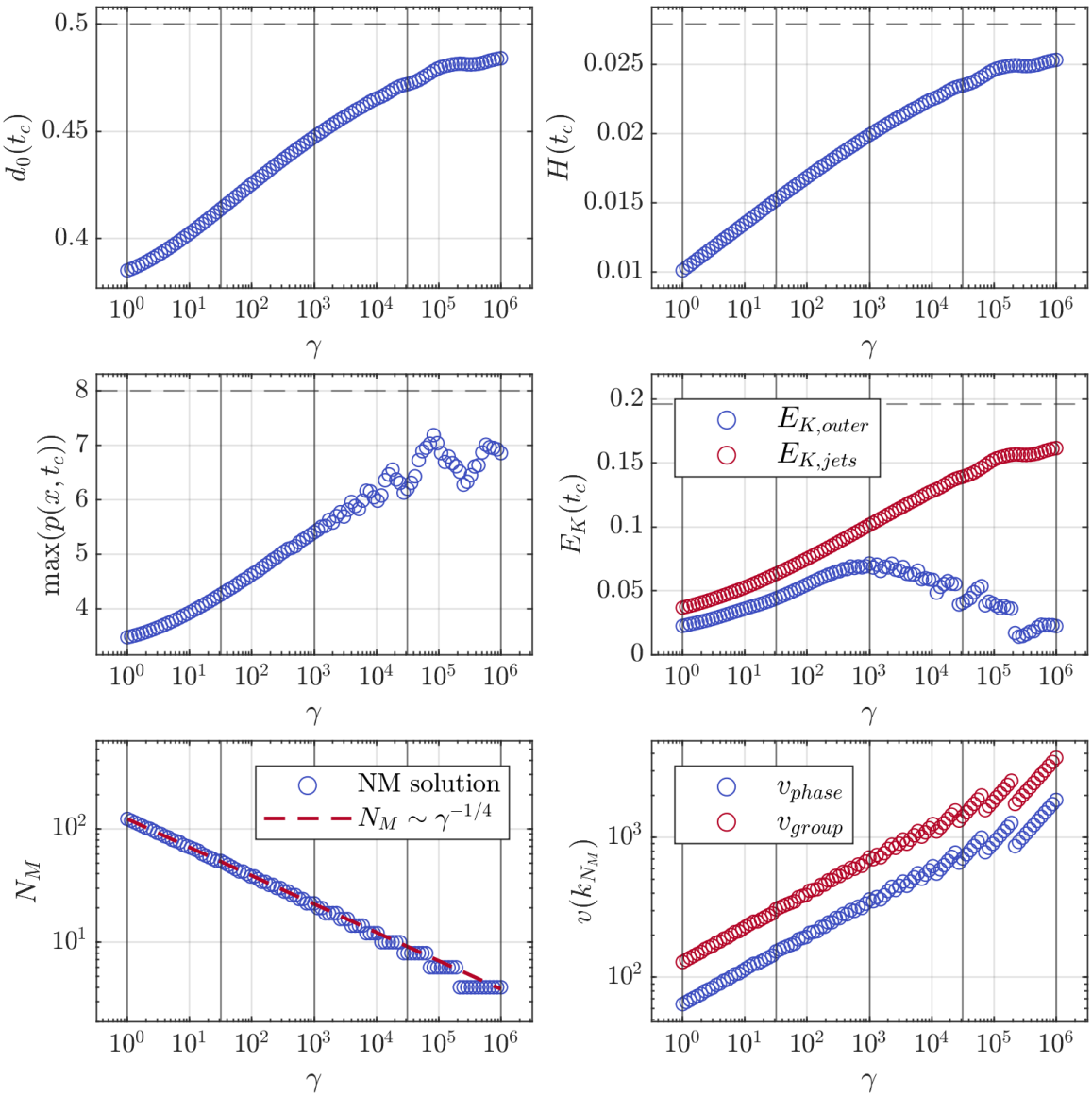

Figure 6.14: Normal modes solution for the turnover point horizontal position $d_0(t_c)$ (3.51), turnover point height $H(t_c)$ (3.90), maximum pressure $\max(p(x,t_c))$ (3.93), and the kinetic energies $E_{K,\text{outer}}(t_c)$ (3.167) and $E_{K,\text{jets}}(t_c)$ (3.170), for time $t_c = 1/16$; as well as the number of modes required to reach convergence, N_M, and the phase and group velocities, $v_{\text{phase}}(k_{N_M})$ and $v_{\text{group}}(k_{N_M})$, given by (6.10).. For all cases, $\delta = 0.125$, $\alpha = 0.1375$ and $\beta = 0$. The horizontal dashed lines denote the stationary membrane solutions, and the vertical lines denote the parameters selected for DNS in Figure 6.16.

that the turnover point velocity experiences temporal oscillations for larger values of γ, which explain the non-monotonic behaviour in the solutions for $d_0(t_c)$, $H(t_c)$ and $\max(p(x,t_c))$ in Figure 6.14.

In Figure 6.16, we plot the DNS solutions for the membrane for the five various γ

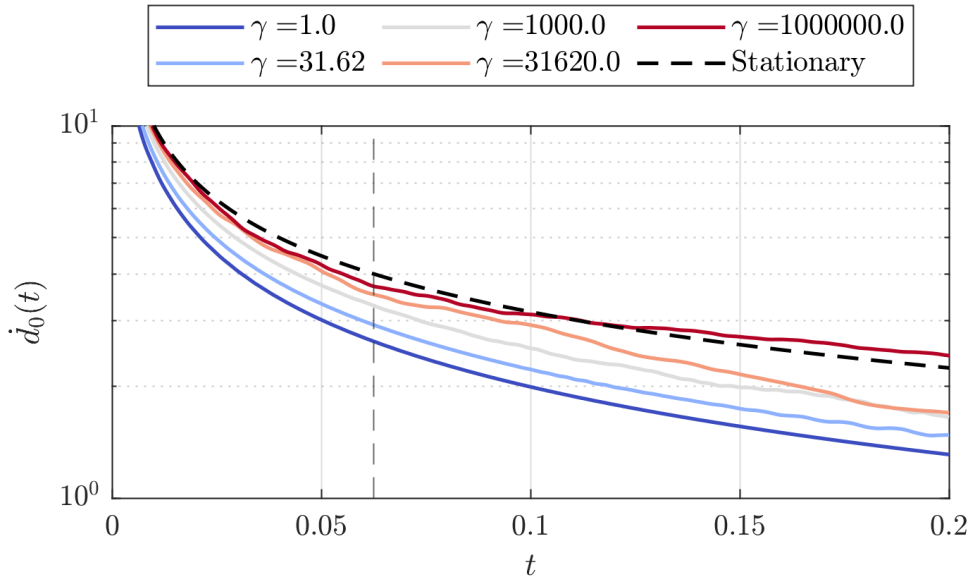

Figure 6.15: Speed of the turnover point, $\dot{d}_0(t)$, from the normal modes solutions denoted by the vertical lines in Figure 6.10, where the vertical dashed line denotes $t = t_c = 1/16$.

cases denoted by the vertical lines in Figure 6.14, ranging across 5 orders of magnitude. As expected, we see that the membranes with lower stiffness have a greater degree of displacement compared to the stiffer membranes. For the lowest value of $\gamma = 1$, the normal modes solution had $N_M = 122$, with group velocity $v_{\text{group}}(k_{N_M}) \approx 129$ and the corresponding DNS case in Figure 6.16 can be seen to exhibit a large number of low-wavelength waves. Given this group velocity, we would expect the reflected waves to return to the centre of the membrane at around $t = 0.25$, and we see from Figure 6.16(b) that at $t = 0.2$, the waves have yet to reach back to the centre. On the other extreme, for $\gamma = 10^6$, the normal modes solution had $N_M = 4$, with a group velocity of $v_{\text{group}}(k_{N_M}) \approx 3700$. For this high stiffness case, very few modes are excited, and the waves reflect back from the edge of the membrane to the centre at around $t = 0.01$. When the stiffness is high, the membrane displacement and velocity are monotonic in space, and oscillate about the initial position. In particular, at $t = 0.2$, Figure 6.16(b) shows that $-w_t(x, t) > 0$ for the $\gamma = 10^6$ case, meaning the membrane is moving into the droplet. The corresponding normal modes solution for $\dot{d}_0(t)$ in Figure 6.15 shows how the turnover point velocity as a result becomes higher than the stationary membrane case at this time. For the intermediate values of γ, we see how the dynamics transitions from one where there are a large number of excited modes with smaller group velocities, onto the cases where the displacement curves become monotonic with larger group velocities, causing rapid reflections from

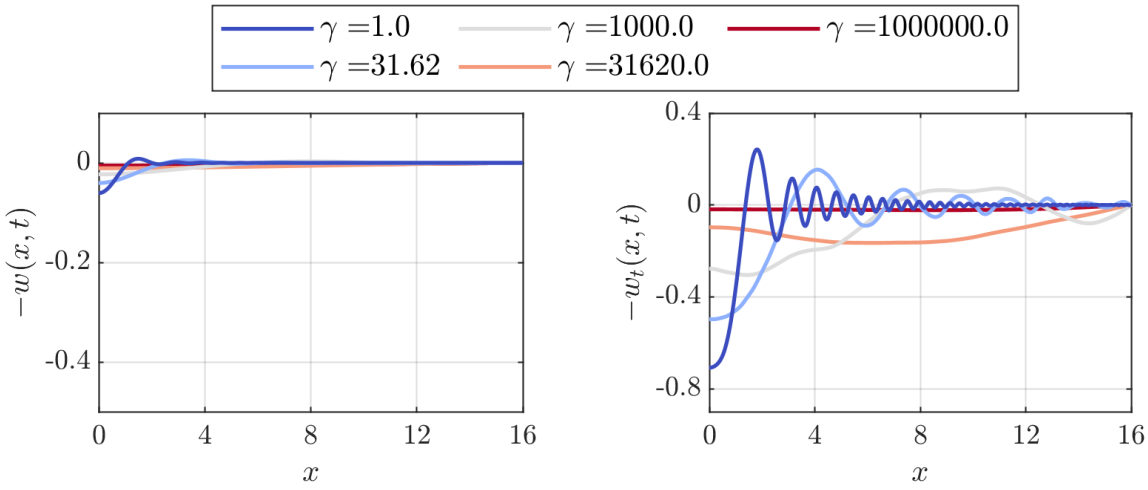

(a) $t = 0.1$

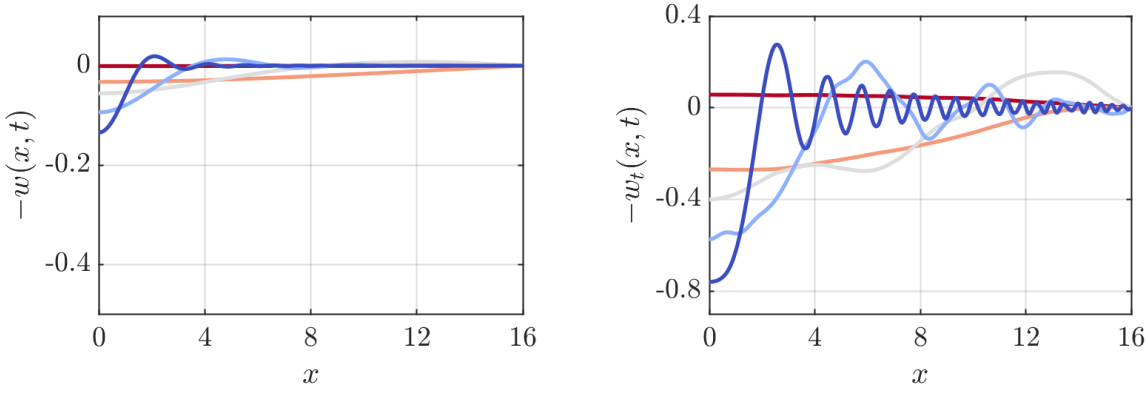

(b) $t = 0.2$

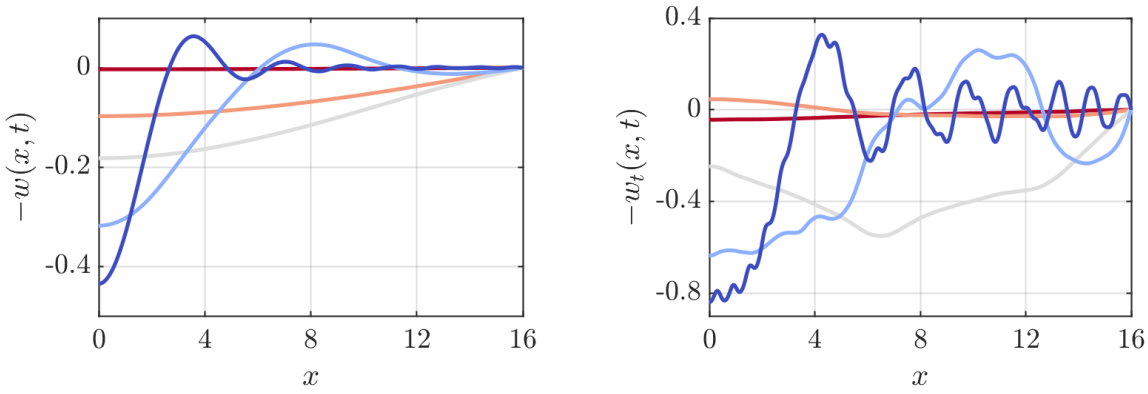

(c) $t = 0.575$

Figure 6.16: DNS solutions for the position of the membrane at $z = -w(x,t)$ and its velocity $-w_t(x,t)$ for $\delta = 0.125$, $\alpha = 0.1375$ and $\beta = 0$. The stiffness factor γ is varied from 1 to 10^6, with the colours changing from blue to red as γ is increased.

the edge of the membrane.

In Figure 6.17, we show the horizontal and vertical positions of the turnover point from the DNS for the various γ cases considered, along with the stationary

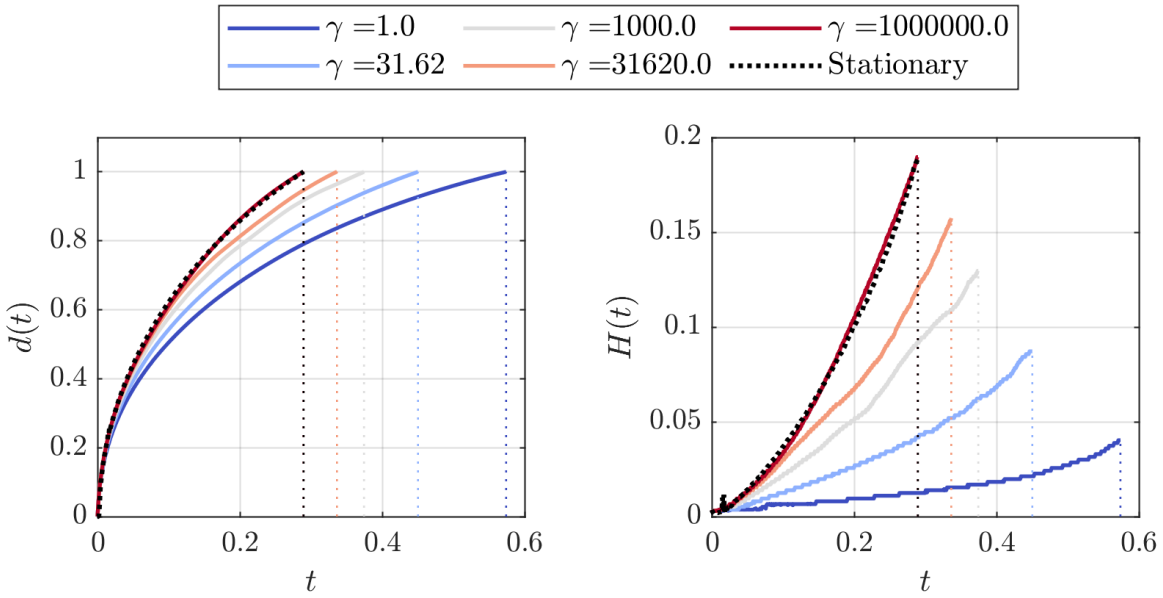

Figure 6.17: DNS solutions for the turnover point horizontal position $d(t)$ and vertical position $H(t)$, for $\delta = 0.125$, $\alpha = 0.1375$ and $\beta = 0$. The stiffness factor γ is varied from 1 to 10^6, with the line colours changing from blue to red as γ is increased, and the black dotted lines denote the stationary membrane solution. The vertical dotted lines denote the times at which $d(t) = 1$.

membrane case. For the lowest γ cases, the solutions grow monotonically in time at rates smaller than the stationary solutions. However for larger values of γ, there are temporal oscillations in the solutions, which we have already seen in Figure 6.15 for the analytical solutions. In particular, for the most extreme case of $\gamma = 10^6$, the solutions for $d(t)$ and $H(t)$ oscillate from being larger and smaller than the stationary membrane solution in time. From this, we see the behaviour that for small γ, the membrane provides little resistant to motion, and therefore the droplet spreading is slowed down. For large γ, the membrane deformation is small (as seen in Figure 6.16), but experiences fast oscillations in time which in turn affect the temporal evolution of the turnover point. This is similar behaviour to what we saw in Chapter 5 for the high-stiffness spring cases.

As before, the fluid-structure interaction is made most clear by studying the pressure on the membrane for which we plot the DNS solutions at $t = 0.1$ in Figure 6.18. For the low values of γ, we see a behaviour similar to Figure 6.13 for the thickness, where lower values of γ result in a greater amount of displacement and therefore a lower pressure. However, for the largest value of $\gamma = 10^6$, the pressure is actually greater than the stationary membrane case at certain points. This is because, at $t = 0.1$, we see from Figure 6.16 that the membrane is actually travelling upwards

into the droplet as $-w_t(x,t) > 0$ across the membrane. This upwards motion acts to increase the pressure in the droplet more so than the stationary membrane case, although the horizontal location of the pressure peak is still lower as the turnover point evolution has been slowed.

In this subsection, we have seen that by reducing the stiffness of the membrane, the initial spreading across the substrate of the droplet can be decreased, along with the thickness of the evolving jet becoming lower. We can relate this back to the experimental findings of Howland et al. (2016) [46], where it was found that droplets were less likely to splash when impacting onto softer substrates. Recall that they proposed that this reduction in splashing was due to a mechanism in the dynamics at early times that reduced the speed at which the droplet lamella emerged. Even though the case results we have presented here are two-dimensional, therefore not directly applicable to experiments, we have confirmed that our model predicts that the spreading is reduced in speed for the less stiff membranes. In particular, we have provided quantitative trends for how the emergence of the turnover point (related to the lamella) is affected as the stiffness of the substrate is changed in Figure 6.14. On the other hand, we also found that very high stiffnesses can cause the membrane to oscillate in time, which in turn causes the evolution of the turnover point position to oscillate about the stationary membrane solution. This means that for certain membrane stiffness values, the turnover point speed can be faster than the stationary membrane case, which may promote splashing to a greater extent.

6.3.3 Membrane tension

The final membrane property we will now study is the membrane tension, which is categorised by the tension factor β. For this case, we will consider a 0.125 mm thick sheet of latex, such that $\delta = 0.125$, $\alpha = 0.1375$ and $\gamma = 1.305$. Latex has the ability to withstand high amounts of tension, so we will vary β from 0.3 up to $30,000$, studying a wide range of tensions across 6 orders of magnitude. As with the thickness and stiffness, increasing the tension makes it more difficult to displace the membrane, however the physical mechanism for which tension resists this motion is different. For the membrane equation (6.1), the stiffness factor changes the strength of the fourth-order spatial derivative term, whilst the stiffness factor acts on the second-order spatial derivative term. Subsequently, when $\beta > 0$ and $\gamma = 0$, the membrane equation (6.1) is equivalent to the wave equation, which is non-dispersive such that all of the normal modes have the same phase and group velocities. The tension will compete against the bending stiffness, such that for $\beta \ll \gamma$, the solution will be

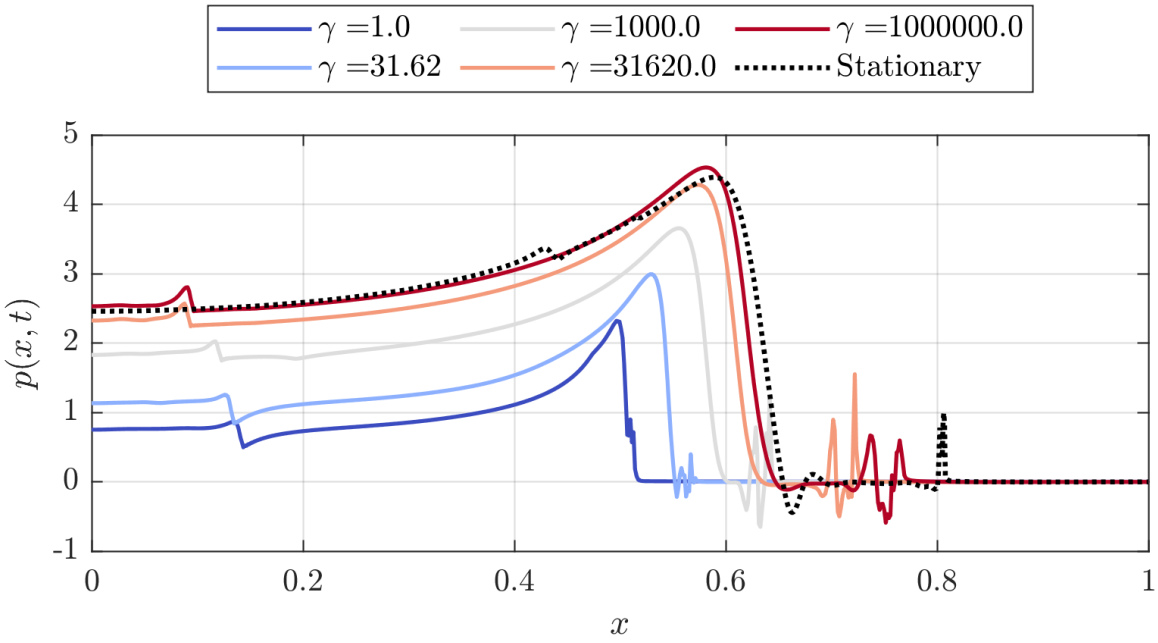

Figure 6.18: DNS solutions for the pressure on the membrane at $t = 0.1$, for $\delta = 0.125$, $\alpha = 0.1375$ and $\beta = 0$. The stiffness factor γ is varied from 1 to 10^6, with the line colours changing from blue to red as γ is increased, and the black dotted line denotes the stationary membrane solution.

dispersive, whereas for $\beta \gg \gamma$, the tension will dominate and the displacement and the solutions will become non-dispersive. In Figure 6.19, we plot the normal modes solutions for $d_0(t_c)$, $H(t_c)$, $\max(p(x, t_c))$, $E_{K,\text{outer}}(t_c)$ and $E_{K,\text{jets}}(t_c)$ for β varying from $\beta = 0.3$ up to $30,000$, where $t_c = 1/16$, as well as the number of modes required for convergence, N_M, and the corresponding phase and group velocities.

When $\beta \ll \gamma$, we expect the solutions to converge onto the cases where the bending stiffness dominates, and the solutions in Figure 6.19 clearly converge onto the $\beta = 0$ case shown with the horizontal dotted lines. As β is increased, the membrane becomes more difficult to displace, and thus the solutions tend towards the stationary membrane case denoted by the horizontal dashed lines. For the solutions shown, we see from the plot of the number of modes that $N_M = 114$ up to $\beta \approx 100$, which is the amount required for the $\beta = 0$ case. As β is increased further, the number of modes decreases, and from (6.36), we can see that $N_\Delta = O(\beta^{-1/2})$ as $\beta \to \infty$. Similarly, we have that the phase velocities satisfy $v_{\text{group}}(k_n) \approx 2v_{\text{phase}}(k_n)$ for small β, however once β becomes large, the phase velocities converge onto each other as the tension dominates.

In Figure 6.20, we plot the DNS solutions for the membrane for the four various β cases denoted by the vertical lines in Figure 6.14, along with the $\beta = 0$ case. For

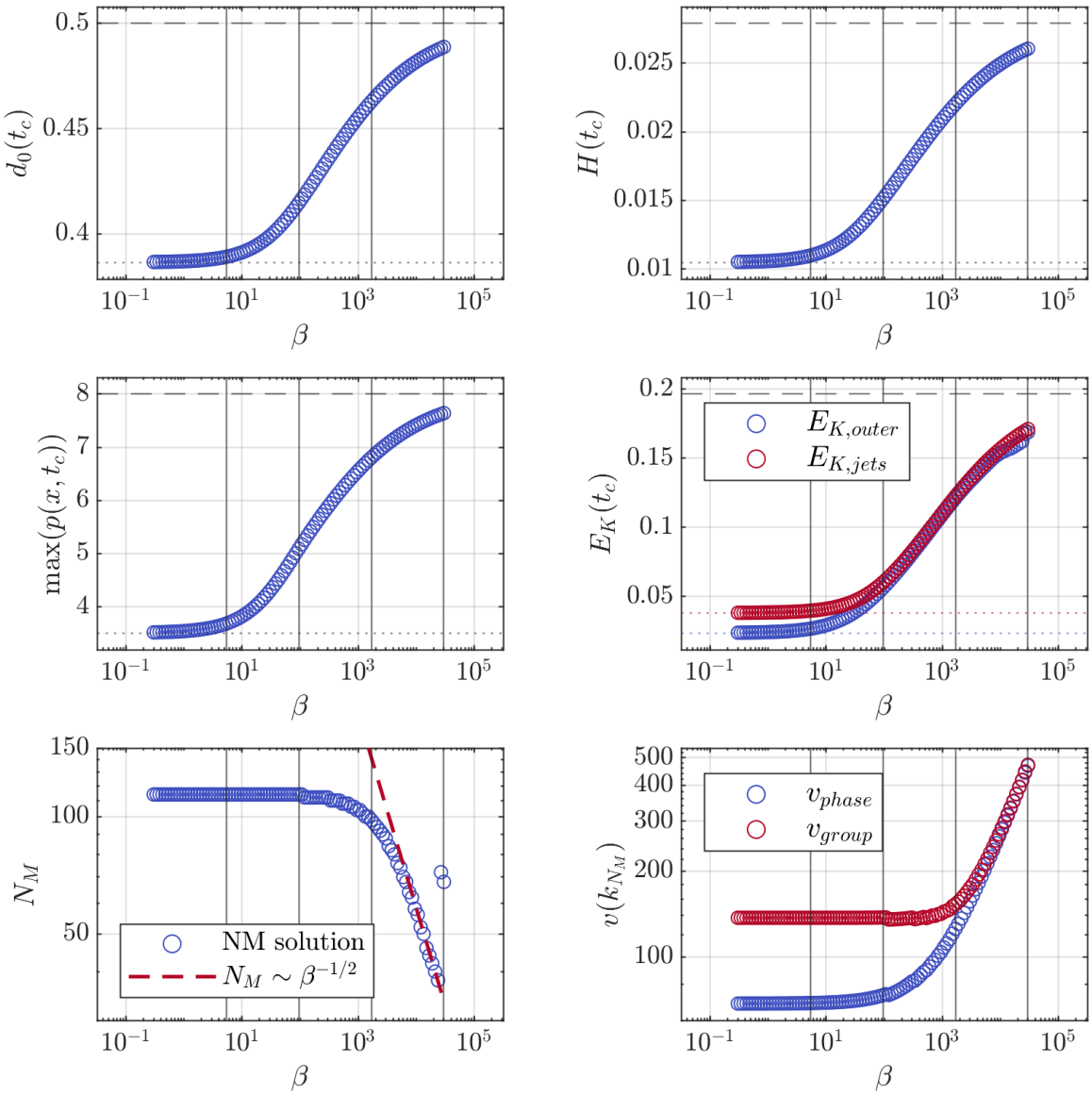

Figure 6.19: Normal modes solution for the turnover point horizontal position $d_0(t_c)$ (3.51), turnover point height $H(t_c)$ (3.90), maximum pressure $\max(p(x,t_c))$ (3.93), and the kinetic energies $E_{K,\text{outer}}(t_c)$ (3.167) and $E_{K,\text{jets}}(t_c)$ (3.170), for time $t_c = 1/16$; as well as the number of modes required to reach convergence, N_M, and the phase and group velocities, $v_{\text{phase}}(k_{N_M})$ and $v_{\text{group}}(k_{N_M})$, given by (6.10).. For all cases, $\delta = 0.125$, $\alpha = 0.1375$ and $\gamma = 1.305$. The horizontal dashed lines denote the stationary membrane solutions, the horizontal dotted lines denote the solutions for $\beta = 0$ and the vertical lines denote the parameters selected for DNS in Figure 6.20.

the low β cases, the bending stiffness dominates over the tension, and the solution exhibits the wave-like behaviour caused by the bending stiffness, with a large number of normal modes. From the previous subsections, we saw that for the $\beta = 0$ cases the velocity curves retain roughly the same shape, but grow in magnitude in time,

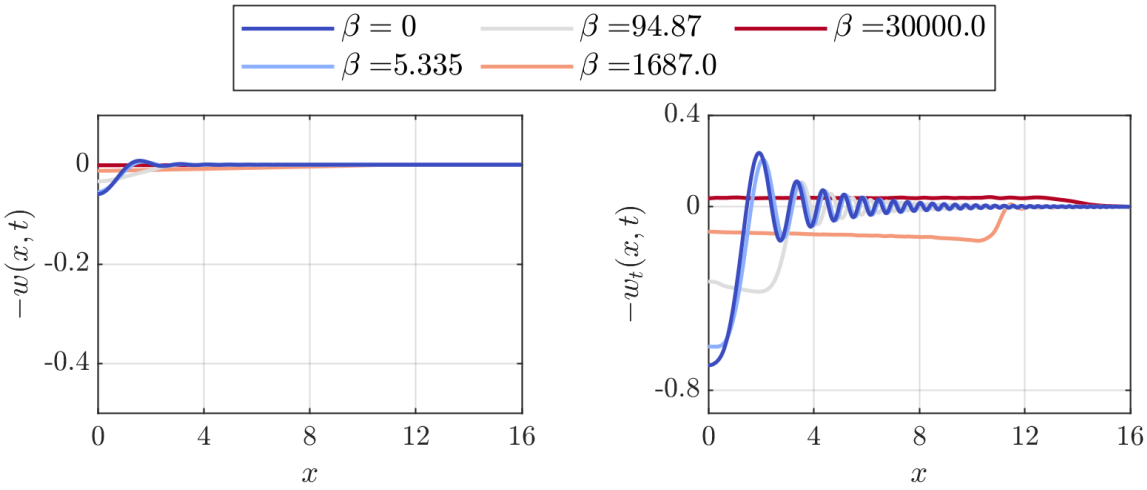

(a) $t = 0.1$

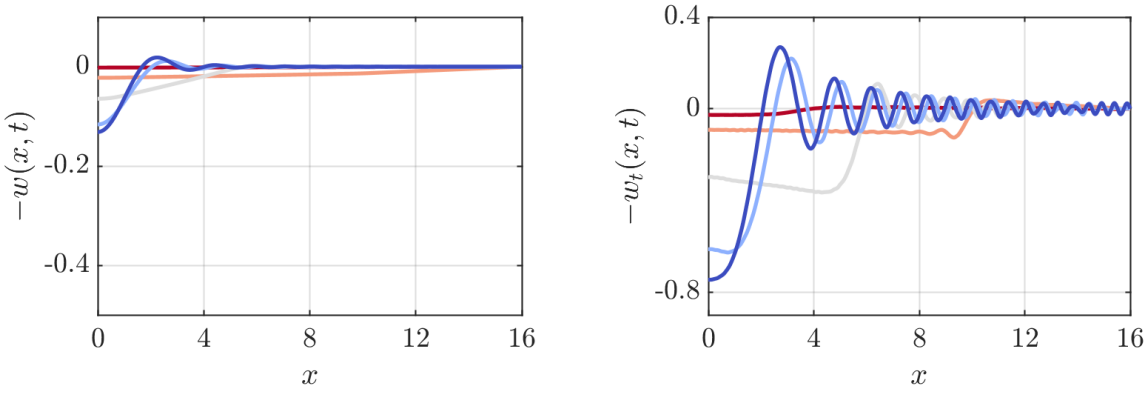

(b) $t = 0.2$

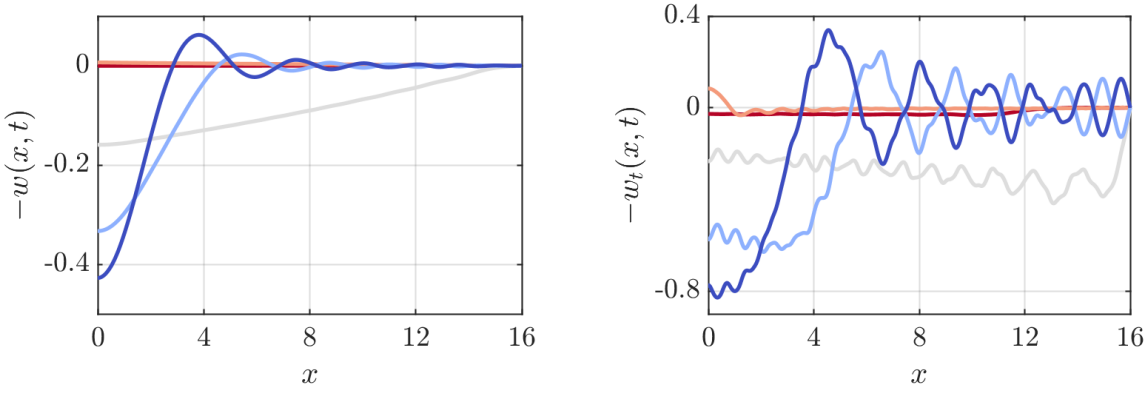

(c) $t = 0.575$

Figure 6.20: DNS solutions for the position of the membrane at $z = -w(x,t)$ and its velocity $-w_t(x,t)$ for $\delta = 0.125$, $\alpha = 0.1375$ and $\gamma = 1.305$. The tension factor β is varied from 0 to 30000, with the colours changing from blue to red as β is increased.

such as in Figure 6.16. However, for the $\beta > 0$ cases here, the tension term causes the velocity profiles to spread out in time. In particular, once the membrane initially

displaces close to the origin, this displacement will travel outwards at the wave speed, which is why we can see the non-parabolic shapes in the velocity appearing close to the origin for $t = 0.1$ and 0.2 in Figure 6.20. For large β, the tension dominates over the bending stiffness, and the phase and group velocities all tend towards $\approx \sqrt{\beta/\alpha}$ as $\beta \to \infty$. This is most visually clear for the $\beta = 94.87$ case for the displacement: the membrane exhibits a monotonic deformation in x, which grows in horizontal extent in time at the wave speed. For the most extreme case where $\beta = 30000$, the wave speed is ≈ 467, meaning the waves return back to the centre of the membrane from the edge at $t \approx t = 0.07$. From the velocities in Figure 6.20, the $\beta = 30000$ case is exhibiting high frequency oscillations in time, even though the velocity and displacement are small. Even though the tension and stiffness have similarities in the sense they both act to decrease the amount the membrane displaces, it is clear from Figure 6.20 that the resulting solutions for the membrane have inherent differences due to the different physical mechanisms that are dominant in each regime.

Turning to how the membrane affects the droplet interface, decreasing the tension again acts to slow down the evolution of the horizontal and vertical position of the turnover point, which are plotted in Figure 6.21. Similar to the case with increasing the membrane thickness, these solutions converge onto the stationary membrane case once the tension is very high, as the membrane only displaces a small amount during the impact process. However, as these high tension cases cause the membrane to oscillate in time, there is a slight oscillation in the solutions for $d(t)$ and $H(t)$ for these high β cases.

Finally, varying the tension again has a strong effect on the pressure. We plot the DNS solutions for the pressure on the membrane at $t = 0.1$ in Figure 6.22. For $\beta = 0$ up to $\beta = 1687$, we see that the pressure is lower than the stationary membrane case, with the pressure peaks occurring with lower horizontal extent due to the slowing of the evolution of the turnover point. However for the $\beta = 30000$ case, the pressure is clearly higher than the stationary membrane case. From the velocity plot in Figure 6.20(a), we know this is due to the fact $-w_t(x, t) > 0$ across the membrane in this case. Similar to the high stiffness cases from §6.3.2, the temporal oscillations of the membrane cause the pressure to oscillate in turn. However for this case, from Figure 6.21, the differences in the turnover point evolution is not as strong as in Figure 6.17 for the varying stiffness case.

Overall, the tension acts to make it more difficult to displace the membrane, with the spreading of the droplet being reduced for the low β cases. In the experimental study of Pepper et al. (2008) [72], droplets were impacted onto membranes of various

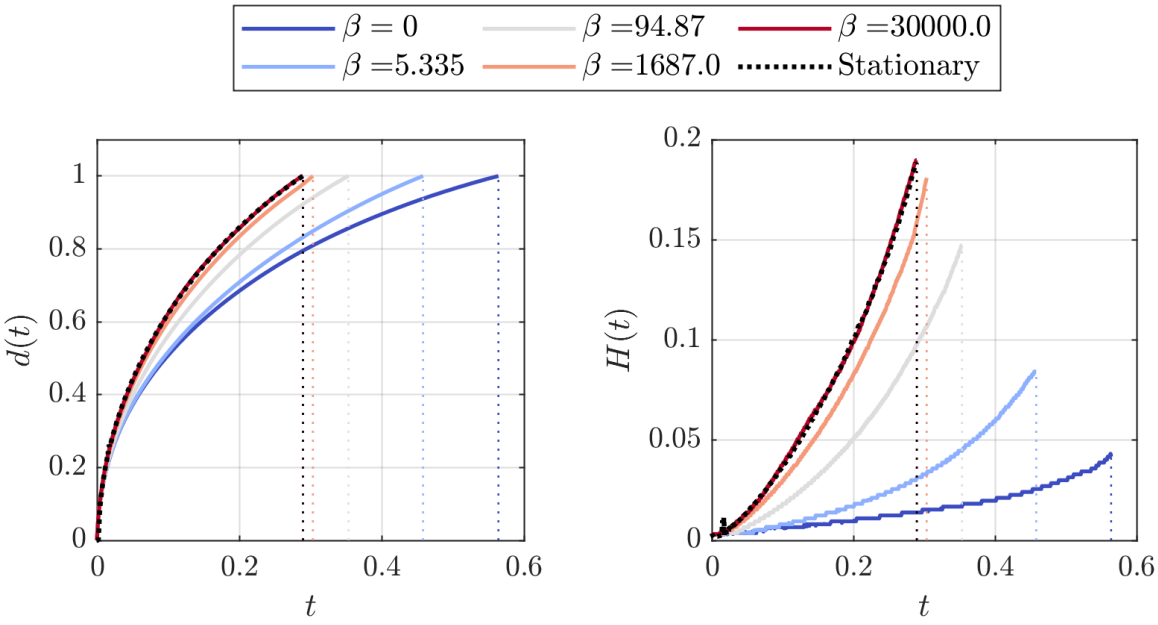

Figure 6.21: DNS solutions for the turnover point horizontal position $d(t)$ and vertical position $H(t)$, for $\delta = 0.125$, $\alpha = 1.375$ and $\gamma = 1.305$. The tension factor β is varied from 0 to 30000, with the line colours changing from blue to red as β is increased, and the black dotted lines denote the stationary membrane solution. The vertical dotted lines denote the times at which $d(t) = 1$.

tension values, and they found that the droplets were less likely to splash when the tension was lower. Similar to the findings of Howland et al. (2016) [46], they proposed that this was due to the lamella being ejected at an initially lower speed for these low tension cases. For our two-dimensional model of droplet impact onto an elastic membrane, we have quantitatively confirmed that the turnover point evolves with a lower speed and height when the tension is reduced, which reflects the findings of Pepper et al. (2008) [72]. As our model is two-dimensional, our results are not directly comparable to these experiments, however we have provided insight into the relevant physics that is at play for this setup.

6.4 Conclusion

In this chapter, we have studied the two-dimensional impact of a droplet onto an elastic membrane. For the analytical model presented in Chapter 3, we developed two different methods to solve for membrane position. The first was the normal modes method, which relied on finding a series solution for the membrane displacement, which reduced the system to a coupled set of ODEs for the time-dependent coefficients of the normal modes. The second technique used the finite difference method to

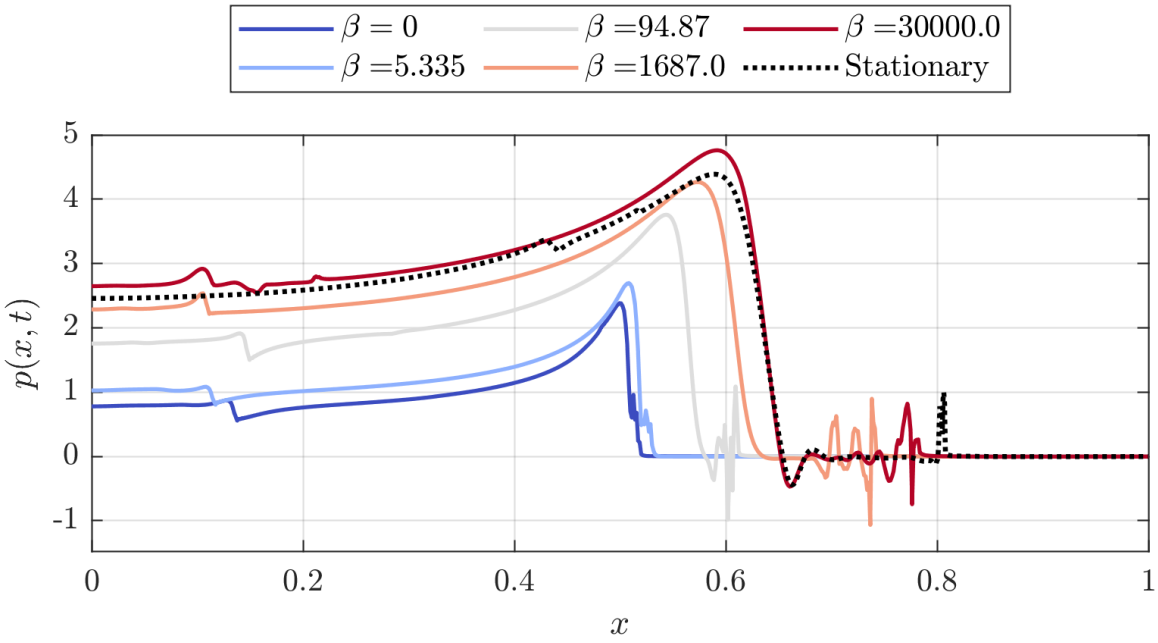

Figure 6.22: DNS solutions for the pressure on the membrane at $t = 0.1$, for $\delta = 0.125$, $\alpha = 1.375$ and $\gamma = 1.305$. The tension factor β is varied from 0 to 30000, with the line colours changing from blue to red as β is increased, and the black dotted line denotes the stationary membrane solution.

directly solve the membrane equation (6.4), which was coupled to the membrane-dependent pressure. The normal modes method relied on making use of the pressure just from the outer region, whilst the finite difference method allowed us to use the composite solution for the pressure between the outer and inner regions. The finite difference method was also used to solve for the membrane displacement in the DNS, which was solved at run-time and coupled back to the fluid via the linearised-boundary method detailed in §4.4.2. By studying the particular case of a droplet impacting onto a 1 mm sheet of latex, we compared the predictions of both analytical methods and the DNS in §6.2. We found that both the normal modes and finite difference method produce a close agreement with the DNS solutions for the membrane displacement and velocity for a representative set of parameter values, with a closer agreement from the finite difference method due to it utilising the composite pressure solution. However the limitations of the normal modes method meant that it is unable to produce a solution for the pressure along the membrane that reflects the DNS solution, whereas the finite difference method allowed us to find a pressure solution that very closely matched the DNS. However, by utilising the solution for the maximum pressure from the inner region (3.93), both the normal modes and finite difference solution gave a prediction for the maximum pressure along the substrate, found using the inner

region solution, which very closely followed the DNS solution. The limitations of the linearised-boundary setup used by the DNS meant that the droplet area decreases in time as fluid is lost through the bottom boundary. In Figure 6.8, we saw how this mass-loss phenomena caused the interface of the jets to be artificially shorter than expected, as the mass loss is localised along the bottom boundary.

As the normal modes solution for a particular set of parameters can be found approximately three orders of magnitude faster than the DNS, we utilised it to conduct an extensive parameter study of the membrane parameters. Specifically, we studied the effects of the membrane thickness, stiffness and tension in §6.3. By varying these three parameters, we studied the diverse range of fluid-structure interaction that can occur between the droplet and different types of elastic membranes. By targeting specific sets of parameters for DNS, we found that reducing the thickness, stiffness and tension of the membrane can cause the turnover point to evolve more slowly with a smaller height. We related this back to the experimental findings of Howland et al. (2016) [46] and Pepper et al. (2008) [72], where it was found that splashing can be inhibited by reducing the stiffness and tension of the substrate, respectively.

The model presented in this chapter is two-dimensional, which limits the degree to which experimental comparisons can be found. In order to directly compare the predictions of the models to real-world experiments, a three-dimensional model would need to be considered. In Chapter 5, we considered the axisymmetric impact of a droplet onto a spring-supported plate. In order to apply our model to experiments, we would need to derive an axisymmetric model for droplet impact onto substrates that can deform in the radial direction, rather than stay rigid as was considered in §3.3. Pegg et al. (2018) [71] derived such an analytical model for the axisymmetric impact of a droplet onto an elastic plate, however this model was specifically derived using the normal modes method. We would need to conduct a similar analysis as was presented in §3.2, where the substrate position was left general, in an axisymmetric geometry in order to use the finite difference method for this case. This finite difference method could also be used to conduct DNS, which would be relatively straight-forward to implement given the fact we already have a framework to conduct DNS in an axisymmetric setting.

As identified in §4.4.2, the limitation of the DNS we have presented in this section is that the linearised-boundary method causes the droplet to lose mass as the membrane displaces. One of the purposes of the DNS for this thesis was to provide solutions which solve the full fluid-structure interaction system without making the assumptions of the analytical model, in order to provide benchmarks with which to

compare the analytical solutions. However, using the linearised-boundary method reduces the predictive power of the DNS, as the mass-loss is an unphysical result of our methodology. An important next step would be to use an alternative method to model the fluid-structure interaction within the DNS which will not have this mass loss effect, in order to increase the reliability of the DNS results. We will discuss possible future-work relating to this problem in Chapter 7.

Overall, in this chapter we have shown that there is a wealth of interesting behaviour found as a consequence of the fluid-structure interaction between the droplet and the membrane. We showed that the analytical model can provide a good approximation to the leading-order dynamics of the system at early times at a fraction of the computational cost of the DNS. The speed of the analytical model solutions meant that we could conduct extensive parameter studies to identify parameter regimes of interest, which allow us to make informed choices in which parameters to target for the DNS.

Chapter 7

Conclusion

The aim of this thesis has been to model the complex fluid-structure interaction of a high-speed droplet impacting onto a movable substrate. To tackle this class of problems, we employed two different modelling techniques. The first was an analytical model, in which we studied the early times of the system, where the inertial forces in the liquid are expected to dominate over the viscous forces, surface tension, gravity and the influence of the surrounding gas, and so we made use of inviscid Wagner theory to find leading-order asymptotic solutions to the problem. Our other modelling technique involved developing and using direct numerical simulations to solve the full governing equations of the system using the finite volume technique in combination with the volume-of-fluid method to account for the fluid-fluid interface inside the flow. These computationally expensive but highly accurate simulations allowed us to take into account the physical effects neglected by the analytical model, as well as studying timescales that are out of reach of analytical model.

Our core strategy in this thesis was to employ a hybrid approach of these two methods to understand the physical systems at hand better than either method in isolation would provide. We used the analytical model to find approximate solutions to the problem with very few computational resources, as well as to provide insight into the leading-order dynamics of the problem by deriving explicit formulae for a selection of physical quantities. This model allowed us to extensively explore parameter spaces with minimal computational cost. From these parameter studies, we identified regimes of interest that we then selected to study using DNS, which are more computationally costly, but granted us a holistic view of the systems with fewer physical assumptions and the ability to study later times of impact. Using this combined approach, in this thesis we have developed a modelling framework for efficiently and accurately investigating these types of fluid-structure interaction problems.

In this chapter, we will summarise the research outcomes outlined in the previous chapters of the thesis, and then discuss future directions for work that could lead on from the progress presented in the thesis.

7.1 Summary of research

In Chapter 1, we introduced the thesis with an extensive literature review into the research area of droplet impact, including discussions on the challenges presented both analytically, experimentally and computationally when investigating these phenomena. We drew focus to existing work studying fluid-structure interaction problems involving impacting droplets, and pointed to the experimental studies of Pepper et al. (2008) [72] and Howland et al. (2016) [46] as two particularly relevant studies for the modelling conducted in this thesis. This led on to Chapter 2, where we defined the mathematical framework and governing equations that were used extensively throughout the thesis.

In Chapter 3, we derived the analytical model used to study the impact of a droplet onto a general substrate. This analysis made use of inviscid Wagner theory, an analytical modelling technique which relies on a series of assumptions stated in §3.1. In §3.2 we derived the leading-order solutions for the two-dimensional impact of a droplet onto a generalised substrate that is allowed to deform as the droplet impacts. In this section, we found leading-order solutions for the velocity, pressure and free-surface location in the four different asymptotic regions, as well as derived expressions for the force on the substrate and the kinetic energy distribution throughout the droplet. In §3.3, we carried out the same analysis for an axisymmetric setup, however making the assumption that the substrate remains flat and rigid throughout the impact process. Throughout Chapter 3, we kept the substrate position general, however to aid the discussion, we derived the solutions for a selection of examples where the substrate had a known imposed motion. This allowed us to better understand the influence of the substrate motion on the leading-order dynamics by comparing these imposed substrate solutions to the case where the substrate was stationary.

We introduced Chapter 4 by discussing the currently available direct numerical simulation methods available for modelling interfacial flow problems such as droplet impact, and justified why the volume-of-fluid method implementation provided by *Basilisk* was the most appropriate for this thesis. We then outlined the numerical scheme used by *Basilisk* to solve for interfacial flow problems with surface tension, and presented our specific computational setup used to model droplet impact. For

the DNS, we used two strategies to model the fluid-structure interaction between the droplet and substrate. When the substrate is rigid, such as the spring-supported plate in Chapter 5, we used a moving frame formulation, where we transformed the system into a frame moving with the substrate. This negated the need for considering embedded boundaries in the computational domain. For non-rigid substrates, such as the elastic membrane in Chapter 6, we used the linearised boundary formulation, in which we assumed that the substrate displacement was small enough that we could apply the kinematic boundary condition on the substrate at the flat bottom boundary of the computational domain. We then provided a thorough validation study to confirm that the spatial resolution chosen for the DNS is sufficient for the quantities we are interested in. Within this validation study, we discussed the limitations of the aforementioned linearised boundary setup in regards to the resulting mass lost through the bottom boundary.

In Chapter 5 we deployed the analytical model and DNS to study the axisymmetric impact of a droplet onto a spring-supported plate. Using this simplified physical system, we investigated how the plate mass, elasticity and damping forces affect the fluid-structure interaction problem. We first started by extensively studying a single parameter case in order to compare the predictions of the analytical model and DNS. Encouragingly, we found good agreement between the analytical and DNS up until the turnover point reached approximately 80% of the droplet radius, which was aided by using the composite solution for the pressure to estimate the force, rather than the leading-order force; the latter being traditional in the literature. Having identified the temporal regimes where the analytical predictions agreed well with the DNS, we then used the analytical model to conduct an extensive parameter study, individually varying the mass of the plate, the stiffness of the spring and strength of the dashpot. This allowed us to identify regimes of interest to target for the DNS, and to find solutions at longer timescales across the entire system. We found that by reducing the plate mass, spring stiffness and dashpot strength, the displacement of the plate was increased, which acted to slow down the spreading of the droplet and reduce the thickness of the splash sheet as it emerged. When the plate parameters were increased, the plate became more difficult to move and therefore the solutions tended towards the stationary plate case. However, we identified an exception when the spring is highly stiff. For certain cases, the high stiffness of the spring caused the plate to oscillate with extremely high frequency vibrations, which could act to increase the speed of spreading. Overall we found that, despite its simplicity, the

plate-spring-dashpot system had a rich dynamic behaviour and the dynamics of the droplet could be significantly changed by adjusting the plate properties.

In Chapter 6, we studied the more complex fluid-structure interaction problem of a two-dimensional droplet impacting onto an elastic membrane. Unlike the substrate in the preceding chapter, the elastic membrane could deform in space, and was governed by a fourth-order in space and second-order in time PDE. For the analytical model, we derived two methods for solving the PDE for the membrane displacement. The first was the normal modes method, a spectral method that reduced the problem to a system of time-dependent ODEs. The second relied on solving the PDE directly using the finite difference method, which we also used for the DNS. In a similar manner to Chapter 5, we first focused on comparing the predictions of the respective models for impact onto a specific membrane setup of a thin latex sheet. We found that both the normal modes and finite difference methods for the analytical model provided good agreement with the DNS predictions for the membrane displacement at the early times of impact. However, the normal modes method was found to be insufficiently accurate in predicting the resulting pressure along the membrane, a result previously identified by Korobkin (1998) [52]. Nonetheless, the normal modes method still provided good predictions for the turnover point evolution and the value of the maximum pressure along the membrane. Once we established the temporal regimes where the analytical model agreed well with the DNS, we conducted a wide parameter study across the different physical properties of the membrane in a similar manner to that in Chapter 5. For this, we made use of the normal modes method to solve the problem for a range of membrane thicknesses, stiffnesses and tensions. We analysed the effect that varying these quantities had on the turnover point location, maximum pressure on the membrane and the kinetic energy distribution, and we used the parameter studies to target regimes of interest with the DNS. We found that decreasing the thickness, stiffness and tension of the membrane acted to slow down the spreading of the droplet and reduce the amount of kinetic energy transferred into the liquid. When the stiffness and tension of the membrane were high, the impacting droplet caused the membrane to oscillate with high temporal frequency. Similar to the vibrating plate in Chapter 5, this could cause the pressure in the droplet to fluctuate about the stationary membrane solutions, and caused the turnover point evolution to become non-monotonic. The normal modes method allowed us to determine the phase and group velocity of the membrane displacement waves, which gained us deeper insight into the dynamics of the membrane displacement such as the interference observed once the waves were reflected back from the edge of the membrane. Although our

model in this case was restricted to two-dimensions, the results presented in Chapter 6 provided insight into effects the membrane dynamics had on the early time spreading behaviour of the droplet, which were identified by Pepper et al. (2008) [72] to be an essential component to understanding the late-time splashing behaviour of droplets impacting onto elastic membranes.

7.2 Future work

In this section, we will briefly detail a selection of future directions which the research presented in this thesis could be applied and extended to. To support this future progress, we have made all of the source code and post-processing tools used for this thesis open-source and freely available at https://github.com/MNegus/DPhil-Thesis.

7.2.1 Axisymmetric impact onto a deformable substrate

The axisymmetric cases studied in this thesis were restricted to droplets impacting onto rigid substrates. The DNS setup presented in Chapter 4 can be readily applied to model axisymmetric impact onto deformable substrates by utilising the linearised boundary setup, similar to that used in Chapter 6 for the elastic membrane in two-dimensions. Previous studies of using inviscid Wagner theory to study axisymmetric impact with a deformable substrate include the work of Scolan (2004) [81] and Pegg et al. (2018) [71]. However, these investigations did not retain full generality, as the normal modes method was utilised in the analysis at the onset to model elastic substrates. As discussed in Chapter 6, the normal modes method has limiting factors, such as slow convergence for the series solution of the pressure on the substrate. Further work in this direction could include conducting an analysis similar to the two-dimensional analytical model in §3.2 where the substrate displacement is kept general, and can therefore provide better predictions for quantities such as the pressure on the substrate by utilising the finite difference method to resolve the substrate dynamics, as well as being able to be applied to model a wider range of substrate types.

7.2.2 DNS for impact onto a deformable substrate

In this thesis, to model impact onto a deformable substrate with DNS, we utilised the linearised boundary setup, which simplified the problem by applying the kinematic boundary condition on the membrane along the stationary bottom boundary

of the computational domain. This method resulted in mass loss through the bottom boundary as the membrane deforms, and meant that the DNS did not strictly solve the full fluid-structure interaction problem. We currently identify two avenues for future work which provide more accurate alternatives to the linearised boundary setup.

The first would be to use the immersed boundary method (see Peskin (2002) [73]) to embed the moving substrate into the computational domain. Within the *Basilisk* framework, stationary embedded boundaries are currently supported for two-phase flow simulations so long as only one phase meets the boundary, such as wave flow over an obstacle. Cases such as droplet impact, where both fluid phases meet the solid boundary, pose a well known computational challenge due to the triple-contact point where the liquid, gas and solid meet. Recent progress has been made by the *Basilisk* community to support these types of two-phase systems (see http://basilisk.fr/sandbox/popinet/contact/sessile-inclined.c), however a substantial amount of development at the fundamental level of the VOF solvers needs to be done before fluid-structure interaction problems such as those considered in this thesis will be supported.

A second alternative would be to consider a moving frame setup similar to what was used for the spring-supported plate in Chapter 5. However, for non-rigid substrates, this would involve transforming the Navier-Stokes equations into a curvillinear coordinate system where the substrate would be flat and stationary. Implementing this would require transforming any spatial derivative used by the VOF solver, such as during the calculation of surface tension, into this curvillinear frame. In addition, the momentum equations would have a number of additional body forcing terms that would be non-trivial to resolve. Similar to the previously mentioned embedded boundary method, implementing the moving frame setup for these cases would require a substantial amount of development of the *Basilisk* source code, however this would be a worthwhile pursuit in order to model these types of fluid-structure interaction problems using *Basilisk*.

7.2.3 Three-dimensional DNS

Throughout this thesis we have regularly discussed the importance of the early times of impact in order to understand the late time splashing behaviour, such as in the experimental works of Pepper et al. (2008) [72] and Howland et al. (2016) [46]. However, splashing is a fully three-dimensional phenomenon that cannot be resolved using an axisymmetric model. In order to actually model the splashing behaviour that is

seen in experiments, we would need to conduct three-dimensional DNS. Implementing these three-dimensional simulations would be a relatively straight-forward extension of the work presented in Chapter 4. The limiting factor with three-dimensional DNS is the extremely large amount of computational resources required compared to two-dimensional/axisymmetric simulations. For example, the simulations we conducted for Chapter 5 typically took approximately 24 CPU hours to resolve, whilst the three-dimensional droplet impact simulations conducted by Cimpeanu & Papageorgiou (2018) [15] required approximately 10^4 CPU hours to resolve. Despite their high cost, three-dimensional DNS will give a better understanding into surface tension dependent effects at late times such as ligament and subsequent drop formation, leading to a better understanding of the splashing outcomes.

7.2.4 Other types of substrate

The analytical model and DNS presented in Chapters 3 and 4 were used to study impact onto two specific types of movable substrates in Chapters 5 and 6. However, there are many more types of movable substrate that appear in both nature and industry, such as leaves or the silicone gels investigated by Howland et al. (2016) [46]. The modelling framework presented in this thesis is general enough that, given the existence of governing equations for the response of the substrate to the stresses from the impacting droplet, it can be readily applied to model other types of substrate.

7.2.5 Conclusion

There are clearly many more avenues which could be explored as an extension to the research presented in this thesis. With the rapid development of both experimental and computational methods, our understanding of these highly complex droplet impact phenomena has increased dramatically over the last two decades. However, there are still a large number of open questions, and we have only just begun to scrape the surface on the effects of the fluid-structure interaction between droplets and substrates.

Appendix A

Quadratic substrate

In this appendix, we derive the leading-order solutions for the two-dimensional problem considered in §3.2 in the case where the substrate is given by an imposed even quadratic function in x. Thus, we say that the leading-order solution in the outer region is given by

$$\hat{w}_0(\hat{x}, t) = a(t) + b(t)\hat{x}^2, \tag{A.1}$$

where $a(t)$ and $b(t)$ are imposed coefficients of our choosing, and recall that $\hat{x} = x/\epsilon$ and $w(x, t) = \hat{w}(\hat{x}, t)$. Given this, the solution for the turnover point $d_0(t)$ can be found from (3.51) to be

$$t - \frac{d_0(t)^2}{4} = a(t) + \frac{1}{2}b(t)d_0(t)^2 \implies d_0(t) = 2\sqrt{\frac{t - a(t)}{1 + 2b(t)}}. \tag{A.2}$$

Therefore, for a valid solution for $d_0(t)$, we must choose our coefficients such that $a(t) < t$ and $b(t) > -1/2$ for all t. We can then readily find the derivative of the turnover point as

$$\dot{d}_0(t) = \frac{(1 + 2b(t))\,(1 - \dot{a}(t)) - 2(t - a(t))\dot{b}(t)}{\sqrt{t - a(t)}(1 + 2b(t))^{3/2}}. \tag{A.3}$$

The leading-order solutions in the outer region for the complex potential (3.31) and pressure (3.69) are given in terms of complex contour integrals involving the function $m(s, t)$, defined in (3.29), whose solution for the quadratic substrate case is

$$m(s, t) = a(t)s + \frac{1}{3}b(t)s^3. \tag{A.4}$$

With the solution for $m(s, t)$ in (A.4), we can find exact solutions for these complex contour integrals. For the complex potential (3.31), we have

$$W(\zeta, t) = \hat{\phi}_0 + i\hat{\psi}_0 = i(\zeta^2 - d_0(t)^2)^{1/2}\left[1 - \dot{a}(t)I_1(\zeta, t) - \frac{1}{3}\dot{b}(t)I_2(\zeta, t)\right], \tag{A.5}$$

where

$$I_1(\zeta,t) = 1 - \frac{\zeta}{(\zeta^2 - d_0(t)^2)^{1/2}},\ I_2(\zeta,t) = \frac{d_0(t)^2}{2} + \zeta^2 - \frac{\zeta^3}{(\zeta^2 - d_0(t)^2)^{1/2}}. \tag{A.6}$$

For the leading-order pressure in the outer region, given by (3.69), we have

$$\hat{p}_0 = \Re\left\{ \frac{i}{(\zeta^2 - d_0(t)^2)^{1/2}} \left[A(t) - \ddot{a}(t) I_3(\zeta,t) - \frac{1}{3}\ddot{b}(t) I_4(\zeta,t) \right] \right\}, \tag{A.7}$$

where

$$I_3(\zeta,t) = \zeta\left((\zeta^2 - d_0(t)^2)^{1/2} - \zeta \right) + \frac{d_0(t)^2}{2}, \tag{A.8}$$

$$I_4(\zeta,t) = \frac{1}{8}\left(4\zeta^2 d_0(t)^2 + 8\zeta^3 \left((\zeta^2 - d_0(t)^2)^{1/2} - \zeta \right) + d_0(t)^4 \right), \tag{A.9}$$

and

$$A(t) = d_0(t)\dot{d}_0(t)\left[1 - \dot{a}(t) - \frac{1}{2}\dot{b}(t) d_0(t)^2 \right] - \left[\frac{1}{2}\ddot{a}(t) d_0(t)^2 + \frac{1}{8}\ddot{b}(t) d_0(t)^4 \right]. \tag{A.10}$$

The free-surface location $\hat{h}_0(\hat{x},t)$ for $\hat{x} > d_0(t)$, from (3.48), is given by

$$\begin{aligned} \hat{h}_0(\hat{x},t) = {} & \frac{1}{2}\hat{x}\sqrt{\hat{x}^2 - d_0(t)^2} + \sqrt{\hat{x}^2 - d_0(t)^2}\left(a(t) I_5(\hat{x},t) + \frac{b(t)}{3} I_6(\hat{x},t) \right) \\ & - \frac{\hat{x}}{\sqrt{\hat{x}^2 - d_0(t)^2}}\left[t - \frac{d_0(t)^2}{4} - a(t) I_1(\hat{x},t) - \frac{b(t)}{3} I_2(\hat{x},t) \right], \end{aligned} \tag{A.11}$$

where

$$I_5(\hat{x},t) = \frac{d_0(t)^2}{(\hat{x}^2 - d_0(t)^2)^{\,3/2}}, \tag{A.12}$$

$$I_6(\hat{x},t) = \frac{\hat{x}\left(2\hat{x}^2\left(\sqrt{\hat{x}^2 - d_0(t)^2} - \hat{x} \right) + d_0(t)^2\left(3\hat{x} - 2\sqrt{\hat{x}^2 - d_0(t)^2} \right) \right)}{(\hat{x}^2 - d_0(t)^2)^{\,3/2}}. \tag{A.13}$$

For the inner region, the substrate was taken to be flat to leading-order, so the only dependence the solutions had on the substrate motion are from the turnover point solution $d_0(t)$ and the jet thickness $J(t)$ from (3.98). The solution for $J(t)$ depends on the function $B(t)$, whose solution in this quadratic substrate case is given by

$$B(t) = \dot{a}(t) + \frac{1}{2}\dot{b}(t) d_0(t)^2. \tag{A.14}$$

The solutions for the velocity and the free surface in the jet regions (3.130) are completely determined by the solutions for $d_0(t)$ and $J(t)$. The pressure (3.122)

explicitly depends on the substrate position and its derivatives, which can readily be found from (A.1).

The leading-order solutions in the outer-outer region depend only on the coefficients $D(t)$ (3.133), $E(t)$ (3.135) and $A(t)$ (3.67), which are found by taking the far-field expansion of the solutions from the outer region. We already found the solution for $A(t)$ in (A.10), and the solutions for $D(t)$ and $E(t)$ are subsequently

$$D(t) = \frac{1}{2}(1 - \dot{a}(t))d_0(t)^2 - \frac{1}{8}\dot{b}(t)d_0(t)^4, \tag{A.15}$$

$$E(t) = \left(t - \frac{d_0(t)^2}{8} - a(t)\right)\frac{d_0(t)^2}{2} - \frac{1}{8}b(t)d_0(t)^4. \tag{A.16}$$

As well as the solutions in each asymptotic region, we have derived more global quantities in Chapter 3. Thus, the leading-order force on the substrate from (3.158) is

$$F_0(t) = \pi A(t), \tag{A.17}$$

as the integral in (3.158) is zero when the substrate is a quadratic. The other components for the composite force $F_{\text{comp}}(t)$ from (3.162) follow naturally.

For the kinetic energy in the outer region, we have $g(\hat{x}, t)$ from (3.168) being given by

$$g(\hat{x}, t) = \left(1 - \dot{a}(t) - \dot{b}(t)\hat{x}^2\right)\left[1 - \dot{a}(t) - \frac{1}{6}\dot{b}(t)\left(2d_0(t)^2 + \hat{x}^2\right)\right], \tag{A.18}$$

such that

$$\begin{aligned} &E_{K,\text{outer}}(t) \\ &\quad\sim \frac{\pi\epsilon^2 d_0(t)^2}{4}(1 - \dot{a}(t))^2 + \frac{5\pi\epsilon^2 d_0(t)^4}{192}\dot{b}(t)\left(6\dot{a}(t) + d_0(t)^2\dot{b}(t) - 6\right), \end{aligned} \tag{A.19}$$

where the kinetic energy in the jets from (3.170) is completely determined by the solutions for $d_0(t)$ and $B(t)$.

The quadratic solution (A.1) can either be used to solve the problem where the substrate is a rigid (where $b(t) = 0$), or where we have a curved substrate with $b(t) \neq 0$. We will make use of both of these cases within Chapter 3 in order to study the effects both type of substrate motion have on the dynamics of the droplet.

Appendix B

Solutions to complex contour integrals

In this appendix, we find the solutions to the complex contour integrals that appear in the outer region solutions for the two-dimensional case in §3.2.

B.1 Complex velocity potential

The solution for the complex velocity potential (3.30) is given in terms of the contour integral

$$I_1 = \int_{-d_0(t)}^{d_0(t)} \frac{s}{(s^2 - d_0(t)^2)^{1/2}(s-\zeta)}\,\mathrm{d}s\,,$$

recalling that the branch cut for $(\zeta^2 - d_0(t)^2)^{1/2}$ is taken to be along the real axis between $-d_0(t)$ and $d_0(t)$, and is shown by the red line in Figure B.1. We write I_1 in terms of a closed contour C by

$$I_1 = -\frac{1}{2}\oint_C \frac{s}{(s^2 - d_0(t)^2)^{1/2}(s-\zeta)}\,\mathrm{d}s\,, \tag{B.1}$$

where C goes anti-clockwise about the branch cut between $s = \pm d_0(t)$, and is shown by the dark blue contour in Figure B.1. We then smoothly deform C to C', shown by the light blue contour in Figure B.1, which is the union of a circle C_R, radius $R > |\zeta|$, about the origin, and a keyhole C_ζ cut out to fit in a circular contour about ζ in the clockwise direction. Therefore $C' = C_R \cup C_\zeta$, where for C_ζ,

$$\frac{1}{2}\oint_{C_\zeta} \frac{s}{(s^2 - d_0(t)^2)^{1/2}(s-\zeta)}\,\mathrm{d}s = \frac{1}{2}(-2\pi i)\frac{\zeta}{(\zeta^2 - d_0(t)^2)^{1/2}} = -\frac{\pi i \zeta}{(\zeta^2 - d_0(t)^2)^{1/2}},$$

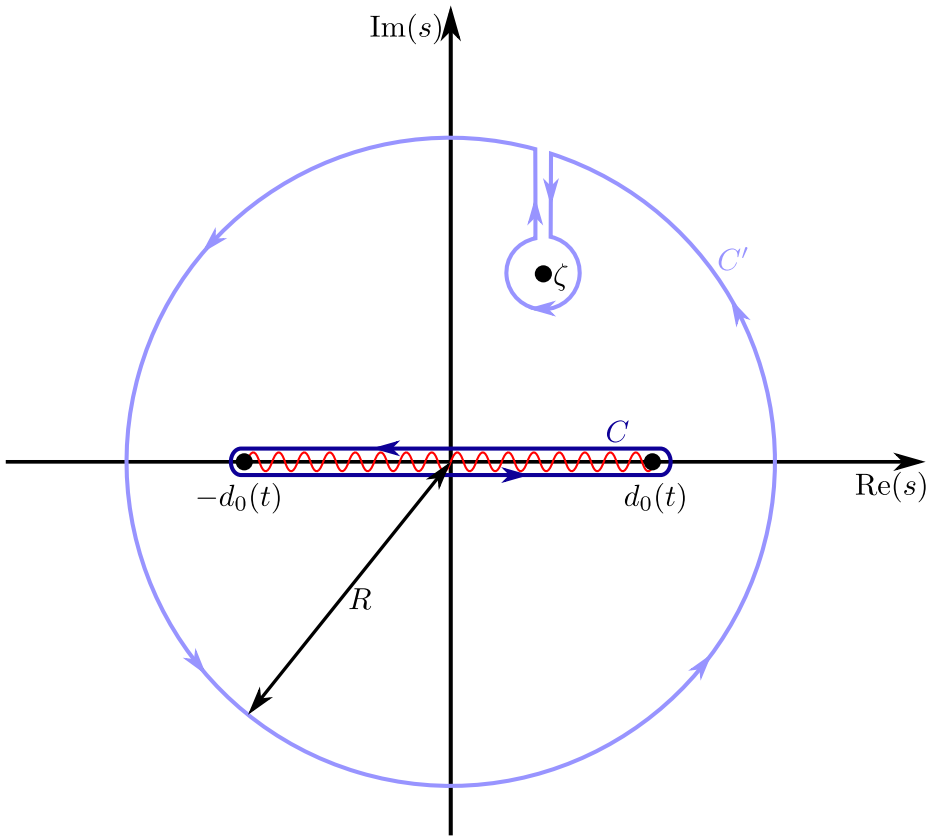

Figure B.1: Schematic showing the contours integration contours in the complex s plane. The red line shows the branch cut for the function $(s^2 - d_0(t)^2)^{1/2}$, the dark blue line depicts the contour C from (B.1) and the light blue line depicts the deformed contour $C' = C_R \cup C_\zeta$.

by the residue theorem. For C_R, we change integration variables $s = Re^{i\theta}$ and expand for $R \gg 1$ to obtain

$$\begin{aligned}\frac{1}{2}\oint_{C_R} \frac{s}{(s^2 - d_0(t)^2)^{1/2}(s-\zeta)}\,\mathrm{d}s &= \frac{1}{2}\int_0^{2\pi} \frac{Re^{i\theta}}{(R^2e^{2i\theta} - d_0(t)^2)^{1/2}(Re^{i\theta}-\zeta)} iRe^{i\theta}\,\mathrm{d}\theta \\ &= \frac{i}{2}\int_0^{2\pi} (1 - d_0(t)^2 e^{-2i\theta}/R^2)^{-1/2}(1-\zeta e^{-i\theta}/R)^{-1}\,\mathrm{d}\theta \\ &= \frac{i}{2}\int_0^{2\pi} 1 + O(1/R)\,\mathrm{d}\theta \to \pi i \text{ as } R \to \infty.\end{aligned}$$

Therefore the integral I_1 is given by,

$$I_1 = \frac{\pi i \zeta}{(\zeta^2 - d_0(t)^2)^{1/2}} - \pi i. \tag{B.2}$$

B.2 Free-surface location

When determining the solution for the free-surface, we have the integral I_2 in the solution for $G(\zeta, t)$ (3.45), given by

$$I_2 = \int_{-d_0(t)}^{d_0(t)} \frac{ts - s^3/6}{(s^2 - d_0(t)^2)^{1/2}(s-\zeta)}\,\mathrm{d}s = -\frac{1}{2}\oint_C \frac{ts - s^3/6}{(s^2 - d_0(t)^2)^{1/2}(s-\zeta)}\,\mathrm{d}s\,, \qquad \text{(B.3)}$$

where C is the same contour in the complex s plane that is depicted in Figure B.1. We again smoothly deform C to $C' = C_R \cup C_\zeta$ where for C_ζ,

$$\frac{1}{2}\oint_{C_\zeta} \frac{ts - s^3/6}{(s^2 - d_0(t)^2)^{1/2}(s-\zeta)}\,\mathrm{d}s = \frac{1}{2}(-2\pi i)\frac{t\zeta - \zeta^3/6}{(\zeta^2 - d_0(t)^2)^{1/2}}$$

by the residue theorem. For C_R, we change variables $s = Re^{i\theta}$ and expand for $R \gg 1$ to obtain

$$\begin{aligned}
&\frac{1}{2}\oint_{C_R} \frac{ts - s^3/6}{(s^2 - d_0(t)^2)^{1/2}(s-\zeta)}\,\mathrm{d}s = \frac{1}{2}\int_0^{2\pi} \frac{tRe^{i\theta} - R^3e^{3i\theta}/6}{(R^2e^{2i\theta} - d_0(t)^2)^{1/2}(Re^{i\theta} - \zeta)} iRe^{i\theta}\,\mathrm{d}\theta \\
&= \frac{i}{2}\int_0^{2\pi} \frac{t - R^2e^{2i\theta}/6}{(1 - d_0(t)^2e^{-2i\theta}/R^2)^{1/2}(1 - \zeta e^{-i\theta}/R)}\,\mathrm{d}\theta \\
&= \frac{i}{2}\int_0^{2\pi} \left(t - \frac{1}{6}R^2e^{2i\theta}\right)\left(1 + \frac{d_0(t)^2e^{-2i\theta}}{2R^2}\right)\left(1 + \frac{\zeta e^{-i\theta}}{R} + \frac{\zeta^2 e^{-2i\theta}}{R^2}\right)\mathrm{d}\theta + O(1/R) \\
&= \frac{i}{2}\int_0^{2\pi} t - \frac{1}{6}\left(\frac{d_0(t)^2}{2} + \zeta^2\right)\mathrm{d}\theta + O(1/R) \\
&\to i\pi\left(t - \frac{1}{6}\left(\frac{d_0(t)^2}{2} + \zeta^2\right)\right) \text{ as } R \to \infty.
\end{aligned}$$

Therefore the solution for the integral I_2 is given by

$$I_2 = i\pi\left[\frac{t\zeta - \zeta^3/6}{(\zeta^2 - d_0(t)^2)^{1/2}} - t + \frac{1}{6}\left(\frac{d_0(t)^2}{2} + \zeta^2\right)\right]. \qquad \text{(B.4)}$$

B.3 Turnover point

When determining the solution for the turnover point, we need to expand the solution for the complex displacement potential (3.46) as $\zeta \to d_0(t)$. Without loss of generality, we let $\zeta = d_0(t)(1+\nu)$, where $0 < \nu \ll 1$, and find the leading-order expansion of (3.46) as $\nu \to 0$. We define the integral that appears in (3.46) to be I_3, where

$$I_3 = \int_{-d_0(t)}^{d_0(t)} \frac{m(s,t)}{\sqrt{d_0(t)^2 - s^2}(s-\zeta)}\,\mathrm{d}s = \frac{1}{d_0(t)}\int_{-1}^{1} \frac{f(\xi,t)}{\sqrt{1-\xi^2}(\xi - (1+\nu))}\,\mathrm{d}\xi \qquad \text{(B.5)}$$

where for convenience we have changed integration variables to $s = d_0(t)\xi$, and defined the function $f(\xi, t) = m(d_0(t)\xi, t)$. We then re-arrange the numerator to isolate the contribution from the end point at $\xi = 1$, such that

$$\begin{aligned} I_3 &= \frac{1}{d_0(t)} \int_{-1}^{1} \frac{f(\xi,t) - f(1,t)}{\sqrt{1-\xi^2}(\xi - 1 - \nu)} \, \mathrm{d}\xi + \frac{1}{d_0(t)} \int_{-1}^{1} \frac{f(1,t)}{\sqrt{1-\xi^2}(\xi - 1 - \nu)} \, \mathrm{d}\xi \\ &= \frac{1}{d_0(t)} \underbrace{\int_{-1}^{1} \frac{f(\xi,t) - f(1,t)}{\sqrt{1-\xi^2}(\xi - 1 - \nu)} \, \mathrm{d}\xi}_{J} - \frac{\pi f(1,t)}{d_0(t)\sqrt{\nu(2+\nu)}}, \end{aligned}$$

where we have used contour integration to determine the second integral. To determine the first integral, labelled J, we introduce an intermediate variable δ, such that $0 < \nu \ll \delta \ll 1$, and split the range of integration to isolate the end point,

$$J = J_1 + J_2 = \left(\int_{-1}^{1-\delta} + \int_{1-\delta}^{1} \right) \frac{f(\xi,t) - f(1,t)}{\sqrt{1-\xi^2}(\xi - 1 - \nu)} \, \mathrm{d}\xi \,. \tag{B.6}$$

For J_1, we have that $\xi - 1 = O(1)$, and hence the expansion for J_1 as $\nu \to 0$ is

$$\begin{aligned} J_1 &= \int_{-1}^{1-\delta} \frac{f(\xi,t) - f(1,t)}{\sqrt{1-\xi^2}(\xi - 1)} \left(1 - \frac{\nu}{\xi - 1}\right)^{-1} \mathrm{d}\xi \\ &= \int_{-1}^{1-\delta} \frac{f(1,t) - f(\xi,t)}{(1-\xi)^{3/2}(1+\xi)^{1/2}} \, \mathrm{d}\xi + O(\nu) \\ &= \sqrt{\frac{2-\delta}{\delta}} \left(f(1,t) - f(1-\delta,t)\right) + d_0(t) \int_{-1}^{1-\delta} \hat{w}_0(d_0(t)\xi, t) \left(\frac{1+\xi}{1-\xi}\right)^{1/2} \mathrm{d}\xi + O(\nu) \\ &= \int_{-1}^{1} \hat{w}_0(d_0(t)\xi, t) \left(\frac{1+\xi}{1-\xi}\right)^{1/2} \mathrm{d}\xi + O(\sqrt{\delta}) + O(\nu) \\ &= 2 \int_{0}^{1} \frac{\hat{w}_0(d_0(t)\xi, t)}{\sqrt{1-\xi^2}} \, \mathrm{d}\xi + O(\sqrt{\delta}) + O(\nu) \\ &= 2 \int_{0}^{d_0(t)} \frac{\hat{w}_0(s,t)}{\sqrt{d_0(t)^2 - s^2}} \, \mathrm{d}s + O(\sqrt{\delta}) + O(\nu), \end{aligned}$$

where we made use of the fact that

$$f_\xi(\xi,t) = \frac{\partial}{\partial \xi} \left(f(\xi,t)\right) = \frac{\partial}{\partial \xi} \left(m(d_0(t)\xi,t)\right) = d_0(t)\hat{w}_0(d_0(t)\xi,t),$$

and that $\hat{w}_0(d_0(t)\xi, t)$ is even in ξ.

For J_2, we have that $\xi - 1 = O(\delta)$, so we make the change of variables $\xi = 1 - \nu\sigma$

and again expand to find

$$\begin{aligned}
J_2 &= \frac{1}{\sqrt{\nu}} \int_0^{\delta/\nu} \frac{f(1,t) - f(1-\nu\sigma,t)}{\sqrt{2\sigma + \nu\sigma^2}(\sigma+1)} \,\mathrm{d}\sigma \\
&= \frac{1}{\sqrt{\nu}} \int_0^{\delta/\nu} \frac{\nu d_0(t)\hat{w}_0(d_0(t),t)\sigma}{\sqrt{2\sigma}(1+\sigma)} + O(\nu^{3/2}) \,\mathrm{d}\sigma \\
&= \frac{\sqrt{\nu} d_0(t)\hat{w}_0(d_0(t),t)}{\sqrt{2}} \int_0^{\delta/\nu} \frac{\sqrt{\sigma}}{1+\sigma} \,\mathrm{d}\sigma + O(\delta\nu^{1/2}) \\
&= \sqrt{2} d_0(t)\hat{w}_0(d_0(t),t) \left(\sqrt{\delta} - \sqrt{\nu} \arctan\left(\sqrt{\frac{\delta}{\nu}} \right) \right) + O(\delta\nu^{1/2}) \\
&= O(\sqrt{\delta}) \ll J_1 \text{ as } \delta \to 0.
\end{aligned}$$

Hence the leading-order contribution to J comes from J_1, and the expansion of the integral I_3 in (B.5) as $\nu \to 0$ is

$$I_3 = -\frac{\pi m(d_0(t),t)}{\sqrt{2\nu} d_0(t)} + 2\int_0^{d_0(t)} \frac{\hat{w}_0(s,t)}{\sqrt{d_0(t)^2 - s^2}} \,\mathrm{d}s + O(\sqrt{\nu}). \tag{B.7}$$

B.4 Pressure

When determining the pressure, we need to find the solution for the integral I_4 from the solution for $H(\zeta,t)$ (3.62), given by

$$I_4 = \int_{-d_0(t)}^{d_0(t)} \frac{(s^2 - d_0(t)^2)^{1/2}}{s-\zeta} \,\mathrm{d}s = -\frac{1}{2} \oint_C \frac{(s^2 - d_0(t)^2)^{1/2}}{s-\zeta} \,\mathrm{d}s\,, \tag{B.8}$$

where C is the contour depicted in Figure B.1. We again smoothly deform C to $C' = C_R \cup C_\zeta$, as shown in Figure B.1, and find for C_ζ

$$-\frac{1}{2} \oint_{C_\zeta} \frac{(s^2 - d_0(t)^2)^{1/2}}{s-\zeta} \,\mathrm{d}s = -\frac{1}{2}(-2\pi i)(\zeta^2 - d_0(t)^2)^{1/2} = \pi i(\zeta^2 - d_0(t)^2)^{1/2};$$

expanding $R \gg 1$ in C_R gives,

$$\begin{aligned}
-\frac{1}{2} \oint_{C_R} \frac{(s^2 - d_0(t)^2)^{1/2}}{s-\zeta} \,\mathrm{d}s &= -\frac{1}{2} \int_0^{2\pi} \frac{(R^2 e^{2i\theta} - d_0(t)^2)^{1/2}}{Re^{i\theta} - \zeta} iRe^{i\theta} \,\mathrm{d}\theta \\
&= -\frac{i}{2} \int_0^{2\pi} Re^{i\theta} \left(1 + O(1/R^2)\right) \left(1 + \frac{\zeta}{Re^{i\theta}} + O(1/R^2)\right) \mathrm{d}\theta \\
&= -\frac{i}{2} \int_0^{2\pi} Re^{i\theta} + \zeta + O(1/R) \,\mathrm{d}\theta = -\frac{i}{2}(2\pi)\zeta + O(1/R) \\
&\to -\pi i\zeta \text{ as } R \to \infty.
\end{aligned}$$

Therefore the integral I_4 is given by

$$I_4 = \pi i(\zeta^2 - d(t)^2)^{1/2} - \pi i\zeta. \tag{B.9}$$

Bibliography

[1] Anderson, D. M., McFadden, G. B., and Wheeler, A. A. Diffuse-interface methods in fluid mechanics. *Annual Review of Fluid Mechanics 30*, 1 (1998), 139–165.

[2] Anderson, E., Bai, Z., Bischof, C., Blackford, S., Demmel, J., Dongarra, J., Du Croz, J., Greenbaum, A., Hammarling, S., McKenney, A., and Sorensen, D. *LAPACK Users' Guide*, third ed. Society for Industrial and Applied Mathematics, Philadelphia, PA, 1999.

[3] Ansys. Ansys Fluent website. `https://www.ansys.com/en-gb/products/fluids/ansys-fluent`. [Online; accessed 29-September-2022].

[4] Ashgriz, N., and Poo, J. FLAIR: Flux line-segment model for advection and interface reconstruction. *Journal of Computational Physics 93*, 2 (1991), 449–468.

[5] Aulisa, E., Manservisi, S., Scardovelli, R., and Zaleski, S. Interface reconstruction with least-squares fit and split advection in three-dimensional Cartesian geometry. *Journal of Computational Physics 225*, 2 (2007), 2301–2319.

[6] Basilisk. Basilisk website. `http://basilisk.fr/`. [Online; accessed 29-September-2022].

[7] Batchelor, G. K. *An Introduction to Fluid Dynamics*. Cambridge University Press, 1999.

[8] Bell, J. B., Colella, P., and Glaz, H. M. A second-order projection method for the incompressible Navier-Stokes equations. *Journal of Computational Physics 85*, 2 (1989), 257–283.

[9] Bennemann, M., Backhaus, S., Scholz, I., Park, D., Mayer, J., and Baumgartner, W. Determination of the Young's modulus of the epicuticle of the smooth adhesive organs of Carausius morosus using tensile testing. *Journal of Experimental Biology 217*, 20 (2014), 3677–3687.

[10] Bonn, D., Eggers, J., Indekeu, J., Meunier, J., and Rolley, E. Wetting and spreading. *Reviews of Modern Physics 81*, 2 (5 2009), 739–805.

[11] Brackbill, J. U., Kothe, D. B., and Zemach, C. A continuum method for modeling surface tension. *Journal of Computational Physics 100*, 2 (1992), 335–354.

[12] Brown, J. W., and Churchill, R. V. *Complex variables and applications*. McGraw-Hill,, 2009.

[13] Chen, S., and Doolen, G. D. Lattice Boltzmann method for fluid flows. *Annual Review of Fluid Mechanics 30*, 1 (1998), 329–364.

[14] Chorin, A. J. On the convergence of discrete approximations to the Navier-Stokes equations. *Mathematics of Computation 23*, 106 (1969), 341–353.

[15] Cimpeanu, R., and Moore, M. R. Early-time jet formation in liquid-liquid impact problems: theory and simulations. *Journal of Fluid Mechanics 856* (12 2018), 764–796.

[16] Cimpeanu, R., and Papageorgiou, D. T. Three-dimensional high speed drop impact onto solid surfaces at arbitrary angles. *International Journal of Multiphase Flow 107* (2018), 192–207.

[17] Cointe, R. Two-Dimensional Water-Solid Impact. *Journal of Offshore Mechanics and Arctic Engineering 111*, 2 (5 1989), 109.

[18] Cointe, R., and Armand, J. L. Hydrodynamic impact analysis of a cylinder. *Journal of Offshore Mechanics and Arctic Engineering 109*, 3 (1987), 237–243.

[19] Cointe, R., Fontaine, E., Molin, B., and Scolan, Y. On energy arguments applied to the hydrodynamic impact force. *Journal of Engineering Mathematics 48*, 3/4 (4 2004), 305–319.

[20] COMSOL Multiphysics. COMSOL Multiphysics website. `https://www.comsol.com/`. [Online; accessed 29-September-2022].

[21] Derby, B. Inkjet Printing of Functional and Structural Materials: Fluid Property Requirements, Feature Stability, and Resolution. *Annual Review of Materials Research 40*, 1 (6 2010), 395–414.

[22] Dobaj, K. Simulation analysis of the EUSAMA Plus suspension testing method including the impact of the vehicle untested side. In *IOP Conference Series: Materials Science and Engineering* (2016), vol. 148, IOP Publishing, p. 012034.

[23] du Chéné, A., Min, C., and Gibou, F. Second-order accurate computation of curvatures in a level set framework using novel high-order reinitialization schemes. *Journal of Scientific Computing 35*, 2 (2008), 114–131.

[24] Eggers, J., Fontelos, M. A., Josserand, C., and Zaleski, S. Drop dynamics after impact on a solid wall: Theory and simulations. *Physics of Fluids 22*, 6 (2010).

[25] Fudge, B. D., Cimpeanu, R., and Castrejón-Pita, A. A. Dipping into a new pool: The interface dynamics of drops impacting onto a different liquid. *Physical Review E 104*, 6 (2021), 065102.

[26] Gakhov, F. D. *Boundary Value Problems*. Elsevier, 1966.

[27] Gart, S., Mates, J. E., Megaridis, C. M., and Jung, S. Droplet impacting a cantilever: A leaf-raindrop system. *Physical Review Applied 3*, 4 (2015), 044019.

[28] Gaylard, A. P., Kirwan, K., and Lockerby, D. A. Surface contamination of cars: A review. *Proceedings of the Institution of Mechanical Engineers, Part D: Journal of Automobile Engineering 231*, 9 (8 2017), 1160–1176.

[29] Gillow, K. *Codimension-Two Free Boundary Problems*. PhD thesis, University of Oxford, 1998.

[30] Good, R. J. Contact angle, wetting, and adhesion: a critical review. *Journal of Adhesion Science and Technology 6*, 12 (1992), 1269–1302.

[31] Gradshteyn, I. S., and Ryzhik, I. M. *Table of integrals, series, and products*. Academic press, 2014.

[32] Greenhow, M. Wedge entry into initially calm water. *Applied Ocean Research 9*, 4 (10 1987), 214–223.

[33] Hansson, T., Oostenbrink, C., and van Gunsteren, W. Molecular dynamics simulations. *Current Opinion in Structural Biology 12*, 2 (2002), 190–196.

[34] Harlow, F. H. The particle-in-cell computing method for fluid dynamics. *Methods in Computational Physics 3* (1964), 319–343.

[35] Harlow, F. H., and Welch, J. E. Numerical calculation of time-dependent viscous incompressible flow of fluid with free surface. *The Physics of Fluids 8*, 12 (1965), 2182–2189.

[36] Harrel, S. K., and Molinari, J. Aerosols and splatter in dentistry: A brief review of the literature and infection control implications. *Journal of the American Dental Association 135*, 4 (2004), 429–437.

[37] Heil, M., and Hazel, A. L. oomph-lib - An Object-Oriented Multi-Physics Finite-Element Library. In *Fluid-structure interaction*. Springer, 2006, pp. 19–49.

[38] Henman, N. I. J., Smith, F. T., and Tiwari, M. K. Pre-impact dynamics of a droplet impinging on a deformable surface. *Physics of Fluids 33* (9 2021), 092119.

[39] Hicks, P. D., and Purvis, R. Air cushioning and bubble entrapment in three-dimensional droplet impacts. *Journal of Fluid Mechanics 649* (4 2010), 135–163.

[40] Hicks, P. D., and Purvis, R. Air cushioning in droplet impacts with liquid layers and other droplets. *Physics of Fluids 23*, 6 (6 2011), 062104.

[41] Hicks, P. D., and Purvis, R. Gas-cushioned droplet impacts with a thin layer of porous media. *Journal of Engineering Mathematics 102*, 1 (2 2017), 65–87.

[42] Holmes, M. H. *Introduction to Perturbation Methods*, vol. 20. Springer Science & Business Media, 2012.

[43] Howell, P., Kozyreff, G., and Ockendon, J. *Applied Solid Mechanics*. Cambridge Texts in Applied Mathematics. Cambridge University Press, 2008.

[44] Howison, S. D., Ockendon, J. R., Oliver, J. M., Purvis, R., and Smith, F. T. Droplet impact on a thin fluid layer. *Journal of Fluid Mechanics 542* (10 2005), 1–23.

[45] Howison, S. D., Ockendon, J. R., and Wilson, S. K. Incompressible water-entry problems at small deadrise angles. *Journal of Fluid Mechanics 222* (1 1991), 215–230.

[46] Howland, C. J., Antkowiak, A., Castrejón-Pita, J. R., Howison, S. D., Oliver, J. M., Style, R. W., and Castrejón-Pita, A. A. It's harder to splash on soft solids. *Physical Review Letters 117* (10 2016), 184502.

[47] Jasak, H., Jemcov, A., Tukovic, Z., et al. OpenFOAM: A C++ library for complex physics simulations. In *International workshop on coupled methods in numerical dynamics* (2007), vol. 1000, IUC Dubrovnik Croatia, pp. 1–20.

[48] Josserand, C., and Thoroddsen, S. Drop Impact on a Solid Surface. *Annual Review of Fluid Mechanics 48*, 1 (1 2016), 365–391.

[49] Khabakhpasheva, T. I., and Korobkin, A. A. Splashing of liquid droplet on a vibrating substrate. *Physics of Fluids 32*, 12 (2020), 122109.

[50] Knoche, M. Effect of droplet size and carrier volume on performance of foliage-applied herbicides. *Crop Protection 13*, 3 (1994), 163–178.

[51] Korobkin, A. A. Formulation of penetration problem as a variational inequality. *Dinamika Sploshnoi Sredy 58* (1982), 73–79.

[52] Korobkin, A. A. Wave impact on the center of an Euler beam. *Journal of Applied Mechanics and Technical Physics 39* (9 1998), 770–781.

[53] Korobkin, A. A., Ellis, A. S., and Smith, F. T. Trapping of air in impact between a body and shallow water. *Journal of Fluid Mechanics 611* (9 2008), 365–394.

[54] Korobkin, A. A., and Khabakhpasheva, T. I. Regular wave impact onto an elastic plate. *Journal of Engineering Mathematics 55*, 1-4 (2006), 127–145.

[55] Korobkin, A. A., and Pukhnachov, V. V. Initial asymptotics in problem of blunt body entrance into liquid. In *Proceedings of 3rd Int. Conf. Numer. Ship Hydrodyn.* (1981).

[56] Korobkin, A. A., and Pukhnachov, V. V. Initial Stage Of Water Impact. *Annual Review of Fluid Mechanics 20*, 1 (1988), 159–185.

[57] Korobkin, A. A., and Scolan, Y.-M. Three-dimensional theory of water impact. Part 2. Linearized Wagner problem. *Journal of Fluid Mechanics 549* (2006), 343–373.

[58] Mandre, S., Mani, M., and Brenner, M. P. Precursors to splashing of liquid droplets on a solid surface. *Phys. Rev. Lett. 102* (Mar 2009), 134502.

[59] Mirjalili, S., Jain, S. S., and Dodd, M. S. Interface-capturing methods for two-phase flows: An overview and recent developments. *Center for Turbulence Research: Annual Research Briefs*, 1 (2017), 117–135.

[60] Mitchell, A. R., and Griffiths, D. F. *The Finite Difference Method in Partial Differential Equations*, 1 ed. Wiley, 1980.

[61] Monaghan, J. J. Smoothed particle hydrodynamics. *Annual review of Astronomy and Astrophysics 30* (1992), 543–574.

[62] Moore, M. R. *New mathematical models for splash dynamics.* PhD thesis, University of Oxford, 2014.

[63] Moore, M. R. Introducing pre-impact air-cushioning effects into the Wagner model of impact theory. *Journal of Engineering Mathematics 129*, 1 (2021), 1–23.

[64] Mundo, C., Sommerfeld, M., and Tropea, C. Droplet-wall collisions: Experimental studies of the deformation and breakup process. *International Journal of Multiphase Flow 21*, 2 (1995), 151–173.

[65] Negus, M. J., Moore, M. R., Oliver, J. M., and Cimpeanu, R. Droplet impact onto a spring-supported plate: analysis and simulations. *Journal of Engineering Mathematics 128* (6 2021), 3.

[66] Oliver, J. M. *Water entry and related problems.* PhD thesis, University of Oxford, 2002.

[67] Osher, S., and Sethian, J. A. Fronts propagating with curvature-dependent speed: Algorithms based on Hamilton-Jacobi formulations. *Journal of Computational Physics 79*, 1 (1988), 12–49.

[68] Palacios, J., Hernández, J., Gómez, P., Zanzi, C., and López, J. Experimental study of splashing patterns and the splashing/deposition threshold in drop impacts onto dry smooth solid surfaces. *Experimental Thermal and Fluid Science 44* (1 2013), 571–582.

[69] Pegg, M. *Impact of liquid droplets with deformable surfaces.* PhD thesis, University of East Anglia, 2019.

[70] Pegg, M., Purvis, R., and Korobkin, A. Droplet impact onto an elastic plate: a new mechanism for splashing. *Journal of Fluid Mechanics 839* (3 2018), 561–593.

[71] Pegg, M., Purvis, R., and Korobkin, A. Droplet impact onto an elastic plate: a new mechanism for splashing. *Journal of Fluid Mechanics 839* (3 2018), 561–593.

[72] Pepper, R. E., Courbin, L., and Stone, H. A. Splashing on elastic membranes: The importance of early-time dynamics. *Physics of Fluids 20* (8 2008), 082103.

[73] Peskin, C. S. The immersed boundary method. *Acta numerica 11* (2002), 479–517.

[74] Philippi, J., Lagrée, P.-Y., and Antkowiak, A. Drop impact on a solid surface: short-time self-similarity. *Journal of Fluid Mechanics 795* (5 2016), 96–135.

[75] Popinet, S. Gerris: A tree-based adaptive solver for the incompressible Euler equations in complex geometries. *Journal of Computational Physics 190*, 2 (2003), 572–600.

[76] Popinet, S. An accurate adaptive solver for surface-tension-driven interfacial flows. *Journal of Computational Physics 228*, 16 (2009), 5838–5866.

[77] Popinet, S. A quadtree-adaptive multigrid solver for the Serre-Green-Naghdi equations. *Journal of Computational Physics 302* (12 2015), 336–358.

[78] Renardy, Y., and Renardy, M. PROST: A parabolic reconstruction of surface tension for the volume-of-fluid method. *Journal of Computational Physics 183*, 2 (2002), 400–421.

[79] Ritchie, D., and Kernighan, B. *The C programming language*. Bell Laboratories, 1988.

[80] Scardovelli, R., and Zaleski, S. Direct Numerical Simulation of Free-Surface and Interfacial Flow. *Annual Review of Fluid Mechanics 31*, 1 (1999), 567–603.

[81] Scolan, Y. M. Hydroelastic behaviour of a conical shell impacting on a quiescent-free surface of an incompressible liquid. *Journal of Sound and Vibration 277*, 1-2 (10 2004), 163–203.

[82] Scolan, Y.-M., and Korobkin, A. Energy distribution from vertical impact of a three-dimensional solid body onto the flat free surface of an ideal fluid. *Journal of Fluids and Structures 17*, 2 (2 2003), 275–286.

[83] Smith, F. T., Li, L., and Wu, G. X. Air cushioning with a lubrication/inviscid balance. *Journal of Fluid Mechanics 482*, 482 (5 2003), 291–318.

[84] Sneddon, I. N. *Mixed boundary value problems in potential theory*. North-Holland, 1966.

[85] Sussman, M., and Puckett, E. G. A coupled level set and volume-of-fluid method for computing 3D and axisymmetric incompressible two-phase flows. *Journal of Computational Physics 162*, 2 (2000), 301–337.

[86] Sussman, M., Smereka, P., and Osher, S. A level set approach for computing solutions to incompressible two-phase flow. *Journal of Computational physics 114*, 1 (1994), 146–159.

[87] Thom, A. The flow past circular cylinders at low speeds. *Proceedings of the Royal Society of London. Series A, Containing Papers of a Mathematical and Physical Character 141*, 845 (1933), 651–669.

[88] Thoraval, M. J., Takehara, K., Etoh, T. G., Popinet, S., Ray, P., Josserand, C., Zaleski, S., and Thoroddsen, S. T. Von Kármán vortex street within an impacting drop. *Physical Review Letters 108* (6 2012), 264506.

[89] Thoroddsen, S. T. The ejecta sheet generated by the impact of a drop. *Journal of Fluid Mechanics 451* (1 2002), 373–381.

[90] Thoroddsen, S. T., Etoh, T. G., and Takehara, K. Air entrapment under an impacting drop. *Journal of Fluid Mechanics* (3 2003), 125–134.

[91] Tryggvason, G., Scardovelli, R., and Zaleski, S. *Direct numerical simulations of gas–liquid multiphase flows*. Cambridge University Press, 2011.

[92] van Brakel, J. P. Robust peak detection algorithm (using z-scores). `https://stackoverflow.com/questions/22583391/peak-signal-detection-in-realtime-timeseries-data`. [Online; accessed 29-September-2022].

[93] von Kármán, T. The impact on seaplane floats during landing. *National Advisory Committee for Aeronautics Technical Notes* (1929), 321.

[94] Wagner, H. Über Stoß- und Gleitvorgänge an der Oberfläche von Flüssigkeiten. *ZAMM - Zeitschrift für Angewandte Mathematik und Mechanik 12* (1932), 193–215.

[95] Weisensee, P. B., Ma, J., Shin, Y. H., Tian, J., Chang, Y., King, W. P., and Miljkovic, N. Droplet impact on vibrating superhydrophobic surfaces. *Physical Review Fluids 2*, 10 (2017), 103601.

[96] Wildeman, S., Visser, C. W., Sun, C., and Lohse, D. On the spreading of impacting drops. *Journal of Fluid Mechanics 805* (2016), 636–655.

[97] Wilson, S. K. *The mathematics of ship slamming*. PhD thesis, University of Oxford, 1989.

[98] Wilson, S. K. A mathematical model for the initial stages of fluid impact in the presence of a cushioning fluid layer. *Journal of Engineering Mathematics 25*, 3 (8 1991), 265–285.

[99] Worthington, A. M. On the forms assumed by drops of liquids falling vertically on a horizontal plate. *Proceedings of the Royal Society of London 25*, 171-178 (12 1877), 261–272.

[100] Xu, L. Liquid drop splashing on smooth, rough, and textured surfaces. *Physical Review E - Statistical, Nonlinear, and Soft Matter Physics 75*, 5 (2007).

[101] Xu, L., Zhang, W. W., and Nagel, S. R. Drop splashing on a dry smooth surface. *Physical Review Letters 94*, 18 (2005).

[102] Yarin, A. Drop Impact Dynamics: Splashing, Spreading, Receding, Bouncing.... *Annual Review of Fluid Mechanics 38*, 1 (2006), 159–192.

[103] Yokoi, K., Vadillo, D., Hinch, J., and Hutchings, I. Numerical studies of the influence of the dynamic contact angle on a droplet impacting on a dry surface. *Physics of Fluids 21*, 7 (2009), 072102.